

# NOTES FOR COMPUTATIONAL MODELING IN ELECTRONICS AND BIOMATHEMATICS

Edited by

**Riccardo Sacco**

Politecnico di Milano, Dipartimento di Matematica, Piazza  
Leonardo da Vinci 32, 20133 Milano, Italy

**Giovanna Guidoboni**

University of Missouri, Department of Electrical Engineering  
and Computer Science, Department of Mathematics, 201 Naka  
Hall, Columbia, 65211, MO, USA

**Aurelio Giancarlo Mauri**

Politecnico di Milano, Dipartimento di Matematica, Piazza  
Leonardo da Vinci 32, 20133 Milano, Italy Micron, Tecnology  
and Development, Via Trento 36, 20871 MB, Italy

“Notes” — 2019/5/17 — 17:39 — page ii — #2

# CONTENTS

## Contents

iii

<b>1. Modeling Fundation</b>	1
1.1. Modeling approaches	1
1.1.1. <i>Physical models</i>	2
1.1.2. <i>Animal models</i>	4
1.1.3. <i>Conceptual models</i>	7
1.1.4. <i>Mathematical models</i>	8
1.2. Synergy between modeling approaches in Life Sciences	13
1.3. Foundations of numerical modeling	14
1.3.1. <i>The modeling step</i>	14
1.3.2. <i>The approximation step</i>	15
1.3.3. <i>The discretization error</i>	18
1.3.4. <i>The equivalence theorem</i>	19
1.3.5. <i>Floating-point numbers</i>	20
1.3.6. <i>The chain of errors</i>	21
1.3.7. <i>Example: choice of the numerical model</i>	23
<b>2. Physics fundation</b>	27
2.1. Conservation principles and balance laws in classical mechanics	27
2.1.1. <i>Balance Laws</i>	27
2.2. Charged material points and their motion	27
2.3. The Newton laws of motion	30
2.4. The Newton laws, work, power and energy	32
2.5. Laws of thermodynamics	33
2.5.1. <i>The thermodynamic approach</i>	34
2.5.2. <i>The concept of work in thermodynamics</i>	35
2.5.3. <i>The concept of heat in thermodynamics</i>	37
2.5.4. <i>The first law of thermodynamics</i>	38
2.5.5. <i>Energy balance law</i>	39
2.6. Laws of electromagnetism	40
2.6.1. <i>The Faraday experiment</i>	41
2.6.2. <i>The Ampère experiment</i>	43
2.6.3. <i>The Gauss law</i>	44
2.6.4. <i>Absence of magnetic monopole</i>	45
2.6.5. <i>The Maxwell equations in integral form</i>	46

iii

<i>2.6.6. The Maxwell equations in local form</i>	47
<i>2.6.7. Mathematical properties of the Maxwell equations</i>	48
<i>2.6.8. Energy balance law associated with the Maxwell equations</i>	50
<b>3. Model reduction for current flow in a circuit</b>	53
3.1. The vector potential	53
3.2. Nondimensionalization and reduced Maxwell equations	54
3.3. Derivation of the Kirchhoff laws for currents and voltages	56
<i>3.3.1. The Kirchhoff current law</i>	56
<i>3.3.2. The Kirchhoff voltage law</i>	57
<b>4. Model Reduction for flow rate in a tube: electric analogy to fluid flow</b>	61
4.1. Hydraulic resistors	61
<i>4.1.1. Linear case: Poiseuille law</i>	61
<i>4.1.2. Nonlinear case: deformable tubes</i>	66
4.2. Hydraulic capacitors	73
<i>4.2.1. Tubes as hydraulic capacitors</i>	73
4.3. Hydraulic inductors	74
<b>5. Model reduction in cellular electrophysiology</b>	77
5.1. Geometrical representation of a cell and its membrane	77
5.2. Reduced order modeling of the cell membrane	77
<i>5.2.1. Local and Whole ODE models</i>	84
5.3. Transmembrane current models	87
<i>5.3.1. Thermodynamic equilibrium for a single ion species</i>	88
<i>5.3.2. The linear resistor model</i>	89
<i>5.3.3. The Goldman-Hodgkin-Katz model</i>	90
<i>5.3.4. A generalized nonlinear resistor model</i>	93
5.4. The Hodgkin-Huxley model	95
5.5. The cable equation	98
<i>5.5.1. The geometric setting</i>	99
<i>5.5.2. Electric equivalent representation</i>	100
<i>5.5.3. The cable equation model</i>	102
<b>6. Reduced order model for cellular functions: the Astrocyte calcium dynamics examples</b>	105
6.1. Reduced models for cell functionalities	105
6.2. Mathematical model of cytosolic calcium dynamics	107
<i>6.2.1. Constitutive relations for the cytosolic calcium fluxes</i>	109
<i>6.2.2. Model of IP<sub>3</sub> dynamics</i>	111
<i>6.2.3. Simulation of the dynamics of free cytosolic calcium in an astrocyte</i>	111

<b>7. General approach to continuum media</b>	117
7.1. Placements, material volumes, mass and material particles	117
7.2. Balance law in integral form	120
<i>7.2.1.Balance law in integral form for a scalar physical quantity</i>	121
<i>7.2.2.Balance laws in integral form for a vector-valued physical quantity</i>	124
<i>7.2.3.Again on Balance of energy</i>	126
7.3. Balance laws in local form	127
<i>7.3.1.Balance of mass</i>	127
<i>7.3.2.Balance of electric charge</i>	128
<i>7.3.3.Balance of energy</i>	128
<i>7.3.4.Balance of linear momentum</i>	129
<i>7.3.5.Balance of angular momentum</i>	130
<i>7.3.6.Final formulation of the energy balance law</i>	130
<b>8. Homogeneous mixtures</b>	133
8.1. Homogeneous mixtures	133
8.2. Balance laws for multicomponent mixtures	134
<i>8.2.1.Balance of mass</i>	134
<i>8.2.2.Balance of electric charge</i>	135
<i>8.2.3.Balance of linear momentum</i>	136
<i>8.2.4.Balance of angular momentum</i>	138
<i>8.2.5.Balance of energy</i>	138
<i>8.2.6.Summary of balance laws in Eulerian local form</i>	139
<b>9. Assiomatic derivaton of Poisson-Nernst-Planck and Drift-Diffusion systems</b>	141
9.1. Kinetic description of ions	141
9.2. From kinetic description to continuum approach via mixture theory	144
9.3. Relationship between the motion of charged particles in the continuum approach and the Maxwell equations	145
9.4. Ions charged fluid as an example of Homogeneous charged mixtures	148
9.5. The velocity-extended Poisson-Nernst-Planck model	154
9.6. The Poisson-Nernst-Planck model	157
9.7. The Drift-Diffusion model for semiconductors	159
<b>10.The Poisson-Nernst-Planck model in 1D-framework</b>	163
10.1. 1-D geometrical model	163
10.2. Biophysical assumptions for 1-D framework	165
10.3. Calculation of the Boundary conditions at channel openings	166
10.4. The PNP model in 1D	168
<i>10.4.1Electrochemical potential with ions space occupation</i>	170

<b>11.The Poisson-Nernst-Planck model of ion pumps and exchangers</b>	173
11.1. Ion pumps and exchangers	173
11.1.1The sodium-potassium ATPase pump	173
11.1.2The calcium-sodium exchanger	174
11.1.3The chloride-bicarbonate exchanger	174
11.1.4The sodium-proton exchanger	174
11.2. The mathematical model of ion pumps and exchangers	174
11.2.1Geometrical description of the problem	176
11.2.2Boundary and initial conditions	178
11.2.3The volumetric force acting on the intrapore fluid	181
<b>12.The Drift Diffusion model</b>	183
12.1. Fermi distribution and Thermal equilibrium	183
12.1.1Intrinsic semiconductor	183
12.1.2Extrinsic semiconductor	186
12.1.3Carrier densities at nonequilibrium condition	188
12.2. Geometrical model and boundary conditions	189
12.3. Physical model for mobility and Recombination and generation terms	192
12.3.1Carrier Mobility	192
12.3.2Generation-Recombination Phenomena	195
12.3.3Bandgap Narrowing and Intrinsic Concentration	199
12.3.4Driving Force	201
<b>13.Numerical Discretization and Solution Algorithms of the Drift Diffusion system</b>	203
13.1. Abstract Newton's Method	203
13.2. Gummel Map iteration algorithm	205
13.2.1Non Linear Poisson Equation	205
13.2.2Linearized continuity equations	207
13.2.3Convergence evaluation	208
13.3. Fully Coupled Newton algorithm	209
13.4. Weak Formulation of the Drift Diffusion system	210
13.4.1Weak form of the Nonlinear Poisson Equation	210
13.4.2Weak form of the Linearized Electron Continuity equation	212
13.5. Finite Element Approximation of Non Linear Poisson equation	214
<b>14.Modeling of advanced non-volatile memory devices</b>	217
14.1. Introduction on semiconductor memory devices	217
14.1.1Basic concepts of nonvolatile memories	217
14.1.2Emerging memories	220
14.2. Modeling of Charge Trap memory devices	221
14.2.1Mathematical model	222

14.3. Modeling of Mass Transport in PCM device	226
14.3.1 Mathematical model for the atomic migration	236
14.4. Modeling of Conductive Bridge RAM device	240
14.4.1 Mathematical model	244
<b>A. Elements of mathematics and numerics</b>	<b>249</b>
A.1. Theorems of vector calculus	249
A.1.1. The divergence theorem	249
A.1.2. The Stokes theorem	250
A.1.3. Leibnitz transport theorem	251
A.1.4. Reynolds transport theorem	251
A.2. Numerical solution of ordinary differential equations	251
A.2.1. The Cauchy problem	251
A.2.2. Numerical approximation: general concepts	252
A.3. The Lax-Milgram Lemma	257



# CHAPTER 1

## Modeling Fundation

The present chapter aims at the foundations of computational methods, that is, the approaches that are usually employed to *numerically compute* the solutions of the mathematical models devised to represent the physical problem of interest, since their *exact computation through analytical techniques* is not possible or, at least, may be considerably difficult to obtain and/or to handle (think, for example, at the solution of the heat equation in a material medium by series expansion through special functions). Computational methods belong to the more general branch of mathematics that is referred to as  
emphnumerical mathematics.

Here below we introduce the fundamental concepts of numerical mathematics, namely (i) the notion of numerical model, which is the approximate version of a mathematical model (see Chapter ??); and (ii) the notion of convergence and its two constitutive ingredients, consistency and stability, which are the quantitative tools for verifying the accuracy of the numerical model versus the mathematical model.

For more details on the material treated in the present chapter we refer the interested reader to [98] and the extensive bibliography cited therein.

In this chapter we will review some basic concepts related to modeling and the many different ways in which modeling can be used in applications. Even though this book focuses on one specific approach to modeling, namely mathematical modeling based on physics, we strongly believe that a synergistic combination of different modeling approaches yields the key to true groundbreaking advances in science and technology.

### 1.1. Modeling approaches

Modeling means, in a broad sense, to create a sort of facsimile, henceforth referred to as *the model*, of a complex system that can be used to study its main features and its behavior under specific conditions. Many different modeling approaches are used for investigation in applied sciences, bioengineering and life sciences. Some major examples include physical models, animal models, conceptual models and mathemat-

ical models. In the remainder of the chapter we provide a description of each of these modeling approaches with specific examples in bioengineering and semiconductor technology.

### 1.1.1. Physical models

Physical models refer to physical replicas of the system under consideration. Physical models are utilized extensively in engineering and architecture, for example to visualize and illustrate important features of the design of structures and buildings, see e.g. [40, 57, 85], or to develop and validate innovative anti-seismic techniques for civil structures, industrial plants, cultural heritage or masterpieces, see, e.g., [59, 78].

Physical models may also be utilized in the life sciences to reproduce some of the main features of a living system and study them in a controlled experimental environment. An example of physical modeling in this context is reported in Figure 1.1, showing a mock circulatory flow loop designed to reproduce and study flow conditions similar to those in the human abdominal aorta [22]. Alterations in blood flow dynamics through the aorta may lead to an abnormal enlargement of the artery, also called *aneurysm*, which is asymptomatic and whose rupture often leads to sudden death [3]. The blood flow in the aorta results from the combined action of local factors, such as the biomechanical properties of the arterial wall, and nonlocal factors, such as the heart function, the compliance of the cardiovascular system and the peripheral vascular resistance. Thus, a physical model, such as that shown in Figure 1.1, can be used to study experimentally the individual contributions of different factors, as well as their complex interaction. To this end, the flow loop was designed to include a left ventricular assist device (LVAD Heart Mate, Thoratec Corp., Woburn, MA) modeling the ventricular pump (Figure 1.1(c)), a latex tube segment modeling the abdominal aorta (Figure 1.1 (d)), two compliance chambers and a reservoir modeling vascular compliance and resistance (Figure 1.1(a,c)). Pressure values at the inlet and outlet of the test segment were measured via pressure transducers. Fluid velocity at different locations inside the latex tube was measured via ultrasonic imaging and Doppler methods. Examples of pressure measurements are reported in Figure 1.2.

Physical models have the great advantage of being illustrative, providing complete control over experiments and measurements, allowing adjustment of physical components and allowing modification of system’s architecture. However, physical models are inherently a simplified version of reality and cannot account for all mechanisms that are at play in real situations. In particular, it is very difficult to extrapolate whether a physical model would function under the same conditions as a living organism, namely, *in vivo*. For example, the latex tube utilized in the mock circulatory flow loop to model the abdominal aorta, Figure 1.1(d), cannot actively alter its diameter in response to metabolic stimuli associated with the local levels of oxygen, carbon

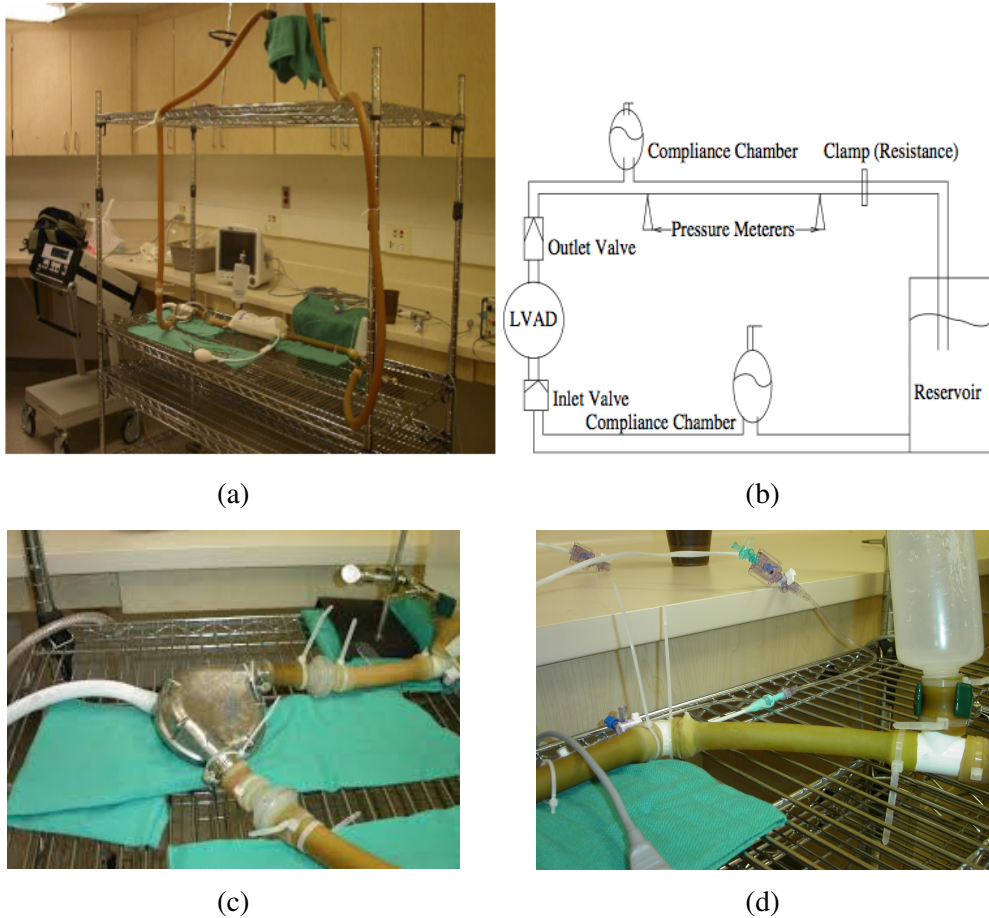


**Figure 1.1** (a) Physical model reproducing the flow of blood in the abdominal aorta, one of the major arteries in our body. (b) Schematic of the mock circulatory flow loop. (c) Left ventricular assist device utilized to model the heart pump. (d) Latex tube utilized to model the abdominal aorta. This flow loop has been developed at the Research Laboratory of the Texas Heart Institute. The figures in panels (a) and (b) are reproduced from S. Čanić, J. Tambača, G. Guidoboni, A. Mikelić, C. J. Hartley, D. Rosenstrauch. *Modeling viscoelastic behavior of arterial walls and their interaction with pulsatile blood flow*. SIAM Journal on Applied Mathematics, 67(1), 164-193 (2006). The figures in panels (c) and (d) are courtesy of Prof. S. Čanić (Department of Mathematics, University of Houston).

dioxide, nitric oxide and endothelin, which is indeed something that a real aorta can do thanks to the activity of various cells (e.g. smooth muscle cells and endothelial cells) constituting its wall. The intertwined biophysical phenomena that govern the

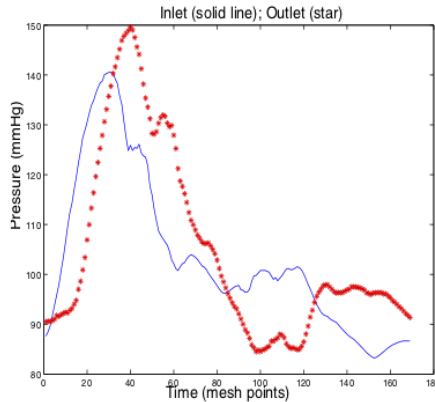


**Figure 1.2** Pressure measurements at the inlet and outlet sections of the test segment modeling the abdominal aorta in the mock circulatory flow loop. S. Čanić, Sunčica, J. Tambača, G. Guidoboni, A. Mikelić, C. J. Hartley, D. Rosenstrauch. *Modeling viscoelastic behavior of arterial walls and their interaction with pulsatile blood flow.* SIAM Journal on Applied Mathematics, 67(1), 164-193 (2006).

dynamics of living organisms can be observed *in vivo* by means of animal models, as discussed next.

### 1.1.2. Animal models

Animal models refer to the replication in an animal of a disease or injury that is similar to a human condition. Many different animal species have been utilized for biomedical research, including mice, dogs, pigs and monkeys. The conditions of interest might be inbred, induced or already existing in the animals. Animal models have been vital to most of the breakthroughs in modern medicine. For example, the research conducted by Frederick Banting showed that the isolates of pancreatic secretion were successful in treating diabetes in dogs. This led to the discovery of insulin in 1922, jointly with John Macleod and Charles Best, and the possibility of treating a previously lethal disease such as diabetes [116]. Another example is provided by the studies on rhesus monkeys conducted by Jonas Salk in the 1940s, which led to the isolation of the polio virus and the creation of a polio vaccine [11]. Since then, animal models have become common practice in biomedical and pharmacological research. By reproducing disease conditions similar to those in humans, animal models allow researchers to test hypotheses on disease processes and their potential treatments by performing measurements and experimental procedures *in vivo*, as this would not be possible on human subjects. For example, imaging chambers implanted in living animals, pre-

dominantly mice, allow researchers to study the hallmarks of cancer, namely the biological characteristics acquired during the initiation and progression of tumors, and to visualize tissues with cellular or subcellular resolution using intravital microscopy techniques [36]. Some illustrations of these techniques are reported in Figure 1.3.

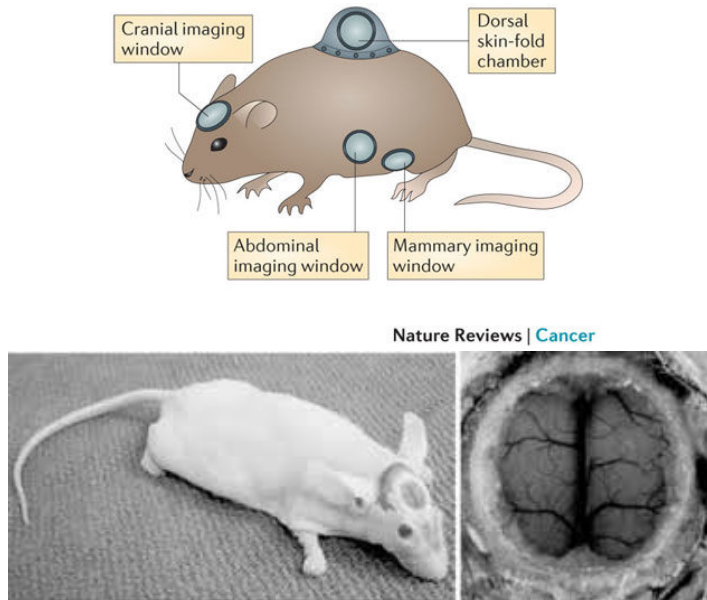


**Figure 1.3** Imaging chambers mounted on mice for intravital visualizations. The figure on the top panel is reproduced from S. I. J. Ellenbroek, J. Van Rheenen. *Imaging hallmarks of cancer in living mice*. *Nature Reviews Cancer*, 14(6), 406-418 (2014). The figure on the bottom panel is reproduced from D. Shepro. *Microvascular research: biology and pathology*, Vol. 1, Elsevier (2005).

Animal models generate a huge amount of data and information, often referred to as *Big Data* (see, e.g., [1, 5, 42]). Thanks to the present storage capabilities and efficient software database construction and organization, Big Data are made available to scientists for subsequent management and elaboration. However, the interpretation of Big Data still remains a challenging task since many different factors, such as hemodynamic, biomechanical and metabolic factors, naturally combine and interact in the physiology of a living organism to determine its functions, thereby making it extremely difficult to single out and characterize the pathogenic contributions associated with each factor in different conditions. A striking example, is the complex interaction between intraocular pressure, blood pressure, cerebrospinal fluid pressure and vascular regulation in glaucoma.

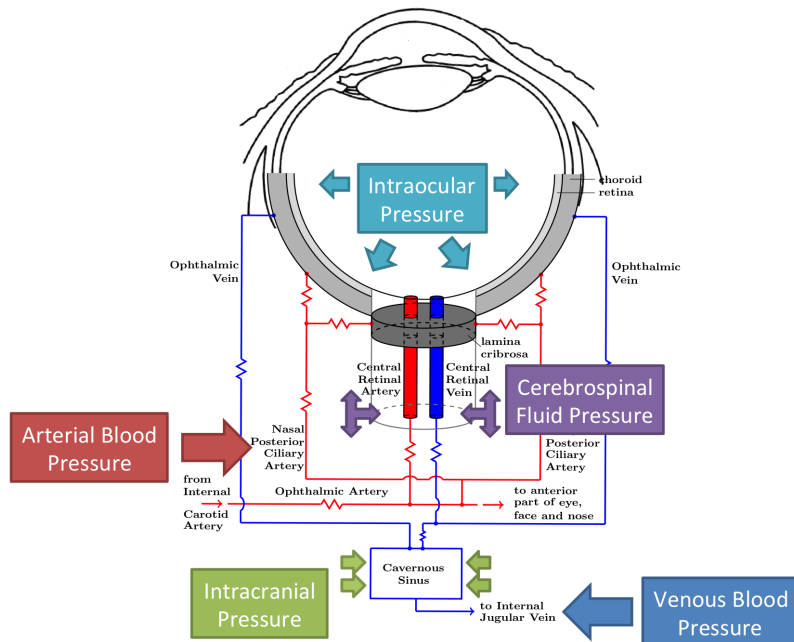


**Figure 1.4** Schematic representation of different factors contributing to ocular perfusion. J. C. Gross, A. Harris, B. A. Siesky, R. Sacco, A. Shah, G. Guidoboni. Mathematical modelling for novel treatment approaches to open-angle glaucoma. *Expert Review of Ophthalmology*, 12(6), 443–455 (2017).

Glaucoma is an optic neuropathy characterized by progressive retinal ganglion cell death, structural changes to the retina and optic nerve head, and irreversible visual field loss. Currently, elevated intraocular pressure (IOP) is the only treatable risk factor for glaucoma, despite overwhelming evidence that many additional factors are involved in the disease process, including alterations in blood pressure, cerebrospinal fluid pressure, intracranial pressure and vascular regulation [72], see Figure 1.4. At present, the only therapeutic strategies available to treat glaucoma are directed at lowering IOP, even though optimal target IOP levels for individual patients are controversial and many glaucoma patients continue to experience disease progression [52, 48, 73]. Furthermore, there are currently no successful therapeutic strategies for those glaucoma patients who suffer optic nerve damage and vision loss despite normal IOP [90, 23] (to date, these patients count over 25% of all glaucoma patients in the United States of America). Despite the fact that low blood pressure has been identified as a glaucoma risk factor, it remains unclear whether it is truly independent of altered IOP values [23]. Furthermore, experimental studies based on animal models have not been

capable, so far, to produce conclusive results regarding the interrelationship between IOP, blood pressure and glaucoma since the distributions of blood and cerebrospinal fluid pressures throughout the body, particularly in the eye, and the functionality of vascular regulation differ among species, thereby hindering the ability of translating experimental findings to humans [23].

Due to the complexity of the interaction among all factors involved in the system, the introduction of conceptual models can help clarify conjectures and mechanisms.

### 1.1.3. Conceptual models

Conceptual models refer to the *schematization of cause-effect relationships* that govern the behavior of a complex system.

In life sciences, conceptual models are often used to schematize chains of reactions and mechanisms regulating specific functions. An example of conceptual model in clinical research is reported in Figure 1.5, where the scheme provides a network of interplaying relations to interpret the causality behind the significance of vascular risk factors in glaucoma [115].

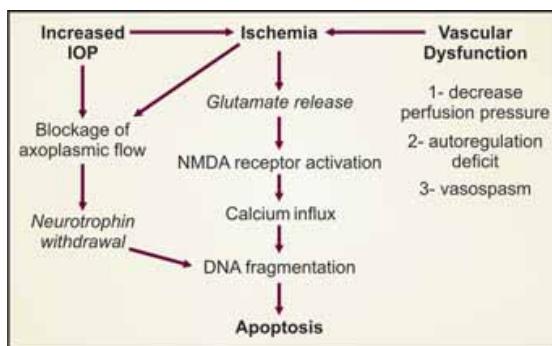


**Figure 1.5** Conceptual model for the causality behind the significance of vascular risk factors in glaucoma. B. Siesky, A. Harris, N. Kheradiya, C. Rospigliosi, L. McCranor, R. Ehrich. *The clinical significance of vascular factors in glaucoma*. Journal of Current Glaucoma Practice, 2, 12-17 (2007).

Another example of conceptual model in the field of biology is reported in Figure 1.6, where the scheme provides a detailed illustration of the biophysical mechanisms involved in the production of aqueous humor in the eye [68].

As pointed out above, conceptual models have the great advantage of illustrating cause-effect relationships and facilitating interpretation of complex interactions. However, conceptual models are not quantitative and, consequently, cannot predict how and to what extent the system behavior will be affected by alterations in specific mecha-

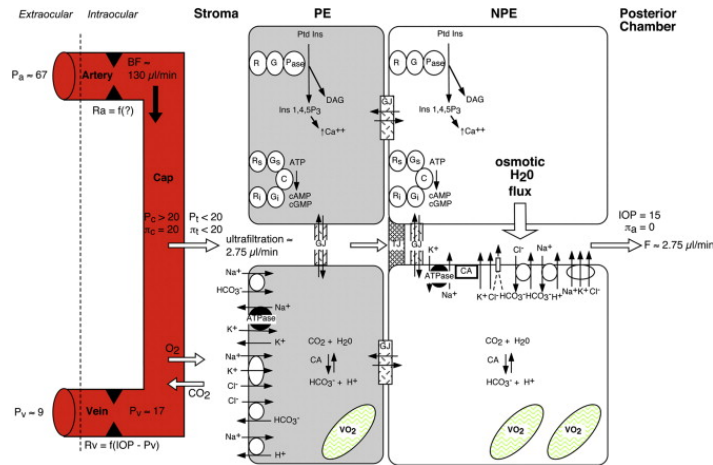


**Figure 1.6** Conceptual model for the biophysical mechanisms governing aqueous humor production in the eye. J. W. Kiel, M. Hollingsworth, R. Rao, M. Chen, H. A. Reitsamer. Ciliary blood flow and aqueous humor production. *Progress in Retinal and Eye Research*, 30(1), 1-17 (2011).

nisms. In this perspective, mathematical models can help provide quantitative tools to study the behavior of a complex system.

#### 1.1.4. Mathematical models

Mathematical models refer to *sets of mathematical equations and formulas* whose solutions describe the behavior of a complex system or the probability that a specific event occurs. There are two main types of mathematical models: data-driven models and mechanism-driven models.

*Data-driven models* aim at identifying patterns and trends within a given dataset. Many different techniques have been developed to achieve this goal, most of which are based on statistical methods. Data-driven models can handle very large datasets and include data acquired by means of physical models, animal models and studies on human subjects. The main outcome is the identification of *correlations* among relevant factors within the dataset. Even though recent developments of data-driven modeling techniques provide insights on how to infer causality beyond correlations, see, e.g., [58, 96], it remains very challenging to gain insights on the fundamental physical and biophysical mechanisms at play.

*Mechanism-driven models* aim at providing qualitative and quantitative assessments of the mechanisms that gave rise to the data in the first place. Mechanism-driven models are based on physical and biophysical principles, are *deterministic* in nature, can include stochastic effects and may involve very different mathematical methods

(e.g., algebraic relationships, ordinary differential equations, partial differential equations, stochastic differential equations, ...). The main outcome of mechanism-driven models is the creation of a *virtual laboratory* that can be used to:

- *simulate* diverse scenarios and predict in a quantitative manner the system behavior, thereby allowing researchers to study the system virtually, test conjectures and formulate new ones;
- *compare* outcomes of existing studies involving physical models, animal models and human subjects with simulations, thereby offering unique opportunities to interpret real data based on conjectured physical and biophysical mechanisms;
- *identify* factors that have the strongest impact on the system behavior, thereby aiding the design of new experimental and clinical studies;
- *explore* a level of detail that often cannot be reached by experiments due to instrumental limitation, thereby allowing the investigation of *microscopic* variables that may significantly affect the *macroscopic* function of the system.

#### **1.1.4.1. Example: mechanism-driven models in medical research**

The work in [49] provides an example of how to utilize *mechanism-driven models* to shed some light on the complex interaction among risk factors in glaucoma. Specifically, a mathematical model is developed to simulate blood flow through the central retinal artery (CRA), central retinal vein (CRV) and retinal microvasculature as current flowing through a network of resistors and capacitors, as illustrated in Figure 1.7. Variable resistances describe active and passive diameter changes due to vascular regulation and intraocular pressure. The blood flow is (*i*) driven by the difference between input and output pressures (denoted by  $P_{in}$  and  $P_{out}$ , respectively); (*ii*) impeded by the action of intraocular pressure (IOP) and retrolaminar tissue pressure (RLTp); and (*iii*) modulated by vascular regulation.

The full details of the model can be found in [49]. In a nutshell, the model reduces to the solution of a nonlinear system of ordinary differential equations whose unknowns are the nodal pressures  $P_i$ ,  $i = 1, 2, 4, 5$ , namely:

$$\left\{ \begin{array}{l} C_1 \frac{dP_1}{dt} = G_1(P_{in} - P_1) - G_2(P_1 - P_2) \\ C_2 \frac{dP_2}{dt} = G_2(P_1 - P_2) - G_3(P_2 - P_4) \\ C_4 \frac{dP_4}{dt} = G_3(P_2 - P_4) - G_4(P_4 - P_5) \\ C_5 \frac{dP_5}{dt} = G_4(P_4 - P_5) - G_5(P_5 - P_{out}) \end{array} \right. \quad (1.1)$$

where the conductances  $G_i$ ,  $i = 1, \dots, 5$ , are determined by the linear and nonlinear resistances in the network. The model is used to simulate retinal blood flow for three

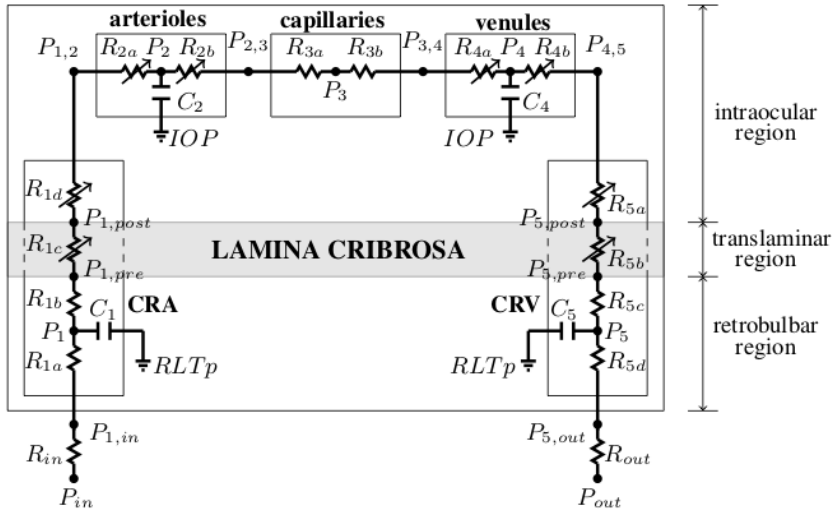


**Figure 1.7** Schematic representation of a mechanism-driven model to study the relationship between intraocular pressure (IOP), blood pressure and blood flow in the retina. G. Guidoboni, A. Harris, S. Cassani, J. Arciero, B. Siesky, A. Amireskandari, L. Tobe, P. Egan, I. Januleviciene, J. Park. *Intraocular pressure, blood pressure, and retinal blood flow autoregulation: a mathematical model to clarify their relationship and clinical relevance.* *Investigative Ophthalmology & Visual Science*, 55(7), 4105-4118 (2014).

theoretical patients with high, normal and low blood pressure. The model predicts that patients with high and normal blood pressure can regulate retinal blood flow as IOP varies between 15 and 23 mm Hg and between 23 and 29 mm Hg, respectively, whereas patients with low blood pressure do not adequately regulate blood flow if IOP is 15 mm Hg or higher. Thus, hemodynamic alterations would be impactful only if IOP changes occur outside of the regulating range, which, most importantly, depend on blood pressure. These theoretical predictions have been recently confirmed by the population-based study conducted by Tham et al. including nearly 10,000 individuals (nearly 20,000 eyes), who found that individuals exhibiting a combination of low blood pressure and elevated intraocular pressure had the highest probability of having glaucoma [117].

#### 1.1.4.2. Example: a mechanism-driven model in semiconductor technology research

Although this volume is focused on the study of problems arising in the context of bioengineering and life sciences, it is important to emphasize that mechanism-driven models are widely employed also in other areas of applied sciences and technology.

An important example is the use of mechanism-driven models in semiconductor technology development, where the progress of research may significantly impact and influence our everyday’s life. As a matter of fact, the continuous increase of electronic data storage capabilities has initiated the so-called *era of cloud computing* (see [7]), in which information (photos, written documents, bank transactions, etc.) is stored *somewhere* in the world but is always (in time) and everywhere (in space) available to *both* producer and user of the data. At the same time, the improvement of transistor performance (increase of operation frequency due to shrinking of device dimensions according to Moore’s law [87]) has increased supercomputing performance, thereby allowing the real-time solution of problems that was almost unaffordable just few years ago, such as in the case of meteo weather forecast simulation (see [2]) or earthquake simulation through fluid-structure interaction models (see [107]).

The design of a modern electronic device requires a chain of highly sophisticated technological processes. The result of these processes is, usually, the realization of an integrated circuit (IC) in which billions of elementary components of very small size are connected together to implement a series of specific functions. Important examples are the multifunctional smart phones and the motherboard contained in the interior of a personal computer. Even if the contribution of data-driven models is mandatory to take into account statistical failure of the technological processes at the level of the single component, the IC final outcome in terms of electric behavior has to be designed according to a careful description of the physical mechanisms that govern the transport of electric current inside the device. Electric current is a *macroscopic* variable that is easily accessible at the device terminals, but its formation is related to the occurrence of *microscopic* mechanisms that involve physical variables often *impossible* to measure directly, such as, for example, the concentration of electron and hole charged particles or the electric field within the material.

Thanks to their ability to simulate microscale phenomena and their impact on macroscale variables, mechanism-driven models can significantly advance modern IC technology by providing a *virtual microscope* capable of zooming on the principal charge transport processes occurring at the atomic level in the material, which ultimately determine the electric current measured at the output device terminals. In the hierarchy of existing mechanism-driven approaches for such a challenging task (see [61] and [65]), the so-called *Drift-Diffusion* (DD) model (see [99]) represents a very good trade-off between complexity and accuracy. The DD model is a set of nonlinearly coupled partial differential equations whose unknowns are the spatial and temporal distributions of the number of electrons and holes per unit volume of material,  $n$  and  $p$ , and the electric potential  $\psi$  inside a semiconductor device. The DD

system in a nutshell, reads:

$$\left\{ \begin{array}{l} q \frac{\partial n}{\partial t} - \nabla \cdot \underline{\mathbf{J}}_n = qG_n - qR_n \\ q \frac{\partial p}{\partial t} + \nabla \cdot \underline{\mathbf{J}}_p = qG_p - qR_p \\ \underline{\mathbf{J}}_n = q\mu_n^{el} n \underline{\mathbf{E}} + qD_n \nabla n \\ \underline{\mathbf{J}}_p = q\mu_p^{el} p \underline{\mathbf{E}} - qD_p \nabla p \\ \nabla \cdot (\epsilon_{sem} \underline{\mathbf{E}}) = q \text{Dop} + qp - qn \\ \underline{\mathbf{E}} = -\nabla \psi, \end{array} \right. \quad (1.2)$$

where  $\underline{\mathbf{J}}_n$  and  $\underline{\mathbf{J}}_p$  are the electron and hole current densities and  $\underline{\mathbf{E}}$  is the electric field. The quantities  $\mu_n^{el}$  and  $\mu_p^{el}$  represent the electrical mobilities of electrons and holes, and are typically expressed by highly nonlinear functions of the system dependent variables, often derived through a nontrivial calibration process of fitting between data and phenomenological relations. The quantity Dop is a given function of position and physically represents the number of dopant impurities per unit volume of material (the so-called “doping profile”),  $q$  denoting the (absolute value) of the elementary electron charge. The quantities  $G_n$ ,  $G_p$  and  $R_n$ ,  $R_p$  represent the generation and recombination rates per unit volume and physically account for all the microscopic processes that locally drive the semiconductor away from thermodynamical equilibrium.

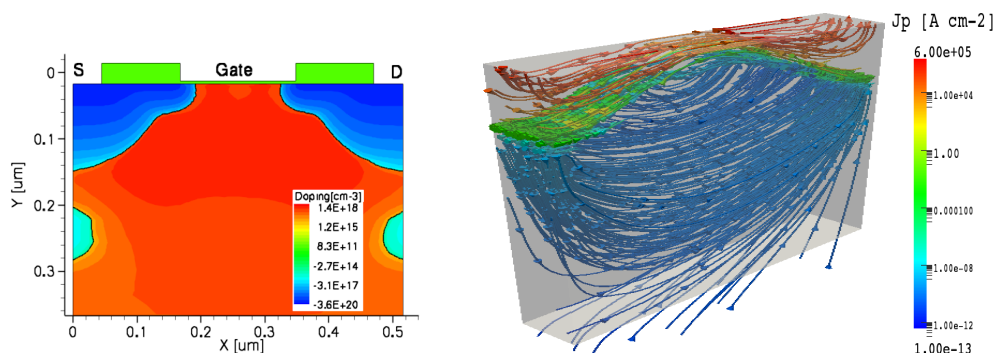


**Figure 1.8** *p*-MOSFET (Metal-Oxide-Semiconductor Field-Effect Transistor) structure: Left: 2D cut of the doping profile. Right: hole current density streamlines at  $V_{\text{gate}}=1.5$  V. A. G. Mauri, A. Bortolossi, G. Novielli, R. Sacco. *3D finite element modeling and simulation of industrial semiconductor devices including impact ionization*. *Journal of Mathematics in Industry*, 5(1), 1-18 (2015).

Through the numerical solution of system (1.2) by appropriate methodologies , it is possible to perform the simulation of most of the devices used in modern technology. As a representative example, we discuss below an application of the DD model to investigate the electric behavior of the fundamental brick of semiconductor technology, the so-called Metal-Oxide-Semiconductor Field-Effect Transistor (MOSFET). To this end, we show in Figure 1.8 (left panel) the simulated doping profile of a *p*-MOSFET, i.e., a device in which the main contribution to the electric current is due to the hole carriers  $p$ , and in Figure 1.8 (right panel) the simulated hole current density streamlines in the case where the transistor is in the “on-state” (i.e. the working condition in which the device is conducting a significant electric current flow). Two important pieces of information can be drawn from the scrutiny of Figure 1.8 (right panel). The first information concerns the thickness  $t_{IL}$  of the inversion layer in the channel region, that is the portion of the volume of the MOSFET very close to the interface with the oxide region (denoted by “Gate” in the scheme of Figure 1.8 (left panel)) where the charged particles preferentially flow in their motion from the source terminal (denoted by “S”) to the drain terminal (denoted by “D” in the scheme of Figure 1.8 (left panel)). The value of  $t_{IL}$  is impossible to measure experimentally and should be kept as small as possible to minimize current dispersion. The second information concerns the value of the current (due to the transport of hole charged particles) at the output drain terminal. Such value can be computed by numerically integrating the normal component of the hole current density over the surface of the drain terminal and then compared to measured data for subsequent model calibration and/or device optimization.

Finally, it is important to point out that the realistic example illustrated above is described by a set of equations, the DD system, sharing the *same* physical principles and mathematical formalism that is used in the simulation of charged ion flow in a transmembrane channel of a living cell

This observation reinforces a conceptual message that we hope to convey with this volume, namely, the importance of assuming an open-minded view on science and technology not seen as adiabatic chambers, rather as communicating vessels.

## 1.2. Synergy between modeling approaches in Life Sciences

In the previous sections, we have illustrated several approaches to devise a model for a given physical and biological problem. Even though this book is focused on mechanism-driven formulations, it is important to emphasize that there is no modeling approach that is good for everything; rather, each approach has pros and cons, and it is part of the creativity of science to combine existing methodologies and propose new ones to understand more about our world and our life. In this respect, a *synergistic approach* to modeling seems to be the winning strategy to develop a formulation that best suits the specific features of the problem at hand and the needs of the end-user of

the formulation itself.

Data collected using physical models and animal models can be analyzed via data-driven models to define the values of biophysical parameters needed within mechanism-driven models. These latter, in turn, can be used to inform statistical methods about cause-effect relationships among interacting factors, thereby reducing the dimension of the parameter space and improving dramatically the effectiveness and the power of statistical analysis in data-driven models. This latter aspect appears to be particularly beneficial nowadays to make sense of Big Data by a judicious combination of deterministic and statistical methods and, ultimately, is the candidate for an optimal approach to the study of Life Sciences.

### 1.3. Foundations of numerical modeling

In this section, we introduce the basic concepts and definitions that represent the foundations of numerical mathematics.

#### 1.3.1. The modeling step

Following Section 1.1.4, the mathematical description of a *physical problem* arising in the context of applications of bioengineering and life sciences represents one of the fundamental objectives of this book. Let us denote by  $x_{ph}$  a (significant) target variable(s) of the physical system under investigation, such as the concentration of a chemical species, the velocity of blood in an artery or the intraocular pressure inside the eye globe. In many cases,  $x_{ph}$  can be measured experimentally, although the factors that concur to determine its value may be of multiple nature and disentangling them is a highly nontrivial task. The representation of a physical system by means of a *mathematical model* can help elucidate the cause-to-effect relationships connecting the various factors that influence the value of  $x_{ph}$  and deepen the understanding of the mechanisms at play. Indeed, several assumptions should be made when developing a mathematical model so that, in general, the solution  $x$  of the mathematical model describing the variable of interest does not coincide with the physical value  $x_{ph}$ . The problem of finding the solutions of a mathematical model given some input data will be referred to as the *mathematical problem*. Conceptually, the mathematical problem can be defined as follows.

**Definition 1.1** (Mathematical problem). *Let  $\mathcal{D}$  be the set of input data for the model and let  $V$  be the set of solutions. Let  $\mathcal{D}$  and  $V$  be vector spaces. The mathematical problem reads*

$$\text{given } d \in \mathcal{D}, \text{ find } x \in V \text{ such that } F(x, d) = 0. \quad (1.3)$$

The mapping  $F$  defined as

$$\begin{aligned} F : V \times \mathcal{D} &\rightarrow \mathcal{Y} \\ (x, d) &\rightarrow F(x, d) \end{aligned} \tag{1.4}$$

is referred to as the mathematical model,  $\mathcal{Y}$  being a vector space that represents the codomain of the mapping  $F$ .

Since  $V$  may be a vector space of infinite dimension the formulation (1.4) is also referred to as the *continuous model* of the physical system. In general, the mathematical problem (1.3) is solvable only under certain conditions, as stated by the following definition of well-posedness.

**Definition 1.2** (Well-posedness of the mathematical problem). *Problem (1.3) is said to be well-posed if:*

1. (existence) given any  $d \in \mathcal{D}$ , there exists  $x \in V$  such that  $F(x, d) = 0$ ;
2. (uniqueness) given any  $d \in \mathcal{D}$ , if there exist  $x, y \in V$  such that  $F(x, d) = 0$  and  $F(y, d) = 0$ , then  $x = y$ ;
3. (continuous dependence on data) given any  $d, d + \delta d \in \mathcal{D}$  and their corresponding unique solutions  $x, x + \delta x \in V$  such that  $F(x, d) = 0$  and  $F(x + \delta x, d + \delta d) = 0$ , there exist two positive constants  $\eta$  and  $K$ , which may depend on  $d$ , such that

$$\text{if } \|\delta d\|_{\mathcal{D}} \leq \eta(d) \text{ then } \|\delta x\|_V \leq K(d)\|\delta d\|_{\mathcal{D}} \tag{1.5}$$

where  $\|\cdot\|_{\mathcal{D}}$  and  $\|\cdot\|_V$  are appropriate norms for  $\mathcal{D}$  and  $V$ , respectively.

Should the solutions of (1.3) not enjoy all of the above properties, then the mathematical problem is said to be not well-posed or ill-posed.

The vector space  $\mathcal{D}$  is also referred to as the set of *admissible data*, namely the set of data for which the mathematical problem (1.3) is well-posed.

**Remark 1.1** (Continuous dependence on data and stability). *The property of continuous dependence on data is also referred to as the property of stability. Indeed, the fact that the solutions of (1.3) depend continuously on the data means that a small perturbation  $\delta d$  in the input data  $d$  for the model leads to a small perturbation  $\delta x$  in the solution  $x$ , as shown in Figure 1.9. In other words, if we change the input data only slightly, the solution will not change that much, thereby meaning that the problem is stable.*

### 1.3.2. The approximation step

Even in the case that the mathematical problem (1.3) is well-posed, it is not always feasible to write its solution in closed form, so that an approximation of  $x$  has to be

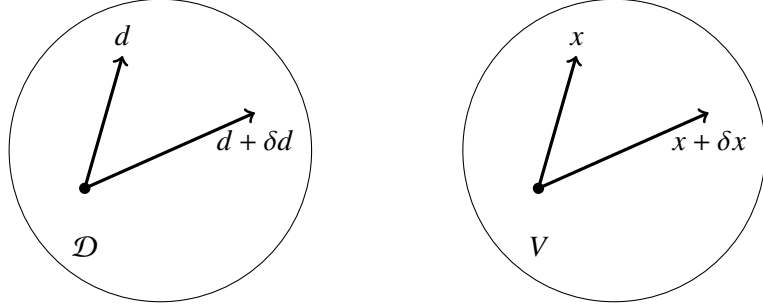


Figure 1.9 Continuous problem with perturbation on data and solution.

found by means of numerical methods. Thus, we will define the *numerical problem* and the *numerical model* as follows.

**Definition 1.3** (Numerical problem). *Let  $\mathcal{D}$  and  $V$  be the vector spaces defining the domain of the mathematical model (1.4). Let  $\mathcal{D}_h$  and  $V_h$  be finite dimensional subspaces of  $\mathcal{D}$  and  $V$ , respectively, so that  $\mathcal{D}_h \subseteq \mathcal{D}$ ,  $V_h \subseteq V$ ,  $\dim \mathcal{D}_h < +\infty$  and  $\dim V_h < +\infty$ . The numerical problem reads*

$$\text{given } d_h \in \mathcal{D}_h, \text{ find } x_h \in V_h \text{ such that } F_h(x_h, d_h) = 0. \quad (1.6)$$

*The mapping  $F_h$  defined as*

$$\begin{aligned} F_h : V_h \times \mathcal{D}_h &\rightarrow \mathcal{Y}_h \\ (x_h, d_h) &\rightarrow F_h(x_h, d_h) \end{aligned} \quad (1.7)$$

*is referred to as the numerical model. Here,  $\mathcal{Y}_h \subseteq \mathcal{Y}$  is a finite dimensional subspace of  $\mathcal{Y}$ , whereas  $d_h$  and  $x_h$  are the approximate data and solution, respectively.*

Since  $\dim V_h < +\infty$ , the formulation (1.7) is also referred to as the *discrete model* and, correspondingly, the real number  $h > 0$  is the *discretization parameter*. The relationship between continuous and discrete spaces is schematized in Figure 1.10. Similarly to what we have done for the mathematical problem, we can define the well-posedness of the numerical problem as follows.

**Definition 1.4** (Well-posedness of the numerical problem). *Problem (1.6) is said to be well-posed if:*

1. (existence) given any  $d_h \in \mathcal{D}_h$ , there exists  $x_h \in V_h$  such that  $F_h(x_h, d_h) = 0$ ;
2. (uniqueness) given any  $d_h \in \mathcal{D}_h$ , if there exist  $x_h, y_h \in V_h$  such that  $F_h(x_h, d_h) = 0$  and  $F_h(y_h, d_h) = 0$ , then  $x_h = y_h$ ;
3. (continuous dependence on data) given any  $d_h, d_h + \delta d_h \in \mathcal{D}_h$  and their corresponding unique solutions  $x_h, x_h + \delta x_h \in V_h$  such that  $F_h(x_h, d_h) = 0$  and  $F_h(x_h + \delta x_h, d_h + \delta d_h) = 0$ .

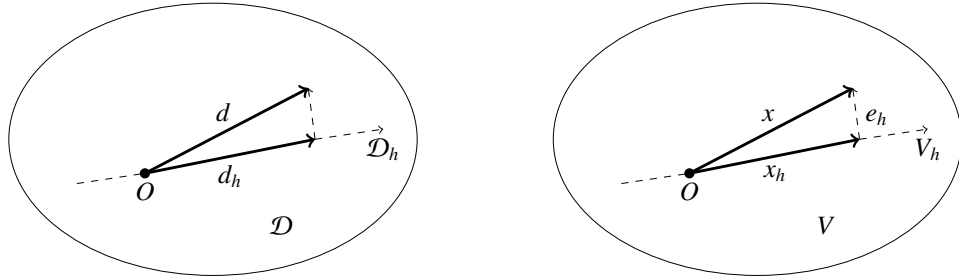


**Figure 1.10** Left panel: space of admissible data and its approximation. Right panel: solution space  $V$  and its finite dimensional approximation  $V_h$ .

$\delta d_h) = 0$ , there exist two positive constants  $\eta_h$  and  $K_h$ , which may depend on  $d_h$ , such that

$$\text{if } \|\delta d_h\|_{\mathcal{D}} \leq \eta_h(d_h) \text{ then } \|\delta x_h\|_V \leq K_h(d_h)\|\delta d_h\|_{\mathcal{D}}. \quad (1.8)$$

Should the solutions of (1.6) not enjoy all of the above properties, then the numerical problem is said to be not well-posed or ill-posed.

**Remark 1.2.** We can use in (1.8) the same norms as in (1.5) because  $\mathcal{D}_h \sqsubseteq \mathcal{D}$  and  $V_h \sqsubseteq V$ .

**Remark 1.3.** The most significant feature of (1.6) is that, for each fixed value of  $h$ , its solution  $x_h$  is computable, unlike (in general) the solution  $x$  of (1.3).

**Definition 1.5** (Stability). The numerical problem (1.6) is said to be stable if its solutions depend continuously on the data as expressed by Definition 1.4.

The residual associated with the numerical model (1.7) is defined as

$$\mathcal{R}_h(x, d) := F_h(x, d) - F(x, d). \quad (1.9)$$

Looking at (1.9) we see that the residual is the “remainder” obtained by forcing into the numerical problem the solution  $x$  and the data  $d$  of the continuous problem.

**Definition 1.6** (Consistency). The numerical model (1.7) is said to be consistent if:

$$\lim_{h \rightarrow 0} d_h = d; \quad (1.10a)$$

$$\lim_{h \rightarrow 0} \mathcal{R}_h(x, d) = 0. \quad (1.10b)$$

Moreover, the numerical model (1.7) is said to be consistent of order  $p$  with respect to the discretization parameter  $h$  if there exist  $C > 0$  independent of  $h$  and  $p > 0$  such that

$$\|\mathcal{R}_h(x, d)\|_{\mathcal{Y}} \leq Ch^p. \quad (1.10c)$$

### 1.3.3. The discretization error

Having both continuous and discrete formulations associated with the same physical system, we are naturally led to inquire about the *quality* with which  $x_h$  represents (better stated, approximates)  $x$ . To this end, we first need introduce the *discretization error*

$$e_h := x - x_h \quad (1.11)$$

where the meaning of the operation of subtraction follows from the operations defined on the vector space  $V$  and its finite dimensional subspace  $V_h$ . Notice that  $e_h$  *cannot* (in general) be computed because  $x$  is not (in general) explicitly available. Fortunately, this does not constitute a serious difficulty, since, after all, what we are actually interested in is the *convergence* of the approximate solution  $x_h$  to the solution  $x$  of the continuous problem as the discretization parameter becomes smaller and smaller, that is, our request is that

$$\lim_{h \rightarrow 0} e_h = 0. \quad (1.12)$$

**Definition 1.7** (Order of convergence). *Assume that there exists a positive constant  $C$  independent of  $h$  and a positive real number  $p$  such that*

$$\|e_h\|_V \leq Ch^p. \quad (1.13)$$

*In such a case, we say that  $x_h$  converges to  $x$  with order  $p$  with respect to  $h$ .*

The condition (1.13) implies that: (i) the larger is  $p$ , the faster is the convergence of the approximation; and (ii) the smaller is  $C$ , the better is the accuracy of the approximation.

**Remark 1.4.** *Applying the logarithm to both sides of condition (1.13) yields*

$$\underbrace{\log(\|e_h\|_V)}_Y \leq \underbrace{\log(C)}_q + \underbrace{\frac{p}{m}}_m \underbrace{\log(h)}_X$$

*that is, the log-plot of the error is a straight line in the X-Y plane, whose slope  $m$  gives us the order of convergence of the method.*

We close this section with definitions of approximation errors that are often used in practice.

**Definition 1.8** (Absolute and relative errors). *Given a norm  $\|\cdot\|_V$  in  $V$  (see Definition ??), we define the absolute and relative errors as:*

$$E_{abs}(x_h) := \|x - x_h\|_V, \quad \text{absolute error} \quad (1.14a)$$

$$E_{rel}(x_h) := \frac{\|x - x_h\|_V}{\|x\|_V}, \quad \text{relative error,} \quad x \neq 0, \quad (1.14b)$$

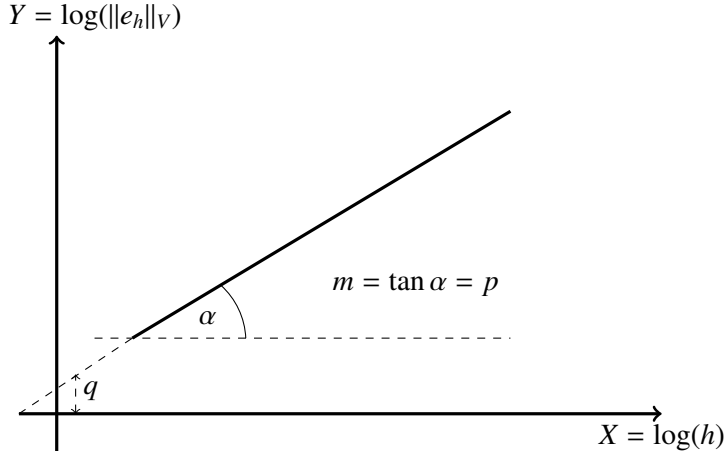


Figure 1.11 Error in log-log scale.

where  $x$  is the solution of the mathematical problem (1.3) and  $x_h$  is the solution of the numerical problem (1.6).

### 1.3.4. The equivalence theorem

The following theorem is the milestone of Numerical Analysis [71].

**Theorem 1.1** (Equivalence theorem (Lax-Richtmyer)). *The numerical problem (1.6) is convergent with respect to the discretization parameter  $h$ , as expressed by Definition 1.7, if and only if it is stable, as expressed by Definition 1.5, and consistent, as expressed by Definition 1.6. Moreover, if (1.10c) holds, then the numerical method (1.7) is convergent of order  $p$  with respect to the discretization parameter  $h$ .*

The fundamental result conveyed by the Lax-Richtmyer theorem is schematized in Figure 1.12.

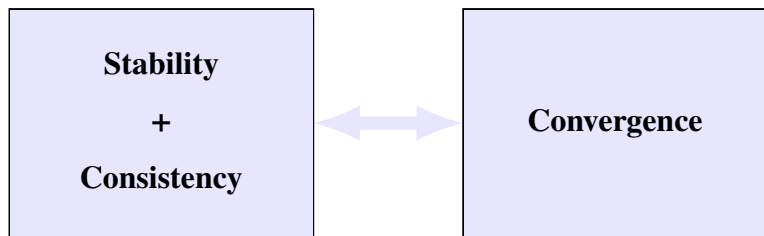


Figure 1.12 The Lax-Richtmyer paradigm.

### 1.3.5. Machine representation of numbers and rounding error

When working on a computer machine, any real number  $x$  is *represented* in the hardware by another real number, called *floating-point number* and denoted by  $fl(x)$ , equal to

$$fl[x] = (-1)^s \cdot (0.\underbrace{a_1 a_2 \dots a_t}_m) \beta^e \quad (1.15)$$

where:

- $\beta$  is the machine base;
- $t$  is the number of significant digits;
- $m$  is the mantissa;
- $e$  is the exponent;
- $s$  is the “sign” bit, with  $s = 0$  if  $x \geq 0$  and  $s = 1$  if  $x < 0$ .

Typically, we have  $\beta = 2$  and  $L \leq e \leq U$ , with  $L < 0$  and  $U > 0$ . Using double precision for number representation (which means 8 bytes of memory, corresponding to a machine word of 64 bits for storing  $fl[x]$ ), 53 digits are typically reserved to store the mantissa and 11 digits to store the exponent, so that  $t = 53$ . Notice that according to this allocation of digits, *no* bit appears to be used to store the sign  $s$ . This (apparent) inconsistency is removed by assuming  $a_1 \neq 0$  in (1.15). This ensures the uniqueness of the machine representation of a number. Moreover, in the case where  $\beta = 2$  (binary arithmetics),  $a_1$  is necessarily equal to 1 and thus it may not be stored in the computer, so that the bit that is being saved from the total amount for the mantissa (called *hidden bit*) may be used to store the sign  $s$ . According to the IEC559 standard (see [91]), in double precision representation we have  $L = -1021$  and  $U = 1024$ . Based on the expression (1.15), we introduce the set of floating-point numbers as the subset of  $\mathbb{R}$  defined as

$$\mathbb{F}(\beta, t, L, U) := \{0\} \cup \left\{ x \in \mathbb{R} : x = (-1)^s \beta^e \sum_{i=1}^t a_i \beta^{-i} \right\}. \quad (1.16)$$

From the above definitions, it follows that the range of numbers that can be represented in a computer machine is *finite*, and in particular it can be seen that

$$|fl[x]| \in [x_{min}, x_{max}], \quad (1.17)$$

where:

$$x_{min} = \beta^{L-1}, \quad (1.18)$$

$$x_{max} = \beta^U (1 - \beta^{-t}). \quad (1.19)$$

Unlike the real set  $\mathbb{R}$ , numbers in  $\mathbb{F}(\beta, t, L, U)$  are distributed in a discrete manner along the real axis. In particular, the power of resolution of a computer machine is

characterized by the following quantity.

**Definition 1.9** (Machine epsilon). *The machine epsilon*

$$\varepsilon_M = \beta^{1-t} \quad (1.20)$$

is the smallest floating point number such that

$$1 + \varepsilon_M > 1.$$

Setting  $\beta = 2$  and  $t = 53$  into (1.20), we obtain  $\varepsilon_M = 2.2204 \cdot 10^{-16}$ .

In general,  $fl(x)$  does not coincide with  $x$ , as stated by the following result.

**Proposition 1.1** (Round-off error). *Let  $x \in \mathbb{R}$  be a given number. If  $x_{min} \leq |x| \leq x_{max}$ , then we have*

$$fl[x] = x(1 + \delta) \quad \text{with } |\delta| \leq u, \quad (1.21)$$

where

$$u = \frac{1}{2}\beta^{1-t} \equiv \frac{1}{2}\varepsilon_M \quad (1.22)$$

is the roundoff unit (or machine precision).

Using (1.21) into the definitions (1.14), we get an estimate of the rounding error  $e_r$  introduced in Section 1.3.6

$$E_{rel}(x) = \frac{|x - fl[x]|}{|x|} = |\delta| \leq u, \quad E_{abs}(x) = |x - fl[x]| \leq \frac{1}{2}\beta^{e-t}.$$

### 1.3.6. The chain of errors

So far, we have introduced the notion of error as that of being, in general, the difference between the solution of the continuous problem, which we call from now on, the *exact solution*, and the solution of the numerical problem, which we call the *approximate, or, numerical solution*. However, our definition of error is not completely precise, because we are neglecting two other important sources of error, namely:

1. the *modeling error* and
2. the *rounding error*.

The modeling error is associated with a possible inaccuracy of the mathematical model describing the real physical application at hand, and/or a possible inaccuracy in the data entering the model formulation (due, for instance, to measurement machine tolerances and/or statistical fluctuations of the phenomena under investigation). For a theoretical approach to the study and estimation of the modeling error we refer to [10] and [92], whereas possible realistic applications of the theory can be found in [93].

The rounding error, described in Section 1.3.5, is, instead, inherently related to the computational process that is implemented in a computer algorithm, namely the

sequence of deterministic machine operations that are run using a software environment (for example, Matlab) on a PC characterized by a specific hardware (i.e., Intel, AMD, etc..) and a specific OS (Linux, Windows). Depending on the machine arithmetic that is being used, the rounding error can be monitored and accurately estimated (see (1.21)).

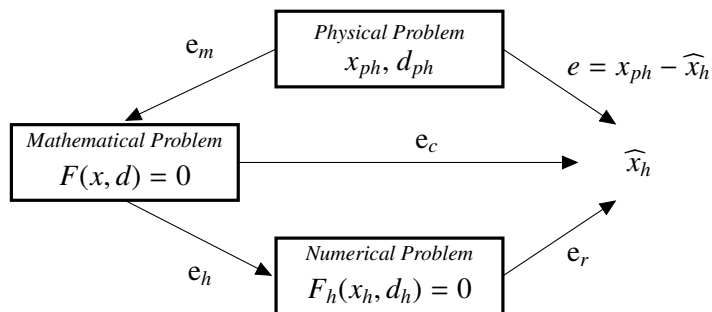


Figure 1.13 Sources of error in a computational process.

The whole chain of errors is schematized in Figure 1.13. In mathematical terms, we have:

- $e_m := x_{ph} - x$ : *modeling error*. It is the difference between the solution  $x_{ph}$  of the real physical problem and the solution  $x$  of the mathematical model;
- $e_h := x - x_h$ : *numerical error*. It is the difference between the solution  $x$  of the mathematical model and the solution  $x_h$  of the numerical problem;
- $e_r := \widehat{x}_h - x_h$ : *rounding error*. It is the difference between the solution  $\widehat{x}_h$  that is actually produced by the computational process and the theoretical solution  $x_h$  of the numerical model.

Letting  $e_c := e_h + e_r$  be the *computational error*, we define the *global error* as

$$e = x_{ph} - \widehat{x}_h = \underbrace{x_{ph} - x}_{e_m} + \underbrace{x - \widehat{x}_h}_{e_c} = x_{ph} - x + (\underbrace{x - x_h}_{e_h} + \underbrace{x_h - \widehat{x}_h}_{e_r}). \quad (1.23)$$

It is important to notice that the *only* quantity that is available to the user is  $\widehat{x}_h$ ; all the other solutions of the various intermediate steps of the process are virtually unaccessible. In particular, throughout the remainder of this text, we shall always neglect the modeling error in the analysis of the numerical methods of processes. Moreover, for ease of notation, we shall write  $x_h$  instead of  $\widehat{x}_h$ , unless otherwise specified, keeping the presence of the rounding error always understood.

### 1.3.7. Example: choice of the numerical model

For a given mathematical model  $F$ , the choice of the numerical model  $F_h$  in (1.7) is not, in general, unique. This means that there may be different ways to define  $F_h$  given  $F$ . However, different choices for  $F_h$  may lead to very different numerical outcomes  $x_h$  as a consequence of different dependence on  $h$  and the presence of round-off errors. The *a priori* analysis of the repercussion of the round-off error on the outcome of  $F_h$  is far beyond the scope of this book and we refer to [121] and [53] for a detailed treatment of this delicate issue. For our purposes, it is enough to remark that the effect of round-off error on the output of a given numerical model may represent a serious problem affecting the reliability of the predictions of the model and is usually identified as *numerical stability* or *algorithm stability*. We illustrate below the potential negative influence of the choice of  $F_h$  on  $x_h$  by considering the computation of the ion current density in a cell membrane channel using the Goldman-Hodgkin-Katz model (see Section 5.3.3). In such a computation (see (5.32)), we need to evaluate the following quantity

$$x(d) = \frac{d}{e^d - 1} \quad (1.24)$$

where  $d$  is a given real number. Using the abstract notation of Section 1.3.1, we have  $F(x, d) = x - d/(e^d - 1)$  with  $V = \mathcal{D} = \mathcal{Y} = \mathbb{R}$ . We are interested here in the case where  $d$  is very close to the value  $d = 0$  (for example,  $d = 10^{-6}$ ). We notice that  $d = 0$  leads to  $x(0) = 0/0$  (undetermined form) which can be easily solved by applying de l'Hopital rule to obtain

$$x(0) = \lim_{d \rightarrow 0^\pm} \frac{1}{e^d} = 1.$$

For the numerical evaluation of  $x(d)$  when  $d$  is close to 0, we consider the following two numerical models:

$$F_h^{(1)}(d_h) = x_h^{(1)}(d_h) - \frac{d_h}{e^{d_h} - 1} \quad (1.25a)$$

$$F_h^{(2)}(d_h) = x_h^{(2)}(d_h) - \frac{d_h}{\sum_{k=0}^{+\infty} \frac{d_h^k}{k!} - 1} = x_h^{(2)}(d_h) - \frac{1}{\sum_{k=1}^{+\infty} \frac{d_h^k}{(k+1)!}}, \quad (1.25b)$$

where we have denoted by  $d_h$  the floating point representation of the datum  $d \in \mathbb{R}$ . It is interesting to notice that, in the present example, the difference between  $d$  and  $d_h$  is related to the round-off error (1.21) so that we may assume  $h \leq u$ ,  $u$  being the round-off unit defined in (1.22). Let us compare the outcomes  $x_h^{(1)}(d_h)$  and  $x_h^{(2)}(d_h)$  computed by the two models (1.25) as a function of the value of  $d_h$  in the neighbourhood of the origin. The values of  $d_h$ , the corresponding outcomes  $x_h^{(1)}(d_h)$  and  $x_h^{(2)}(d_h)$  and the

number of terms  $k$  that are needed for the series at the denominator of  $F_h^{(2)}$  to converge, are reported in Table 1.1.

$d_h$	$x_h^{(1)}(d_h)$	$x_h^{(2)}(d_h)$	$k$
$10^{-3}$	$9.995000833332891e - 01$	$9.99500083333318e - 01$	6
$10^{-5}$	$9.999950000180351e - 01$	$9.99995000008333e - 01$	4
$10^{-8}$	$1.000000006077471e + 00$	$9.999999950000000e - 01$	3
$10^{-12}$	$9.999111073202700e - 01$	$9.999999999995000e - 01$	3
$10^{-15}$	$9.007199254740993e - 01$	$9.999999999999996e - 01$	3

**Table 1.1** The first column of the table lists the values of the datum  $d_h$ . The second and third columns report the values of  $x_h$  computed by the two numerical models in (1.25). The last column reports the number of terms to be summed in (1.25b).

Results clearly show that the two numerical models  $F_h^{(1)}$  and  $F_h^{(2)}$  provide different solutions  $x_h^{(1)}(d_h)$  and  $x_h^{(2)}(d_h)$  as  $d_h \rightarrow 0^+$ . Specifically, as  $d_h$  becomes smaller and smaller, the numerical model (1.25b) yields a sequence of values *monotonically* converging to the limiting value  $x(0) = 1$ , whereas the numerical model (1.25a) yields a sequence of values that *oscillate* around the limiting value  $x(0) = 1$ .

$d_h$	$e_h^{abs}$	$e_h^{\%}$
$10^{-3}$	$4.274358644806853e - 14$	$4.276496536700498e - 12$
$10^{-5}$	$9.701794922989393e - 12$	$9.701843432125705e - 10$
$10^{-8}$	$1.107747094053479e - 08$	$1.107747099592215e - 06$
$10^{-12}$	$8.889267922995714e - 05$	$8.889267923000158e - 03$
$10^{-15}$	$9.928007452590026e - 02$	$9.928007452590030e + 00$

**Table 1.2** The first column of the table lists the values of the datum  $d_h$ . The second column reports the values of the absolute error  $e_h$  associated with the evaluation of the inverse of the Bernoulli function using (1.25a). The third column contains the values of the percentage error.

Let us now quantitatively analyze the accuracy of method (1.25a) with respect to the exact evaluation of the inverse of the Bernoulli function for  $x$  close to 0. With this aim we assume the exact evaluation  $x(d)$  to coincide with the quantity computed by

method (1.25b), so that the absolute error (1.14a) can be defined as

$$e_h^{abs} := |x_h^{(2)}(d_h) - x_h^{(1)}(d_h)|$$

and the percentage error as the relative error (1.14b) multiplied by 100

$$e_h\% := \frac{|x_h^{(2)}(d_h) - x_h^{(1)}(d_h)|}{|x_h^{(2)}(d_h)|} \times 100.$$

Table 1.2 reports the values of  $e_h$  as a function of  $d_h$ . Results show that for  $d_h$  sufficiently far from the limiting value  $d_h = 0$ , the accuracy of method (1.25a) is reasonably good. This is not the case, however, when  $d_h = 10^{-15}$ . In this case, method (1.25a) provides a substantially inaccurate evaluation of (1.24). This behavior is to be ascribed to the fact that the numerical model (1.25b) is numerically stable whereas the numerical model (1.25a) is not.

“Notes” — 2019/5/17 — 17:39 — page 26 — #34

# CHAPTER 2

## Physics fundation

In this chapter, we will review the foundations of mechanics, electromagnetism and thermodynamics that serve as the pillars on which the approach of continuum will be constructed and developed. In doing this, we will examine the basic entities that characterize the mathematical description of a charged material point, that is:

1. mass and charge as intrinsic properties of matter;
2. conservation principles, laws of motion, constitutive laws;
3. energy.

### 2.1. Conservation principles and balance laws in classical mechanics

#### 2.1.1. Balance Laws

Let us denote by  $C$  a quantity that is conserved in a closed and isolated system, such as mass, electric charge and energy. Let us denote by  $\mathbb{V} \subset \mathbb{R}^3$  the domain in which we would like to study the dynamics of  $C$ . In Figure 2.1,  $\mathbb{V}$  is represented by the blue shadowed volume. The balance law for the quantity  $C$  can be expressed as the algebraic sum of the amounts of  $C$  flowing in and out the boundary of  $\mathbb{V}$  (see green and red arrows in Figure 2.1) and those produced or removed within the volume (see dark blue arrows in Figure 2.1), namely

$$\text{rate of change of } C = \text{flow in} - \text{flow out} + \text{volumetric source} - \text{volumetric sink}. \quad (2.1)$$

We mention that the last two volumetric terms are often collected into one single term named net production rate, namely

$$\text{net production rate} = \text{volumetric source} - \text{volumetric sink}. \quad (2.2)$$

### 2.2. Charged material points and their motion

In our first courses in physics, we have been introduced to the laws regulating the motion of point-like objects. Thus, let us begin by clarifying the difference between a mathematical point and a point-like object or, more precisely, a charged material point.

**Definition 2.1** (Mathematical point). A mathematical point, say  $\underline{x}$ , is an element of

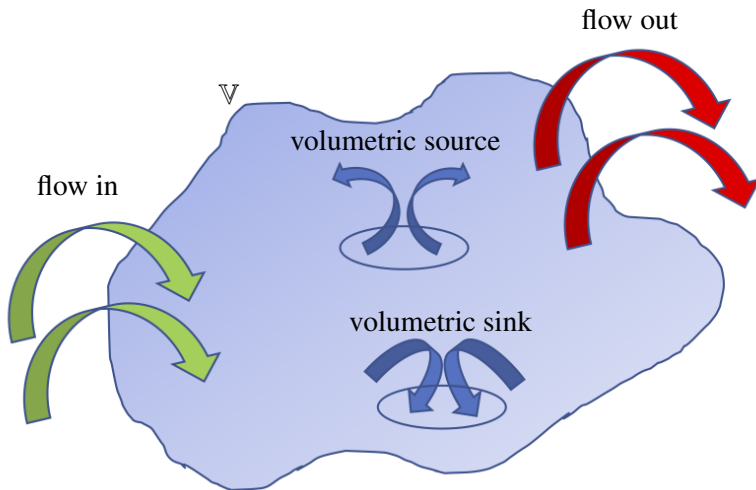


Figure 2.1 Schematic representation of a balance law in the volume  $\mathbb{V}$ .

the three-dimensional space, namely  $\underline{x} \in \mathbb{R}^3$ . A mathematical point is an example of zero-dimensional manifold in the three-dimensional space.

**Definition 2.2** (Charged material point). *A charged material point is a mathematical model for a body  $\mathcal{B}$  whose total mass  $M$  and total electric charge  $Q$  are assumed to be located at a single mathematical point.*

Interestingly, the case  $Q = 0$  is admissible in the analysis of the body’s dynamics, since it corresponds to a situation of electric neutrality. On the other hand, the case  $M = 0$  is *not* admissible in the context of classical mechanics, which is the focus of this book, since all bodies are assumed to have a non-zero (strictly positive) mass.

**Remark 2.1.** *In physics, charged material points are also referred to as point charges. In the particular case of an electrically neutral body, namely  $Q = 0$ , charged material points are simply called material points.*

The basic assumptions underlying the representation of a body  $\mathcal{B}$  as a charged material points are:

1. the *mass* of the charged material point equals the total mass  $M$  of the body  $\mathcal{B}$ ;
2. the *electric charge* of the charged material point equals the total electric charge  $Q$  of the body  $\mathcal{B}$ ;
3. the *position* of the body  $\mathcal{B}$  at each instant of time  $t$  is completely defined by a particular point in space. The vector of the three-dimensional space identifying

the position of the body  $\mathcal{B}$  (with respect to the origin of the geometrical reference frame) at time  $t$  is called *position vector*;

4. the *motion* of the charged material point is described by the time evolution of its position vector, namely by the mapping

$$(motion) \quad \underline{\varphi} : (0, T) \rightarrow \mathbb{V} \quad (2.3)$$

$$t \rightarrow \underline{\varphi}(t)$$

that provides the position vector  $\underline{\varphi}(t)$  in the physical space  $\mathbb{V} \subseteq \mathbb{R}^3$  that the body  $\mathcal{B}$  occupies at time  $t$ . As discussed in Example ??, we may adopt different mathematical representations for the space  $\mathbb{V}$  and, consequently, for the position vector  $\underline{\varphi}(t)$ . For example, we may decide to use a Cartesian framework, as in Figure 2.2, or it may find more convenient to use a cylindrical or spherical coordinate systems depending on the particular application.

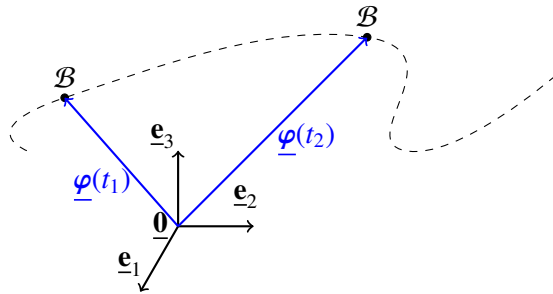


**Figure 2.2** A charged material point is a mathematical model for the body  $\mathcal{B}$  whose total mass  $M$  and total electric charge  $Q$  are assumed to be located at a single mathematical point. The motion of a charged material point is represented by the time evolution of the position vector  $\underline{\varphi}(t)$  identifying the position of the material point, i.e., the body, at time  $t$ .

Assuming that the mapping  $\underline{\varphi}$  describing the motion of the material point is smooth enough, velocity and acceleration of the material point can be defined as

$$(velocity) \quad \underline{v} : (0, T) \rightarrow \mathbb{V} \quad (2.4)$$

$$t \rightarrow \underline{v}(t) := \frac{d\underline{\varphi}}{dt}(t)$$

and

$$(acceleration) \quad \underline{a} : (0, T) \rightarrow \mathbb{V} \quad (2.5)$$

$$t \rightarrow \underline{a}(t) := \frac{d\underline{v}}{dt}(t) = \frac{d^2\underline{\varphi}}{dt^2}(t)$$

respectively. Another important physical quantity is the linear momentum of a charged material point, which is defined as

$$(linear\ momentum) \quad \underline{\mathbf{p}} : (0, T) \rightarrow \mathbb{V} \quad (2.6)$$

$$t \quad \rightarrow \quad \underline{\mathbf{p}}(t) := M \underline{\mathbf{v}}(t)$$

where  $M$  is the total mass of the body. The linear momentum plays a crucial role in determining the motion.

**Remark 2.2.** *The representation of a body as a charged material point may be useful, for example, when the dimensions of the body are much smaller than the dimensions of its path during the motion. However, it does not allow to study the deformation of the body or the redistribution of mass and/or electric charge inside the body. These limitations motivate the study of the continuum approach developed in PART II to model body motion.*

**Remark 2.3.** *From the mathematical viewpoint, following the definitions given in (2.3)-(2.5), position, velocity and acceleration are vector fields defined from  $(0, T) \subset \mathbb{R}$  into  $\mathbb{V} \subseteq \mathbb{R}^3$ . Velocity and acceleration involve time differentiations and, therefore, can be computed under the hypotheses that the motion is twice differentiable with respect to time.*

### 2.3. The Newton laws of motion

Newton's laws describe the relationship between the forces acting upon a body and its motion in response to such forces. Newton's laws have been expressed in several different ways over nearly three centuries and they are summarized below in the case of a point-like model for a body.

**Newton's first law of motion.** *When viewed in an inertial reference frame, a body either remains at rest or continues to move at a constant velocity, unless acted upon by an external force.* Thus, in the absence of a net force (either there are no forces acting on the body or, if present, they cancel each other out), the velocity of the body will not change. If that velocity is zero, then the body remains at rest. Let  $\underline{\mathbf{F}}$  be the vector sum of the external forces and  $\underline{\mathbf{v}}$  the velocity vector. Then Newton's first law of motion states that

$$\underline{\mathbf{F}} = \underline{\mathbf{0}} \quad \iff \quad \frac{d\underline{\mathbf{v}}}{dt} = \underline{\mathbf{0}}. \quad (2.7)$$

It is important to emphasize that, when the resultant of forces is zero, the velocity remain constant as a vector, namely both in magnitude and direction! Let us write  $\underline{\mathbf{v}}(t) = v(t) \underline{\mathbf{e}}(t)$ , where  $v(t)$  is the velocity magnitude and  $\underline{\mathbf{e}}(t)$  is the velocity direction. Thus, in the case of Figure 2.3(a), the velocity remains constant in both magnitude and

direction as time goes by, implying that the resultant of forces acting on the body is zero. In the case of Figure 2.3(b), the velocity is changing direction even though its magnitude is constant, implying that a non-zero net force is acting upon the body.

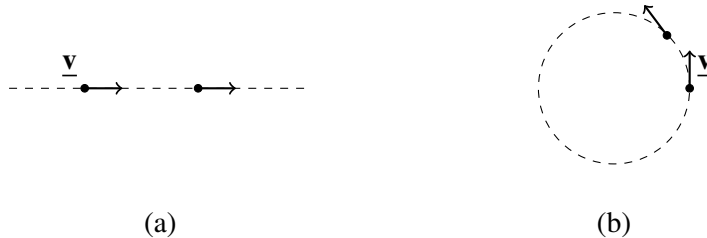


**Figure 2.3** Schematic representation of Newton’s First Law. (a) The velocity remains constant in both magnitude and direction as time goes by, implying that the resultant of forces acting on the body is zero. (b) The velocity is changing direction even though its magnitude is constant, implying that a non-zero net force is acting upon the body.

**Newton’s second law of motion.** The vector sum of the external forces  $\underline{F}$  acting on a body is equal to the rate of change of its linear momentum  $\underline{p}$ . The linear momentum for a material point has been defined in (2.6). Thus, Newton’s second law of motion states that

$$\underline{F} = \frac{d\underline{p}}{dt} = \frac{d(M\underline{v})}{dt} \quad (2.8)$$

which, in the case of  $M$  constant, leads to the celebrated equation

$$\underline{F} = M \frac{d\underline{v}}{dt} = M\underline{a}. \quad (2.9)$$

The physical unit of a force is Newton, denoted by N, which equation (2.9) characterizes as

$$[force] = [N] = \left[ \text{Kg} \frac{\text{m}}{\text{s}^2} \right]. \quad (2.10)$$

**Remark 2.4.** Newton’s second law of motion expressed by equation (2.8) is also known as balance of linear momentum, as it explicitly relates the rate of change of linear momentum to the resultant of forces acting on the body.

**Newton’s third law of motion.** When one body exerts a force on a second body, the second body simultaneously exerts a force equal in magnitude and opposite in direction on the first body. The third law states that all forces exist in pairs: if one body  $\mathcal{A}$  exerts a force  $\underline{F}_{\mathcal{A}\mathcal{B}}$  on a second body  $\mathcal{B}$ , then  $\mathcal{B}$  simultaneously exerts a force  $\underline{F}_{\mathcal{B}\mathcal{A}}$  on

$\mathcal{A}$ , and the two forces are equal and opposite, namely  $\underline{\mathbf{F}}_{\mathcal{A}\mathcal{B}} = -\underline{\mathbf{F}}_{\mathcal{B}\mathcal{A}}$ . This law is also known as the action-reaction law.

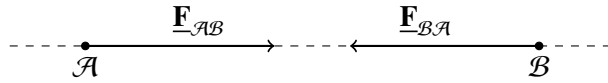


**Figure 2.4** Schematic representation of Newton's Third Law, which is also known as the action-reaction law.

## 2.4. The Newton laws, work, power and energy

Let us assume that a body  $\mathcal{B}$  can be represented as a charged material point, whose motion is described by the vector field  $\underline{\varphi}(t)$ , as depicted in Figure 2.2. In particular, the dashed curve in Figure 2.2 represents the trajectory of the body. Since the trajectory is not a straight line, it follows from first Newton's law, see (2.7), that the resultant  $\underline{\mathbf{F}}$  of external forces is different from zero. Let us begin by introducing the notions of work and power associated with the force (or resultant of forces)  $\underline{\mathbf{F}}$ .

**Definition 2.3** (Work and power). *The work  $\mathcal{W}$  performed by  $\underline{\mathbf{F}}$  during the time interval  $I = (t_1, t_2)$  is given by the integral*

$$\mathcal{W} = \int_{\underline{\varphi}(t_1)}^{\underline{\varphi}(t_2)} \underline{\mathbf{F}}(t) \cdot d\underline{\varphi}(t) \quad (2.11)$$

where  $d\underline{\varphi}(t)$  is the differential element along the curve that represents the trajectory. The time rate of change of the work  $\mathcal{W}$  is called power, which is denoted by  $\Pi$ , so that

$$\frac{d\mathcal{W}(t)}{dt} = \Pi(t) \text{ for } t \in I \quad \text{or} \quad \mathcal{W}(t) = \int_I \Pi(t) dt. \quad (2.12)$$

Since  $\underline{\varphi} = \underline{\varphi}(t)$ , using the chain rule we can write

$$d\underline{\varphi} = \frac{d\underline{\varphi}}{dt} dt = \underline{\mathbf{v}} dt \quad (2.13)$$

which allows us to rewrite the work as

$$\mathcal{W} = \int_{t_1}^{t_2} \underline{\mathbf{F}} \cdot \frac{d\underline{\varphi}}{dt} dt = \int_I \underline{\mathbf{F}} \cdot \underline{\mathbf{v}} dt \quad (2.14)$$

from which it follows that

$$\Pi(t) = \underline{\mathbf{F}}(t) \cdot \underline{\mathbf{v}}(t). \quad (2.15)$$

In general, the work  $\mathcal{W}$  depends on the force  $\underline{\mathbf{F}}$ , the time interval  $I$  and the trajectory  $\varphi$ , so that we can write

$$\mathcal{W} = \mathcal{W}(\underline{\mathbf{F}}, I, \varphi). \quad (2.16)$$

Using the International System of units, the work  $\mathcal{W}$  is expressed in Joule (J), which, according to Equation (2.14), is characterized by the following relation

$$[\text{work}] = [\text{J}] = [\text{N}] \cdot [\text{m}] = \left[ \text{Kg} \frac{\text{m}^2}{\text{s}^2} \right]. \quad (2.17)$$

As a consequence of (2.12), the units of power are  $\text{J s}^{-1}$ .

Let us now consider again Newton's second law (2.9). Multiplying by  $\underline{\mathbf{v}}$  both sides of the equation, we obtain

$$M \frac{d\underline{\mathbf{v}}(t)}{dt} \cdot \underline{\mathbf{v}}(t) = \underline{\mathbf{F}}(t) \cdot \underline{\mathbf{v}}(t). \quad (2.18)$$

Observing that

$$M \frac{d\underline{\mathbf{v}}}{dt}(t) \cdot \underline{\mathbf{v}}(t) = \frac{M}{2} \frac{d|\underline{\mathbf{v}}(t)|^2}{dt} = \frac{d}{dt} \left( \frac{M}{2} |\underline{\mathbf{v}}(t)|^2 \right),$$

defining the kinetic energy  $\mathcal{K}$  as

$$\mathcal{K}(t) := \frac{M}{2} |\underline{\mathbf{v}}(t)|^2 \quad (2.19)$$

and recalling the definition (2.15) of power  $\Pi$ , relationship (2.18) implies that

$$\frac{d\mathcal{K}(t)}{dt} = \Pi(t). \quad (2.20)$$

The above relationship, also known as the **balance law for the energy of a material point**, is a direct consequence of Newton's second law and states that the rate of change of the kinetic energy  $\mathcal{K}$  of the material point is equal to the power  $\Pi$  of the resultant of forces  $\underline{\mathbf{F}}$  acting on the body  $\mathcal{B}$ , modeled as a point-like object whose mass  $M$  is assumed to be constant. Relationship (2.20) is a particular case of a more general balance law for the energy of a system, which must also account for heat exchange and internal energy. These concepts are introduced by the laws of thermodynamics, as discussed in the next section.

## 2.5. Laws of thermodynamics

In this section, we aim at providing a short introduction to the basic concepts and mathematical formalism of thermodynamics, referring to the specialized literature, such as [39] and [123], for a more detailed and structured presentation of the subject.

### 2.5.1. The thermodynamic approach

In Section 2.3, we saw how Newton’s laws provide a mechanistic description of the motion of a body. Many engineering and life science applications, though, involve large ensembles of bodies interacting with each other and their surrounding environment. The application of Newton’s laws to study such systems would require the solution of a huge number of (possibly nonlinear) equations. This procedure, despite theoretically correct, is not practically affordable even with the present supercomputing capabilities. The laws of thermodynamics provide a viable alternative to this issue by introducing the concept of *thermodynamic variables*, or *state variables*, which are properties characterizing the system as a whole, even though their value is dictated by the average motion of the ensemble of bodies within the system. Thus, thermodynamic variables describe macroscopic properties of the system resulting from some microscopic average. State variables include temperature  $\Theta$  (units: K), pressure  $p$  (units:  $\text{Nm}^{-2}$ ), volume  $V$  (units:  $\text{m}^{-3}$ ), internal energy  $\mathcal{E}$  (units: J), enthalpy  $H$  (units:  $\text{J Kg}^{-1}$ ), and, in some cases, entropy  $\mathcal{S}$  (units:  $\text{JK}^{-1}$ ) (see Section ??). Thermodynamic variables are related one to each other through *equations of state* which can be written as

$$f(\Theta, V, p, \mathcal{E}, H, \mathcal{S}) = 0. \quad (2.21)$$

For example, in the case of an *ideal* gas the equation of state takes the well-known form

$$pV = n\mathcal{R}\Theta \quad (2.22)$$

where  $n$  is the number of moles of gas (units: mol) and  $\mathcal{R} = 8.314472$  is the universal gas constant (units:  $\text{J mol}^{-1} \text{K}$ ). Equation (2.22) contains, as particular cases, the Boyle, Gay-Lussac and Avogadro laws. Other instances of (2.21) include the Van der Waals law for real gases

$$\left(p + \frac{a}{V^2}\right)(V - b) = \mathcal{R}\Theta \quad (2.23)$$

where  $a$  and  $b$  are the so-called van der Waals constants that have different values for each gas, and the Clausius-Clapeyron law for water vapor

$$\frac{1}{p} \frac{dp}{d\Theta} = \frac{H_v}{\mathcal{R}_v \Theta^2} \quad (2.24)$$

where  $H_v$  is the enthalpy of vaporization (units:  $\text{J Kg}^{-1}$ ), also known as latent heat of vaporization, and  $\mathcal{R}_v = 461.5$  (units:  $\text{J Kg}^{-1} \text{K}$ ) is the specific gas constant for water vapor.

### 2.5.2. The concept of work in thermodynamics

The concept of work was already introduced in Section 2.4 in the case of forces acting on a single body. Thanks to the relationship between macroscopic and microscopic variables we can now extend the concept of work to thermodynamic systems. To this end, we begin by providing the following definitions for equilibrium state and reversible and irreversible processes.

**Definition 2.4** (Equilibrium state). *Assume that the external conditions acting on a thermodynamic system do not experience any spatial and temporal variation. Then, a thermodynamic state of the system is called an equilibrium state if the thermodynamic variables characterizing the properties of the system, such as pressure, temperature and volume, do not experience any spatial and temporal variation. The equilibrium state is also referred to as thermodynamic equilibrium.*

**Definition 2.5** (Reversible and irreversible process). *A thermodynamic process, or transformation, is said to be reversible when the system evolves from its initial state towards its final state through a sequence of equilibrium states in the sense of Definition 2.4. A process that is not reversible is said to be irreversible.*

A reversible process has the property that its direction can be "reversed" by inducing infinitesimal changes to some properties of the system via its surrounding environment. On the other hand, when the thermodynamic process is irreversible, the system and the surrounding environment cannot go back to their initial state. In the case of a real transformation, we can consider that the process is reversible if it occurs in an almost static way or, equivalently, if the states through which the system evolves differ only infinitesimally from an equilibrium state.

Let us assume that the gas in Figure 2.5 is expanding slowly, namely through a sequence of *equilibrium states*. Thus, the gas expansion can be regarded as reversible according to Definition 2.5. Indicating with  $dx_3$  the infinitesimal displacement experienced by the piston during a single step of the gas expansion, we can define the velocity  $\underline{v}$  of the piston as

$$\underline{v} = \frac{dx}{dt} \underline{e}_3$$

and Equation (2.14) allows us to write the infinitesimal work  $d\widetilde{W}$  performed by the gas on the piston as

$$d\widetilde{W} = \underline{F} \cdot \underline{v} dt.$$

In addition, we note that

$$\underline{v} dt = dx_3 \underline{e}_3.$$

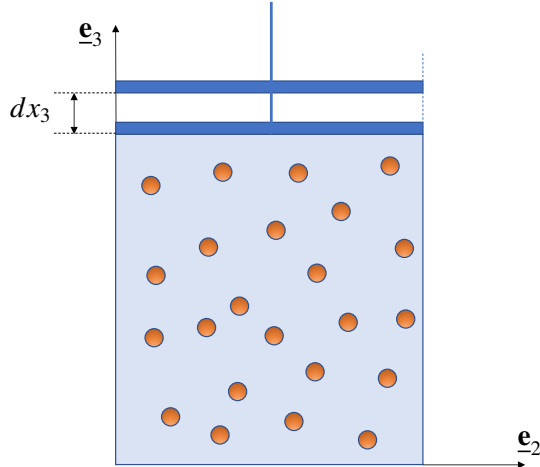


**Figure 2.5** Schematic representation of a container filled with gas particles. A piston confines the gas particles within the container and undergoes an infinitesimal vertical displacement  $dx_3$ .

**Remark 2.5.** *The third Newton law tells us that the piston exerts on the gas a force that is equal and opposite to the force that the gas exerts on the piston. Thus, the infinitesimal work  $d\tilde{W}$  performed by the piston on the gas is equal and opposite to the infinitesimal work  $d\tilde{W}$  performed by the gas on the piston, namely,  $d\tilde{W} = -d\tilde{W}$ .*

Recalling that the force  $\underline{F}$  acting on the piston is given by the gas pressure  $p$  multiplied by the piston surface area  $A$ , namely  $\underline{F} = pA\underline{e}_3$  as seen in Section ??, we can rewrite the infinitesimal work  $d\tilde{W}$  as

$$d\tilde{W} = pAdx_3 = pdV \quad (2.25)$$

where  $dV = Adx_3$  is the infinitesimal volume associated with the infinitesimal displacement  $dx_3$  of the piston. Denoting by  $V_i$  and  $V_f$  the initial and final volumes occupied by the expanding gas, the total work performed by the gas on the piston during the transformation is given by

$$\tilde{W} = \int_{V_i}^{V_f} pdV. \quad (2.26)$$

As implicitly expressed by the equation of state (2.21), the work  $\tilde{W}$  depends, in general, on the path followed by the gas expansion in the transformation from the initial to the final state. In the special case where the gas satisfies (2.22) we can identify the following three distinct physical situations:

1. *isothermal* transformation ( $\Theta = \text{const}$ ): Equation (2.26) becomes

$$\tilde{\mathcal{W}} = n\mathcal{R}\Theta \int_{V_i}^{V_f} \frac{dV}{V} = n\mathcal{R}\Theta \ln\left(\frac{V_f}{V_i}\right); \quad (2.27)$$

2. *isobaric* transformation ( $p = \text{const}$ ): Equation (2.26) becomes

$$\tilde{\mathcal{W}} = \frac{n\mathcal{R}}{p} \int_{\Theta_i}^{\Theta_f} dT = \frac{n\mathcal{R}}{p}(\Theta_f - \Theta_i); \quad (2.28)$$

3. *isochoric* transformation ( $V = \text{const}$ ): Equation (2.26) is simply

$$\tilde{\mathcal{W}} = 0. \quad (2.29)$$

### 2.5.3. The concept of heat in thermodynamics

In Section 2.5.2, the system of Figure 2.5 has been characterized from the point of view of the mechanical work resulting from gas expansion. However, a closer look at the physical conditions inside the container reveals that the system exchanges also a certain amount of heat  $Q$  with the external environment. Experience shows that, in analogy with what happens for the work  $\mathcal{W}$ , also  $Q$  depends, in general, on the path followed by the gas in the transformation from the initial to the final state. To better illustrate this issue, let us consider the two thermodynamic systems schematically represented in Figure 2.6.

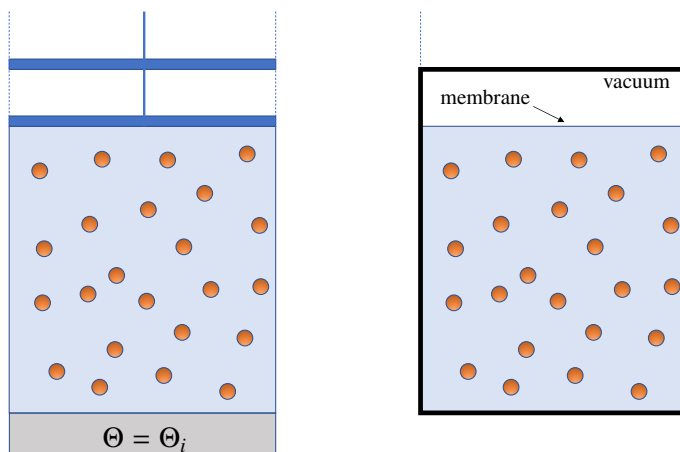


**Figure 2.6** Schematic representation of an ideal gas that undergoes an isothermal expansion (left panel) and an adiabatic expansion (right panel). The initial volume  $V_i$  is the same in the two configurations. In the case of the adiabatic expansion,  $V_i$  is the result of the confinement of the gas by a membrane located on its top and separating the gas from the vacuum region. After the membrane is removed the gas undergoes a free expansion without performing any work.

The system on the left panel consists of a container, a thermal reservoir on the bottom and a piston on the top that confines the gas inside the container occupying a volume  $V_i$ . The system on the right panel consists of a container and of a membrane. This latter confines the gas at the volume  $V_i$  and, at the same time, separates the gas from a neighbouring vacuum region. The final volume  $V_f$  is the same for both systems. To thermodynamically investigate the two systems in Figure 2.6, two different transformations are considered, specifically, an isothermal transformation (Figure 2.6, left panel) and an adiabatic transformation (Figure 2.6, right panel). We emphasize that:

- during the *isothermal transformation*, the gas receives the heat from the thermal reservoir kept at a fixed temperature  $\Theta_i$  and the volume variation results from the piston motion;
- during the *adiabatic transformation*, no heat exchange is allowed between the gas and the external environment across the container walls, and the volume variation results from the gas free expansion.

During the isothermal expansion, the gas absorbs a quantity  $Q$  of heat by the thermal reservoir in such a way that its temperature is kept constant during the transformation, so that  $\Theta_f = \Theta_i$  and  $V_f > V_i$ . During the adiabatic transformation, the gas does not perform any work and does not exchange any amount of heat with the external environment. The above described conceptual experiment of gas expansion shows that the final thermodynamical state of the gas, identified by the theremodynamic variables  $\Theta_f$  and  $V_f$ , is the same in both transformations depicted in Figure 2.6 but the amount of exchanged heat  $Q$  is not. This allows us to draw the following conclusion.

**Remark 2.6.** *In a thermodynamic system, the work  $W$  and the heat  $Q$  depend on the transformation path that connects the initial state to the final state.*

Finally, we remark that the process described in the left panel of Figure 2.6 is reversible since we can compress slowly the gas to go back to the initial state, while the process described in right panel of Figure 2.6 is irreversible since after the gas expansion the system cannot go back to its initial state.

#### 2.5.4. The first law of thermodynamics

The first law of thermodynamics expresses the balance of energy for a thermodynamic system, namely the fact that, during a thermodynamic transformation, the variation of energy of the system is equal to the energy that the system receives from or loses within the surrounding environment. To make this statement more quantitative, we need to define how thermodynamic variables are related to thermodynamic transformations.

**Definition 2.6** (Thermodynamic variable). *In thermodynamics, a variable is said to*

be a thermodynamic variable, or state variable, if its value depends only on the thermodynamic state and not on the particular way through which that thermodynamic state is reached.

Neither heat nor work satisfy Definition 2.6 as pointed out in Remark 2.6. On the contrary, for a given thermodynamic system, it is possible to consider the quantity  $Q + W$ . Experience shows that the variation of this quantity is not related to the particular path followed during the evolution but it is an intrinsic property of the initial and final state of the transformation. If we consider infinitesimal transformations, namely processes in which the initial and final states differ only by an infinitesimal variation of system properties, the quantity  $dQ + dW$  defines a state thermodynamic variable denoted by  $dE$ . This concept is expressed by the first principle of thermodynamics

**The first law of thermodynamics.** *For a thermodynamic system, the infinitesimal variation  $dE$  of the internal energy depends only on the initial and final states attained by the system during a thermodynamic transformation. Furthermore,  $dE$  equals the sum between the infinitesimal heat  $dQ$  exchanged by the system and the infinitesimal work  $dW$  performed or received by the system, namely*

$$dE = dQ + dW. \quad (2.30)$$

By convention, the heat  $Q$  is positive when it is *absorbed* by the system and the work  $W$  is positive when it is *performed on* the system. The first law of thermodynamics also tells us that the heat  $Q$  is measured in the same units as the work  $W$ , namely, Joule (J).

A significant application of (2.30) is the case of a *cyclic reversible transformation* that is characterized by the property that the final state coincides with the initial state. In this case we obviously have  $dE = 0$ , implying that

$$dQ = -dW. \quad (2.31)$$

Equation (2.31) clearly indicates the equivalence between two macroscopic forms of energy: the heat and the work. It is also possible to apply (2.30) to a number of different transformations. For an isocoric transformation, Equation (2.29) implies that

$$dE = dQ, \quad (2.32)$$

whereas for an adiabatic transformation (see Figure 2.6, left panel), we have

$$dE = dW. \quad (2.33)$$

### 2.5.5. Energy balance law

The first law of thermodynamics expresses a relationship between heat and work in the case of infinitesimal transformations. Following [37], we can view relation-

ship (2.30) as a particular case of a general balance law for the energy of a system, which is the mathematical formalization of the principle of conservation of energy postulated at the beginning of this chapter.

**Energy balance law.** *The rate of change of the sum between kinetic energy  $\mathcal{K}$  and internal energy  $\mathcal{E}$  is equal to the rate of change of the sum between heat  $Q$ , work  $\mathcal{W}$  and other types of energy  $\mathcal{U}_\alpha$ , with  $\alpha \geq 0$ , that enter or leave the system, namely*

$$\frac{d\mathcal{K}}{dt} + \frac{d\mathcal{E}}{dt} = \frac{dQ}{dt} + \frac{d\mathcal{W}}{dt} + \sum_{\alpha} \frac{d\mathcal{U}_{\alpha}}{dt}. \quad (2.34)$$

The terms  $\mathcal{U}_\alpha$  may be due, for example, to the presence of an electromagnetic field or chemical reactions. It is very interesting to notice that:

1. recalling that the time rate of change of work is defined as power  $\Pi$ , see Section 2.4, and introducing the notations  $\Pi_Q$  and  $\Pi_{\mathcal{U}_\alpha}$  to indicate the time rate of change of  $Q$  and  $\mathcal{U}_\alpha$ , respectively, relationship (2.34) can be rewritten as

$$\frac{d\mathcal{K}}{dt} + \frac{d\mathcal{E}}{dt} = \Pi_Q + \Pi + \sum_{\alpha} \Pi_{\mathcal{U}_{\alpha}} \quad (2.35)$$

2. relationship (2.35) reduces to (2.20) in the case of a purely mechanical system ( $\Pi_Q = \Pi_{\mathcal{U}_\alpha} = 0$ ) composed of a single material point, for which we are not modeling variations in its internal energy ( $d\mathcal{E}/dt = 0$ );
3. the notion of *potential energy* that is often utilized in the study of dynamical systems is profoundly different from the notion of *internal energy* introduced by the first law of thermodynamics. Specifically, the work  $\mathcal{W}$  may be written as the sum of the work of conservative and nonconservative forces, denoted by  $\mathcal{W}_c$  and  $\mathcal{W}_{nc}$ , respectively, so that  $\mathcal{W} = \mathcal{W}_c + \mathcal{W}_{nc}$ . In the case of conservative forces, we can introduce a potential energy  $\mathcal{U}$  so that  $\mathcal{W}_c = -\mathcal{U}$  and (2.34) can be written as

$$\frac{d\mathcal{K}}{dt} + \frac{d\mathcal{E}}{dt} + \frac{d\mathcal{U}}{dt} = \Pi_Q + \Pi_{nc} + \sum_{\alpha} \Pi_{\mathcal{U}_{\alpha}} \quad (2.36)$$

where  $\Pi_{nc} = d\mathcal{W}_{nc}/dt$  is the power associated with nonconservative forces.

## 2.6. Laws of electromagnetism

After reviewing the Newton laws and the laws of thermodynamics, in the present section we introduce the *Maxwell equations*, which describe the relationship between the electric sources acting upon a charged body and the electromagnetic field in response to such sources. Our presentation follows the historical path that led James Clerk Maxwell to derive the mathematical laws of electromagnetism in differential form [82, 83] starting from two famous experiments due to Faraday and Ampère, from

Gauss' law and from the experimental evidence of the absence of magnetic monopoles.

### 2.6.1. The Faraday experiment

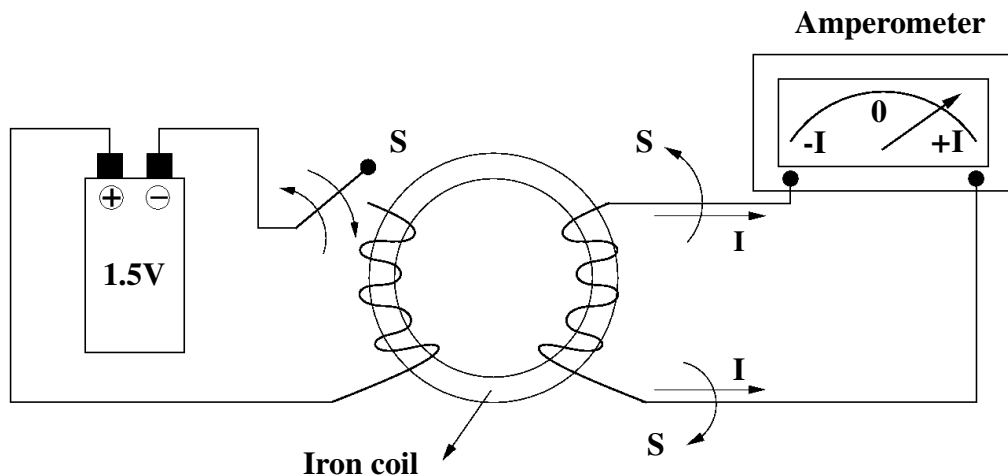


**Figure 2.7** Schematic representation of Faraday's experiment. In the right circuit, the amperometer measures a positive electric current  $+I$  when the switch  $S$  is closed (clockwise arrow) and a negative electric current  $-I$  when the switch is open (counterclockwise arrow).

Figure 2.7 provides a schematic representation of Faraday's experiment on electric induction. The electric circuit on the left (composed by a battery and an electric wire) and the electric circuit on the right (composed by an electric wire and an amperometer) are not physically connected. At the beginning of the experiment, the switch  $S$  is open and no current flows through the amperometer. When the switch is closed (clockwise arrow) the magnetic flux in the iron coil increases from zero to a maximum value that depends on the geometrical and physical properties of the circuit and a magnetic field is generated in all the iron coil. This has the effect of generating an electric current flowing counterclockwise in the right circuit which, is measured as a positive electric current  $+I$  by the amperometer. Viceversa, if the switch is open (counterclockwise arrow) the magnetic flux in the iron coil decreases from its maximum value to zero and an electric current starts flowing clockwise in the right circuit, which is measured as a negative electric current  $-I$  by the amperometer. The main conclusion that can be drawn by this experiment is that *a temporal variation of the magnetic flux in the iron coil induces an electromotive force in the circuit which elicits the motion of charged carriers in the electric wire on the right. Measurements made by the amperometer indicate that the resulting electric current in the wire flows in the opposite direction*

with respect to the increase or decrease of the magnetic flux in the iron coil.

**Mathematical formulation of Faraday’s experiment.** Let  $\mathcal{S}$  be an arbitrarily chosen *fixed* open surface whose boundary is the closed curve  $\Gamma_{\mathcal{S}} := \partial\mathcal{S}$ . For example, in Faraday’s experiment the open surface embraced by the electric wire in the right side of the circuit may be a suitable choice for  $\mathcal{S}$ . Let us denote by  $\underline{n}(\underline{x})$  the unit normal vector to the surface  $\mathcal{S}$  at any given point  $\underline{x} \in \mathcal{S}$  and by  $\underline{t}(\underline{x})$  the unit tangent vector to the curve  $\Gamma_{\mathcal{S}}$  at any given point  $\underline{x} \in \Gamma_{\mathcal{S}}$ , with  $\underline{t}$  oriented counterclockwise along  $\Gamma$  and  $\underline{n}$  directed in accordance with the right-hand rule, as schematized in Figure 2.8. Finally, let us denote by  $\underline{\mathbf{E}} = \underline{\mathbf{E}}(\underline{x}, t)$  and  $\underline{\mathbf{B}} = \underline{\mathbf{B}}(\underline{x}, t)$  the electric field (units:  $\text{Vm}^{-1}$ , where V means Volt) and the magnetic induction field (units:  $\text{Vs m}^{-2}$ ), respectively, and by  $\text{EMF}(t)$  (units: V) the electromotive force.

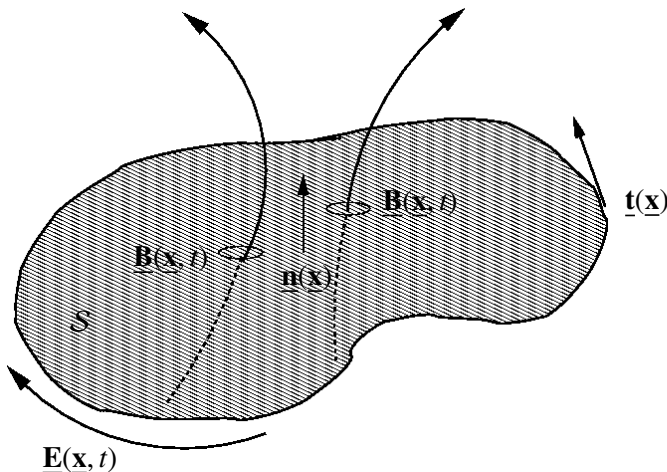


Figure 2.8 Schematic representation of Faraday’s law.

The mathematical formulation of Faraday’s experiment is

$$\text{EMF}(t) = -\frac{d\Phi(t)}{dt} \quad \forall t \quad (2.37a)$$

where

$$\text{EMF}(t) = \oint_{\Gamma_{\mathcal{S}}} \underline{\mathbf{E}}(\underline{x}, t) \cdot \underline{t}(\underline{x}) d\Gamma_{\mathcal{S}} \quad \forall t \quad (2.37b)$$

is the *circulation* of the electric field  $\underline{\mathbf{E}}$  along the line  $\Gamma_{\mathcal{S}}$  (see Definition A.2), whereas

$$\Phi(t) = \int_{\mathcal{S}} \underline{\mathbf{B}}(\underline{x}, t) \cdot \underline{n}(\underline{x}) dS \quad \forall t \quad (2.37c)$$

is the *flux* of the magnetic induction field  $\mathbf{B}$  across the surface  $S$  (see Definition A.1). The left-hand side of (2.37a) expresses the voltage drop associated with the circulation of the electric field across the line  $\Gamma$  at time  $t$ . This voltage drop can be regarded as an equivalent supply power force (usually referred to as *electromotive force*) that drives an electric current along  $\Gamma_S$  flowing in the opposite direction with respect to the time rate of change of the flux of the magnetic induction field across  $S$ . This physical principle is the basis for all rotor-stator alternators used to produce alternate current in electric networks.

## 2.6.2. The Ampère experiment

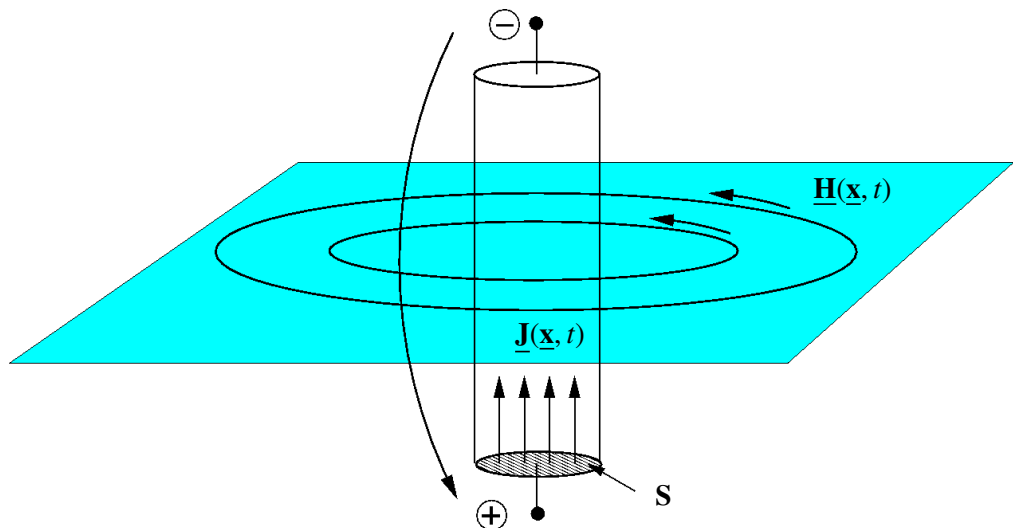


**Figure 2.9** Schematic representation of Ampère’s experiment. A conducting wire with a cross-sectional area  $S$  is carrying a conduction current density  $\underline{\mathbf{J}}$ . As a result, a magnetic field  $\underline{\mathbf{H}}$  is generated around the wire. The same happens if  $\underline{\mathbf{J}}$  is replaced by a displacement current density  $\partial \mathbf{D} / \partial t$  induced by a time-dependent voltage drop applied across the length of the wire.

Figure 2.9 provides a schematic representation of Ampère’s experiment on magnetic induction. The circuit is composed by an electric wire of cross-sectional area  $S$  that is carrying a conduction current density  $\underline{\mathbf{J}} = \underline{\mathbf{J}}(\underline{\mathbf{x}}, t)$  (units:  $\text{Am}^{-2}$ , where A means ampere). This means that the electric current associated with  $\underline{\mathbf{J}}$  is due to the motion of charged carriers inside the wire along the axial direction of the wire. As a result of the application of this conduction current density, a magnetic field  $\underline{\mathbf{H}} = \underline{\mathbf{H}}(\underline{\mathbf{x}}, t)$  (units:  $\text{Am}^{-1}$ ) is generated around the wire and the magnetic field lines are closed circles surrounding the wire, with  $\underline{\mathbf{H}}$  directed tangentially to the circles and oriented according to

the right-hand rule. It is amazing to observe that the same induction of a magnetic field in the wire occurs if we replace the externally applied conduction current source with a time-dependent battery across the end points of the wire. The result of this external source is that a *displacement* current density  $\underline{\mathbf{J}}_{disp} = \partial \underline{\mathbf{D}} / \partial t$ , where  $\underline{\mathbf{D}} = \underline{\mathbf{D}}(\underline{\mathbf{x}}, t)$  (units:  $\text{Am}^{-2}\text{s}^{-1}$ ) is the electric displacement vector field, which is electrically comparable to the conduction current density *without* implying or requiring the microscopic motion of any charge carrier inside the wire. The introduction of the displacement current density was due to the intuition of James Clerk Maxwell and constitutes the main contribution he gave to the theory of electromagnetism. The main conclusion that can be drawn by the above experiment is that *a conduction or displacement current density carried by the wire induces a magnetic field inside the wire that propagates in the medium around the wire*.

**Mathematical formulation of Ampère’s experiment.** Let  $\mathcal{S}$  be an arbitrarily chosen *fixed* open surface whose boundary is the closed curve  $\Gamma_{\mathcal{S}} := \partial \mathcal{S}$ . For example, in Ampère’s experiment the cross-sectional area of the electric wire may be a suitable choice for  $\mathcal{S}$ . Let us denote by  $\underline{\mathbf{n}}(\underline{\mathbf{x}})$  the unit normal vector to the surface  $\mathcal{S}$  at any given point  $\underline{\mathbf{x}} \in \mathcal{S}$  and by  $\underline{\mathbf{t}}(\underline{\mathbf{x}})$  the unit tangent vector to the curve  $\Gamma_{\mathcal{S}}$  at any given point  $\underline{\mathbf{x}} \in \Gamma_{\mathcal{S}}$ , with  $\underline{\mathbf{t}}$  oriented counterclockwise along  $\Gamma$  and  $\underline{\mathbf{n}}$  directed in accordance with the right-hand rule. The mathematical formulation of Ampère’s experiment is

$$\oint_{\Gamma} \underline{\mathbf{H}}(\underline{\mathbf{x}}, t) \cdot \underline{\mathbf{t}}(\underline{\mathbf{x}}) d\Gamma_{\mathcal{S}} = I_{tot}(t) \quad \forall t \quad (2.38a)$$

where

$$I_{tot}(t) = \int_{\mathcal{S}} \left( \underline{\mathbf{J}}(\underline{\mathbf{x}}, t) + \frac{\partial \underline{\mathbf{D}}(\underline{\mathbf{x}}, t)}{\partial t} \right) \cdot \underline{\mathbf{n}}(\underline{\mathbf{x}}) d\mathcal{S} \quad \forall t \quad (2.38b)$$

is the *total current* (units: A) flowing through the surface  $\mathcal{S}$  at time  $t$ . The physical principle expressed by Ampère’s law (2.38a) is the basis for all antennas used in modern communication systems.

### 2.6.3. The Gauss law

Figure 2.10 provides a schematic description of Gauss’ law on the balance of electric charge. Let the volume  $\mathbb{W}$  be a fixed arbitrary open bounded region of  $\mathbb{R}^3$  whose boundary is the surface  $\mathcal{S}_{\mathbb{W}} := \partial \mathbb{W}$ . Let the unit outward normal vector  $\underline{\mathbf{n}}(\underline{\mathbf{x}})$  be defined at each point  $\underline{\mathbf{x}} \in \mathcal{S}_{\mathbb{W}}$ . Let the electric charge density  $\rho^{el} = \rho^{el}(\underline{\mathbf{x}}, t)$  (units:  $\text{Cm}^{-3}$ , where C means Coulomb) be defined for all  $\underline{\mathbf{x}} \in \mathbb{W}$  and for all  $t$ . The Gauss law states that the electric charge density acts as a source (if  $\rho^{el} > 0$ ) or sink (if  $\rho^{el} < 0$ ) for the electric displacement field  $\underline{\mathbf{D}}$ .

**Mathematical formulation of Gauss’ law.** The mathematical formulation of Gauss’

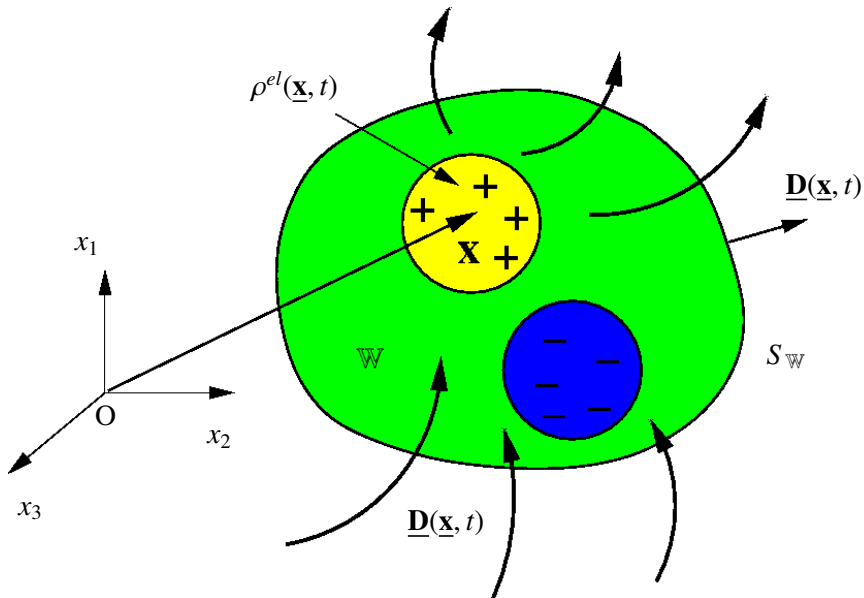


Figure 2.10 Schematic representation of Gauss' law.

law is

$$\int_{S_W} \underline{D}(\underline{x}, t) \cdot \underline{n}(\underline{x}) dS_W = Q_W(t) \quad \forall t \quad (2.39a)$$

where

$$Q_W(t) = \int_W \rho^{el}(\underline{x}, t) dW \quad \forall t \quad (2.39b)$$

is the *total electric charge* (units: C) contained in  $\mathbb{W}$  at time  $t$ . The physical principle expressed by the Gauss law (2.39a) is that *the total electric charge  $Q_W$  contained in the volume  $\mathbb{W}$  at time  $t$  equals the net flux of the electric displacement vector  $\underline{D}$  across the surface  $S_W$* .

#### 2.6.4. Absence of magnetic monopole

The classical theory for electromagnetism assumes that a magnetic counterpart to the electric charge, namely a magnetic monopole, does not exist. This assumption, however, has been matter of debate for almost a century. The theoretical investigation on the existence of magnetic monopoles was initiated by P. A. M. Dirac in [33], where the author analyzed the quantum dynamics of an electron (with electric charge  $-q = -1.602 \cdot 10^{-19}$ C) in presence of a magnetic monopole of magnetic charge  $q_m$ . In

the mentioned reference it was shown that wave functions describing the motion of the electron may exist only if the following relation is satisfied

$$q q_m = \frac{n}{2} \hbar c \quad n = 0, \pm 1, \pm 2, \dots, \quad (2.40)$$

where  $\hbar = h/(2\pi)$  is the reduced Planck constant ( $h = 6.626 \cdot 10^{-34}$  Js) and  $c$  is the velocity of light. Relation (2.40) has two important implications:

1. the quantized nature of the electric charge appears as a natural consequence of the existence of a magnetic monopole;
2. conversely, the existence of isolated magnetic poles appears to undergo the same quantized nature as of the electric charge which was experimentally measured by R. A. Millikan in 1909 and documented in [84].

After the milestone work [33] (followed by another article written by the same author [34]), an intensive theoretical and experimental activity has been devoted over the years to produce clear evidences of the existence of magnetic monopoles. A survey of such activity can be found in the recent article [86]. However, despite all of these efforts, no experimental evidence has been provided to support the existence of a magnetic monopole density corresponding to the electric charge density  $\rho^{el}$ . Thus, in this book we retain the classical assumption that the magnetic monopole density is always equal to zero, implying that *the net flux of the magnetic induction field across the surface  $S_W$  surrounding an arbitrary fixed open bounded region  $W \subset \mathbb{R}^3$  is equal to zero at all times  $t$* .

**Mathematical formulation of the absence of magnetic monopole.** Let the volume  $W$  be a fixed arbitrary open bounded region of  $\mathbb{R}^3$  whose boundary is the surface  $S_W := \partial W$ . Let the unit outward normal vector  $\underline{n}(\underline{x})$  be defined at each point  $\underline{x} \in S_W$ . The mathematical formulation of the absence of magnetic monopole is

$$\int_{S_W} \underline{B}(\underline{x}, t) \cdot \underline{n}(\underline{x}) dS_W = 0 \quad \forall t. \quad (2.41)$$

### 2.6.5. The Maxwell equations in integral form

The Maxwell equations in integral form are obtained by collecting the four main mathematical statements of the physical principles of electromagnetism that have been illustrated in the previous sections, and read:

$$\oint_{\Gamma_S} \underline{E}(\underline{x}, t) \cdot \underline{t}(\underline{x}) d\Gamma_S = -\frac{d}{dt} \int_S \underline{B}(\underline{x}, t) \cdot \underline{n}(\underline{x}) dS \quad \forall t, \quad (2.42a)$$

$$\oint_{\Gamma_S} \underline{H}(\underline{x}, t) \cdot \underline{t}(\underline{x}) d(\underline{x}) = \int_S \left( \underline{J}(\underline{x}, t) + \frac{\partial \underline{D}(\underline{x}, t)}{\partial t} \right) \cdot \underline{n}(\underline{x}) dS \quad \forall t, \quad (2.42b)$$

$$\int_{S_{\mathbb{W}}} \underline{\mathbf{D}}(\underline{\mathbf{x}}, t) \cdot \underline{\mathbf{n}}(\underline{\mathbf{x}}) dS = \int_{\mathbb{W}} \rho^{el}(\underline{\mathbf{x}}, t) d\mathbb{W} \quad \forall t, \quad (2.42c)$$

$$\int_{S_{\mathbb{W}}} \underline{\mathbf{B}}(\underline{\mathbf{x}}, t) \cdot \underline{\mathbf{n}}(\underline{\mathbf{x}}) dS = 0 \quad \forall t. \quad (2.42d)$$

In (2.42a) and (2.42b),  $S$  is an open bounded fixed surface in  $\mathbb{R}^3$  whose boundary is the closed curve  $\Gamma_S$ . In (2.42c) and (2.42d),  $\mathbb{W}$  is an open bounded fixed volume in  $\mathbb{R}^3$  whose boundary is the closed surface  $S_{\mathbb{W}}$ .

### 2.6.6. The Maxwell equations in local form

Starting from the integral form of the laws of electromagnetism reported in Section 2.6.5 it is possible to derive their corresponding local (or differential) form by applying Stokes' and Gauss' Theorems introduced in Section A.1. Precisely, the application of Stokes' Theorem (A.6) to the left-hand side of the Faraday law (2.42a) and the Ampère law (2.42b) yields:

$$\int_S \left( \nabla_{\underline{\mathbf{x}}} \times \underline{\mathbf{E}}(\underline{\mathbf{x}}, t) + \frac{\partial \underline{\mathbf{B}}(\underline{\mathbf{x}}, t)}{\partial t} \right) \cdot \underline{\mathbf{n}}(\underline{\mathbf{x}}) dS = 0 \quad \forall t, \quad (2.43a)$$

$$\int_S \left( \nabla_{\underline{\mathbf{x}}} \times \underline{\mathbf{H}}(\underline{\mathbf{x}}, t) - \underline{\mathbf{J}}(\underline{\mathbf{x}}, t) - \frac{\partial \underline{\mathbf{D}}(\underline{\mathbf{x}}, t)}{\partial t} \right) \cdot \underline{\mathbf{n}}(\underline{\mathbf{x}}) dS = 0 \quad \forall t, \quad (2.43b)$$

We notice that it has been possible to move the time derivative on the right-hand side of Faraday's law inside the integral, replacing the symbol  $d/dt$  with  $\partial/\partial t$ , because the surface  $S$  is fixed. Proceeding similarly, the application of the Divergence Theorem (A.1) to the left-hand side of the Gauss law (2.42c) and to the law of absence of magnetic monopole (2.42d) yields:

$$\int_{\mathbb{W}} \left( \nabla_{\underline{\mathbf{x}}} \cdot \underline{\mathbf{D}}(\underline{\mathbf{x}}, t) - \rho^{el}(\underline{\mathbf{x}}, t) \right) d\mathbb{W} = 0 \quad \forall t, \quad (2.43c)$$

$$\int_{\mathbb{W}} \nabla_{\underline{\mathbf{x}}} \cdot \underline{\mathbf{B}}(\underline{\mathbf{x}}, t) d\mathbb{W} = 0 \quad \forall t. \quad (2.43d)$$

Since the fixed surface  $S$  and the fixed volume  $\mathbb{W}$  are chosen arbitrarily in  $\mathbb{R}^3$ , the integral equations (2.43) leads to the *local form* of the Maxwell equation system, which reads:

$$\nabla_{\underline{\mathbf{x}}} \times \underline{\mathbf{E}}(\underline{\mathbf{x}}, t) = - \frac{\partial \underline{\mathbf{B}}(\underline{\mathbf{x}}, t)}{\partial t} \quad \forall \underline{\mathbf{x}} \in \mathbb{R}^3 \text{ and } \forall t, \quad (2.44a)$$

$$\nabla_{\underline{\mathbf{x}}} \times \underline{\mathbf{H}}(\underline{\mathbf{x}}, t) = \underline{\mathbf{J}}(\underline{\mathbf{x}}, t) + \frac{\partial \underline{\mathbf{D}}(\underline{\mathbf{x}}, t)}{\partial t} \quad \forall \underline{\mathbf{x}} \in \mathbb{R}^3 \text{ and } \forall t, \quad (2.44b)$$

$$\nabla_{\underline{\mathbf{x}}} \cdot \underline{\mathbf{D}}(\underline{\mathbf{x}}, t) = \rho^{el}(\underline{\mathbf{x}}, t) \quad \forall \underline{\mathbf{x}} \in \mathbb{R}^3 \text{ and } \forall t, \quad (2.44c)$$

$$\nabla_{\underline{\mathbf{x}}} \cdot \underline{\mathbf{B}}(\underline{\mathbf{x}}, t) = 0 \quad \forall \underline{\mathbf{x}} \in \mathbb{R}^3 \text{ and } \forall t. \quad (2.44d)$$

Maxwell’s equations must be completed with constitutive laws characterizing the microscopic electromagnetic properties of the medium. In the case of a linear, homogeneous and isotropic medium, we can write:

$$\underline{\mathbf{D}} = \epsilon_m \underline{\mathbf{E}} \quad (2.45a)$$

$$\underline{\mathbf{B}} = \mu_m \underline{\mathbf{H}} \quad (2.45b)$$

where the dielectric permittivity  $\epsilon_m$  (units:  $\text{Fm}^{-1}$ , where F means Farad) and the magnetic permeability  $\mu_m$  (units:  $\text{Hm}^{-1}$ , where H means Henry) are assumed to be given positive constant quantities. In the case of a linear anisotropic material, the dielectric permittivity and the magnetic permeability may assume the form of  $3 \times 3$  tensors; if the material is nonlinear,  $\epsilon_m$  and  $\mu_m$  may be nonlinear functions of  $\underline{\mathbf{E}}$  and  $\underline{\mathbf{H}}$  (see [60] and [17, Chapter 11]). To solve the Maxwell equation system (2.44)-(2.45) we need to supply suitable initial and boundary conditions. Examples of initial value/boundary value problems associated with the Maxwell equations are discussed in [82, 83] and in the more recent references [60, 17]. For a numerical treatment of the Maxwell equations in a three-dimensional geometry, we refer to [8] and to the recent book [18].

## 2.6.7. Mathematical properties of the Maxwell equations

In this section we illustrate two important properties that mathematically characterize the Maxwell equations and their solutions.

### 2.6.7.1. Compatibility condition between the sources

In the typical framework of Maxwell’s equations,  $\rho^{el}$  and  $\underline{\mathbf{J}}$  are given data for the system and, as such, are assumed to be known. However, the specific mathematical structure of Maxwell’s equations requires that  $\rho^{el}$  and  $\underline{\mathbf{J}}$  satisfy a strict compatibility condition, meaning that we do not have the freedom to choose  $\rho^{el}$  and  $\underline{\mathbf{J}}$  independently of each other. In order to derive the compatibility condition, we apply the divergence operator to Equation (2.44b) to obtain

$$\nabla_{\underline{\mathbf{x}}} \cdot (\nabla_{\underline{\mathbf{x}}} \times \underline{\mathbf{H}}(\underline{\mathbf{x}}, t)) = \nabla_{\underline{\mathbf{x}}} \cdot \underline{\mathbf{J}}(\underline{\mathbf{x}}, t) + \nabla_{\underline{\mathbf{x}}} \cdot \frac{\partial \underline{\mathbf{D}}(\underline{\mathbf{x}}, t)}{\partial t} \quad \forall \underline{\mathbf{x}} \in \mathbb{R}^3 \text{ and } \forall t,$$

which, recalling that the divergence of a cross product is zero and assuming that  $\underline{\mathbf{D}}$  is smooth enough to switch the time derivative with the divergence operator, leads to

$$\frac{\partial}{\partial t} (\nabla_{\underline{\mathbf{x}}} \cdot \underline{\mathbf{D}}(\underline{\mathbf{x}}, t)) + \nabla_{\underline{\mathbf{x}}} \cdot \underline{\mathbf{J}}(\underline{\mathbf{x}}, t) = 0 \quad \forall \underline{\mathbf{x}} \in \mathbb{R}^3 \text{ and } \forall t. \quad (2.46)$$

Let us now consider Equation (2.44c). By differentiating with respect to time we obtain

$$\frac{\partial}{\partial t} (\nabla_{\underline{\mathbf{x}}} \cdot \underline{\mathbf{D}}(\underline{\mathbf{x}}, t)) = \frac{\partial \rho^{el}(\underline{\mathbf{x}}, t)}{\partial t} \quad \forall \underline{\mathbf{x}} \in \mathbb{R}^3 \text{ and } \forall t. \quad (2.47)$$

Thus, combining equations (2.46) and (2.47) we obtain the compatibility condition

$$\frac{\partial \rho^{el}(\underline{x}, t)}{\partial t} + \nabla_{\underline{x}} \cdot \underline{J}(\underline{x}, t) = 0 \quad \forall \underline{x} \in \mathbb{R}^3 \text{ and } \forall t \quad (2.48)$$

which imposes a strong differential constraint on the choice for data to be assigned on  $\rho^{el}$  and  $\underline{J}$ . This constraint must be satisfied at every point in space and time in order for Maxwell’s equations to hold.

**Remark 2.7** (The continuity equation). *In the context of Electromagnetism and its applications (for example, the study of charge transport in semiconductor devices), the compatibility condition (2.48) is usually referred to as the continuity equation for the electric charge density and current density (see [60] and [113, 79, 61]).*

### 2.6.7.2. Helmholtz decomposition and Maxwell’s equations

In this section we follow the analysis of [44, Section 3.3] and, for sake of simplicity, we assume that the arbitrary fixed open bounded region  $\mathbb{W} \subset \mathbb{R}^3$  introduced in Section 2.6.3 is simply connected. Then, we denote by  $\mathcal{S}_{\mathbb{W}}$  the boundary of  $\mathbb{W}$ , by  $\underline{n}(\underline{x})$  the unit outward normal vector at any point  $\underline{x} \in \mathcal{S}_{\mathbb{W}}$  and we indicate by  $L^2(\mathbb{W})$  and  $(L^2(\mathbb{W}))^3$  the spaces of scalar and vector-valued functions that are square integrable in the Lebesgue sense over the domain  $\mathbb{W}$ . Finally, we introduce the following functional spaces:

$$H^1(\mathbb{W}) = \left\{ \phi : \mathbb{W} \rightarrow \mathbb{R} \mid \phi \in L^2(\mathbb{W}), \nabla_{\underline{x}} \phi \in (L^2(\mathbb{W}))^3 \right\}, \quad (2.49a)$$

$$H(\text{div}; \mathbb{W}) = \left\{ \underline{\tau} : \mathbb{W} \rightarrow \mathbb{R}^3 \mid \underline{\tau} \in (L^2(\mathbb{W}))^3, \nabla_{\underline{x}} \cdot \underline{\tau} \in L^2(\mathbb{W}) \right\}, \quad (2.49b)$$

$$H_0(\text{div}; \mathbb{W}) = \left\{ \underline{\tau} \in H(\text{div}; \mathbb{W}) \mid \underline{\tau} \cdot \underline{n} = 0 \text{ on } \mathcal{S}_{\mathbb{W}} \right\}. \quad (2.49c)$$

The following result, known as Helmholtz decomposition principle, can be proved.

**Theorem 2.1** (Orthogonal decomposition of  $(L^2(\mathbb{W}))^3$ ).

$$(L^2(\mathbb{W}))^3 = H \oplus H^\perp, \quad (2.50a)$$

where:

$$H = \left\{ \underline{\tau} \in H_0(\text{div}; \mathbb{W}) \mid \nabla_{\underline{x}} \cdot \underline{\tau} = 0 \right\}, \quad (2.50b)$$

$$H^\perp = \left\{ \nabla_{\underline{x}} q, q \in H^1(\mathbb{W}) \right\}. \quad (2.50c)$$

The characterization of Theorem 2.1 is expressed by the result stated below.

**Theorem 2.2.** *Let  $\underline{v}$  be any vector belonging to  $(L^2(\mathbb{W}))^3$ . Then,  $\underline{v}$  admits the decomposition*

$$\underline{v} = \underline{v}_{\text{div-free}} + \underline{v}_{\text{curl-free}}, \quad (2.51a)$$

where  $\underline{\mathbf{v}}_{\text{div-free}} \in H$  and  $\underline{\mathbf{v}}_{\text{curl-free}} \in H^\perp$  are the solenoidal and irrotational components of  $\underline{\mathbf{v}}$ , respectively, defined as:

$$\underline{\mathbf{v}}_{\text{div-free}} = \nabla_{\underline{\mathbf{x}}} \times \underline{\phi}, \quad (2.51\text{b})$$

$$\underline{\mathbf{v}}_{\text{curl-free}} = \nabla_{\underline{\mathbf{x}}} p. \quad (2.51\text{c})$$

The vector field  $\underline{\phi} \in (H^1(\mathbb{W}))^3$  is the weak solution of the following boundary value problem:

$$-\Delta_{\underline{\mathbf{x}}}\underline{\phi} = \nabla_{\underline{\mathbf{x}}} \times \underline{\mathbf{v}} \quad \text{in } \mathbb{W}, \quad (2.52\text{a})$$

$$\nabla_{\underline{\mathbf{x}}} \cdot \underline{\phi} = 0 \quad \text{in } \mathbb{W}, \quad (2.52\text{b})$$

$$\underline{\phi} \times \underline{\mathbf{n}} = \underline{\mathbf{0}} \quad \text{on } S_{\mathbb{W}}. \quad (2.52\text{c})$$

The scalar field  $p \in H^1(\mathbb{W}) \setminus \mathbb{R}$  is the weak solution of the following boundary value problem:

$$\Delta_{\underline{\mathbf{x}}} p = \nabla_{\underline{\mathbf{x}}} \cdot \underline{\mathbf{v}} \quad \text{in } \mathbb{W}, \quad (2.53\text{a})$$

$$\nabla_{\underline{\mathbf{x}}} p \cdot \underline{\mathbf{n}} = \underline{\mathbf{v}} \cdot \underline{\mathbf{n}} \quad \text{on } S_{\mathbb{W}}. \quad (2.53\text{b})$$

Using (2.52b) and the fact that  $\nabla_{\underline{\mathbf{x}}} \times (\nabla_{\underline{\mathbf{x}}} \times \underline{\phi}) = \nabla_{\underline{\mathbf{x}}}(\nabla_{\underline{\mathbf{x}}} \cdot \underline{\phi}) - \Delta_{\underline{\mathbf{x}}}\underline{\phi}$ , we see that the decomposition (2.51a) defines in an unique manner the vector field  $\underline{\mathbf{v}}$  by specifying its curl and its divergence. In this sense, assuming for sake of simplicity that  $\epsilon_m$  and  $\mu_m$  are positive constants, we see that the Maxwell equations (2.44) in tandem with the constitutive laws (2.45), provide a complete characterization of the electric field  $\underline{\mathbf{E}}$  (through Equations (2.44a), (2.44c) and (2.45a)) and of the magnetic field  $\underline{\mathbf{H}}$  (through Equations (2.44b), (2.44d) and (2.45b)). The Helmholtz decomposition principle is a powerful tool for the theoretical investigation of the solutions of Maxwell's equations and for their numerical approximation with the finite element method (see [9] and the recent book [18]).

### 2.6.8. Energy balance law associated with the Maxwell equations

In Section 2.5.5, we wrote the balance law for the energy of a system, see Equation (2.35). In this section we will show that the Maxwell equations (2.44) equipped with the constitutive laws (2.45) provide an energy balance for the propagation of electromagnetic waves inside a linear and homogeneous medium.

Let us begin by substituting the constitutive relationship (2.45a) into (2.44b). Multiplying the resulting equation by  $\underline{\mathbf{E}}$  and integrating over an arbitrary volume  $\mathbb{W} \subset \mathbb{R}^3$  we obtain

$$\frac{d}{dt} \int_{\mathbb{W}} \frac{\epsilon_m}{2} |\underline{\mathbf{E}}|^2 d\mathbb{W} = - \int_{\mathbb{W}} \underline{\mathbf{J}} \cdot \underline{\mathbf{E}} d\mathbb{W} + \int_{\mathbb{W}} \nabla_{\underline{\mathbf{x}}} \times \underline{\mathbf{H}} \cdot \underline{\mathbf{E}} d\mathbb{W}. \quad (2.54)$$

Analogously, substituting the constitutive relationship (2.45b) into (2.44a), multiply-

ing the resulting equation by  $\underline{\mathbf{H}}$  and integrating over an arbitrary volume  $\mathbb{W} \subset \mathbb{R}^3$ , we obtain

$$\frac{d}{dt} \int_{\mathbb{W}} \frac{\mu_m}{2} |\underline{\mathbf{H}}|^2 d\mathbb{W} = - \int_{\mathbb{W}} \nabla_{\underline{x}} \times \underline{\mathbf{E}} \cdot \underline{\mathbf{H}} d\mathbb{W}. \quad (2.55)$$

Adding (2.54) and (2.55) we obtain

$$\frac{d\mathcal{E}_{EH}}{dt} = - \int_{\mathbb{W}} \underline{\mathbf{J}} \cdot \underline{\mathbf{E}} d\mathbb{W} + \int_{\mathbb{W}} (\nabla_{\underline{x}} \times \underline{\mathbf{H}} \cdot \underline{\mathbf{E}} - \nabla_{\underline{x}} \times \underline{\mathbf{E}} \cdot \underline{\mathbf{H}}) d\mathbb{W} \quad (2.56)$$

where

$$\mathcal{E}_{EH} := \int_{\mathbb{W}} \frac{\epsilon_m}{2} |\underline{\mathbf{E}}|^2 d\mathbb{W} + \int_{\mathbb{W}} \frac{\mu_m}{2} |\underline{\mathbf{H}}|^2 d\mathbb{W} \quad (2.57)$$

which, utilizing the notation introduced in Section ?? for the functional norm defined in  $L^2(\mathbb{W})$ , can also be written as

$$\mathcal{E}_{EH}(t) = \frac{\epsilon_m}{2} \|\underline{\mathbf{E}}(t)\|_{L^2(\mathbb{W})}^2 + \frac{\mu_m}{2} \|\underline{\mathbf{H}}(t)\|_{L^2(\mathbb{W})}^2. \quad (2.58)$$

Utilizing formula (??), identity (2.56) can be rewritten as

$$\frac{d\mathcal{E}_{EH}}{dt} = - \int_{\mathbb{W}} \underline{\mathbf{J}} \cdot \underline{\mathbf{E}} d\mathbb{W} - \int_{\mathbb{W}} \nabla_{\underline{x}} \cdot \underline{\mathbf{S}} d\mathbb{W} \quad (2.59)$$

where  $\underline{\mathbf{S}}$  denotes the *Poynting vector* defined as

$$\underline{\mathbf{S}} := \underline{\mathbf{E}} \times \underline{\mathbf{H}}. \quad (2.60)$$

Thanks to the divergence theorem, we finally obtain

$$\frac{d\mathcal{E}_{EH}}{dt} = \underbrace{- \int_{\mathbb{W}} \underline{\mathbf{J}} \cdot \underline{\mathbf{E}} d\mathbb{W}}_{\Pi_1} - \underbrace{\int_{\partial\mathbb{W}} \underline{\mathbf{S}} \cdot \underline{\mathbf{n}}_{\underline{x}} d(\partial\mathbb{W})}_{\Pi_2}. \quad (2.61)$$

which shows that the propagation of electromagnetic waves inside a linear and homogeneous medium is characterized by a potential energy  $\mathcal{E}_{EH}$  associated with the electric field  $\underline{\mathbf{E}}$  and the magnetic field  $\underline{\mathbf{H}}$ , whose rate of change is dictated by the power  $\Pi_1$  associated with the Joule effect and the power  $\Pi_2$  associated with the energy flux through the boundary of  $\mathbb{W}$ .

“Notes” — 2019/5/17 — 17:39 — page 52 — #60

## CHAPTER 3

# Reduction of the Maxwell partial differential system

It is possible, and convenient, to elaborate the Maxwell equations (2.44)-(2.45) to obtain a more tractable formulation that allows us to quantitatively characterize the conditions under which the effect of magnetic induction can be neglected. By doing so, we will obtain a set of reduced Maxwell equations where the computation of the electric field is decoupled from that of the magnetic field. Starting from this reduced description of electromagnetic phenomena, we will derive a set of algebraic equations known as Kirchhoff current and voltage laws that are the pillars of circuit theory and simulation (see [31]).

### 3.1. The vector potential

Equation (2.44d) can be satisfied by setting

$$\underline{\mathbf{B}} = \nabla \times \underline{\mathbf{A}} \quad (3.1)$$

where  $\underline{\mathbf{A}}$  is the *vector potential* (units:  $\text{Vsm}^{-1}$ ). Let us now determine the divergence of  $\underline{\mathbf{A}}$ . Replacing (3.1) into (2.44a), yields

$$\nabla \times \left( \underline{\mathbf{E}} + \frac{\partial \underline{\mathbf{A}}}{\partial t} \right) = \underline{\mathbf{0}}$$

from which it follows that there exists a *scalar potential*  $\psi$  such that

$$\underline{\mathbf{E}} + \frac{\partial \underline{\mathbf{A}}}{\partial t} = -\nabla \psi. \quad (3.2)$$

Assume from now on that  $\epsilon_m$  is a constant scalar quantity. Then, multiplying (3.2) by  $\epsilon_m$ , taking the divergence of both sides and using (2.45a) and (2.44c), we get

$$\rho^{el} + \epsilon_m \frac{\partial}{\partial t} \nabla \cdot \underline{\mathbf{A}} = -\nabla \cdot (\epsilon_m \nabla \psi).$$

We complete the definition of the vector potential  $\underline{\mathbf{A}}$  by specifying its divergence using the so-called Lorentz gauge

$$\nabla \cdot \underline{\mathbf{A}} := -\frac{1}{c^2} \frac{\partial \psi}{\partial t}$$

where  $c = (\mu_0 \epsilon_0)^{-1/2}$  is the speed of light,  $\mu_0$  and  $\epsilon_0$  being the magnetic permeability and dielectric permittivity of vacuum, respectively. Replacing this latter relation into the previous equation we obtain the following second-order hyperbolic equation satisfied by the scalar potential  $\psi$

$$\frac{\epsilon_m}{c^2} \frac{\partial^2 \psi}{\partial t^2} + \nabla \cdot (-\epsilon_m \nabla \psi) = \rho^{el}. \quad (3.3)$$

Eq. (3.3) expresses the propagation of an electric wave throughout the medium, the wave speed  $v_w$  being equal to

$$v_w = \frac{1}{\sqrt{\mu_m \epsilon_m}} = \frac{1}{\sqrt{\mu_0 \epsilon_0 \mu_r \epsilon_r}} = \frac{c}{\sqrt{\mu_r \epsilon_r}}$$

where  $\mu_r$  and  $\epsilon_r$  are the relative magnetic permeability and relative dielectric permittivity of the medium, respectively.

### 3.2. Nondimensionalization and reduced Maxwell equations

To assess the importance of the first term on the left-hand side of (3.3) with respect to the second term, it is useful to rewrite the wave equation in dimensionless form. This procedure is analogous to the nondimensionalization of the Navier-Stokes equations used to derive the Stokes system. Let  $\{t\}$  and  $\{\psi\}$  indicate the characteristic values of time and scalar potential, so that we can write  $t = \{t\} \hat{t}$  and  $\psi = \{\psi\} \hat{\psi}$ . Furthermore, let us assume that the spatial coordinates can be scaled using the same characteristic length  $\{x\}$ , so that  $\{x_1\} = \{x_2\} = \{x_3\} = \{x\}$  and, consequently,  $\underline{x} = \{x\} \hat{\underline{x}}$ . Substituting these quantities in (3.3), we obtain

$$\frac{\{x\}^2}{c^2 \{t\}^2} \frac{\partial^2 \hat{\psi}}{\partial \hat{t}^2} - \hat{\nabla} \cdot \hat{\nabla} \hat{\psi} = \hat{\rho}^{el}$$

where  $\hat{\rho}^{el} = \rho^{el}/\{\rho^{el}\}$  with  $\{\rho^{el}\} = \epsilon_m \{\psi\} / \{x\}^2$ . From the above dimensionless wave equation, we see that neglecting the first term on the left-hand side is equivalent to assuming

$$\{x\} \ll c \{t\}. \quad (3.4)$$

Typical choices for the characteristic length  $\{x\}$  and the characteristic time  $\{t\}$  are  $\{x\} = R_{max}$  and  $\{t\} = 1/f_{max}$ , where  $R_{max}$  is the characteristic length of the medium and  $f_{max}$  is the highest frequency traveling through the medium, with  $\lambda_w = c/f_{max}$  being the

associated wavelength. With these choices for the characteristic values of space and time, condition (3.4) implies that

$$R_{max} \ll \frac{c}{f_{max}} := \lambda_w. \quad (3.5)$$

If condition (3.5) is satisfied, the first term in (3.3) can be neglected to obtain the so-called *Poisson equation* that relates the *scalar potential*  $\psi$  to the electric charge density  $\rho^{el}$

$$\nabla \cdot (-\varepsilon_m \nabla \psi) = \rho^{el}. \quad (3.6)$$

**Remark 3.1.** Condition (3.5) is amply satisfied in many applications arising in engineering and life sciences. For example, if we are interested in studying the electromagnetic propagation in ion channels or in semiconductor devices for nanoelectronics applications,  $R_{max}$  is typically of the order of nm. However, even high-frequency signals, typically of the order of 100 GHz =  $10^{11}$  Hz (like that in cellular phone transmission), have a wavelength  $\lambda_w \approx 3\text{mm}$  which is much larger than  $R_{max}$ .

Combining the Poisson equation (14.13d) with (2.44c), (2.45a) and (2.44a), we see that satisfying condition (3.5) is equivalent to assuming that

$$\frac{\partial \mathbf{B}}{\partial t} \simeq 0. \quad (3.7)$$

Thus, assuming that the magnetic induction varies slowly in time allows us to approximate the Faraday law (2.44a) by

$$\nabla \times \mathbf{E} = \mathbf{0}. \quad (3.8)$$

The consequence of (3.8) is that there exists a scalar potential  $\psi = \psi(\mathbf{x}, t)$  such that

$$\mathbf{E} = -\nabla \psi, \quad (3.9)$$

in such a way that, replacing (3.9) into (2.45a) and (2.44c) we get (14.13d). Equation (3.9) characterizes the relationship between the scalar potential  $\psi$  and the electric field  $\mathbf{E}$ , under the assumption that time variations of the magnetic induction can be neglected. For this reason, the scalar potential  $\psi$  is also called *electric potential*.

**Remark 3.2** (Quasi-static fields). Assumption (3.7) is referred to as quasi-static approximation (QSA) and has the effect of decoupling the electric field dynamics from that of the magnetic field. QSA is valid until the characteristic scale length of the problem at hand is sufficiently small with respect to the wavelength associated with the maximum frequency of the signal that is propagating in the physical system.

The Maxwell equations under the QSA assumption become:

$$\frac{\partial \rho^{el}}{\partial t} + \nabla \cdot \underline{\mathbf{J}} = 0 \quad \text{Continuity equation (3.10a)}$$

$$\nabla \cdot \underline{\mathbf{D}} = \rho^{el} \quad \text{Gauss Law (3.10b)}$$

$$\underline{\mathbf{D}} = \epsilon_m \underline{\mathbf{E}} = -\epsilon_m \nabla \psi. \quad \text{Constitutive law for electric displacement (3.10c)}$$

### 3.3. Derivation of the Kirchhoff laws for currents and voltages

In this section we derive the Kirchhoff current and voltage laws used in circuit theory and analysis (see [31]) starting from the Maxwell equations illustrated in Section 2.6.6.

#### 3.3.1. The Kirchhoff current law

Let  $\mathbb{W}_{\underline{x}}$  denote an open volume centered at a given point  $\underline{x} \in \mathbb{R}^3$  and  $\partial\mathbb{W}_{\underline{x}}$  be the boundary surface of  $\mathbb{W}_{\underline{x}}$  on which a unit normal outward vector  $\underline{n}_{\underline{x}}$  is defined. Integrating the continuity equation (2.48) inside  $\mathbb{W}_{\underline{x}}$ , applying the divergence theorem (A.1) we obtain

$$i_{cond}^{\underline{x}}(t) + i_{displ}^{\underline{x}}(t) = 0 \quad \forall t, \quad (3.11a)$$

where:

$$i_{cond}^{\underline{x}}(t) := \int_{\partial\mathbb{W}_{\underline{x}}} \underline{\mathbf{J}}(\underline{x}, t) \cdot \underline{n}_{\underline{x}} d\mathbb{W} \quad (3.11b)$$

$$i_{displ}^{\underline{x}}(t) := \int_{\partial\mathbb{W}_{\underline{x}}} \frac{\partial \underline{\mathbf{D}}(\underline{x}, t)}{\partial t} \cdot \underline{n}_{\partial\mathbb{W}_{\underline{x}}} d\mathbb{W} \quad (3.11c)$$

are the total conduction and displacement currents across the surface embracing  $\mathbb{W}_{\underline{x}}$ , respectively. Equation (3.11a) is the *Kirchhoff Current Law* (KCL) and expresses the physical property that, for each time  $t$ , the net total current flux across a closed surface is equal to zero.

The use of KCL is particularly helpful when dealing with a *lumped representation of circuits*, which consists in assuming that the attributes of the circuit, including resistance, capacitance and inductance, are concentrated into idealized electrical components, including resistors, capacitors and inductors, joined by a network of perfectly conducting wires. For example, in the schematic representation of Figure 3.1 we can identify four lumped elements, namely B1, B2, B3 and B4 (also called *bipoles*). The bipoles connect at circuit *nodes* and electric currents flow through circuit *branches* connecting the nodes.

The interpretation of the KCL in a lumped circuit is that the sum of the currents flowing in the branches departing from a circuit node centered at  $\underline{x}$  is equal to zero for all  $t$ , namely

$$\sum_{k=1}^{N_{\underline{x}}} i_k^{\underline{x}}(t) = 0 \quad \forall t, \quad (3.11d)$$

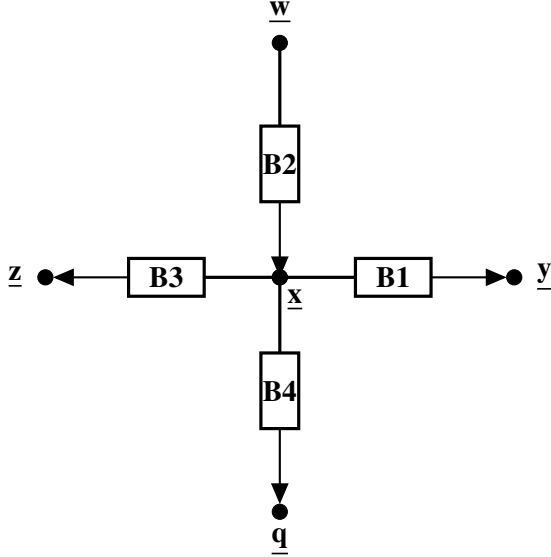


**Figure 3.1** Schematic representation of the Kirchhoff Current Law. In this example  $N_{\underline{x}} = 4$ . Arrows indicate the direction of the current in each branch.  $B_1, B_2, B_3$  and  $B_4$  are bipoles (active or passive, linear or nonlinear) whereas  $\underline{y}, \underline{z}, \underline{w}$  and  $\underline{q}$  are the neighboring nodes of node  $\underline{x}$ .

where  $N_{\underline{x}}$  is the number of branches departing from node  $\underline{x}$  and

$$i_k^{\underline{x}}(t) := i_{k,cond}^{\underline{x}}(t) + i_{k,displ}^{\underline{x}}(t) \quad k = 1, \dots, N_{\underline{x}} \quad \forall t,$$

is the current flowing through the  $k$ -th branch, divided into its conduction and displacement contributions. In the sum in (3.11d) we assume the convention that  $i_k^{\underline{x}}$  is positive if it departs from node  $\underline{x}$  whereas  $i_i^{\underline{x}}$  is negative if it enters node  $\underline{x}$ . In the example of Figure 3.1, the KCL becomes

$$i_1^{\underline{x}}(t) - i_2^{\underline{x}}(t) + i_3^{\underline{x}}(t) + i_4^{\underline{x}}(t) = 0 \quad \forall t.$$

### 3.3.2. The Kirchhoff voltage law

Let  $S_{\underline{x}}$  denote an open surface centered at a given point  $\underline{x} \in \mathbb{R}^3$ . Let us also define on  $S_{\underline{x}}$  a unit normal outward vector  $\underline{n}_{S_{\underline{x}}}$  and denote by  $\Gamma_{\underline{x}}$  the boundary line of  $S_{\underline{x}}$ . Applying the Stokes theorem (A.6) to the Faraday law (2.44a) yields

$$\text{EMF}_{\Gamma_{\underline{x}}}(t) = -\frac{d}{dt}\Phi_{S_{\underline{x}}}(\underline{B}) \quad \forall t, \tag{3.12a}$$

where:

$$\text{EMF}_{\Gamma_{\underline{x}}}(t) := \oint_{\Gamma_{\underline{x}}} \underline{\mathbf{E}}(\underline{\mathbf{x}}, t) \cdot d\underline{l} \quad (3.12b)$$

$$\Phi_{S_{\underline{x}}}^{\mathbf{B}}(t) := \int_{S_{\underline{x}}} \underline{\mathbf{B}}(\underline{\mathbf{x}}, t) \cdot \underline{\mathbf{n}}_{S_{\underline{x}}} dS \quad (3.12c)$$

are the induced electromotive force (per unit charge) around the surface  $S_{\underline{x}}$  and the time rate of change of the flux of the magnetic induction across the surface  $S_{\underline{x}}$ , respectively. Equation (3.12a) expresses the physical property that, for each time  $t$ , a transient current is induced in a circuit as a result of a temporal variation of the magnetic flux across the circuit. Upon assuming the validity of the QSA (see Remark 3.2), the right-hand side of (3.12a) is set equal to zero so that (3.12a) becomes

$$\oint_{\Gamma_{\underline{x}}} \underline{\mathbf{E}}(\underline{\mathbf{x}}, t) \cdot d\underline{l} = 0 \quad \forall t. \quad (3.12d)$$

The above relation can be given a more significant expression if we partition the boundary line  $\Gamma_{\underline{x}}$  into a finite, large number,  $M_{\underline{x}}$ , of oriented elements  $d\underline{l}_k$ ,  $k = 1, \dots, M_{\underline{x}}$ , and define on such partition the *nodal electric potential*  $\psi_k(t) := \psi(\underline{\mathbf{x}}_k, t)$ ,  $k = 1, \dots, M_{\underline{x}}$ , with the convention that  $\psi_{M_{\underline{x}}+1}(t) \equiv \psi_{M_1}(t)$  (see Figure 3.2).

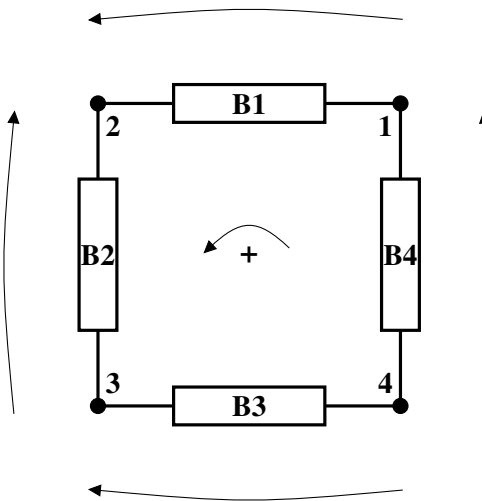


**Figure 3.2** Schematic representation of the KVL. In this example  $M_{\underline{x}} = 4$ . Curved arrows indicate the direction of the voltage in each branch.  $B_1, B_2, B_3$  and  $B_4$  are bipoles (active or passive, linear or nonlinear) whereas 1, 2, 3 and 4 are the circuit nodes. A branch voltage is positive if the branch curved arrow is counterclockwise, otherwise the voltage branch is negative.

Defining  $v_k^x := \psi_{k+1}(t) - \psi_k(t)$ , to be the *voltage* associated with branch  $k$  of the circuit,  $k = 1, \dots, M_x$ , the *Kirchhoff Voltage Law* (KVL) reads

$$\sum_{i=1}^{M_x} v_k^x(t) = 0 \quad \forall t. \quad (3.12e)$$

In the sum in (3.12e) we assume the convention that  $v_k^x$  is positive if the corresponding branch arrow is counterclockwise, otherwise  $v_k^x$  is negative. In the example of Fig. 3.2, the KVL becomes

$$v_1^x(t) - v_2^x(t) - v_3^x(t) + v_4^x(t) = 0 \quad \forall t.$$

“Notes” — 2019/5/17 — 17:39 — page 60 — #68

## CHAPTER 4

# Model Reduction for flow rate in a tube: electric analogy to fluid flow

In Chapter 3 we illustrated how the Kirchhoff current and voltage laws are able to represent the main physical aspects of electric circuits composed by lumped elements. Due to its extensive utilization in electronic engineering, the theory of lumped electric circuits is well established, see, e.g., [31]. Thus, if a physical problem (not necessarily involving electric currents and voltages) can be described with the same mathematical formulation as used in lumped electric circuits, then, a vast spectrum of theoretical and computational techniques already developed for electronic applications can be applied in its solution. This translational and unifying power of mathematics is fully leveraged when establishing the electric analogy to fluid flow. Such analogy finds extensive applications in human physiology, for example in the study of blood flow through the cardiovascular system [41] or cerebrospinal fluid flow in the subarachnoid space and ventricles [110]. In this chapter, we aim at establishing the fundamental correspondance between electric and hydraulic quantities.

### 4.1. Hydraulic resistors

In the elecric circuiti the Ohm law establishes a linear relationship between voltage and current. In Section 4.1.1, we will show that the Poiseuille law allows us to establish an analogous linear relationship between the pressure drop at the ends of a rigid cylindrical tube and the volumetric flow rate of the fluid running through the tube. However, if the tube is not rigid, the relationship between pressure drop and volumetric flow rate ceases to be linear. In Section 4.1.2, we will derive the nonlinear hydraulic resistances characterizing compliant and collapsible tubes, which are often utilized to model arterial and venous vascular segments, respectively.

#### 4.1.1. Linear case: Poiseuille law

Let us consider the Poiseuille flow of a Newtonian viscous fluid that occupies the infinite slab

$$\Omega = \mathbb{R} \times \mathbb{R} \times (0, H). \quad (4.1)$$

62 A comprehensive physically based approach to modeling in bioengineering and life sciences

Let us assume that the resultant of external body forces is zero, namely  $\underline{\mathbf{b}} = \underline{\mathbf{0}}$  and that the fluid motion is described by the Stokes equations

$$\nabla_{\underline{\mathbf{x}}} \cdot \underline{\mathbf{v}} = 0 \quad (4.2a)$$

$$-\nabla p + \mu \Delta_{\underline{\mathbf{x}}} \underline{\mathbf{v}} = \underline{\mathbf{0}}, \quad (4.2b)$$

equipped with the boundary conditions

$$\underline{\mathbf{v}}(\underline{\mathbf{x}}) = \underline{\mathbf{0}} \quad \text{for } \underline{\mathbf{x}} \in \Sigma_0 \cup \Sigma_H \quad (4.3)$$

where:

$$\Sigma_0 = \{\underline{\mathbf{x}} \in \mathbb{R}^3 : x_3 = 0\} \quad (4.4)$$

$$\Sigma_H = \{\underline{\mathbf{x}} \in \mathbb{R}^3 : x_3 = H\}. \quad (4.5)$$

Since the Stokes problem is not time-dependent, initial conditions are not required. Let us look for a particular solution of this problem in the form

$$\underline{\mathbf{v}}(\underline{\mathbf{x}}) = V(x_3) \underline{\mathbf{e}}_2, \quad \nabla_{\underline{\mathbf{x}}} p(\underline{\mathbf{x}}) = A \underline{\mathbf{e}}_2 \quad (4.6)$$

with  $A > 0$  constant, as illustrated in Figure 4.1.

It is easy to verify that the velocity field is solenoidal, thereby satisfying the incompressibility condition. Substituting (4.6) into (4.2) and (4.3) we simply obtain:

$$-A + \mu \frac{d^2 V}{dx_3^2} = 0 \quad (4.7a)$$

$$V(0) = 0 \quad (4.7b)$$

$$V(H) = 0 \quad (4.7c)$$

whose solution is

$$V(x_3) = -\frac{A}{2\mu} x_3 (H - x_3) \quad (4.8)$$

so that

$$\underline{\mathbf{v}}(\underline{\mathbf{x}}) = -\frac{A}{2\mu} x_3 (H - x_3) \underline{\mathbf{e}}_2. \quad (4.9)$$

Interestingly, the velocity profile results to be (i) quadratic in  $x_3$ , (ii) positive in magnitude when the pressure gradient  $A$  is negative, meaning that the fluid flows from higher to lower pressures, (iii) directly proportional to the magnitude of the prescribed pressure gradient  $A$ , (iv) inversely proportional to the viscosity  $\mu$  of the fluid.

Let us consider the Poiseuille flow of a Newtonian viscous fluid in a rigid cylindri-

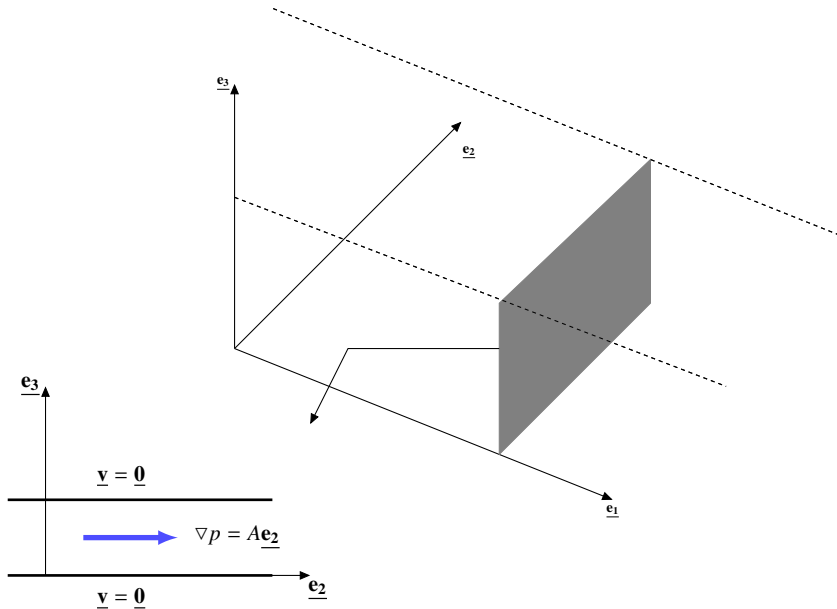


**Figure 4.1** Particular form of the pressure gradient  $\nabla_x p(\underline{x}) = A \underline{e}_2$  and boundary conditions of the Stokes equations (4.2) to obtain the Poiseuille solution.

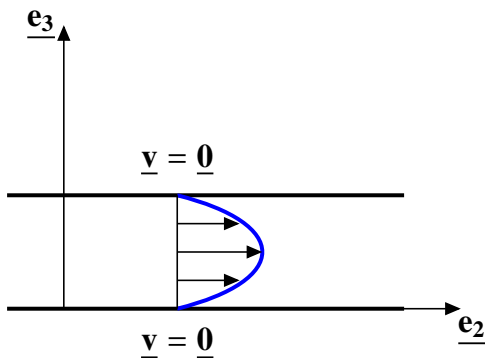


**Figure 4.2** Representation of the Poiseuille profile of the fluid velocity as obtained by solving Equations (4.7).

cal tube of radius  $r$  and length  $\ell$ . Thus, the fluid domain  $\Omega$  can be written as

$$\Omega = \{(x_r \cos x_\theta, x_r \sin x_\theta, x_z) \in \mathbb{R}^3 : x_r \in [0, r], x_\theta \in [0, 2\pi), x_z \in (0, \ell)\} \quad (4.10)$$

and its lateral, inlet and outlet boundaries can be written as:

$$\Sigma_l = \{(x_r \cos x_\theta, x_r \sin x_\theta, x_z) \in \mathbb{R}^3 : x_r = r, x_\theta \in [0, 2\pi), x_z \in (0, \ell)\} \quad (4.11)$$

$$\Sigma_{in} = \{(x_r \cos x_\theta, x_r \sin x_\theta, x_z) \in \mathbb{R}^3 : x_r \in [0, r], x_\theta \in [0, 2\pi), x_z = 0\} \quad (4.12)$$

$$\Sigma_{out} = \{(x_r \cos x_\theta, x_r \sin x_\theta, x_z) \in \mathbb{R}^3 : x_r \in [0, r], x_\theta \in [0, 2\pi), x_z = \ell\} \quad (4.13)$$

respectively. Adopting the same assumptions as those listed for the derivation of Poiseuille flow in an infinite slab, with the appropriate adjustments due to the fact that now the main direction of flow is the axial direction  $\underline{\mathbf{e}}_z$  of the tube and that the problem is naturally described in the cylindrical, rather than Cartesian, coordinate system, we can look for a solution in the form

$$\underline{\mathbf{v}}(\underline{\mathbf{x}}) = V(x_r) \underline{\mathbf{e}}_z, \quad \nabla_{\underline{\mathbf{x}}} p(\underline{\mathbf{x}}) = A \underline{\mathbf{e}}_z, \quad (4.14)$$

where  $A$  is the imposed pressure gradient in the axial direction. The function  $V = V(x_r)$  is the solution of the following differential problem:

$$-A + \mu \frac{1}{x_r} \frac{d}{dx_r} \left( x_r \frac{dV}{dx_r} \right) = 0 \quad (4.15a)$$

$$V'(0) = 0 \quad (4.15b)$$

$$V(r) = 0 \quad (4.15c)$$

corresponding to (4.7). Equation (4.15a) can be rewritten as

$$\frac{d}{dx_r} \left( x_r \frac{dV}{dx_r} \right) = \frac{A}{\mu} x_r. \quad (4.16)$$

Integrating (4.16) with respect to  $x_r$  from 0 to  $r$  and utilizing the boundary condition (4.15b), we obtain

$$x_r \frac{dV}{dx_r} = \frac{A}{\mu} \frac{x_r^2}{2}. \quad (4.17)$$

Dividing (4.17) by  $x_r$  and integrating between  $x_r$  and  $r$ , we obtain

$$V(x_r) = -\frac{A}{4\mu} (r^2 - x_r^2). \quad (4.18)$$

Since  $A$  is the imposed pressure gradient in the axial direction, the fluid pressure is of the form

$$p(x_z) = A x_z + B. \quad (4.19)$$

Assuming now that the pressure at the inlet and outlet boundaries is prescribed as

$$p(0) = p_{in} \quad \text{and} \quad p(1) = p_{out} \quad (4.20)$$

we can specify the constants  $A$  and  $B$  as

$$A = \frac{p_{out} - p_{in}}{\ell} \quad \text{and} \quad B = p_{in}. \quad (4.21)$$

As a result, we can write velocity and pressure as:

$$\underline{v} = V(x_r) \underline{e}_z = \frac{p_{in} - p_{out}}{4\mu\ell} (r^2 - x_r^2) \underline{e}_z \quad (4.22)$$

$$p(x_z) = -\frac{p_{in} - p_{out}}{\ell} x_z + p_{in}. \quad (4.23)$$

Let us now define the volumetric flow rate  $Q_v$  as

$$Q_v = \int_S \underline{v} \cdot \underline{n} dS \quad (4.24)$$

where  $S$  is any cross section of the tube. For the particular problem under consideration,  $S$  remains constant along the tube (i.e. the tube is rigid with constant circular cross section) and  $\underline{v} = V(x_r) \underline{e}_z$  is independent of  $x_z$ . Therefore, the resulting  $Q_v$  is constant along the tube and equal to

$$\begin{aligned} Q_v &= \int_0^{2\pi} \int_0^r V(x_r) \underline{e}_z \cdot \underline{e}_z x_r dx_r dx_\theta = \frac{(p_{in} - p_{out})\pi}{2\mu\ell} \int_0^r (r^2 - x_r^2) x_r dx_r \\ &= \frac{(p_{in} - p_{out})\pi}{2\mu\ell} \left( \frac{r^4}{2} - \frac{r^4}{4} \right) \end{aligned}$$

which finally leads to the renown *Poiseuille law*

$$Q_v = \frac{\pi r^4}{8\mu\ell} (p_{in} - p_{out}). \quad (4.25)$$

From the abstract mathematical viewpoint, the Poiseuille law (4.25) is identical to the Ohm law for a linear resistor, upon establishing the *correspondance* between:

$$\text{fluid volumetric flow rate } Q_v \leftrightarrow \text{electric current } i \quad (4.26a)$$

$$\text{fluid pressure difference } \Delta p \leftrightarrow \text{electric voltage } v \quad (4.26b)$$

where  $\Delta p$  denotes the pressure difference between the poles of the element, thus  $\Delta p = p_{in} - p_{out}$  in the case of a resistor. Furthermore, noticing that  $Q_v$  represents the fluid volume per unit time passing through the tube cross section and  $i$  represents the electric charge per unit time passing through the circuit branch, we can establish a further correspondance between fluid volume  $V$  and electric charge  $Q$  as

$$\text{fluid volume } V \leftrightarrow \text{electric charge } Q. \quad (4.26c)$$

In addition, since the electric voltage  $v$  is defined as the difference between the value

of the electric potential  $\psi$  at the end nodes of the circuit branch, we can say that

$$\text{fluid pressure } p \leftrightarrow \text{electric potential } \psi. \quad (4.26d)$$

In this perspective, we can define a *hydraulic conductance*  $G_{hyd}$  and a *hydraulic resistance*  $R_{hyd} = G_{hyd}^{-1}$  as

$$G_{hyd} = \frac{\pi r^4}{8\mu\ell} \quad \text{and} \quad R_{hyd} = \frac{8\mu\ell}{\pi r^4} \quad (4.27)$$

so that we can write

$$Q_v = G_{hyd} (p_{in} - p_{out}) \quad \text{and} \quad p_{in} - p_{out} = R_{hyd} Q_v. \quad (4.28)$$

**Bio-warning 4.1.** *The characterization of the hydraulic conductance  $G_{hyd}$  and resistance  $R_{hyd}$  given in (4.27) shows that the most effective way to alter the proportionality constant between volumetric flow rate  $Q_v$  and pressure difference  $p_{in} - p_{out}$  in the Poiseuille law (4.25) is to alter the tube radius  $r$ . This fundamental principle is at the basis of vascular regulation, namely, the ability of blood vessels to actively alter their diameter in order to modulate the blood flow rate upon changes in blood pressure and metabolic needs. The exact biochemical mechanisms that contribute to vascular regulation and the types of blood vessels that actively regulate vary among different vascular beds in the human body. As a matter of fact, these issues are still subject of investigation in biology and physiology.*

#### 4.1.2. Nonlinear case: deformable tubes

One of the main assumptions in deriving the Poiseuille law (4.25) is the fact that the tube is a rigid circular cylinder. However, many applications of interest in bioengineering and life sciences involve tubes that are not rigid. Some examples in the human body are blood vessels in the cardiovascular system and airways in the lungs. Following the presentation in [24], in this section we show how to derive an expression for the hydraulic resistance of tubes that are deformable.

Consider a straight cylinder  $\Omega$  with cross-section  $\mathcal{S}$  (with general shape, thus not necessarily circular) and length  $\ell$  in a Cartesian coordinate system  $\underline{x} = (x_1, x_2, x_3)$ , as shown in Figure 4.3; that is  $\Omega = \mathcal{S} \times (0, \ell)$ . Let  $\mathbf{e}_i$ , with  $i = 1, 2, 3$  be the unit vectors in the  $x_1$ ,  $x_2$  and  $x_3$  directions, respectively, and let  $\mathbf{e}_3$  be directed along the tube axis. Let the boundary  $\partial\Omega$  of the domain  $\Omega$  be composed of three parts, namely inlet, outlet and lateral boundaries denoted by  $\Sigma_{in}$ ,  $\Sigma_{out}$  and  $\Sigma_{lat}$ , respectively, where:

$$\Sigma_{in} = \{\underline{x} \in \mathbb{R}^3 : (x_1, x_2) \in \mathcal{S}, x_3 = 0\} \quad (4.29)$$

$$\Sigma_{out} = \{\underline{x} \in \mathbb{R}^3 : (x_1, x_2) \in \mathcal{S}, x_3 = \ell\} \quad (4.30)$$

$$\Sigma_{lat} = \{\underline{x} \in \mathbb{R}^3 : (x_1, x_2) \in \partial\mathcal{S}, x_3 \in (0, \ell)\} \quad (4.31)$$

where  $\partial\mathcal{S}$  denotes the boundary of the cross section  $\mathcal{S}$ .

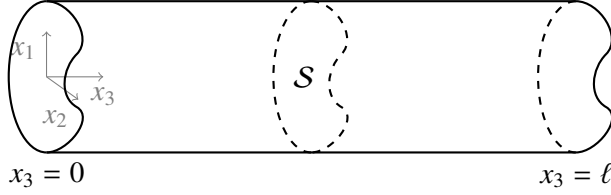


**Figure 4.3** Representative cylinder  $\Omega$  in the Cartesian coordinate system  $(x_1, x_2, x_3)$  with cross-section  $\mathcal{S}$  and length  $\ell$ . The figure is reproduced from S. Cassani. *Blood circulation and aqueous humor flow in the eye: multi-scale modeling and clinical applications. PhD Thesis. Purdue University, Indianapolis, IN (2016).* [https://scholarworks.iupui.edu/bitstream/handle/1805/10903/Cassani\\_phd\\_thesis.pdf?sequence=1](https://scholarworks.iupui.edu/bitstream/handle/1805/10903/Cassani_phd_thesis.pdf?sequence=1).

Let us assume that the motion inside the cylinder  $\Omega$  can be described by the Stokes equations:

$$\nabla_{\underline{x}} \cdot \underline{v} = 0 \quad (4.32a)$$

$$-\nabla_{\underline{x}} p + \mu \Delta_{\underline{x}} \underline{v} = \underline{0}, \quad (4.32b)$$

equipped with the boundary conditions:

$$p = p_{in} \quad \text{for } \underline{x} \in \Sigma_{in} \quad (4.33)$$

$$p = p_{out} \quad \text{for } \underline{x} \in \Sigma_{out} \quad (4.34)$$

$$\underline{v} = \underline{0} \quad \text{for } \underline{x} \in \Sigma_{lat}. \quad (4.35)$$

The no-slip boundary condition (4.35) can also be interpreted as

$$\underline{v}_{\mathcal{S}} \cdot \underline{n}_{\mathcal{S}} = 0 \quad \text{and} \quad v_3 = 0 \quad (4.36)$$

where  $\underline{v} = \underline{v}_{\mathcal{S}} + v_3 \mathbf{e}_3$ , with  $\underline{v}_{\mathcal{S}} = v_1 \mathbf{e}_1 + v_2 \mathbf{e}_2$ , and  $\underline{n}_{\mathcal{S}}$  is the outward normal vector to  $\Sigma_{lat}$ . In the following we will assume that:

(A1) the shape of the cross section  $\mathcal{S}$  is constant along the tube;

(A2) the fluid pressure  $p$  is constant on each cross section  $\mathcal{S}$ , thereby implying that

$$p = p(x_3);$$

(A3) the fluid axial velocity  $v_3$  can be written as

$$v_3 = \bar{v}(x_3)f(\mathcal{S})$$

where  $\bar{v}(x_3)$  represents the average axial velocity on the cross-section  $\mathcal{S}$  and  $f(\mathcal{S})$

is an appropriate shape function satisfying

$$\int_{\mathcal{S}} f(\mathcal{S}) d\mathcal{S} = \mathcal{A}$$

where  $\mathcal{A}$  is the cross sectional area, which does not depend on  $x_3$  thanks to Assumption (A1);

(A4) axial motion is predominant, thus

$$\|\underline{\mathbf{v}}_{\mathcal{S}}\| \ll |v_3|,$$

where  $\|\cdot\|$  is a possible vector norms in appropriate space.

A model reduction is performed by integrating the equations in system (4.32) on the cross-section  $\mathcal{S}$ . Although not applied here, it is worth mentioning that a more sophisticated analysis can be obtained by integrating over the infinitesimal volume  $\mathcal{S} \times (x_3 - dx_3, x_3 + dx_3)$  with  $dx_3 \rightarrow 0$ , as shown in [41]. Let us define the volumetric flow rate  $Q_v$  through the cross-section  $\mathcal{S}$  as

$$Q_v(x_3) = \int_{\mathcal{S}} v_3 d\mathcal{S}. \quad (4.37)$$

Thus, assumption (A3) implies that

$$Q_v(x_3) = \int_{\mathcal{S}} v_3 d\mathcal{S} = \bar{v}(x_3) \int_{\mathcal{S}} f(\mathcal{S}) d\mathcal{S} = \bar{v}(x_3) \mathcal{A}. \quad (4.38)$$

Let us now consider again the incompressibility condition (4.32a) and let us split the divergence operator in its transversal and axial components to emphasize the contribution of the different directions of motion, so that we can write

$$\nabla_{\underline{x}} \cdot \underline{\mathbf{v}} = \nabla_{\mathcal{S}} \cdot \underline{\mathbf{v}}_{\mathcal{S}} + \frac{\partial v_3}{\partial x_3} \quad \text{with} \quad \nabla_{\mathcal{S}} \cdot \underline{\mathbf{v}}_{\mathcal{S}} = \frac{\partial v_1}{\partial x_1} + \frac{\partial v_2}{\partial x_2}. \quad (4.39)$$

Then, integrating over the cross section, taking into account the no-slip boundary condition (4.35) and Assumptions (A1) and (A3), we obtain

$$\begin{aligned} 0 &= \int_{\mathcal{S}} \nabla_{\underline{x}} \cdot \underline{\mathbf{v}} d\mathcal{S} = \int_{\mathcal{S}} \nabla_{\mathcal{S}} \cdot \underline{\mathbf{v}}_{\mathcal{S}} d\mathcal{S} + \int_{\mathcal{S}} \frac{\partial v_3}{\partial x_3} d\mathcal{S} \\ &= \int_{\partial\mathcal{S}} \underbrace{\underline{\mathbf{v}}_{\mathcal{S}} \cdot \underline{\mathbf{n}}_{\mathcal{S}}}_{=0} d\mathcal{S} + \frac{d}{dx_3} (\bar{v}(x_3) \mathcal{A}) = \frac{d Q_v(x_3)}{dx_3} \end{aligned} \quad (4.40)$$

thereby implying that the volumetric flow rate is constant along the tube. Let us now consider the balance of linear momentum (4.32b). Thanks to Assumptions (A2) and (A4), we can retain only the axial component of the balance of linear momentum

which, thanks to Assumption (A3), can be written as

$$-\frac{dp}{dx_3} + \mu \Delta_S v_3 + \mu \frac{\partial^2 v_3}{\partial x_3^2} = 0 \quad \text{with} \quad \Delta_S v_3 = \frac{\partial^2 v_3}{\partial x_1^2} + \frac{\partial^2 v_3}{\partial x_2^2}. \quad (4.41)$$

It is useful to notice that

$$\Delta_S v_3 = \nabla_S \cdot (\nabla_S v_3). \quad (4.42)$$

Then, integrating over the cross section, taking into account the no-slip boundary condition (4.35) and Assumptions (A1) and (A3), we obtain

$$\begin{aligned} 0 &= - \int_S \frac{dp}{dx_3} dS + \mu \int_S \nabla_S \cdot (\nabla_S v_3) dS + \mu \int_S \frac{\partial^2 v_3}{\partial x_3^2} dS \\ &= -\mathcal{A} \frac{dp}{dx_3} + \mu \bar{v} \int_{\partial S} (\underline{n}_S \cdot \nabla_S f(S)) d(\partial S) + \mu \mathcal{A} \frac{d^2 \bar{v}}{dx_3^2}. \end{aligned}$$

If we further assume that:

- (A5) the viscous dissipation in the axial direction is negligible;
- (A6) the pressure is linear in  $x_3$ , so that

$$p(x_3) = -\frac{p_{in} - p_{out}}{\ell} x_3 + p_{in},$$

then we can write

$$0 = \frac{\mathcal{A}}{\ell} (p_{in} - p_{out}) - k_r \bar{v} \quad \text{with} \quad k_r = -\mu \int_{\partial S} (\underline{n}_S \cdot \nabla_S f(S)) d(\partial S). \quad (4.43)$$

We emphasize that the factor  $k_r$  (units:  $\text{N m}^2 \text{ s}$ ) depends on the specific profile  $f(S)$  that is chosen a priori for the fluid motion. In the case of a parabolic velocity profile, such as the one exhibited in the Poiseuille flow, we have  $k_r = 8\pi\mu$  [24, 41]. Thus, the balance of linear momentum in the axial direction leads to

$$p_{in} - p_{out} = \frac{k_r \ell}{\mathcal{A}^2} Q_v. \quad (4.44)$$

It is easy to verify that, in the case of a rigid tube with a circular cross section of radius  $r$ , the expression above coincides with the Poiseuille law (4.25). However, in the case of deformable tubes, the cross-sectional area  $\mathcal{A}$  depends on the pressure difference across the tube wall. More precisely, denoting by  $p_{ext}$  the external pressure acting on the tube, we need to provide a *constitutive equation* characterizing the mechanical behavior of the tube wall, also referred to as *tube law* [21, 47, 95, 114]. To this end, let us introduce the dimensionless cross-sectional area  $\alpha$  as  $\alpha = \mathcal{A}/\mathcal{A}_{ref}$ , where  $\mathcal{A}_{ref}$  is a reference value for the cross-sectional area. Then, characterizing the tube law consists

70 A comprehensive physically based approach to modeling in bioengineering and life sciences

in defining a function  $P = P(\alpha)$  such that

$$P(\alpha) = \frac{\bar{p} - p_{ext}}{k_p} \quad (4.45)$$

with

$$\bar{p} = \frac{p_{in} + p_{out}}{2} \quad (4.46)$$

where  $\bar{p}$  is the mean pressure in the tube and  $k_p$  (units:  $N m^{-2}$ ) is a constant that embodies the geometrical and mechanical properties of the tube. The explicit form of the constitutive function  $P(\alpha)$  depends on the particular system under consideration. In the following, we consider the cases of *compliant* and *collapsible* tubes, as detailed next.

#### 4.1.2.1. Compliant tubes

In the case of a compliant tube, the cross-section is assumed to be circular and to remain circular after the deformation, as indicated in Figure 4.4. In this case, the radial displacement  $\eta$  is computed using the membrane law (??), namely

$$\eta = \frac{(1 - \nu^2)r_{ref}^2(\bar{p} - p_{ext})}{Eh} \quad (4.47)$$

where  $E$ ,  $\nu$  and  $h$  are the tube Young modulus, Poisson ratio and wall thickness, respectively, and the reference cross-sectional area is  $\mathcal{A}_{ref} = \pi r_{ref}^2$ .

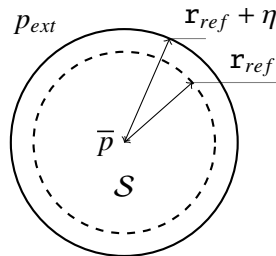


**Figure 4.4** Deformation of a compliant tube for a positive transmural pressure difference  $\bar{p} - p_{ext} > 0$ . The cross-section  $S$  remains circular after the deformation and the radial displacement is denoted by  $\eta$ .

Noticing that

$$\frac{\eta}{r_{ref}} = \frac{r_{ref} + \eta}{r_{ref}} - \frac{r_{ref}}{r_{ref}} = \frac{\sqrt{\mathcal{A}/\pi}}{\sqrt{\mathcal{A}_{ref}/\pi}} - 1 = \alpha^{1/2} - 1. \quad (4.48)$$

and setting

$$k_p = \frac{E}{12(1 - \nu^2)} \left( \frac{h}{r_{ref}} \right)^3 \quad \text{and} \quad k_L = 12 \left( \frac{r_{ref}}{h} \right)^2. \quad (4.49)$$

expression (4.47) can be written as

$$k_L(\alpha^{1/2} - 1) = \frac{\bar{p} - p_{ext}}{k_p} \quad (4.50)$$

so that we can characterize  $P = P(\alpha)$  as follows

$$P(\alpha) = k_L(\alpha^{1/2} - 1). \quad (4.51)$$

Expression (4.51) represents the tube law for a compliant tube whose deformation is described by the membrane law (4.47). Recalling that  $\alpha = \mathcal{A}/\mathcal{A}_{ref}$ , formula (4.50) can be solved for  $\mathcal{A}$  to obtain

$$\mathcal{A} = \mathcal{A}_{ref} \left( \frac{\bar{p} - p_{ext}}{k_p k_L} + 1 \right)^2. \quad (4.52)$$

Finally, substituting (4.52) into (4.44), we obtain

$$p_{in} - p_{out} = R_{comp} Q_v \quad \text{with} \quad R_{comp} = \frac{k_r \ell}{\mathcal{A}_{ref}^2} \left( \frac{\bar{p} - p_{ext}}{k_p k_L} + 1 \right)^{-4} \quad (4.53)$$

where  $R_{comp}$  is a nonlinear function of the fluid pressure, namely  $R_{comp} = R_{comp}(\bar{p})$ , that characterizes the hydraulic resistance of a compliant tube.

#### 4.1.2.2. Collapsible tubes

In the case of collapsible tubes, the cross section  $\mathcal{S}$  exhibits a marked change in shape depending on whether the pressure  $\bar{p}$  inside the tube is larger or smaller than the external pressure  $p_{ext}$ . Experiments on collapsible tubes have shown that  $\mathcal{S}$  changes shape from circular, to elliptic to highly collapsed as  $\bar{p} - p_{ext}$  decreases, as illustrated in Figure 4.5. The phenomenon of tube collapse under negative transmural pressure difference is also known as *Starling resistor* effect and plays a crucial role in veins and airways [95, 47, 49].

In the case of a collapsible tube, the tube law (4.45) is inspired by experimental data and defined as to capture phenomenologically the behavior schematized in Figure 4.5. When the transmural pressure difference is positive, the vessel dilates and it maintains a circular cross-section. However, when the transmural pressure difference is negative, the cross-section changes shape, first becoming elliptical and then collapsing until two opposite sides of the inner wall touch each other. In this region, the vessel is more resistant and thus large changes in the transmural pressure difference yield small changes in the cross-sectional area. This behavior is mathematically represented by

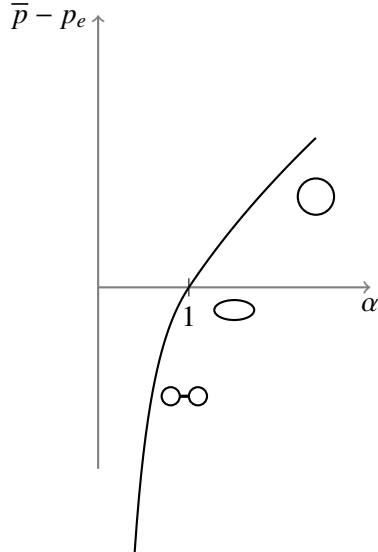


**Figure 4.5** Illustration of experimental results for a collapsible tube, adapted from [21, 47, 95, 114]. The cross-section shape changes from circular to elliptic to highly collapsed as the transmural pressure difference  $\bar{p} - p_e$  decreases.

the following constitutive equation

$$P(\alpha) = \begin{cases} 1 - \alpha^{-3/2} & \text{for } \alpha \leq 1 \\ k_L(\alpha^{1/2} - 1) & \text{for } \alpha > 1 \end{cases}. \quad (4.54)$$

In particular, we notice that a collapsible tube is assumed to behave in the same way as a compliant tube if  $\alpha > 1$ . Next, an expression for  $\alpha$  can be obtained by manipulating (4.54) to write

$$\alpha = \begin{cases} (1 - P(\alpha))^{-2/3} & \text{for } \alpha \leq 1 \\ \left(\frac{P(\alpha)}{k_L} + 1\right)^2 & \text{for } \alpha > 1 \end{cases} = \begin{cases} \left(1 - \frac{\bar{p} - p_e}{k_p}\right)^{-2/3} & \text{for } \alpha \leq 1 \\ \left(\frac{\bar{p} - p_e}{k_p k_L} + 1\right)^2 & \text{for } \alpha > 1 \end{cases} \quad (4.55)$$

Recalling that  $\alpha = \mathcal{A}/\mathcal{A}_{ref}$ , we can substitute the expression above into (4.44) to ob-

tain

$$p_{in} - p_{out} = R_{coll} Q_v \quad \text{with} \quad R_{coll} = \begin{cases} \frac{k_r \ell}{\mathcal{A}_{ref}^2} \left(1 - \frac{\bar{p} - p_{ext}}{k_p}\right)^{4/3} & \text{for } \alpha \leq 1 \\ \frac{k_r \ell}{\mathcal{A}_{ref}^2} \left(\frac{\bar{p} - p_{ext}}{k_p k_L} + 1\right)^{-4} & \text{for } \alpha > 1 \end{cases} \quad (4.56)$$

where  $R_{coll}$  is a nonlinear function of the fluid pressure, namely  $R_{coll} = R_{coll}(\bar{p})$ , that characterizes the hydraulic resistance of a collapsible tube.

## 4.2. Hydraulic capacitors

The general constitutive law characterizing a capacitor in the context of lumped electric circuits is given as

$$i = \frac{dQ}{dt} \quad \text{with} \quad Q = Q(v)$$

where  $i$  is the electric current passing through the capacitor,  $Q$  is the electric charge stored in the capacitor and  $v$  is the voltage across the capacitor. The basic correspondence between electric and hydraulic variables established in (4.26) tells us that a hydraulic capacitor must be described by a constitutive law of the form

$$Q_v = \frac{dV}{dt} \quad \text{with} \quad V = V(\Delta p). \quad (4.57)$$

where  $Q_v$  is the volumetric flow rate passing through the capacitor,  $V$  is the fluid volume stored in the capacitor and  $\Delta p$  is the pressure difference between the poles of the capacitor. Thus, a hydraulic capacitor is capable of storing and releasing fluid volume dynamically, thereby creating a flow through the element.

This implies that: (i) a hydraulic capacitor must be able to deform and accommodate changes in fluid volume with time, and (ii) the constitutive relationship between fluid volume and pressure drop across the capacitor characterizes the behavior of the specific element.

### 4.2.1. Tubes as hydraulic capacitors

In Sections 4.1.1 and 4.1.2 we have considered the fluid flow in rigid and deformable tubes from the point of view of their hydraulic resistances. Since rigid tubes cannot alter their shape, they cannot accommodate changes in volume and, as a consequence, cannot be modeled as hydraulic capacitors. Conversely, deformable tubes can change their shape and therefore act as hydraulic capacitors.

Let us consider the cases of compliant and collapsible tubes that were discussed in Section 4.1.2. We recall that  $\mathcal{A}$  is the cross-sectional area of the tube, which is

74 A comprehensive physically based approach to modeling in bioengineering and life sciences

assumed to be constant along the length  $\ell$  of the tube. Thus, the tube volumes in the deformed and reference configurations, denoted by  $V$  and  $V_{ref}$  respectively, can be written as

$$V = \mathcal{A} \ell \quad \text{and} \quad V_{ref} = \mathcal{A}_{ref} \ell. \quad (4.58)$$

Thus, the constitutive law characterizing a compliant tube as a hydraulic capacitor can be obtained from (4.52) leading to

$$V = V_{ref} \left( \frac{\Delta p}{k_p k_L} + 1 \right)^2 \quad \text{with} \quad \Delta p = \bar{p} - p_{ext}. \quad (4.59)$$

Analogously, the constitutive law characterizing a collapsible tube as a hydraulic capacitor can be obtained from (4.55) leading to

$$V = \begin{cases} V_{ref} \left( 1 - \frac{\Delta p}{k_p} \right)^{-2/3} & \text{for } V \leq V_{ref} \\ V_{ref} \left( \frac{\Delta p}{k_p k_L} + 1 \right)^2 & \text{for } V > V_{ref} \end{cases} \quad \text{with} \quad \Delta p = \bar{p} - p_{ext}. \quad (4.60)$$

We can see that, in both the compliant and collapsible cases, the pressure difference  $\Delta p$  across the hydraulic capacitor is the transmural pressure difference  $\bar{p} - p_{ext}$ , with  $\bar{p}$  denoting the average pressure inside the tube.

### 4.3. Hydraulic inductors

The constitutive law characterizing a linear time-invariant inductor in the context of lumped electric circuits was given as

$$\mathbf{v} = L \frac{di}{dt}$$

where  $i$  is the electric current passing through the inductor and  $\mathbf{v}$  is the voltage across the inductor. Since the electric equivalent of the electric current  $i$  is the volumetric flow rate  $Q_v$ , the magnetic energy described above corresponds to a kinetic energy. Thus, the correspondence between electric and hydraulic inductors should be sought in the inertial part of the fluid equations.

For the sake of simplicity, let us consider a rigid tube of length  $\ell$  and circular cross section  $\mathcal{S}$  of radius  $\mathbf{r}$ . Let us start now from the time-dependent Stokes systems that is written as

$$\begin{aligned} \nabla_{\underline{x}} \cdot \underline{\mathbf{v}} &= 0 \\ \rho \frac{\partial \underline{\mathbf{v}}}{\partial t} + \rho (\underline{\mathbf{v}} \cdot \nabla_{\underline{x}}) \underline{\mathbf{v}} &= -\nabla_{\underline{x}} p + \mu \Delta_{\underline{x}} \underline{\mathbf{v}} \end{aligned}$$

and let us simplify them by adopting the same assumptions as in Section 4.1.2, with the only differences that now  $v_3 = \bar{v}_3(x_3, t) f(\mathcal{S})$  and  $p = p(x_3, t)$ . Thus, the balance of linear momentum can be reduced to its axial component that can be written as

$$\rho \frac{\partial v_3}{\partial t} = -\frac{\partial p}{\partial x_3} + \mu \Delta_S v_3 + \mu \frac{\partial^2 v_3}{\partial x_3^2} \quad \text{with} \quad \Delta_S v_3 = \frac{\partial^2 v_3}{\partial x_1^2} + \frac{\partial^2 v_3}{\partial x_2^2} \quad (4.61)$$

where the partial derivative has been used for the pressure because, in this instance, it may depend on both  $x_3$  and  $t$ .

Let us integrate the above equation over the cross section  $\mathcal{S}$ . Since the tube is rigid, the cross section is constant in time and so the acceleration term on the left-hand side simply gives

$$\rho \int_{\mathcal{S}} \frac{\partial v_3}{\partial t} d\mathcal{S} = \rho \frac{\partial Q_v}{\partial t} = \rho \frac{d Q_v}{dt}. \quad (4.62)$$

The change from partial to ordinary derivative with respect to time is justified by the fact that the integration over the cross section of the incompressibility condition reveals that  $Q_v$  is independent of  $x_3$ , as shown in (4.40). The integration over the cross section of the right hand side of Equation (4.61) has already been performed in Section 4.1.2, resulting in

$$\int_{\mathcal{S}} \left( -\frac{\partial p}{\partial x_3} + \mu \Delta_S v_3 + \mu \frac{\partial^2 v_3}{\partial x_3^2} \right) d\mathcal{S} = \frac{\mathcal{A}}{\ell} (p_{in} - p_{out}) - \frac{k_r}{\mathcal{A}} Q_v. \quad (4.63)$$

Finally, substituting (4.62) and (4.63) into (4.61) we obtain

$$\rho \frac{d Q_v}{dt} + \frac{k_r}{\mathcal{A}} Q_v = \frac{\mathcal{A}}{\ell} (p_{in} - p_{out}). \quad (4.64)$$

In the *inviscid case*, we can set  $k_r = 0$  to obtain

$$\Delta p = \frac{\rho \ell}{\mathcal{A}} \frac{d Q_v}{dt} \quad \text{with} \quad \Delta p = p_{in} - p_{out} \quad (4.65)$$

from which we can obtain a characterization of the hydraulic conductance as

$$L_{hyd} = \frac{\rho \ell}{\mathcal{A}}. \quad (4.66)$$

“Notes” — 2019/5/17 — 17:39 — page 76 — #84

## CHAPTER 5

# Model reduction in cellular electrophysiology

In this chapter, we develop a mathematical model of electric activity in excitable cells. The model is based on a lumped parameter mathematical representation of the cell membrane constituted by two dipoles connected in parallel, a capacitor and a resistor. The capacitance of the capacitor is a linear time-invariant electric parameter whereas the conductance of the resistor is a nonlinear function of the membrane potential and of ion concentrations inside and outside the cell. The capacitance accounts for the temporal variation of the double charge layer that accumulates on both sides of the membrane, whereas the conductance accounts for the physical motion of ions across the pore of the membrane proteins.

### 5.1. Geometrical representation of a cell and its membrane

In this section we describe the simplified geometric representation of the cell

Figure 5.1 shows a schematic view of a cell. The cell is represented as a sphere of radius  $R_{cell}$  (units: m) and surface  $S_{cell} = 4\pi R_{cell}^2$ . The lipid bilayer constituting the cell membrane is considered to be a dielectric medium with constant thickness  $t_m$  (units: m) and dielectric permittivity  $\epsilon_m = \epsilon_m^r \epsilon_0$ ,  $\epsilon_0$  being the permittivity of vacuum (units:  $\text{Fm}^{-1}$ ) and  $\epsilon_m^r = 80$  being the relative dielectric permittivity of water.

### 5.2. Reduced order modeling of the cell membrane

In this section we illustrate the first member of the hierarchy of models considered in this chapter for cellular electrophysiology, the so-called lumped parameter equation model. This formulation consists of an electric equivalent model of the cell membrane that can represent the neighbourhood of a given point  $\underline{x} \in S_{cell}$  (see Figure 5.1, left part) or the whole cell (see Figure 5.1, right part). In the former case the resulting approach is referred to as a *local* ordinary differential model whereas in the latter case it is referred to as *whole-cell* ordinary differential model. To construct both approaches we refer to Figure 5.2 reporting the schematic representation of a three-dimensional (3D) portion of the cell membrane of an excitable cell.

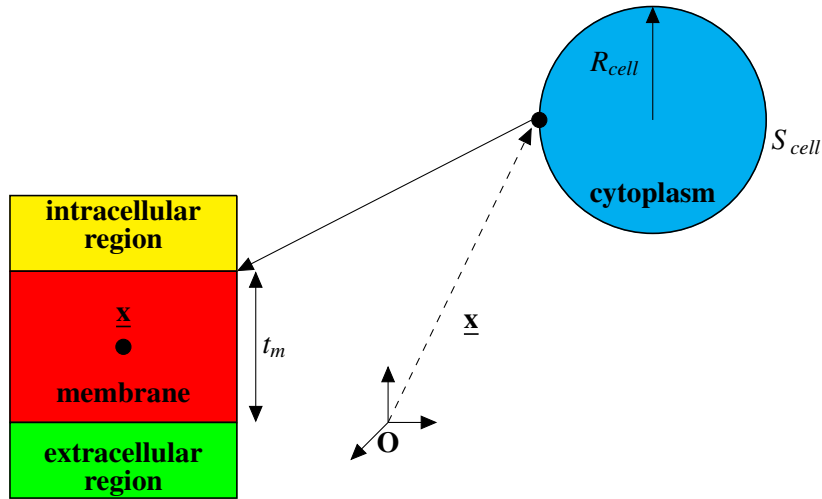


**Figure 5.1** A schematic multiscale description of the cell. The microscopic view of the cell (shown on the left) is constituted by the detailed zoom of the membrane lipid bilayer in the neighbourhood of the point  $\underline{x}$  on the cell surface. The macroscopic view of the cell (on the right) is constituted by a sphere of radius  $R_{cell}$  and surface  $S_{cell}$ .

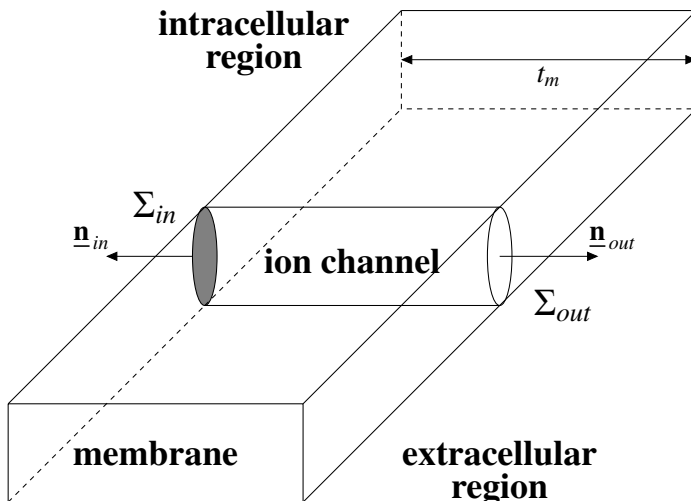


Figure 5.2 Three-dimensional detail of the cell membrane.

In the figure, the cylinder is the pore of the membrane protein through which ions are transported in and out the cell volume whereas the remainder of the structure is the lipid double layer constituting the cell membrane. In this chapter, we consider only the case of passive ion transport through an *ion channel* down along an electrochemical

gradient across the cell membrane. The quantities  $\underline{n}_{in}$  and  $\underline{n}_{out}$  are the outward unit normal vectors on the surfaces  $\Sigma_{in}$  and  $\Sigma_{out}$ , respectively, whereas  $\underline{n}_{lat}$  is the outward unit normal vector on the lateral surface  $\Sigma_{lat}$  of the cylinder.

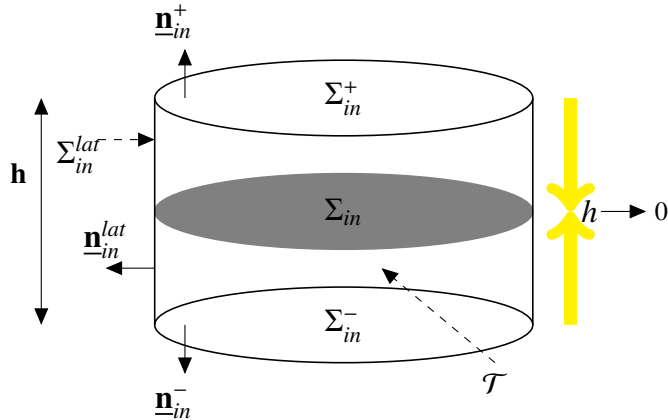


Figure 5.3 Three-dimensional control volume across  $\Sigma_{in}$ .

Across the bottom surface  $\Sigma_{in}$  we construct the three-dimensional control volume  $\mathcal{T}$  depicted in Figure 5.3. The control volume is a cylinder whose bottom and top surfaces are denoted by  $\Sigma_{in}^-$  and  $\Sigma_{in}^+$ , respectively, and whose lateral surface is denoted by  $\Sigma_{in}^{lat}$ . The height of the cylindrical control volume is denoted by  $h$ . The outward unit normal vectors on  $\Sigma_{in}^-$  and  $\Sigma_{in}^+$  are  $\underline{n}_{in}^-$  and  $\underline{n}_{in}^+$  whereas the outward unit normal vector on the lateral surface  $\Sigma_{in}^{lat}$  is  $\underline{n}_{in}^{lat}$ . We notice that  $\underline{n}_{in}^- = \underline{n}_{in}$ ,  $\underline{n}_{in}^+ = \underline{n}_{out}$  and  $\underline{n}_{in}^{lat} = \underline{n}_{lat}$ .

We integrate equation (3.10a) in the volume  $\mathcal{T}$ , to obtain

$$\int_{\mathcal{T}} \frac{\partial \rho^{el}}{\partial t} d\mathcal{T} + \int_{\mathcal{T}} \nabla_{\underline{x}} \cdot \underline{J} d\mathcal{T} = 0. \quad (5.1)$$

Assuming that the function  $\rho^{el} = \rho^{el}(\underline{x}, t)$  is sufficiently smooth with respect to the time variable, we can exchange the time differentiation with the integral operator to get

$$\int_{\mathcal{T}} \frac{\partial \rho^{el}}{\partial t} d\mathcal{T} = \frac{d}{dt} \int_{\mathcal{T}} \rho^{el}(\underline{x}, t) d\mathcal{T}.$$

Then, we apply the divergence theorem (A.1) to the second integral in Equation (5.1) to obtain

$$\frac{d}{dt} \int_{\mathcal{T}} \rho^{el}(\underline{x}, t) d\mathcal{T} + \int_{\Sigma_{in}^-} \underline{J}(\underline{x}, t) \cdot \underline{n}_{in}^- dS + \int_{\Sigma_{lat}} \underline{J}(\underline{x}, t) \cdot \underline{n}_{in}^{lat} dS - \int_{\Sigma_{in}^+} \underline{J}(\underline{x}, t) \cdot \underline{n}_{in}^+ dS = 0 \quad (5.2)$$

Let us take the limit  $h \rightarrow 0$  in Equation (5.2). We have

$$\lim_{h \rightarrow 0} \int_{\Sigma_{lat}} \underline{\mathbf{J}}(\underline{\mathbf{x}}, t) \cdot \underline{\mathbf{n}}_{in}^{lat} dS = 0.$$

Let us assume that the following limit is finite

$$Q_{in}(t) := \lim_{h \rightarrow 0} \int_{\mathcal{T}} \rho^{el}(\underline{\mathbf{x}}, t) d\mathcal{T}, \quad (5.3a)$$

and let us define the following quantities:

$$\Phi_{\underline{\mathbf{J}},in}^-(t) := \int_{\Sigma_{in}^-} \underline{\mathbf{J}}(\underline{\mathbf{x}}, t) \cdot \underline{\mathbf{n}}_{in}^- dS, \quad (5.3b)$$

$$\Phi_{\underline{\mathbf{J}},in}^+(t) := \int_{\Sigma_{in}^+} \underline{\mathbf{J}}(\underline{\mathbf{x}}, t) \cdot \underline{\mathbf{n}}_{in}^+ dS. \quad (5.3c)$$

Taking the limit  $h \rightarrow 0$  in Equation (5.2) and using the definitions (5.3), we obtain the following ordinary differential equation (ODE)

$$\frac{dQ_{in}(t)}{dt} + \Phi_{\underline{\mathbf{J}},in}^-(t) + \Phi_{\underline{\mathbf{J}},in}^+(t) = 0. \quad (5.4)$$

The quantity  $Q_{in}$  is the *electric charge* that accumulates on the left and on the right intracellular sides of the membrane in correspondance of the surface  $\Sigma_{in}$  (units: C). The quantities  $\Phi_{\underline{\mathbf{J}},in}^-$  and  $\Phi_{\underline{\mathbf{J}},in}^+$  are the fluxes of the current density  $\underline{\mathbf{J}}$  across  $\Sigma_{in}^-$  and  $\Sigma_{in}^+$ , respectively (units:  $\text{Cs}^{-1}$ ). Current densities of cations and anions flowing from the intracellular side across the surface  $\Sigma_{in}$ , and ion charge that accumulates in the intracellular side of the membrane close to the channel pore entrance are schematically illustrated in Figure 5.4.

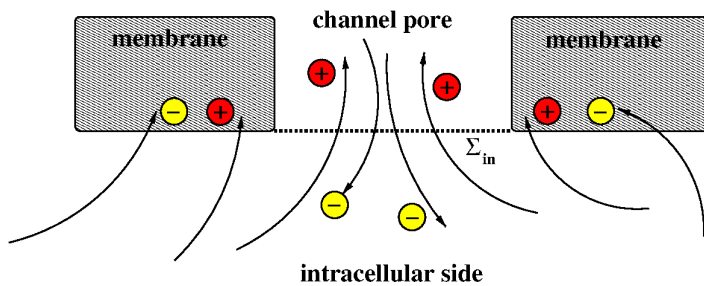


**Figure 5.4** The figure shows ion current densities flowing from the intracellular side into the channel pore across the surface  $\Sigma_{in}$ , and ion charges that accumulate in the membrane layer in the neighbourhood of the channel pore entrance. Cations are represented by red circles and anions by a yellow circle.

The ODE (5.4) expresses the balance of three electric currents:

1. two conduction currents,  $\Phi_{J,in}^-(t)$  and  $\Phi_{J,in}^+(t)$ , flowing across the inner surface  $\Sigma_{in}$  and associated with the physical motion of ions from the intracellular region into the pore channel;
2. a displacement current,  $\frac{dQ_{in}(t)}{dt}$ , associated with the time rate of change of the immobile electric charge accumulated on the intracellular side of the membrane in the immediate vicinity of the pore channel entrance.

Let us denote the barycenter of  $\Sigma_{in}$  by  $\underline{x}'$ . We define the following quantities:

$$\sigma_{in}(\underline{x}', t) := \frac{Q_{in}(t)}{\mathcal{S}}, \quad (5.5a)$$

$$J_{in}^{tot}(\underline{x}', t) := -\frac{\Phi_{J,in}^-(t)}{\mathcal{S}}, \quad (5.5b)$$

$$J_{in}^{tm}(\underline{x}', t) := \frac{\Phi_{J,in}^+(t)}{\mathcal{S}}, \quad (5.5c)$$

where  $\mathcal{S}$  denotes the area of the surfaces  $\Sigma_{in}$  and  $\Sigma_{out}$ . The quantity  $\sigma_{in}$  is the *surface electric charge density* accumulated on the left and on the right intracellular sides of the membrane in correspondance of the surface  $\Sigma_{in}$  (units:  $\text{Cm}^{-2}$ ). The quantity  $J_{in}^{tot}$  is the *total ion current density* flowing from the cytoplasm into the ion channel (units:  $\text{Am}^{-2}$ ). The quantity  $J_{in}^{tm}$  is the transmembrane current density that reaches the channel region (units:  $\text{Am}^{-2}$ ). Definitions (5.5b) and (5.5c) are based on the convention that the current density is assumed to be positive if flowing out of the control volume  $\mathcal{T}$ , negative if flowing into the control volume. Dividing out the three terms in (5.4) by  $\mathcal{S}$  and using definitions (5.5), we obtain the following balance of current densities

$$\frac{\partial \sigma_{in}(\underline{x}', t)}{\partial t} + J_{in}^{tm}(\underline{x}', t) = J_{in}^{tot}(\underline{x}', t) \quad \text{at } \Sigma_{in}, \quad (5.6)$$

where the symbol of time differentiation  $d/dt$  has been changed into the symbol of partial differentiation with respect to the time variable  $\partial/\partial t$  because  $\sigma_{in}$  is now also a function of space through the definition (5.5a).

**Remark 5.1** (Biophysical meaning of the balance law). *The balance law (5.6) has a relevant biophysical interpretation. The total electric current density  $J_{in}^{tot}$  that reaches the cell membrane from the intracellular side at point  $\underline{x}'$  and at time  $t$ , will contribute to the change in surface charge density  $\frac{\partial \sigma_{in}(\underline{x}', t)}{\partial t}$  or will pass through the membrane as transmembrane current density  $J_{in}^{tm}(\underline{x}', t)$ .*

Following a completely similar procedure as above at  $\Sigma_{out}$  we obtain

$$\frac{dQ_{out}(t)}{dt} + \Phi_{\underline{\mathbf{J}},out}^-(t) + \Phi_{\underline{\mathbf{J}},out}^+(t) = 0. \quad (5.7)$$

The quantity  $Q_{out}$  is the *electric charge* that accumulates on the left and on the right extracellular sides of the membrane in correspondance of the surface  $\Sigma_{out}$  (units: C). The quantities  $\Phi_{\underline{\mathbf{J}},out}^-$  and  $\Phi_{\underline{\mathbf{J}},out}^+$  are the fluxes of the current density  $\underline{\mathbf{J}}$  across  $\Sigma_{out}^-$  and  $\Sigma_{out}^+$ , respectively (units:  $\text{Cs}^{-1}$ ). In analogy with what done at  $\Sigma_{in}$ , we denote by  $\underline{\mathbf{x}}''$  the barycenter of  $\Sigma_{out}$  and define the following quantities:

$$\sigma_{out}(\underline{\mathbf{x}}'', t) := \frac{Q_{out}(t)}{\mathcal{S}}, \quad (5.8a)$$

$$J_{out}^{tm}(\underline{\mathbf{x}}'', t) := -\frac{\Phi_{\underline{\mathbf{J}},out}^-(t)}{\mathcal{S}}, \quad (5.8b)$$

$$J_{out}^{tot}(\underline{\mathbf{x}}'', t) := \frac{\Phi_{\underline{\mathbf{J}},out}^+(t)}{\mathcal{S}}. \quad (5.8c)$$

Dividing out the three terms in (5.7) by  $\mathcal{S}$  and using definitions (5.8), we obtain the following balance of current densities

$$\frac{\partial \sigma_{out}(\underline{\mathbf{x}}'', t)}{\partial t} - J_{out}^{tm}(\underline{\mathbf{x}}'', t) = -J_{out}^{tot}(\underline{\mathbf{x}}'', t) \quad \text{at } \Sigma_{out}, \quad (5.9)$$

The quantity  $\sigma_{out}$  is the surface electric charge density that accumulates on the left and on the right extracellular sides of the membrane in correspondance of the surface  $\Sigma_{out}$ . The quantity  $J_{out}^{tm}$  is the transmembrane current density that reaches the surface  $\Sigma_{out}$  from the ion channel (units:  $\text{Am}^{-2}$ ) whereas  $J_{out}^{tot}$  is the total ion current density flowing out from the cell into the extracellular region (units:  $\text{Am}^{-2}$ ).

**Assumption 5.1.** *We introduce the following further assumptions.*

**1.** *The cell membrane is electroneutral. This amounts to stating that*

$$\sigma_{in}(\underline{\mathbf{x}}', t) + \sigma_{out}(\underline{\mathbf{x}}'', t) = 0. \quad (5.10)$$

**2.** *No production or reaction mechanisms occur in the channel pore. This amounts to stating that*

$$J_{out}^{tm}(\underline{\mathbf{x}}'', t) = J_{in}^{tm}(\underline{\mathbf{x}}', t). \quad (5.11)$$

**3.** *The membrane and its surface electric charge layers together behave like a capacitor. This amounts to stating that:*

$$\sigma_{in}(\underline{\mathbf{x}}', t) = c_m \psi_m(\underline{\mathbf{x}}, t), \quad (5.12)$$

$$\sigma_{out}(\underline{\mathbf{x}}'', t) = -c_m \psi_m(\underline{\mathbf{x}}, t), \quad (5.13)$$

where

$$c_m = \frac{\varepsilon_m}{t_m} = \frac{\varepsilon'_m \varepsilon_0}{t_m} \quad (5.14)$$

is the specific capacitance of the membrane (units:  $\text{Fm}^{-2}$ ), and  $\psi_m(\underline{x}, t) := \psi(\underline{x}', t) - \psi(\underline{x}'', t)$  is the membrane potential, having made the identifications  $\psi^{(in)}(\underline{x}, t) \equiv \psi(\underline{x}', t)$  and  $\psi^{(out)}(\underline{x}, t) \equiv \psi(\underline{x}'', t)$ .

**Remark 5.2** (Charge double layer). Assumption (5.10) means that any charge accumulation on one side of the membrane is instantaneously counterbalanced by charge accumulation of opposite sign on the other side of the membrane. This is the mathematical representation of the physical process of the formation of a charge double layer across the membrane thickness.

Summing the balance laws (5.6) and (5.9) we obtain

$$J_{out}^{tot}(\underline{x}'', t) - J_{in}^{tot}(\underline{x}', t) = 0, \quad (5.15a)$$

or, equivalently, using (5.5b) and (5.8c), we get

$$\Phi_{\underline{J}, out}^+(t) + \Phi_{\underline{J}, in}^-(t) = 0. \quad (5.15b)$$

**Remark 5.3** (Current balance across the membrane). Equations (5.15) express the physical fact that any current that comes onto the membrane from one side is exactly counterbalanced by current leaving the membrane from the other side, i.e., that there is no net charge accumulation at the membrane. Equivalently, the charge accumulation on one face of the membrane is exactly cancelled by the charge accumulation on the opposite face, in agreement with Remark 5.2.

The balance of current densities at  $\underline{x}'$  expressed by Equation (5.6) (or, similarly, the current density balance at  $\underline{x}''$  expressed by Equation (5.9)), can be conveniently interpreted as the Kirchhoff law for current densities enforced at the node  $\underline{x}'$  (or at node  $\underline{x}''$ ) of the electric equivalent lumped parameter circuit illustrated in Figure 5.5.

The circuit shown in Figure 5.5 consists of an input time-dependent current density source  $J_{in}^{tot}(\underline{x}', t)$  connected in series with a current density divider constituted by the parallel between a linear capacitor of specific capacitance  $c_m$  given by (5.14) and a nonlinear resistor of specific conductance  $g_m$  (units:  $\text{Sm}^{-2}$ ) that may depend, in general, on the membrane potential  $\psi_m(\underline{x}, t)$  and on the concentrations at  $\underline{x}'$  and  $\underline{x}''$  of the ion species that are flowing throughout the channel pore. In the next sections we use the electric scheme of Figure 5.5 to devise local and whole-cell models of cellular electrophysiology based on ordinary differential equations.

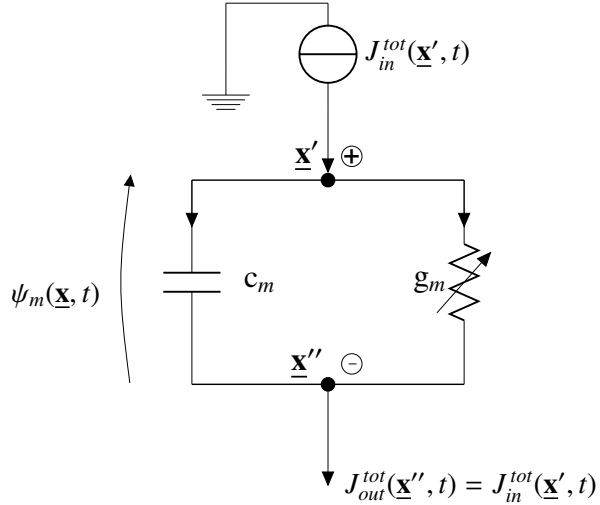


**Figure 5.5** Equivalent electric circuit representation of Equation (5.6), expressing the balance of current densities across the cell membrane. The element on the top of the electric circuit is a current density source representing the term  $J_{in}^{tot}(\underline{x}', t)$ . The capacitor, whose specific capacitance is  $c_m$ , accounts for the term  $\frac{\partial \sigma_{in}(\underline{x}', t)}{\partial t}$ . The nonlinear resistor, whose specific conductance is  $g_m$ , accounts for the transmembrane current density  $J_{in}^{tm}(\underline{x}', t)$ . The arrow superposed to the symbol of the resistor indicates that the considered electric parameter is a nonlinear function of the membrane potential  $\psi_m = \psi_m(\underline{x}, t) = \psi_m(\underline{x}', t) - \psi_m(\underline{x}'', t)$ .

### 5.2.1. Local and Whole ODE models

In this section we characterize the differential/algebraic equations that mathematically represent the model corresponding to the scheme of Figure 5.5. We first start with the following definitions:

- $I_{in}^{tot}(\underline{x}, t) := J_{in}^{tot}(\underline{x}, t) \times S$ : total conduction current flowing across the inlet section of the ion channel at  $\Sigma_{in}$  from the intracellular region (units: A);
- $I_{out}^{tot}(\underline{x}, t) := J_{out}^{tot}(\underline{x}, t) \times S$ : total conduction current flowing out of the outlet section of the ion channel at  $\Sigma_{out}$  (units: A);
- $\psi_m(\underline{x}, t)$ : membrane potential across the channel (units: V);
- $\sigma_m(\underline{x}, t)$ : surface charge density accumulated on each side of the membrane at point  $\underline{x}$  and time level  $t$  (units:  $Cm^{-2}$ );
- $Q_m^{tm}(\underline{x}, t) = \sigma_m(\underline{x}, t) \times S$ : total charge accumulated on each side of the membrane (units: C);
- $I_{cap}^{tm}(\underline{x}, t) := \frac{d\sigma_m(\underline{x}, t)}{dt} \times S = \frac{dQ_m(\underline{x}, t)}{dt}$ : transmembrane capacitive current (units: A);
- $I_{cond}^{tm}(\underline{x}, t) = J_{cond}^{tm}(\underline{x}, t) \times S$ : transmembrane conduction current (units: A).

**Definition 5.1** (Local ODE model for cell electrophysiology). *The equivalent electric scheme of Figure 5.5 is a local reduced order model (or local ODE model) of cellular electrophysiology because the complex effort required by the solution of the partial differential equation (PDE) (3.10a), in correspondance of every point  $\underline{x} \in S_{cell}$ , is reduced to the solution of the following ordinary differential equation (ODE) at every point  $\underline{x} \in S_{cell}$ :*

$$I_{out}^{tot}(\underline{x}, t) - I_{cap}^{tm}(\underline{x}, t) - I_{cond}^{tm}(\underline{x}, t) = 0 \quad t > t_0 \quad (5.16a)$$

$$I_{cap}^{tm}(\underline{x}, t) = \frac{dQ_m(\underline{x}, t)}{dt} \quad (5.16b)$$

$$I_{cond}^{tm}(\underline{x}, t) = I_{cond}^{tm}(\psi_m(\underline{x}, t)) \quad (5.16c)$$

where  $t_0$  is the initial time of the electrophysiological analysis. Equation (5.16a) is the classic Kirchhoff Current Law (KCL) enforced at the “plus” or “minus” pole in Figure 5.6.

Let us consider now the scheme of Figure 5.6.

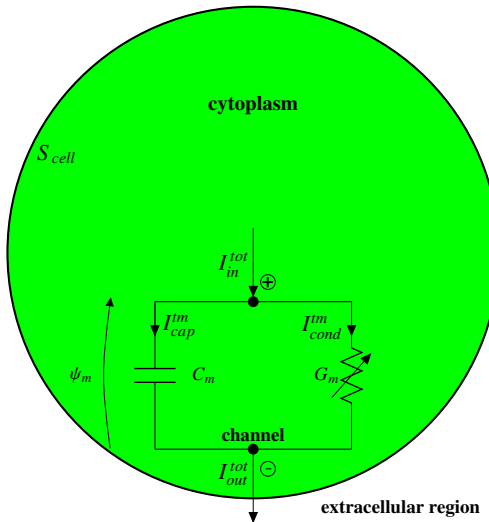


**Figure 5.6** Scheme of a whole-cell model for current flow across the membrane of a cell through the use of an electric equivalent representation. The model is a consequence of the current continuity equation (see Section 5.2).

**Definition 5.2** (Whole-cell ODE model for cell electrophysiology). *The equivalent electric scheme of Figure 5.6 can be regarded as a whole-cell reduced order model (or whole-cell ODE model) of cellular electrophysiology upon assuming the following*

averaged *definitions*:

$$I_{in}^{tot}(t) = \int_{S_{cell}} J_{out}^{tot}(\underline{x}, t) d\Sigma, \quad (5.17a)$$

$$I_{out}^{tot}(t) = \int_{S_{cell}} J_{out}^{tot}(\underline{x}, t) d\Sigma, \quad (5.17b)$$

$$I_{cap}^{tm}(t) = \int_{S_{cell}} J_{cap}^{tm}(\underline{x}, t) d\Sigma, \quad (5.17c)$$

$$I_{cond}^{tm}(t) = \int_{S_{cell}} J_{cond}^{tm}(\underline{x}, t) d\Sigma, \quad (5.17d)$$

$$Q_m^{tm}(t) = \int_{S_{cell}} \sigma_m(\underline{x}, t) d\Sigma, \quad (5.17e)$$

$$\psi_m(t) = \frac{\int_{S_{cell}} \psi_m(\underline{x}, t) d\Sigma}{S_{cell}}. \quad (5.17f)$$

The whole-cell ODE model for cell electrophysiology is the following system of ODEs and algebraic equations:

$$I_{out}^{tot}(t) - I_{cap}^{tm}(t) - I_{cond}^{tm}(t) = 0 \quad t > t_0 \quad (5.18a)$$

$$I_{cap}^{tm}(t) = \frac{dQ_m(t)}{dt} = C_m \frac{\psi_m(t)}{dt} \quad (5.18b)$$

$$I_{cond}^{tm}(t) = I_{cond}^{tm}(\psi_m(t)), \quad (5.18c)$$

where  $I_{cond}^{tm} = I_{cond}^{tm}(t)$  is a (generally) nonlinear function of the whole-cell membrane potential  $\psi_m = \psi_m(t)$ .

**Remark 5.4.** The electric currents  $I_{in}^{tot}$ ,  $I_{out}^{tot}$ ,  $I_{cap}^{tm}$  and  $I_{cond}^{tm}$  introduced in (5.17) are obtained by integrating over the cell surface the corresponding current densities  $J_{in}^{tot}$ ,  $J_{out}^{tot}$ ,  $J_{cap}^{tm}$  and  $J_{cond}^{tm}$ , defined at each point  $\underline{x} \in S_{cell}$ . Similarly, the total electric charge  $Q_m$  accumulated on the cell membrane walls is obtained by integrating over the cell surface the surface charge density  $\sigma_m$ , defined at each point  $\underline{x} \in S_{cell}$ . Finally, the cell membrane potential  $\psi_m$  is the integral mean value of the function  $\psi_m = \psi_m(\underline{x}, t)$  over the cell surface. According to definitions (5.17), all the electrophysiological variables of the whole-cell model are functions of the sole time variable  $t$ .

**Remark 5.5.** The whole-cell ODE model for cell electrophysiology can be also written

considering the current densities as:

$$J_{out}^{tot}(t) - J_{cap}^{tm}(t) - J_{cond}^{tm}(t) = 0 \quad t > t_0 \quad (5.19a)$$

$$J_{cap}^{tm}(t) = \frac{dQ_m(t)}{dt} = c_m \frac{\psi_m(t)}{dt} \quad (5.19b)$$

$$J_{cond}^{tm}(t) = J_{cond}^{tm}(\psi_m(t)), \quad (5.19c)$$

where  $J_{cond}^{tm} = J_{cond}^{tm}(t)$  is a (generally) nonlinear function of the whole-cell membrane potential  $\psi_m = \psi_m(t)$ .

### 5.3. Transmembrane current models

In this section we discuss the models for the transmembrane current density  $J_\alpha^{tm}$  that are most commonly used in the theoretical and computational description of cellular electric activity. For a fully detailed treatment of this complex subject, we refer to [67, 54, 38]. Figure 5.7 represents a schematic view of ion electrodiffusion across a cell membrane of thickness  $t_m$ . Let us indicate with  $s \in [0, t_m]$  the variable indicating the position along the channel axis.

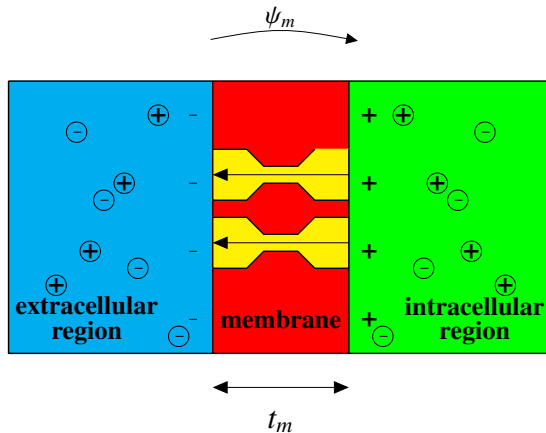


**Figure 5.7** Schematics of ion electrodiffusion across the cell membrane. The region in cyan color is the extracellular site. The region in green color is the intracellular site. The region in brown color is the lipid bilayer. The two regions in yellow color are two channel pores. The surface charge layers accumulating on the two sides of the membrane are denoted by the "+" and "-" symbols. The black arrow indicates the electric field whereas the curved arrow indicates the membrane potential. Cations and anions are indicated by circles with "+" and "-" inside, respectively.

### 5.3.1. Thermodynamic equilibrium for a single ion species

Let  $J_\alpha^{tm}$  the transmembrane current density (units:  $\text{Acm}^{-2}$ ) flowing in the channel pore related to the ion species  $\alpha$ . The following expression defines the Nernst-Planck equation for the transmembrane current density.

**Definition 5.3** (Nernst-Planck equation). *We define the Nernst-Planck expression of the transmembrane current density  $J_\alpha^{tm}$  the following expression*

$$J_\alpha^{tm} = -qz_\alpha D_\alpha \left( \frac{\partial n_\alpha}{\partial s} - \frac{z_\alpha q}{K_B \Theta} n_\alpha E \right) \quad \alpha = 1, \dots, M_{ion} \quad s \in [0, t_m], \quad (5.20a)$$

where  $n_\alpha$  is the number density of the ion species  $\alpha$  (units:  $\text{cm}^{-3}$ ),  $D_\alpha^{el}$  the diffusivity of the species  $\alpha$  (units:  $\text{cm}^2 \text{s}^{-1}$ ),  $z_\alpha$  the charge number of the ion  $\alpha$ ,  $\Theta$  is the temperature (units: K) and  $K_B$  the Boltzman constant (units:  $\text{JK}^{-1}$ ).

**Definition 5.4** (Thermodynamic equilibrium in the case of a single ion species). *We say that the transmembrane channel is under the thermodynamic equilibrium if*

$$J_\alpha^{tm}(s) = 0 \quad s \in [0, t_m]. \quad (5.21)$$

**Remark 5.6** (Exact cancellation of diffusion and drift current densities). *In thermodynamic equilibrium conditions, the transmembrane current density  $J_\alpha^{tm}$  is null although both the separate drift and diffusion contributions may be, in general, not equal to zero. More precisely*

$$J_{\alpha,drift}^{tm}(s) = -J_{\alpha,diff}^{tm}(s) \quad s \in [0, t_m], \quad (5.22)$$

where  $J_{\alpha,drift}^{tm}$  and  $J_{\alpha,diff}^{tm}$  are the drift and diffusion current densities defined as:

$$J_{\alpha,drift}^{tm}(s) = q|z_\alpha|\mu_\alpha^{el} n_\alpha E \quad (5.23)$$

$$J_{\alpha,diff}^{tm}(s) = -qz_\alpha D_\alpha \frac{\partial n_\alpha}{\partial s} \quad (5.24)$$

where we have used the Einstein relation 5.25 to express the electric mobility (units:  $\text{cm}^2 \text{V}^{-1} \text{s}^{-1}$ ) as a function of the diffusivity,

$$D_\alpha = \frac{K_B \Theta}{|z_\alpha|q} \mu_\alpha^{el}. \quad (5.25)$$

The thermodynamic equilibrium condition (5.22) may be quite difficult to verify in numerical computations because it requires exact cancellation between drift and diffusion current density contributions.

**Definition 5.5** (Nernst potential). *By applying the Thermodynamic equilibrium to the Nernst-Planck equation 5.20a and solving the obtained ordinary differential equation*

we have

$$E_{c,\alpha} = \frac{K_B\Theta}{qz_\alpha} \ln\left(\frac{n_\alpha^{(out)}}{n_\alpha^{(in)}}\right) = \frac{R\Theta}{Fz_\alpha} \ln\left(\frac{n_\alpha^{(out)}}{n_\alpha^{(in)}}\right), \quad (5.26)$$

where  $E_{c,\alpha}$  is the Nernst potential (units: V) associated with the ionic species  $\alpha$ ,  $R$  is the universal gas constant (units: J mol<sup>-1</sup> K<sup>-1</sup>) and  $F$  is Faraday’s constant (units: C mol<sup>-1</sup>).

**Remark 5.7** (The built-in electric field). *In order to enforce the condition  $J_\alpha^{tm}(s) = 0$  for all  $s \in [0, t_m]$ , a “built-in” electric field  $E_{bi} = E_{bi}(s)$  needs to develop inside the ion channel pore in such a way that the drift and diffusion contributions to the total transmembrane current density mutually cancel out, as prescribed by Equation (5.22). It turns out that such a built-in electric field satisfies the condition*

$$E_{c,\alpha} = - \int_0^{t_m} E_{bi}(\xi) d\xi. \quad (5.27)$$

It is important to notice that thermodynamic equilibrium is a dynamical state in which, at the microscopic level, particles manifest continuously the tendency to diffuse and drift across the cellular membrane because of thermal agitation. Correspondingly, thermodynamic equilibrium is indispensable to introduce the Nernst potential that is a fundamental quantity in the analysis of the electrical activity of every excitable cell.

### 5.3.2. The linear resistor model

This is the simplest current-voltage relationship for the ion current density  $J_\alpha^{tm}$  and reads

$$J_\alpha^{tm} = g_\alpha (\psi_m - E_{c,\alpha}) = g_\alpha \left( \psi^{(in)} - \psi^{(out)} - \frac{1}{z_\alpha} V_{th} \ln\left(\frac{n_\alpha^{(out)}}{n_\alpha^{(in)}}\right) \right), \quad (5.28)$$

where  $V_{th} = K_B\Theta/q$  is the thermal voltage ( $K_B$  Boltzmann’s constant units: JK<sup>-1</sup>), whereas  $g_\alpha$  and  $E_{c,\alpha}$  are the specific conductance and the Nernst potential associated with the ion species  $\alpha$ , respectively,  $E_{c,\alpha}$  being computed with Equation (5.26). The units of  $g_\alpha$  are

$$[g_\alpha] = \text{A V}^{-1} \text{ m}^{-2} = \text{S m}^{-2}.$$

The graphical representation of the current-voltage relationship (5.28) in the  $(\psi_m, J)$  plane, illustrated in Figure 5.8, is a straight line whose slope is equal to  $g_\alpha$ . Despite its simplicity, the linear resistor model has been successfully employed in the simulation of realistic biophysical problems (see [43]).

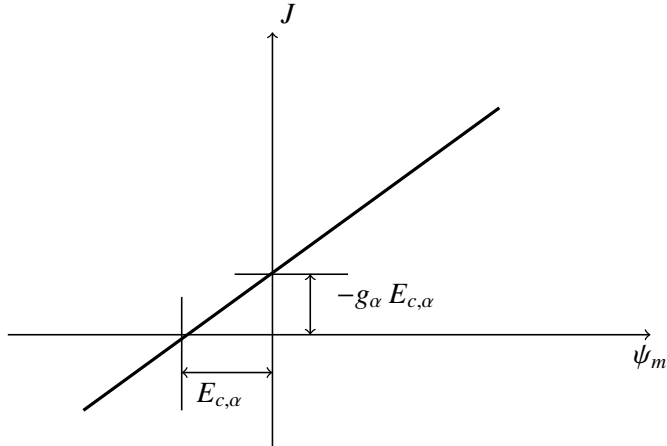


Figure 5.8 Characteristic  $J-\psi_m$  curve for the linear resistor model.

### 5.3.3. The Goldman-Hodgkin-Katz model

The Goldman-Hodgkin-Katz (GHK) model is an improvement of the linear resistor formulation and is based on the following assumptions (see also [67, 105]):

1. the ion current density of the species  $\alpha$  is mathematically described by the Nernst-Planck model (5.3)
2. the electric field is constant across the membrane;
3. the ion current density  $J_\alpha^{tm}$  is constant across the membrane.

The application of assumption 2 and the use of (3.9) and yield

$$E = -\frac{\partial \psi}{\partial s} = \text{constant} = -\frac{\psi^{(out)} - \psi^{(in)}}{t_m} = \frac{\psi_m}{t_m}. \quad (5.29)$$

Replacing (5.29) in (5.3), we get

$$J_\alpha^{tm} = -qz_\alpha D_\alpha \left( \frac{\partial n_\alpha}{\partial s} - \frac{z_\alpha q}{K_B \Theta} n_\alpha \frac{\psi_m}{t_m} \right). \quad (5.30)$$

Then, applying assumption 3 to (5.30) we obtain

$$J_\alpha^{tm} = \text{constant} \implies \frac{\partial J_\alpha^{tm}}{\partial s} = 0 \implies \frac{\partial^2 n_\alpha}{\partial s^2} - \frac{z_\alpha q}{K_B \Theta} \cdot \frac{\psi_m}{t_m} \cdot \frac{\partial n_\alpha}{\partial s} = 0.$$

The solution of the above differential equation is given by

$$n_\alpha(s) = A + B \exp \left( \frac{z_\alpha q}{K_B \Theta} \psi_m \frac{s}{t_m} \right) \quad (5.31)$$

where  $A$  and  $B$  are arbitrary constants that can be found by imposing the following boundary conditions at the two sides of the channel:

$$\begin{cases} n_\alpha(0) = n_\alpha^{(in)} \\ n_\alpha(t_m) = n_\alpha^{(out)} \end{cases} \implies \begin{cases} A + B = n_\alpha^{(in)} \\ A + Be^{\frac{z_\alpha q}{K_B \Theta} \psi_m} = n_\alpha^{(out)} \end{cases} \implies \begin{cases} A = -\frac{(n_\alpha^{(out)} - n_\alpha^{(in)}) e^{\frac{z_\alpha q}{K_B \Theta} \psi_m}}{e^{\frac{z_\alpha q}{K_B \Theta} \psi_m} - 1} \\ B = \frac{n_\alpha^{(out)} - n_\alpha^{(in)}}{e^{\frac{z_\alpha q}{K_B \Theta} \psi_m} - 1}. \end{cases}$$

For notational simplicity, we introduce the dimensionless variable

$$\Phi := z_\alpha \frac{\psi_m}{K_B \Theta / q}$$

which has the physical meaning of a normalized membrane potential. Then, to compute the constant current density throughout the channel we replace (5.31) into (5.30) to obtain

$$J_\alpha^{tm} = -qz_\alpha D_\alpha \left( B \frac{\Phi}{t_m} \exp\left(\Phi \frac{s}{t_m}\right) - \frac{\Phi}{t_m} A - B \frac{\Phi}{t_m} \exp\left(\Phi \frac{s}{t_m}\right) \right).$$

The first and third term in the braces on the right-hand side mutually cancel out, and we are left with the following expression of the constant ion current density

$$J_\alpha^{tm} = qz_\alpha D_\alpha \frac{\Phi}{t_m} A = -qz_\alpha D_\alpha \frac{1}{t_m} \left[ \frac{\Phi}{e^\Phi - 1} n_\alpha^{(out)} - \frac{\Phi e^\Phi}{e^\Phi - 1} n_\alpha^{(in)} \right]. \quad (5.32)$$

It is useful to introduce the definition of the inverse of the Bernoulli function

$$\mathcal{B}(\Phi) := \frac{\Phi}{e^\Phi - 1}. \quad (5.33a)$$

A plot of  $\mathcal{B}(\Phi)$  and  $\mathcal{B}(-\Phi)$  is reported in Figure 5.9.

The function  $\mathcal{B}(\Phi)$  enjoys the following properties:

$$\mathcal{B}(\Phi) > 0 \quad \forall \Phi \in \mathbb{R}; \quad (5.33b)$$

$$\mathcal{B}(0) = 1; \quad (5.33c)$$

$$e^\Phi \mathcal{B}(\Phi) = \mathcal{B}(-\Phi) = \Phi + \mathcal{B}(\Phi); \quad (5.33d)$$

$$\lim_{\Phi \rightarrow +\infty} \mathcal{B}(\Phi) = 0^+, \quad \lim_{\Phi \rightarrow -\infty} \mathcal{B}(\Phi) = -\Phi; \quad (5.33e)$$

$$\lim_{\Phi \rightarrow +\infty} \mathcal{B}(-\Phi) = \Phi, \quad \lim_{\Phi \rightarrow -\infty} \mathcal{B}(\Phi) = 0^+. \quad (5.33f)$$

Using Definition (5.33a) and Property (5.33d), the constant current density can be written as

$$J_\alpha^{tm} = -qz_\alpha D_\alpha \frac{1}{t_m} \left[ \mathcal{B}\left(\frac{z_\alpha \psi_m}{K_B \Theta / q}\right) n_\alpha^{(out)} - \mathcal{B}\left(-\frac{z_\alpha \psi_m}{K_B \Theta / q}\right) n_\alpha^{(in)} \right]. \quad (5.34)$$

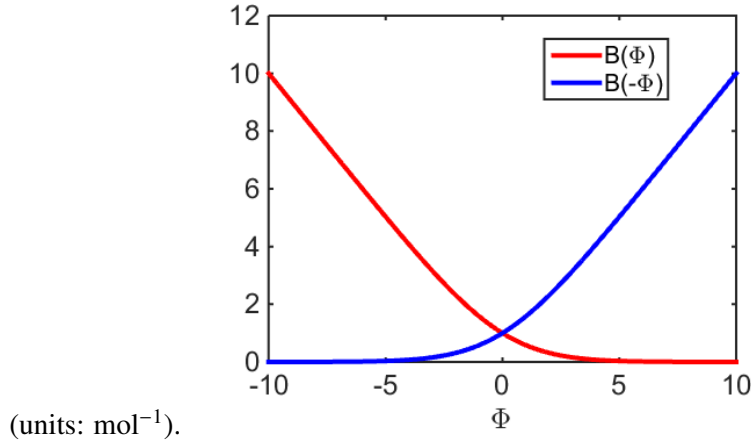


Figure 5.9 Plot of  $B(\Phi)$  (red line) and of  $B(-\Phi)$  (blue line).

Relation (5.34) is the celebrated *Goldman-Hodgkin-Katz (GHK)* equation for the current density associated with the ion species  $\alpha$ ,  $\alpha = 1, \dots, M_{ion}$ .

Let us check that (5.34) satisfies Definition 5.4 of thermodynamic equilibrium. Using Property (5.33d), we have

$$J_\alpha^{tm} = 0 \quad \implies \quad n_\alpha^{(out)} - n_\alpha^{(in)} \exp\left(z_\alpha \frac{q\psi_m}{K_B\Theta}\right) = 0$$

from which we get

$$\psi_m = \frac{K_B\Theta}{z_\alpha q} \ln\left(\frac{n_\alpha^{(out)}}{n_\alpha^{(in)}}\right) \equiv E_{c,\alpha}$$

that is, the membrane potential coincides with the Nernst potential as required at thermodynamic equilibrium. Conversely, setting  $\psi_m = E_{c,\alpha}$  into (5.34) yields

$$J_\alpha^{tm} = -qz_\alpha D_\alpha \frac{1}{t_m} \left[ \frac{\frac{qz_\alpha}{K_B\Theta} \cdot \frac{K_B\Theta}{qz_\alpha} \ln\left(\frac{n_\alpha^{(out)}}{n_\alpha^{(in)}}\right)}{\frac{n_\alpha^{(out)}}{n_\alpha^{(in)}} - 1} n_\alpha^{(out)} - \frac{-\frac{qz_\alpha}{K_B\Theta} \cdot \frac{K_B\Theta}{qz_\alpha} \ln\left(\frac{n_\alpha^{(out)}}{n_\alpha^{(in)}}\right)}{\frac{n_\alpha^{(in)}}{n_\alpha^{(out)}} - 1} n_\alpha^{(in)} \right] = 0,$$

which is the thermodynamic equilibrium condition.

The GHK current density enjoys other interesting properties. Assume that  $\psi_m = 0$  (i.e., the intra- and extracellular potentials have the same value). Then, using Prop-

erty (5.33c) the GHK current density degenerates to

$$J_{\alpha}^{tm} = -qz_{\alpha}D_{\alpha} \frac{n_{\alpha}^{(out)} - n_{\alpha}^{(in)}}{t_m}.$$

This formula corresponds to a *pure diffusion* ion flow across the membrane in agreement with the Nernst-Planck relation (5.30) in absence of electric field.

Conversely, assume that  $n_{\alpha}^{(out)} = n_{\alpha}^{(in)} = \bar{n}_{\alpha}$  (i.e., the intra- and extracellular ion concentrations have the same value  $\bar{n}_{\alpha}$ ). Then, using Property (5.33d) the GHK current density degenerates to

$$J_{\alpha}^{tm} = -qz_{\alpha}D_{\alpha} \frac{\bar{n}_{\alpha}}{t_m} \left( -z_{\alpha} \frac{\psi_m}{K_B \Theta / q} \right).$$

Using (9.45) and (5.29), the previous relation becomes

$$J_{\alpha}^{tm} = q|z_{\alpha}| \mu_{\alpha} \bar{n}_{\alpha} E.$$

This formula corresponds to a *pure drift* ion flow across the membrane in agreement with the Nernst-Planck relation (5.30) in absence of a concentration gradient.

The above analysis shows that the GHK expression of the ion current density *automatically* adapts itself to all possible transport regimes.

### 5.3.4. A generalized nonlinear resistor model

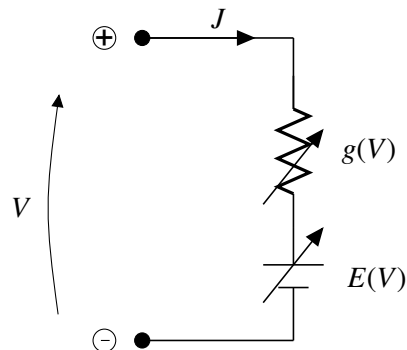


**Figure 5.10** Electric representation of a nonlinear resistor.  $J$  is the current density flowing in the resistor.  $V$  is the voltage drop across the circuit.  $g(V)$  is the specific conductance and  $E(V)$  is a voltage source. Both  $g$  and  $E$  nonlinearly depend on  $V$ .

In this section we illustrate the general mathematical formulation to represent the current-voltage characteristic of a nonlinear resistor and we show that the two current models described in Sections 5.3.2 and 5.3.3 are special instances of such formulation.

For ease of presentation, assume that the conduction current density is transported by the sole ion species  $\alpha$  with chemical valence  $z_\alpha$  and intracellular and extracellular molar densities  $c_\alpha^{(in)}$ ,  $c_\alpha^{(out)}$  (units: mM). Let us consider the equivalent electric scheme of a nonlinear resistor shown in Figure 5.10. The  $J$ - $V$  relation for the circuit of Figure 5.10 is

$$J(V) = g(V)(V - E(V)). \quad (5.35)$$

#### 5.3.4.1. The case of the linear resistor model

In the case of the linear resistor model we simply have:

$$g(V) = g_\alpha, \quad (5.36a)$$

$$E(V) = E_{c,\alpha} = \frac{V_{th}}{z_\alpha} \ln\left(\frac{c_\alpha^{(out)}}{c_\alpha^{(in)}}\right). \quad (5.36b)$$

#### 5.3.4.2. The case of the GHK model

In the case of the GHK model the  $J$ - $V$  relation reads

$$J(V) = -qz_\alpha \frac{D_\alpha}{t_m} \left[ \mathcal{B}\left(\frac{z_\alpha V}{V_{th}}\right) n_\alpha^{(out)} - \mathcal{B}\left(-\frac{z_\alpha V}{V_{th}}\right) n_\alpha^{(in)} \right] \quad (5.37)$$

where the ion number densities  $n_\alpha^{(out)}$  and  $n_\alpha^{(in)}$  (units:  $\text{m}^{-3}$ ) can be computed from the ion molar densities  $c_\alpha^{(out)}$  and  $c_\alpha^{(in)}$  by the relations:

$$n_\alpha^{(out)} = c_\alpha^{(out)} N_{Av}, \quad n_\alpha^{(in)} = c_\alpha^{(in)} N_{Av},$$

$N_{Av} = 6.022 \cdot 10^{23} \text{ mol}^{-1}$  being the Avogadro constant. Setting  $\Phi := z_\alpha V / V_{th}$  and using Property (5.33d), we can write (5.37) as

$$J(\Phi) = -qz_\alpha \frac{D_\alpha}{t_m} \left[ \mathcal{B}(\Phi) n_\alpha^{(out)} - (\Phi + \mathcal{B}(\Phi)) n_\alpha^{(in)} \right] = qz_\alpha \frac{D_\alpha}{t_m} n_\alpha^{(in)} \left[ \Phi - \frac{n_\alpha^{(out)} - n_\alpha^{(in)}}{n_\alpha^{(in)}} \mathcal{B}(\Phi) \right].$$

Replacing the definition of  $\Phi$  in the previous relation we finally obtain

$$J(V) = \frac{qz_\alpha^2 n_\alpha^{(in)}}{V_{th}} \frac{D_\alpha}{t_m} \left[ V - \frac{V_{th}}{z_\alpha} \left( \frac{n_\alpha^{(out)}}{n_\alpha^{(in)}} - 1 \right) \mathcal{B}\left(\frac{z_\alpha V}{V_{th}}\right) \right].$$

Comparing the above equation with (5.35) we see that, in the case of the GHK model, we have:

$$g(V) = \frac{qz_\alpha^2 n_\alpha^{(in)}}{V_{th}} \frac{D_\alpha}{t_m} = \frac{qz_\alpha^2 N_{Av} c_\alpha^{(in)}}{V_{th}} \frac{D_\alpha}{t_m}, \quad (5.38a)$$

$$E(V) = \frac{V_{th}}{z_\alpha} \left( \frac{n_\alpha^{(out)}}{n_\alpha^{(in)}} - 1 \right) \mathcal{B}\left(\frac{z_\alpha V}{V_{th}}\right) = \frac{V_{th}}{z_\alpha} \left( \frac{c_\alpha^{(out)}}{c_\alpha^{(in)}} - 1 \right) \mathcal{B}\left(\frac{z_\alpha V}{V_{th}}\right). \quad (5.38b)$$

Relation (5.38a) can be mathematically regarded as an *effective* specific conductance for the ion species  $\alpha$ . Its constant value represents a macroscopic model parameter that can be determined from the knowledge of microscopic data such as the diffusion coefficient of the ion species  $\alpha$  in the protein channel, the thickness of the membrane lipid bilayer and the intracellular ion concentration in the proximity of the intracellular side of the ion channel. Similarly, relation (5.38b) can be mathematically regarded as an *effective* Nernst potential for the ion species  $\alpha$ . Its value is *not* a constant but nonlinearly depends on  $V$  and on the ion concentrations in the proximity of the intracellular and extracellular sides of the ion channel.

#### 5.4. The Hodgkin-Huxley model

In a series of historical papers [55, 56] that owned them the Nobel Prize in Medicine in 1963, Hodgkin and Huxley (HH) proposed and analyzed a differential/algebraic mathematical model for transmembrane ion current conduction in the squid giant axon. The original form of the HH model falls into the category of whole-cell models

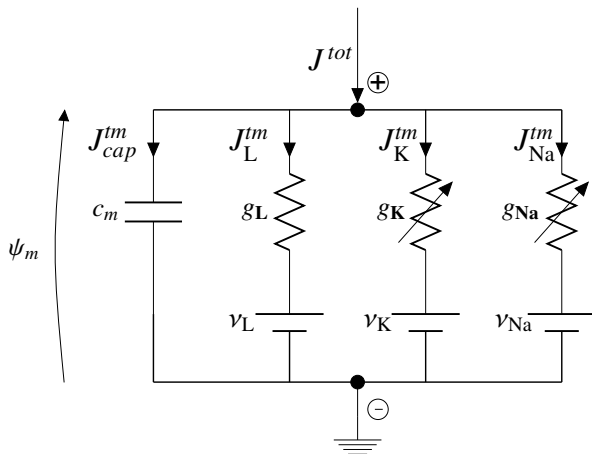


Figure 5.11 Equivalent electric representation of the Hodgkin-Huxley model.

The HH model is characterized by the following main properties:

- the capacitance  $C_m$  is linear;
- the conductance  $G_m$  is a nonlinear function of  $\psi_m$ .

Figure 5.11 gives a schematic illustration of the electric equivalent circuit of the HH whole-cell model. Three ion species,  $\text{Na}^+$ ,  $\text{K}^+$  and  $\text{Cl}^-$ , are included in the biophysical picture of ion current conduction in the squid giant axon. Experimental evidences indicate that the principal ion currents are due to  $\text{Na}^+$  and  $\text{K}^+$  ions. The remaining

ion currents are conventionally associated with the  $\text{Cl}^-$  ion. Since this current is small compared to the principal currents, it is usually referred to as *leakage current* (see [67, 54, 38]).

The symbol  $c_m$  is the membrane specific capacitance (units:  $\text{F m}^{-2}$ ), defined as

$$c_m := \frac{C_m}{S_{cell}}. \quad (5.39)$$

The symbols  $J_{\text{Na}}^{tm}$  and  $J_{\text{K}}^{tm}$  denote the current densities of sodium and potassium ions whereas  $J_L^{tm}$  is the leakage current density. The symbol  $v_m$  is related to the membrane potential  $\psi_m$  by the following relation

$$v_m := \psi_m - E_{c,m}, \quad (5.40)$$

where  $E_{c,m}$  is the membrane *resting potential* (i.e., the equilibrium potential of the membrane)

The variable  $v_m$  biophysically represents the *displacement* of the membrane potential from the resting state of the membrane, which corresponds to the situation of thermodynamic equilibrium introduced in Definition 5.4 in the case of a single ion species. Correspondingly, the quantities  $v_K$ ,  $v_{\text{Na}}$  and  $v_L$  represent the deviations of the Nernst potentials of potassium, sodium and chloride from the membrane resting potential, and are treated in [56] as model fitting parameters (so-called “adjusted potentials”). All potentials  $v_m$ ,  $v_K$ ,  $v_{\text{Na}}$  and  $v_L$  are expressed in mV, and, precisely, the shifted reversal potentials are set equal to

$$v_K = -12 \text{ mV}, \quad v_{\text{Na}} = 115 \text{ mV}, \quad v_L = 10.613 \text{ mV}.$$

The specific membrane capacitance  $c_m$  is equal to  $1 \mu\text{F cm}^{-2}$ .

Applying the KCL to the circuit of Figure 5.11 with  $J^{tot} = 0$  we obtain the following nonlinear system of ODEs and algebraic equations, which is referred to as the HH model:

$$c_m \frac{dv_m}{dt} = -(J_{\text{K}}^{tm} + J_{\text{Na}}^{tm} + J_L^{tm}) \quad (5.41a)$$

$$J_{\text{K}}^{tm} = n^4 g_{\text{K}}(v_m - v_K) \quad (5.41b)$$

$$J_{\text{Na}}^{tm} = h m^3 g_{\text{Na}}(v_m - v_{\text{Na}}) \quad (5.41c)$$

$$J_L^{tm} = g_L(v_m - v_L) \quad (5.41d)$$

$$\frac{\partial m}{\partial t} = \alpha_m(1 - m) - \beta_m m \quad (5.41e)$$

$$\frac{\partial n}{\partial t} = \alpha_n(1 - n) - \beta_n n \quad (5.41f)$$

$$\frac{\partial h}{\partial t} = \alpha_h(1 - h) - \beta_h h, \quad (5.41g)$$

where the time rates  $\alpha_j$  and  $\beta_j$ ,  $j = m, n, h$ , are positive coefficients that nonlinearly depend on the potential  $v_m$  as specified below. The dimensionless functions of time  $n$ ,  $m$  and  $h$  are the so-called *gating variables*. This terminology is motivated by the fact that they describe the opening state of the channel. Their introduction, and, more importantly, their phenomenological characterization, is the main contribution of the HH theory and permits the simulation of the propagation of an action potential, as shown below in the numerical examples. The variables  $m$ ,  $n$  and  $h$  typically vary between 0 and 1, and, at each point of the membrane, are governed by the ODEs (5.41e)-(5.41g), where the time rates  $\alpha_s$  and  $\beta_s$ ,  $s = m, n, h$ , are experimentally determined functions expressed in  $\text{ms}^{-1}$ . Hodgkin and Huxley [56] used the following expressions for them:

$$\alpha_m(v_m) = \mathcal{B}((25 - v_m)/10) \quad (5.42a)$$

$$\beta_m(v_m) = 4 \exp(-v_m/18) \quad (5.42b)$$

$$\alpha_n(v_m) = 0.1\mathcal{B}((10 - v_m)/10) \quad (5.42c)$$

$$\beta_n(v_m) = 0.125 \exp(-v_m/80) \quad (5.42d)$$

$$\alpha_h(v_m) = 0.07 \exp(-v_m/20) \quad (5.42e)$$

$$\beta_h(v_m) = C((30 - v_m)/10) \quad (5.42f)$$

where  $\mathcal{B}(t) := t/(e^t - 1)$  and  $C(t) := 1/(e^t + 1)$ . The constant specific conductances  $g_K$ ,  $g_{Na}$  and  $g_L$  are expressed in  $\text{mS cm}^{-2}$  and are set equal to

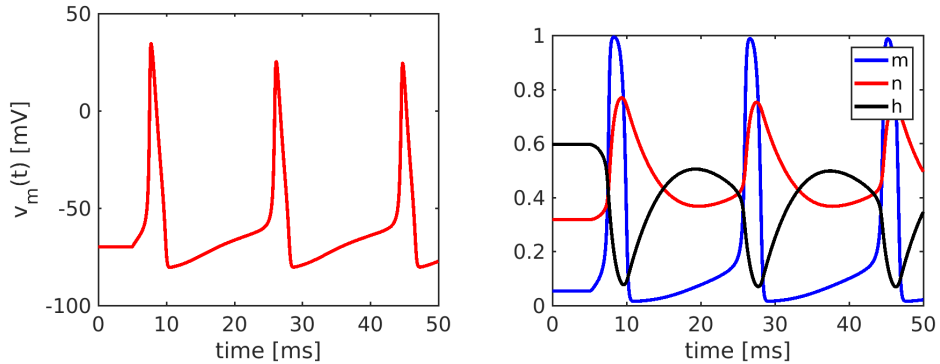
$$g_K = 36 \text{ mS cm}^{-2}, \quad g_{Na} = 120 \text{ mS cm}^{-2}, \quad g_L = 0.3 \text{ mS cm}^{-2}.$$

**Example 5.1** (Action potential simulation using the HH model). *To conclude this section we apply the HH model (5.41) to the simulation of the elicitation of an action potential in an excitable cell and its subsequent propagation along a nerve fiber. The action potential occurs in response of the external stimulus (a voltage or a current stress) that solicits the excitable cell. Let us consider the case of a current density stimulus  $J_{out} \neq 0$ . Applying the KCL to the circuit in Figure 5.11 with an external current source, Equation (5.41) becomes*

$$c_m \frac{dv_m}{dt} = -(J_K^{tm} + J_{Na}^{tm} + J_L^{tm}) + J_{out} \quad (5.43)$$

where  $J_K^{tm}$ ,  $J_{Na}^{tm}$  and  $J_L^{tm}$  are given in (5.41). Assuming a cell radius of  $5 \cdot 10^{-3} \text{ cm}$  and an external stimulus of  $J_{out} = 2 \cdot 10^{-6} \mu\text{A cm}^{-2}$  we obtain the results illustrated in

*Figures 5.12 and 5.13.*



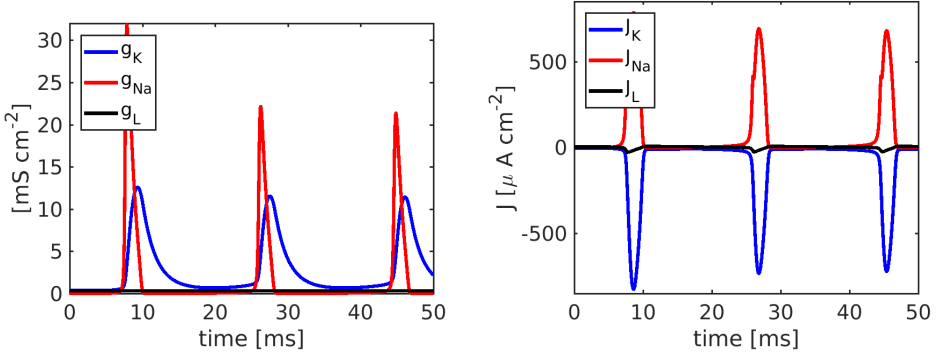
**Figure 5.12** Simulation of the elicitation of an action potential in an excitable cell using the HH model. Left panel: action potential. Right panel: gating variables.

Figure 5.12 shows the action potential and gating variables predicted by the HH equation system (5.41): the fast rise of the potential is determined by the opening of the  $\text{Na}^+$  channel controlled by the gating variable  $m$  (blue line in the right panel) whereas the slow ramp down is driven by the  $\text{K}^+$  ions whose conduction is determined by the gating variable  $n$  (red line in the right panel) till the  $\text{K}^+$  Nernst potential is reached. It is worth noting that the ion channel conductance in the Hodgkin-Huxley model is not constant but is determined by the solution of the gating variable system as illustrated in Figure 5.13 (left panel). Figure 5.13 (right panel) shows the current density  $J_K^{tm}$  associated with potassium (blue line) and the current density  $J_{\text{Na}}^{tm}$  associated with sodium (red line): they have opposite sign, corresponding to the fact that  $\text{Na}^+$  flows out of the cell whereas  $\text{K}^+$  flows into the cell. As anticipated, simulation results indicate that the leakage current density  $J_L^{tm}$  associated with  $\text{Cl}^-$  (black line) is far smaller than the other two principal current densities.

A complete mathematical analysis of the ODE system (5.41) goes beyond the scope of this section and can be found in [67] and [38].

## 5.5. The cable equation

In Chapter 5 we have illustrated in detail the function of electric activity in excitable cells through the adoption of a lumped parameter mathematical representation of the cellular membrane. This approach leads to an ordinary differential equation (ODE) that expresses the Kirchhoff current law at each point of the membrane (the so-called local cell model, see (5.16)) or across the whole surface of the cell (the so-called whole-cell ODE model, see (5.19)). In this chapter we consider a mathematical de-



**Figure 5.13** Left panel: channel ion conductances. Right panel: ion current densities predicted by the Hodgkin-Huxley model.

scription of cellular electric activity based on the use of a partial differential equation (PDE) model. To this purpose, we illustrate the so-called *cable equation model* of cellular electric activity, a parabolic initial value/boundary value problem to mathematically describe the biophysical mechanism of intercellular communication through the propagation of an action potential along an axon fiber. Our presentation is based on [88] and [38, Chapter 1], to which we refer for further details.

### 5.5.1. The geometric setting

Let us consider the schematic representation of a biophysical connection between an excitable cell (e.g., a neuron) and a terminal output with resistive load  $R_{out}$  via a nerve fiber (e.g., an axon) shown in Figure 5.14, where  $c_m$  (units:  $\text{Fm}^{-2}$ ) is the membrane capacitance per unit area (of the cell and of the cylindrical axon) and  $j_m^{ion}$  (units:  $\text{Am}^{-2}$ ) is the membrane ion current density described with any of the mathematical models discussed in Section 5.3.

The excitable cell (a neuron, for example) is subject to an external stimulus (the applied voltage signal  $V_{in}$ ). The signal gives rise to a modification of the membrane potential  $\psi_m$  which is transmitted to the output receiving terminal (the resistive load  $R_{out}$ ) giving rise to the output voltage drop  $\psi_{m,out}$ . The transmission is operated by the “biological cable” represented in the scheme by a cylinder of radius  $a$  and length  $L$ . In the realistic case, such a cable is a nerve fiber that constitutes the protrusion of the neuron’s body (soma) towards the environment surrounding the cell. Such nerve fiber has the same physiological content as that of the mother cell and has the fundamental role of transmitting a nervous signal (in the form of an electric impulse) to a receiving terminal. In what follows, we indicate by  $S = \pi a^2$  the cross section of the axon fiber. In the case of a motor neuron located in the spinal cord of the human body we typically

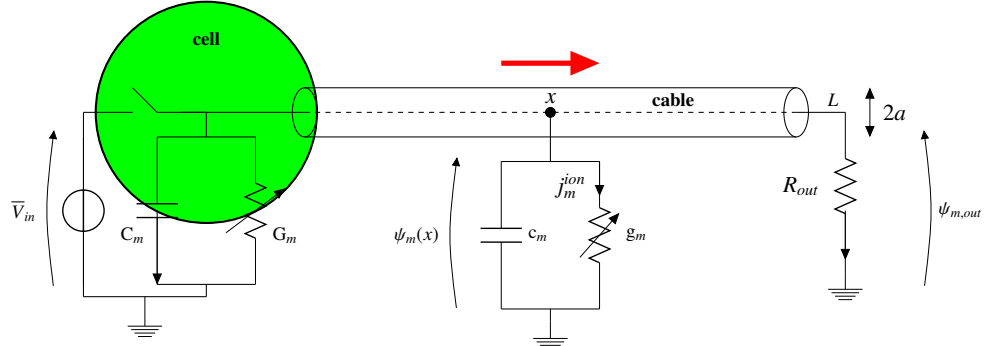


**Figure 5.14** Schematic view of a biophysical connection between an excitable cell (for example, a neuron) and a terminal output (indicated by a resistive load  $R_{out}$ ). The connecting cable is the simplified representation of a nerve fiber (an axon),

have  $a = 50\mu\text{m}$  and  $L = 1\text{m}$  so that  $a/L = 5 \cdot 10^{-5}$ . In the case of the squid giant axon analyzed in [56] we have  $a = 0.25\text{mm}$  and  $L = 5\text{cm}$  so that  $a/L = 5 \cdot 10^{-3}$ . Therefore, we see that in both cases we have  $a/L \ll 1$  but with a significant variability of the range. In the case of the squid giant axon the ratio  $a/L$  is 100 times larger than in the case of the axon in the spinal cord of the human body.

### 5.5.2. Electric equivalent representation

To derive the mathematical model of the spatial propagation of the input signal  $\bar{V}_{in} = \bar{V}_{in}(t)$  we introduce the following assumptions on the biophysical system under investigation:

1. the intra and extracellular regions are characterized by spatially constant ion concentrations;
2. the extracellular region is *equipotential* (for convenience we set its potential equal to zero);
3. the intracellular region has a uniform electric resistivity  $\rho_{elec,ax}$  (units:  $\Omega\text{m}$ ).

Assumption 3 implies that the resistance of an infinitesimal piece  $dx$  of axon is equal to

$$dR(x) = \frac{\rho_{elec,ax}dx}{S} = \frac{\rho_{elec,ax}dx}{\pi a^2}. \quad (5.44a)$$

As a consequence, applying the Ohm law between two points along the axis of the cable at  $x$  and  $x + dx$ , respectively, with the convention that the current  $I_{in}$  is positive if flowing from  $x$  to  $x + dx$  as in Figure 5.15, we get

$$d\psi_m(x, t) := \psi_m(x, t) - \psi_m(x + dx, t) = -(\psi_m(x + dx, t) - \psi_m(x, t))$$

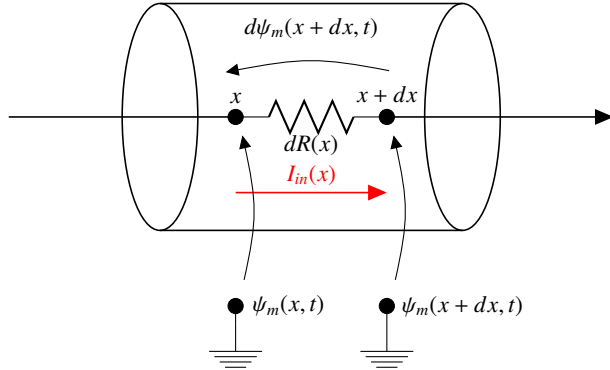


Figure 5.15 Ohm's law for an infinitesimal piece of axon of length  $dx$ .

$$= dR(x)I_{in}(x, t) = \frac{\rho_{elec,ax}dx}{\pi a^2}I_{in}(x, t)$$

from which, letting  $dx$  tend to zero, we obtain the following differential relation for the longitudinal electric current flowing along the axon axis due to the intracellular longitudinal gradient of the membrane potential

$$I_{in}(x, t) = -\frac{\pi a^2}{\rho_{elec,ax}} \frac{\partial \psi_m}{\partial x}(x, t). \quad (5.44b)$$

Having identified the expression of ohmic current flow in the direction of the axon axis, we need now to complete the cable transmission model with the balance of currents flowing in and out across a volumetric differential element of the cable, since capacitive and ohmic effects occur also in the transversal direction of the fiber. To mathematically describe ion electrodynamics in the direction perpendicular to the axon fiber we consider the scheme represented in Figure 5.16.

Using the KCL (3.11d), the balance of currents at  $x + dx/2$  yields

$$I_{in}(x, t) = I_{in}(x + dx, t) + \frac{dQ_m^{cap}}{dt}(x + dx/2, t) + I_{ion}(x + dx/2, t) \quad (5.44c)$$

where:

- $I_{in}(x, t)$  and  $I_{in}(x + dx, t)$  are the longitudinal currents entering and leaving the infinitesimal volume, respectively;
- 

$$\frac{dQ_m^{cap}}{dt}(x + dx/2, t) = c_m \times 2\pi a dx \frac{\partial \psi_m}{\partial t}(x + dx/2, t) \quad (5.44d)$$

is the time rate of change of the infinitesimal amount of charge stored at each side of the membrane and distributed over a surface differential area equal to  $2\pi a dx$ ;

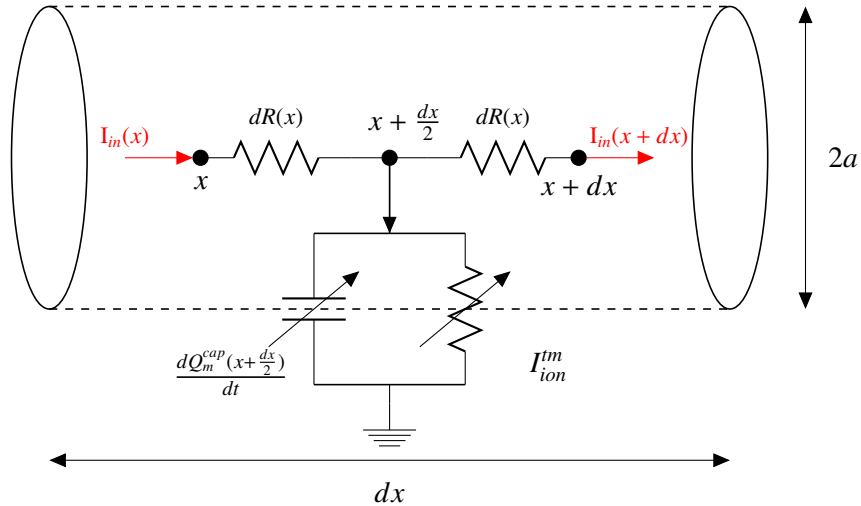


**Figure 5.16** Kirchhoff current law for an infinitesimal volume of axon fiber of length  $dx$ , lateral surface  $2\pi a$  and cross-sectional area  $S = \pi a^2$ .

$$I_{ion}(x+dx/2, t) = j_m^{ion}(x+dx/2, t) \times 2\pi a dx \quad (5.44e)$$

is the transmembrane current, as analyzed in chapter 5.

Replacing (5.44d) and (5.44e) into (5.44c), dividing out both sides by  $2\pi a dx$  and letting  $dx$  tend to zero, we obtain the following balance of longitudinal and transversal current densities at point  $x$  and time instant  $t$

$$-\frac{1}{2\pi a} \frac{\partial I_{in}}{\partial x}(x, t) = c_m \frac{\partial \psi_m}{\partial t}(x, t) + j_m^{ion}(x, t) \quad (5.44f)$$

where  $I_{in}(x, t)$  is given by (5.44b).

### 5.5.3. The cable equation model

Collecting the relations obtained in Section 5.5.1, the cable equation model describing the propagation of an electric impulse along the axis of a nerve fiber consists of the following PDEs, to be solved in the space-time cylinder  $Q_{T_{fin}} := (0, L) \times (0, T_{fin})$ :

$$c_m \frac{\partial \psi_m}{\partial t}(x, t) + \frac{1}{2\pi a} \frac{\partial I_{in}}{\partial x}(x, t) = -j_m^{ion}(x, t) \quad (5.45a)$$

$$I_{in}(x, t) = -\frac{\pi a^2}{\rho_{elec,ax}} \frac{\partial \psi_m}{\partial x}(x, t) \quad (5.45b)$$

where  $T_{fin}$  is the length of the simulation time and the ion current density  $j_m^{ion}$ .

The boundary conditions corresponding to the configuration shown in Figure 5.14 are:

$$\psi_m(0, t) = \bar{V}_{in}(t) \quad t \in (0, T_{fin}) \quad (5.46a)$$

$$-I_{in}(L, t) + \frac{1}{R_{out}}\psi_m(L, t) = 0 \quad t \in (0, T_{fin}) \quad (5.46b)$$

while the initial condition is

$$\psi_m(x, 0) = \psi_m^0(x) \quad x \in (0, L). \quad (5.46c)$$

We note that if the longitudinal resistivity of the cable  $\rho_{elec,ax} \rightarrow +\infty$  then the cable equation model degenerates into the ODE formulation.

“Notes” — 2019/5/17 — 17:39 — page 104 — #112

## CHAPTER 6

# Reduced order model for cellular functions: the Astrocyte calcium dynamics example

The chapter is devoted to the derivation of a mathematical model based on ordinary differential equations (ODEs) to describe the temporal evolution of the concentration of physical quantities averaged over the volume of a specific subregion of a cell. Then we apply the ODE formulation to describe the dynamics of  $Ca^{++}$  ions in the astrocyte.

### 6.1. Reduced models for cell functionalities

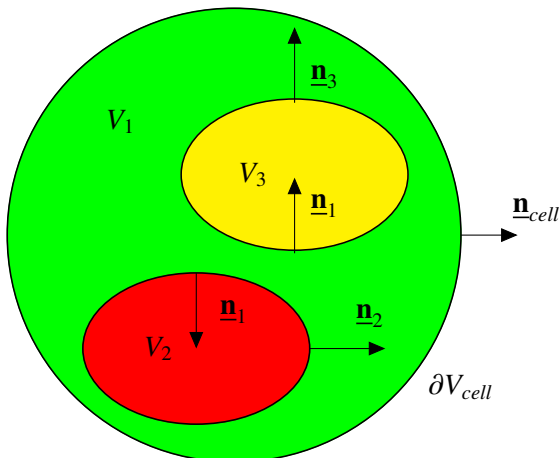


**Figure 6.1** Schematic representation of a cell.  $V_{cell}$  is the three-dimensional fixed region of space occupied by the cell. In this simplified picture, the volume of the cell is divided into  $M_{reg} = 3$  subregions, denoted by  $V_i$ ,  $i = 1, \dots, M_{reg}$ . The vectors  $\underline{n}_i$  denote the unit outward normal vectors on the boundary  $\partial V_i$  of the volume  $V_i$ . The vector  $\underline{n}_{cell}$  is the unit outward normal vector on the surface of the cell  $\partial V_{cell}$ .

Let us denote by  $V_{cell} \subset \mathbb{R}^3$  the three-dimensional region of space occupied by a

given cell (see Figure 6.1). For the sake of simplicity, we will assume that  $V_{cell}$  does not change in time. We denote by  $\partial V_{cell}$  the smooth two-dimensional surface representing the boundary of  $V_{cell}$ , by  $\underline{\mathbf{n}}_{cell}$  the unit outward normal vector on  $\partial V_{cell}$  and by  $|V_{cell}|$  the positive number representing the volume of the cell. We may think of the considered cell as an astrocyte, a smooth muscle cell, a neuron or any other type of cell in the human body. The cell region  $V_{cell}$  can be divided into the union of a finite number  $M_{reg}$  of three-dimensional subregions  $V_k$ , with  $k \in \mathcal{L}_{reg}$ , where  $\mathcal{L}_{reg}$  is the index set of the subregions of dimension  $M_{reg}$ . Each subregion  $V_k$  has a specific biophysical function, and may correspond to the cytosol, the sarcoplasmic/endoplasmic reticulum, the organelles (e.g., mitochondria) and the nucleus, to name a few. In the scheme of Figure 6.1 we have  $M_{reg} = 3$  and

$$\mathcal{L}_{reg} = \{1, 2, 3\}.$$

Let now consider the following general balance laws in a local form associated with a given ion, enzyme or chemical species whose concentration is  $C = C(\underline{\mathbf{x}}, t)$  with  $\underline{\mathbf{x}} \in V_{cell}$  and  $t \in (0, T)$ .

$$\frac{\partial C}{\partial t}(\underline{\mathbf{x}}, t) + \nabla_{\underline{\mathbf{x}}} \cdot \underline{\mathbf{J}}(\underline{\mathbf{x}}, t) = \beta(\underline{\mathbf{x}}, t) \quad \forall \underline{\mathbf{x}} \in \Omega_t, \forall t \in (0, T). \quad (6.1)$$

where  $\underline{\mathbf{J}}(\underline{\mathbf{x}}, t)$  is the flux of  $C = C(\underline{\mathbf{x}}, t)$  associated to the boundary  $\partial V_k$  and  $\beta(\underline{\mathbf{x}}, t)$  is the net production rate within  $V_k$ . Let integrate (6.1) over  $V_k$  and divide by  $|V_k|$  that is the volume of the region  $V_k$ .

Let now define the spatial average  $u_k = u_k(t)$  of the concentration over the subregion  $V_k$  as

$$u_k(t) := \frac{\int_{V_k} C(\underline{\mathbf{x}}, t) dV_k}{|V_k|} \quad k \in \mathcal{L}_{reg}, t \in (0, T) \quad (6.2)$$

Next, applying the divergence theorem (A.1) to the second term of the integrated (6.1), we obtain

$$\frac{du_k(t)}{dt} = \frac{\int_{V_k} \beta(\underline{\mathbf{x}}, t) dV_k}{|V_k|} - \frac{\int_{\partial V_k} \underline{\mathbf{J}}(\underline{\mathbf{x}}, t) \cdot \underline{\mathbf{n}}_k d(\partial V_k)}{|V_k|} \quad k \in \mathcal{L}_{reg}, t \in (0, T) \quad (6.3)$$

where  $\underline{\mathbf{n}}_k$  is the unit outward normal vector on the boundary  $\partial V_k$  of the subregion  $V_k$ . Finally, we introduce the following definitions:

$$b_k(t) := \frac{\int_{V_k} \beta(\underline{\mathbf{x}}, t) dV_k}{|V_k|} \quad k \in \mathcal{L}_{reg}, t \in (0, T) \quad (6.4a)$$

$$j_k(t) := \frac{\int_{\partial V_k} \underline{\mathbf{J}}(\underline{\mathbf{x}}, t) \cdot \underline{\mathbf{n}}_k d(\partial V_k)}{|V_k|} \quad k \in \mathcal{L}_{reg}, t \in (0, T). \quad (6.4b)$$

The quantity  $b_k = \beta_k(t)$  is the *average net production rate* of the considered chemical component in the subregion  $V_k$ . The quantity  $J_k = j_k(t)$  is the *average net flux* of the considered chemical component across the boundary of the subregion  $V_k$ . Both  $\beta_k$  and  $j_k$  have the units of a concentration per unit time. Definitions (6.4) allow us to write relation (6.3) in the following concise form

$$\frac{du_k(t)}{dt} = b_k(t) - J_k(t) \quad k \in \mathcal{L}_{reg}, t \in (0, T). \quad (6.5)$$

Relation (6.5) is an ordinary differential equation (ODE) that describes the evolution of the considered chemical component, spatially averaged in the subregion  $V_k$ . To solve it, we need specify, for each  $k \in \mathcal{L}_{reg}$ :

- *constitutive relations* for  $b_k$  and  $J_k$ , which depend on the considered chemical species and on the region  $V_k$ ,  $k \in \mathcal{L}_{reg}$ . Thus, the explicit characterization of constitutive relations can be done only on the basis of the knowledge of the specific problem at hand;
- *the initial condition*  $u_k^0 = u_k(0)$ ,  $k \in \mathcal{L}_{reg}$ . The initial condition in biological applications is often the so-called *baseline value* of the considered chemical species. This value is mathematically defined as the steady-state solution of (6.5) obtained when all the inputs are set equal to their physiological values.

## 6.2. Mathematical model of cytosolic calcium dynamics

In this section we employ the approach illustrated in Section 6.1 to derive a mathematical model describing the evolution of the concentration of the calcium ion in the cytosol of an astrocyte schematically represented in Figure 6.2. Thus, here we have  $M_{reg} = 2$ , with the two subregions representing the cytosol (green area) and the endoplasmic reticulum (yellow area), so that we can write  $\mathcal{L}_{reg} = \{Cyt, ER\}$ .

Let us start from the averaged balance law (6.5) and let us assume that  $b_k(t) \equiv 0$ ,  $k \in \mathcal{L}_{reg}$ . This corresponds to assuming that the calcium dynamics is regulated only by the influx and outflux of calcium through the cell membrane and the ER, and not by net production mechanisms occurring inside the volumes  $V_{cyt}$  and  $V_{ER}$ . According to the scheme of Figure 6.2, we assume that there are five biophysical mechanisms determining the average net flux of calcium in the cytosol:

1. *calcium flux through transmembrane calcium channels*. These channels are characterized by a passive transport of calcium ions and are triggered by the difference between the calcium concentration  $[Ca_{extra}]$  outside the cell (typically 2.5 – 5mM) and the free calcium concentration  $[Ca_{free}]$  inside the cytosol (typically 0.05 – 0.1μM), thereby producing the calcium flux  $J_{ch}$  from the extracellular site into the cytosol (influx);
2. *calcium flux through transmembrane calcium pumps mediated by adenosine triphosphate (ATP)*. These pumps produce an outflux  $J_{pump}$  of calcium from the cytosol

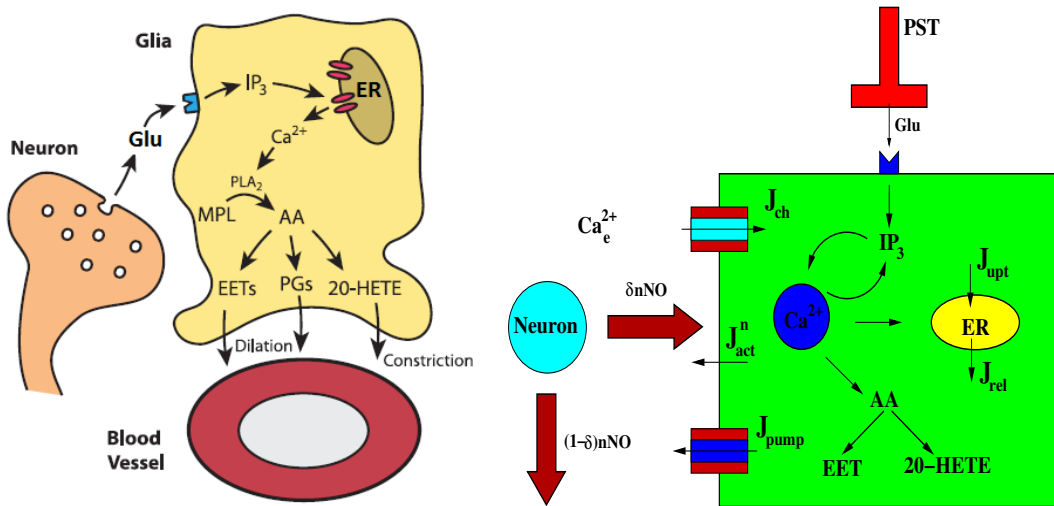


**Figure 6.2** Schematic representation of the system composed by an astrocyte and a neuron. PST: post-synaptic terminal. Glu: glutamate input stimulus.  $[IP_3]$ : inositol triphosphate. ER: endoplasmic reticulum. AA: arachidonic acid. EET: vasodilating agent. 20-HETE: vasoconstricting agent.  $J_{upt}$ : calcium flux uptake by the ER.  $J_{rel}$ : calcium flux release from ER. Calcium channel and calcium pump fluxes are represented by  $J_{ch}$  and  $J_{pump}$ , respectively.  $Ca_{\text{extra}}$ : calcium concentration in the extracellular site.  $Ca_{\text{free}}$ : free calcium concentration in the cytosol.  $Ca_{\text{ER}}$ : calcium concentration in the endoplasmic reticulum.  $J_{act}^n$ : active transport calcium flux in the intracellular site mediated by nNO.

into the extracellular site at the expense of consumption of ATP. This is an active mechanism and it is acting against the diffusion process that would naturally drive calcium ions from the extracellular site into the cell according to the Fick law;

3. *calcium uptake by the receptors localized over the ER membrane.* This mechanism is biophysically analogous to that regulating the transmembrane calcium pumps and produces an outflux  $J_{upt}$  of calcium from the cytosol into the ER, whose calcium concentration  $[Ca_{\text{ER}}]$  is typically  $2\mu\text{M}$ ; this mechanism is acting against the diffusion process that would naturally drive calcium ions from the ER into the cytosol according to Fick’s law;
4. *calcium release from the channels localized over the ER membrane.* This mechanism is biophysically analogous to that regulating the transmembrane calcium channels and produces an influx  $J_{rel}$  of calcium from the ER into the cytosol. However, unlike the calcium flux due to transmembrane calcium channels, calcium release from the ER into the cytosol is modulated by the level of inositol triphosphate  $[IP_3]$  that is produced by the glutamate receptors located on the cell membrane;
5. *active transport of calcium from the cytosol to the extracellular site mediated by the neuron nearby the astrocyte.* This mechanism is biophysically analogous to

that of calcium flux through transmembrane calcium pumps mediated by the concentration of adenosine triphosphate [ATP], except that in this case calcium flux  $J_{act}^n$  from the cytosol into the extracellular site is mediated by the fraction  $\delta[n\text{NO}]$  of the amount  $[n\text{NO}]$  produced by the neuron that is absorbed by the astrocyte,  $\delta$  being a parameter in the range  $[0, 1]$  (see Remark ??).

Constitutive relations for the calcium fluxes described above will be provided in Section 6.2.1.

Based on the theory developed in Section 6.1, using Remark ?? and the scheme in Figure 6.2, the mathematical model of the dynamics of the free calcium concentration  $[\text{Ca}_{\text{free}}]$  in the cytosol is represented by the following Cauchy problem:

$$\frac{d[\text{Ca}_{\text{free}}]}{dt} = \eta (J_{rel} - J_{upt} + J_{ch} - J_{pump} - J_{act}^n) \quad t \in (t_0, t_0 + T_w], \quad (6.6a)$$

$$[\text{Ca}_{\text{free}}](t_0) = [\text{Ca}_{\text{free}}]_0 \quad (6.6b)$$

where  $t_0$  is the initial time,  $T_w$  is the time of the observational time window and  $[\text{Ca}_{\text{free}}]_0$  is a nonnegative real number representing the initial datum. The number  $\eta$  represents the fraction of cytosolic Calcium that is not buffered within the cytosol:

$$[\text{Ca}_{\text{free}}] = \eta[\text{Ca}_{\text{cyt}}], \quad (6.7a)$$

The Cauchy problem (6.6) needs to be completed by constitutive laws for the fluxes on the right-hand side of (6.6a). This issue is addressed in the next section.

### 6.2.1. Constitutive relations for the cytosolic calcium fluxes

In this section, we follow the modeling choices adopted in [51] to characterize the fluxes  $J_{rel}$ ,  $J_{upt}$ ,  $J_{ch}$  and  $J_{pump}$ , whereas the constitutive relation for  $J_{act}^n$  is of the same form as that suggested in [69] to describe active calcium transport across the cell membrane.

The calcium flux release  $J_{rel}$  from the ER into the cytosol is given by

$$J_{rel} = J_{\text{Ca} \leftarrow \text{IP}_3} + J_{\text{leak}}. \quad (6.8a)$$

The first contribution on the right-hand side of (6.8a) is the  $[\text{IP}_3]$ -mediated calcium production. The second contribution on the right-hand side of (6.8a) is the passive calcium leak flux. Adopting the generalized Hodgkin-Huxley formalism, the  $[\text{IP}_3]$ -mediated calcium production term is expressed by the following set of equations:

$$J_{\text{Ca} \leftarrow \text{IP}_3} = c_1 v_1 x^3 y^3 z^3 ([\text{Ca}_{\text{ER}}] - [\text{Ca}_{\text{free}}]), \quad (6.8ba)$$

$$x = \frac{[\text{IP}_3]}{[\text{IP}_3] + d_1}, \quad (6.8bb)$$

$$y = \frac{[\text{Ca}_{\text{free}}]}{[\text{Ca}_{\text{free}}] + d_5}, \quad (6.8bc)$$

110 A comprehensive physically based approach to modeling in bioengineering and life sciences

$$\frac{dz}{dt} = \frac{z_\infty - z}{\tau_z}, \quad (6.8bd)$$

$$z_\infty = \frac{Q_2}{Q_2 + [\text{Ca}_{\text{free}}]}, \quad (6.8be)$$

$$\tau_z = \frac{1}{a_2(Q_2 + [\text{Ca}_{\text{free}}])}, \quad (6.8bf)$$

$$Q_2 = d_2 \left( \frac{[\text{IP}_3] + d_1}{[\text{IP}_3] + d_3} \right), \quad (6.8bg)$$

where  $x$ ,  $y$  and  $z$  represent the probabilities that the calcium activation,  $\text{IP}_3$  activation and calcium inhibition sites, respectively, are occupied.

Following [66], the passive calcium leak flux  $J_{\text{leak}}$  from ER to cytosol is assumed to be driven by the difference in calcium concentration between ER and cytosol and can be written as

$$J_{\text{leak}} = c_1 v_2 ([\text{Ca}_{\text{ER}}] - [\text{Ca}_{\text{free}}]) \quad (6.8c)$$

where  $v_2$  is a positive constant. The ATP-dependent uptake calcium flux  $J_{\text{upt}}$  from the cytosol to the ER is expressed by the Hill equation with  $p = 2$

$$J_{\text{upt}} = \frac{v_3 [\text{Ca}_{\text{free}}]^2}{[\text{Ca}_{\text{free}}]^2 + k_3^2} \quad (6.8d)$$

$v_3$  and  $k_3$  being positive constants.

As in the case of the passive calcium leak flux  $J_{\text{leak}}$ , following [66], we assume the mechanism driving the calcium flux  $J_{\text{ch}}$  across transmembrane channels to depend on the difference in calcium concentration between the extracellular medium and the cytosol, so that the constitutive law for  $J_{\text{ch}}$  is given by

$$J_{\text{ch}} = v_{\text{ch}} ([\text{Ca}_{\text{extra}}] - [\text{Ca}_{\text{free}}]) \quad (6.8e)$$

where  $v_{\text{ch}}$  is a positive constant and  $[\text{Ca}_{\text{extra}}$ ] is the calcium concentration in the extracellular site, which we assume to be a positive constant quantity.

The calcium flux from the cytosol into the extracellular site due to the action of ATP-dependent membrane pumps is described by the Hill equation with  $p = 2$

$$J_{\text{pump}} = \frac{v_{\text{pump}} [\text{Ca}_{\text{free}}]^2}{[\text{Ca}_{\text{free}}]^2 + k_{\text{pump}}^2} \quad (6.8f)$$

$v_{\text{pump}}$  and  $k_{\text{pump}}$  being positive constants.

Finally, the active transport of calcium from the cytosol to the extracellular site mediated by the absorption of the NO produced by the neuron nearby (nNO) is described

as in [69] by the following relations:

$$J_{act}^n = \alpha_{ast}([nNO])[Ca_{free}], \quad (6.8ga)$$

$$\alpha_{ast}([nNO]) = \alpha_1^{ast} + k_1^{ast}\delta[nNO], \quad (6.8gb)$$

where  $\alpha_1^{ast}$  and  $k_1^{ast}$  are positive constants and  $\delta$  is a given value in the interval  $[0, 1]$ .

### 6.2.2. Model of $IP_3$ dynamics

In neurons and glial cells the concentration of  $[IP_3]$  is not constant in time because of the presence of glutamate receptors in the cell membrane that are responsible of the so-called calcium sparks (see [27]). To take into account also this mechanism we need to consider a balance equation for the inositol triphosphate molecule. Following [51], this balance reads as:

$$\frac{d[IP_3]}{dt} = J_{IP_3 \leftarrow Glu} + J_{IP_3 \leftarrow Ca_{free}} - \frac{1}{\tau_r}([IP_3] - [IP_3]^*) \quad t \in (t_0, t_0 + T_w], \quad (6.8a)$$

$$[IP_3](t_0) = [IP_3]_0, \quad (6.8b)$$

where  $[IP_3]_0$  is the initial datum for  $IP_3$ . The flux  $J_{IP_3 \leftarrow Glu}$  represents the production of  $[IP_3]$  due to glutamate receptors located on the cell membrane, the flux  $J_{IP_3 \leftarrow Ca_{free}}$  represents the production of  $[IP_3]$  mediated by the free cytosolic calcium, whereas the third term on the right-hand side of (6.8a) mathematically expresses relaxation of  $[IP_3]$  to its reference value  $[IP_3]^*$  with a relaxation time constant equal to  $\tau_r$ . Below, we illustrate the constitutive relations for the fluxes on the right-hand side of (6.8a) that have been proposed in [51] on the basis of physiological and experimental considerations.

The flux  $J_{IP_3 \leftarrow Glu}$  is modeled by the following Hill equation

$$J_{IP_3 \leftarrow Glu} = \frac{v_g [Glu]^p}{k_g^p + [Glu]^p}, \quad (6.9a)$$

where  $[Glu]$  is the glutamate concentration and  $v_g$ ,  $k_g$  and  $p$  are given constants. The flux  $J_{IP_3 \leftarrow Ca_{free}}$  is modeled by a modified Contois equation (see [28])

$$J_{IP_3 \leftarrow Ca_{free}} = \tilde{v} \left( \frac{[Ca_{free}] + (1 - \alpha)k_4}{[Ca_{free}] + k_4} \right), \quad (6.9b)$$

where  $\alpha$  and  $k_4$  are given constants, whereas  $\tilde{v}$  depends on  $[Glu]$  as follows

$$\tilde{v} = v_4 + \alpha_4[Glu]. \quad (6.9c)$$

### 6.2.3. Simulation of the dynamics of free cytosolic calcium in an astrocyte

In this section we numerically investigate the model constituted by Equations (6.6), (6.8), (6.8) and (6.9), in the simulation of the dynamics of free cytosolic calcium and

inositol triphosphate. We will start by defining the baseline conditions of the cell (see Section 6.1), which will then be used as initial conditions for the simulation of the cell dynamic behavior upon application of: (i) a glutamate (Glu) input signal produced by a post-synaptic terminal (PST); and neglecting the effect of (ii) neuronal nitric oxide (nNO) i.e.  $j_{act}^n = 0$ .

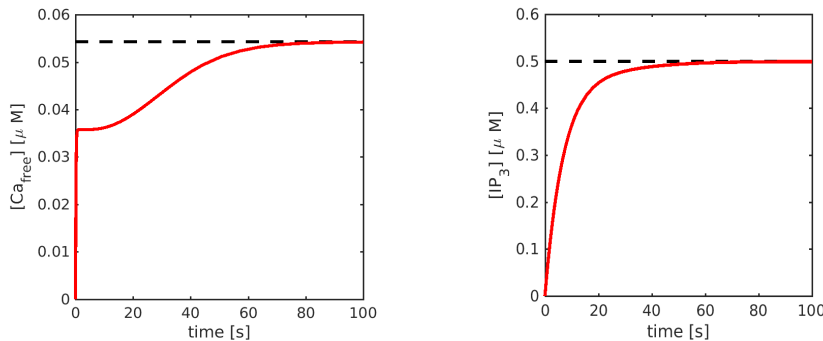


**Figure 6.3** Left panel: cytosolic free calcium evolution. Right panel: inositol triphosphate evolution. In both panels, the dashed black lines indicate the baseline values obtained by solving the time-independent problem, whereas the blue curves represent the evolution to steady-state of the time-dependent solution, as illustrated in Section ???. The results reported in this figure have been obtained by setting the external stimuli equal to their baseline values for all the simulation time, namely,  $[Glu] = [Glu]_b = 0 \mu M$  and  $[nNO] = [nNO]_b = 0.1 \mu M$ .

To determine the baseline values  $[Ca_{free}]_b$  and  $[IP_3]_b$  of the free cytosolic calcium concentration and  $IP_3$  it is possible to follow two different approaches. In the first approach, we solve the nonlinear system of algebraic equations obtained by setting equal to zero the time derivatives in Equations (6.6) and (6.8). In the second approach we solve the coupled system of ODEs associated with Equations (6.6), (6.8), (6.8) and (6.9), with the initial conditions:

$$[Ca_{free}](t_0) = [IP_3](t_0) = 0 \mu M,$$

until steady-state conditions are reached.

The two methods calculates the same of  $[Ca_{free}]_b = 5.43 \cdot 10^{-2} \mu M$  and  $[IP_3]_b = 4.99 \cdot 10^{-1} \mu M$ . It is important to check that the model reproduces the correct biophysical baseline value of the quantities under investigation.

By numerically solving the ODE system constituted by Equations (6.6), (6.8), (6.8) and (6.9), using the model parameters listed in Tables 6.1, 6.2 and 6.3 it is possible to look at the dynamics of free cytosolic calcium and  $IP_3$  as a function of the Glutamate stimuli.

We set  $t_0 = 0$ s and  $T_w = 300$ s and the initial conditions are  $[Ca_{free}](t_0) = [Ca_{free}]_b$

Symbol	Description	Value	Source
$[Ca_t]$	Total concentration of calcium in an astrocyte	$2.0 \mu M$	[51, 29]
$a_2$	Calcium inhibition constant	$0.14 \mu M^{-1}s^{-1}$	[51, 119]
$c_1$	ER-to-cytosol volume ratio	0.185	[51, 29]
$d_1$	IP <sub>3</sub> disassociation constant	$0.13 \mu M$	[51, 119]
$d_2$	disassociation constant for calcium inhibition	$1.049 \mu M$	[51, 119]
$d_3$	IP <sub>3</sub> disassociation constant	$0.9434 \mu M$	[51, 119]
$d_5$	Calcium activation constant	$0.082 \mu M$	[51, 119]
$k_3$	Half-saturation point for calcium pump	$0.1 \mu M$	[51, 74]
$v_1$	Maximum calcium channel flux (ER-to-cytosol)	$6.0 s^{-1}$	[51, 119]
$v_2$	Calcium leak constant (ER-to-cytosol)	$0.11 s^{-1}$	[51, 119]
$v_3$	Maximum calcium pump capacity (ER-to-cytosol)	$2.2 \mu M s^{-1}$	[51, 119]
$K_D$	Buffer disassociation constant	$20 \mu M$	[51, 120]
$B_T$	Total buffer concentration	$10 \mu M$	[51, 120]

**Table 6.1** Parameter values for free cytosolic calcium in the model that describes the coupled evolution of free cytosolic calcium and IP<sub>3</sub>.

Symbol	Description	Value	Source
[IP <sub>3</sub> ] <sup>*</sup>	Reference concentration of inositol triphosphate	$0.16 \mu M$	[51, 119]
$\tau_r$	IP <sub>3</sub> loss constant	7.14 s	[51, 119]
$v_g$	Rate of IP <sub>3</sub> production by glutamate	$0.062 \mu M s^{-1}$	[51, 119]
$k_g$	Glutamate stimulation of IP <sub>3</sub>	$0.78 \mu M$	[51, 119]
$p$	Hill coefficient for IP <sub>3</sub> production via glutamate	0.3	[51, 119]
$\alpha$	Relative weighting of the two IP <sub>3</sub> production pathways	0.8	[51, 119]
$k_4$	Disassociation constant for calcium stimulation of IP <sub>3</sub>	$1.1 \mu M$	[51, 74]
$v_4$	Maximum production rate of IP <sub>3</sub>	$0.2 \mu M s^{-1}$	[51, 119]

**Table 6.2** Parameter values for IP<sub>3</sub> in the model that describes the coupled evolution of free cytosolic calcium and IP<sub>3</sub>.

and  $[IP_3](t_0) = [IP_3]_b$ .

To this purpose, the glutamate stimulus is set equal to three different values, equal to 1, 5 and  $10 \mu M$ , in the time interval  $t \in (50, 150)$  s and to its baseline value (zero) elsewhere.

Results are shown in Figures 6.4 and 6.5. First of all we note that in all cases after the glutamate stimulus is switched off, the free cytosolic calcium and IP<sub>3</sub> return to their baseline values. The black lines report the case where the glutamate stimulus is at the baseline value: as expected, both free cytosolic calcium and IP<sub>3</sub> concentrations remain at their baseline values. The blue lines report the case where the glutamate stimulus is

Symbol	Description	Value
$v_{ch}$	Rate of passive transmembrane calcium flux	$2 \cdot 10^{-5} \text{ s}^{-1}$
$[\text{Ca}_{\text{extra}}]$	extracellular calcium concentration	$2 \cdot 10^3 \mu\text{M}$
$v_{\text{pump}}$	Maximum calcium pump capacity (cytosol-to-extracellular site)	$2.2 \mu\text{Ms}^{-1}$
$k_{\text{pump}}$	Half-saturation point for calcium pump	$0.1 \mu\text{M}$
$\alpha_1^{\text{ast}}$	Rate of nNO-mediated calcium flux	$0.05 \text{ s}^{-1}$
$k_1^{\text{ast}}$	Rate of nNO-mediated calcium flux per unit of concentration	$0.015 \mu\text{Ms}^{-1}$
$\delta$	nNO fraction absorbed by an astrocyte	0.98
$\alpha_4$	Relative weighting of the two $\text{IP}_3$ production pathways	$0.03 \text{ s}^{-1}$

**Table 6.3** Further parameter values for free cytosolic calcium and  $\text{IP}_3$  in the model that describes the coupled evolution of free cytosolic calcium and  $\text{IP}_3$ .

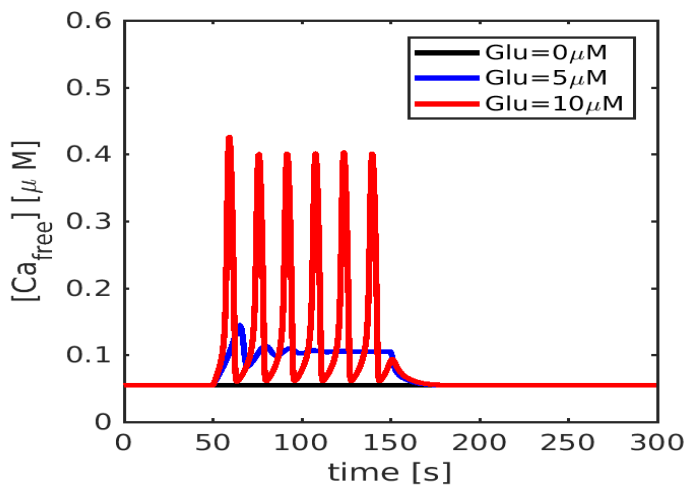


**Figure 6.4** Time evolution of cytosolic free calcium. The dashed black line indicates the baseline value  $[\text{Ca}_{\text{free}}]_b$ . Results are obtained in the case where the neuronal NO stimulus is equal to its baseline value for all the simulation time and the glutamate stimulus is equal to  $1, 5, 10 \mu\text{M}$  in the time interval  $t \in (50, 150) \text{ s}$  and zero elsewhere.

set at the value of  $5 \mu\text{M}$ : the free cytosolic calcium and  $\text{IP}_3$  concentrations increase but no oscillations are found. The red lines report the case where the glutamate stimulus is set at the value of  $10 \mu\text{M}$ : the free cytosolic calcium and  $\text{IP}_3$  concentrations significantly increase and, moreover, oscillations are found in agreement with what reported in [51]. As a final comment, we note that the variation of the free calcium concentration during the stimulus is in the range of 1 order of magnitude with respect to its baseline value  $[\text{Ca}_{\text{free}}]_b$  whereas the  $\text{IP}_3$  concentration becomes about 3 times higher than its baseline value  $[\text{IP}_3]_b$ .

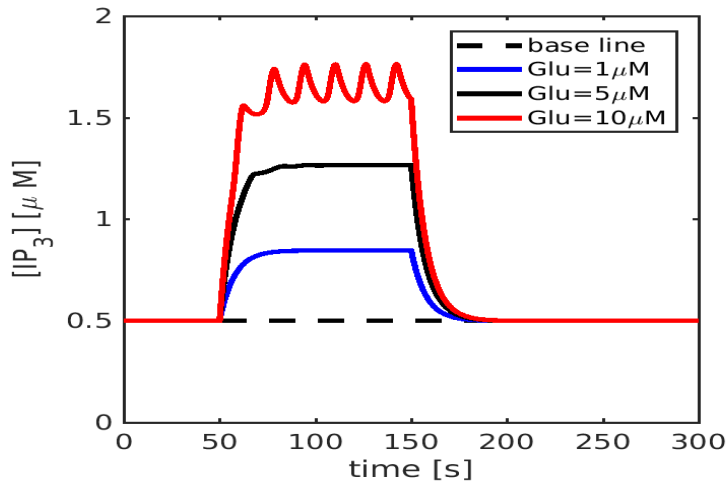


**Figure 6.5** Time evolution of  $IP_3$ . The dashed black line indicates the baseline value  $[IP_3]_b$ . Results are obtained in the case where the neuronal NO stimulus is equal to its baseline value for all the simulation time and the glutamate stimulus is equal to  $1, 5, 10 \mu M$  in the time interval  $t \in (50, 150)$  s and zero elsewhere.

“Notes” — 2019/5/17 — 17:39 — page 116 — #124

## CHAPTER 7

# General approach to continuum media

To introduce the axiomatic approach to the continuum mechanics, for the sake of simplicity, we consider a Cartesian frame of reference and we refer the reader to specialized books in continuum mechanics, e.g., [46], for a more general geometrical framework. Thus, let us denote by  $O$  the origin of the Cartesian frame of reference and by  $\underline{\mathbf{e}}_i$ , with  $i = 1, 2, 3$ , the orthonormal basis vectors of  $\mathbb{R}^3$ .

### 7.1. Placements, material volumes, mass and material particles

We recall that in Chapter 2 we have introduced a simple model to describe the motion of a body  $\mathcal{B}$ , called *charged material point*, where all the mass and electric charge of the body are assumed to be concentrated in a zero-dimensional manifold, represented with a mathematical point. We would like to extend the description of body motion to account for the fact that mass and electric charge of  $\mathcal{B}$  are actually spread over a three-dimensional in a volume within the physical space.

A continuum  $\mathcal{B}$  can change its shape and deform during the motion, occupying a different region of space at each instant of time, as shown in Figure 7.1. This leads to the definition of placement given below.

**Definition 7.1.** *The placement (or configuration) of  $\mathcal{B}$  at time  $t$  is the region of space  $\Omega_t \subseteq \mathbb{R}^3$  that the body  $\mathcal{B}$  occupies at time  $t$ .*

**Remark 7.1.** *Unless otherwise stated, we will assume that  $\Omega_t$  is an open subset of  $\mathbb{R}^3$ , whose boundary  $\partial\Omega_t$  is smooth enough to admit a well-defined outward normal unit vector  $\underline{\mathbf{n}}_t$  at every point on the boundary and at every instant of time. In terms of differential geometry, this means that  $\partial\Omega_t$  is a differentiable manifold of dimension two in the three-dimensional space.*

Let us denote by  $\mathcal{P}$  any part of  $\mathcal{B}$ , even amounting to the whole  $\mathcal{B}$ . As it happens for  $\mathcal{B}$ , also  $\mathcal{P}$  can change its shape and deform during the motion, occupying a different region of space at each instant of time. This leads to the definition of material volume given below.

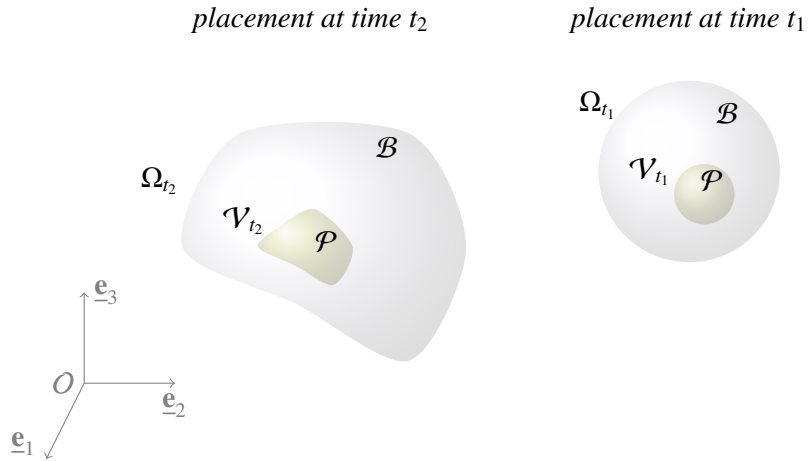


**Figure 7.1** A body  $\mathcal{B}$  occupies the domain  $\Omega_{t_1}$  at time  $t_1$  and the domain  $\Omega_{t_2}$  at time  $t_2$ . Thus,  $\Omega_{t_1}$  and  $\Omega_{t_2}$  are two different placements of the same body  $\mathcal{B}$  at different times. Similarly, the domains  $\mathcal{V}_{t_1}$  and  $\mathcal{V}_{t_2}$  are two different placements of the same part  $\mathcal{P}$  within the body  $\mathcal{B}$  at different times.

**Definition 7.2.** *The placement of a given part  $\mathcal{P}$  of  $\mathcal{B}$  at time  $t$  is called **material volume** and is denoted by  $\mathcal{V}_t$ .*

**Remark 7.2.** *Unless otherwise stated, we will assume that  $\mathcal{V}_t$  is a measurable subset of  $\Omega_t$ . In the case where  $\mathcal{P}$  is the whole body, namely  $\mathcal{P} \equiv \mathcal{B}$ , we have  $\mathcal{V}_t \equiv \Omega_t$ .*

The region (or domain)  $\Omega_t$  can be described as a parametrized set of points. Thus, we also know that each mathematical point in  $\Omega_t$  can be identified by a vector  $\underline{x}$ . However, the main question is: *what is the physical meaning of the mathematical point indicated by the position  $\underline{x}$ ?* Should we think of a continuum as a collection of charged material points, whose definition was given in Chapter 2? The answer is obviously no, since a *charged material point*, by itself, is a model for the *whole body* where the whole body mass and electric charge are assumed to be concentrated in one point.

The basic assumption underlying the continuum approach can be formalized mathematically as follows.

**Assumption 7.1.** *The mass  $M$  and the electric charge  $Q$  of the body  $\mathcal{B}$  are absolutely continuous functions of the volume. Thus, thanks to the Fundamental Theorem of Lebesgue Integral Calculus, any part  $\mathcal{P}$  of the body  $\mathcal{B}$  at time  $t$  contains a mass  $M(\mathcal{P}, t)$  and an electric charge  $Q(\mathcal{P}, t)$  that can be expressed as the Lebesgue integral of density*

functions, denoted by  $\rho$  and  $\zeta$  respectively, leading to

$$M(\mathcal{P}, t) = \int_{\mathcal{V}_t} \rho dV_t \quad \text{and} \quad Q(\mathcal{P}, t) = \int_{\mathcal{V}_t} \zeta dV_t \quad (7.1)$$

where the material volume  $\mathcal{V}_t$  represents the placement of the part  $\mathcal{P}$  at time  $t$ . We refer to  $\rho$  and  $\zeta$  as mass density and electric charge density, respectively.

Equation (7.1) shows that the density  $\rho$  is a mass per unit volume and that the density  $\zeta$  is an electric charge per unit volume, as we are used to learn in physics. We remark that, if the system is closed, then mass and electric charge of any part  $\mathcal{P}$  are constant with respect to time. At this stage, results from measure theory are extremely helpful to fully grasp the physical meaning of the mathematical point identified by the position vector  $\underline{x}$  in the continuum framework. At almost every  $\underline{x} \in \mathcal{V}_t$ , the mass density is the ultimate ratio of mass to volume in the following sense:

**Lemma 7.1.** *If  $\mathcal{P}_k$ ,  $k \geq 0$ , is a suitably chosen sequence of nested parts,  $\mathcal{P}_{k+1} \subset \mathcal{P}_k$ , such that (i) all the  $\mathcal{P}_k$  have a single substantial point in common, identified by the vector  $\underline{x}$  at time  $t$ , and that (ii) the measure of the volume  $\mathcal{V}_t^k$  occupied by  $\mathcal{P}_k$  at time  $t$  vanishes as  $k$  goes to infinity, namely  $|\mathcal{V}_t^k| \rightarrow 0$  as  $k \rightarrow \infty$ , then*

$$\rho(\underline{x}, t) = \lim_{k \rightarrow \infty} \frac{M(\mathcal{P}_k, t)}{|\mathcal{V}_t^k|} \quad \zeta(\underline{x}, t) = \lim_{k \rightarrow \infty} \frac{Q(\mathcal{P}_k, t)}{|\mathcal{V}_t^k|}. \quad (7.2)$$

An important consequence of Lemmas 7.1 is that we are allowed to assign a mass density  $\rho(\underline{x}, t)$  and an electric charge density  $\zeta(\underline{x}, t)$  to each mathematical point of  $\Omega_t$  identified by the vector  $\underline{x}$ . This leads to the definition of charged material particle given below.

**Definition 7.3.** *A charged material particle identified by the position vector  $\underline{x}$  is an infinitesimally small volume of material characterized by the mass density  $\rho(\underline{x}, t)$  and an electric charge density  $\zeta(\underline{x}, t)$  in the sense of Lemma 7.1. Thus, in the spirit of the integral definition of mass and electric charge given in Equation (7.1), the volume occupied by a charged material particle can be denoted by  $dV_t$  and should be thought of as an infinitesimally small volume centered at  $\underline{x}$  at a given time  $t$ .*

In conclusion, we should not think of the continuum body  $\mathcal{B}$  as a collection of charged material points; rather, we should think of the continuum body  $\mathcal{B}$  as a collection of charged material particles, namely infinitesimally small volumes within which mass and electric charge are distributed according to a mass density function  $\rho(\underline{x}, t)$  and an electric charge density function  $\zeta(\underline{x}, t)$  in the sense of Lemma 7.1. Thus, we can state that the vector  $\underline{x}$  in the continuum approach represents the position vector of a charged material particle, in the sense of Definition 7.3.

We began this chapter by stating that matter is particulate in nature and yet we assumed that mass and electric charge are absolutely continuous functions, see Assump-

tion 7.1. Indeed, the relationship between particulate nature and continuum description of matter deserves a closer look.

Let us assume that a volume  $V$  is filled with many little charged spheres with a small radius  $r$  such that their volume  $V_{sphere} = \frac{4}{3}\pi r^3$  is much smaller than the dimensions of  $V$ . Each of these spheres represents a molecule of the matter under consideration. Let  $N$  be the total number of the little spheres,  $m_p$  be the mass of each sphere and  $qz_p$  be the electric charge of each sphere, where  $q$  is the elementary charge and  $z_p$  is the valence of the charged spheres. The total mass  $M_{tot}$  of the spheres contained in  $V$  can be calculated as  $M_{tot} = m_p N$ . Analogously, the total electric charge  $Q_{tot}$  of the spheres contained in  $V$  can be calculated as  $Q_{tot} = qz_p N$ . Then, in this particulate perspective, the densities of mass and electric charge, denoted by  $\tilde{\rho}$  and  $\tilde{\zeta}$ , respectively, can be computed as the ratios

$$\tilde{\rho} = \frac{M_{tot}}{V} = \frac{m_p N}{V} \quad \text{and} \quad \tilde{\zeta} = \frac{Q_{tot}}{V} = \frac{qz_p N}{V}, \quad (7.3)$$

whereas, adopting a continuum description of matter, mass and electric charge densities have been defined as

$$\rho(\underline{x}, t) = \lim_{k \rightarrow \infty} \frac{M(\mathcal{P}_k, t)}{|\mathcal{V}_t^k|} \quad \text{and} \quad \zeta(\underline{x}, t) = \lim_{k \rightarrow \infty} \frac{Q(\mathcal{P}_k, t)}{|\mathcal{V}_t^k|} \quad (7.4)$$

as stated in Lemma 7.1. Even though, effectively, we can write Relationships (7.3) and (7.4) hide a profound conceptual difference. Specifically, by proceeding as in (7.3), we acknowledge the distinct presence of all the  $N$  spheres in  $V$ , thereby adopting a discrete viewpoint. On the other hand, when proceeding as in (7.4), we conceptually replace all the spheres with a single body. Thus, in the continuum viewpoint, the spheres cannot be distinguished anymore, regardless of how much we zoom in a single point, as all the mass is effectively smeared over the volume.

## 7.2. Balance law in integral form

A balance law provides an abstract expression for the budget of fluxes, sources and sinks that may alter the total amount of a certain physical quantity in a region of space. Adopting a similar perspective as that outlined in [112], we will focus on balance laws for *scalar physical quantities* (specifically densities of mass, electric charge and energy) and *vector-valued physical quantities* (specifically densities of linear and angular momentum) defined on a material volume  $\mathcal{V}_t$ , namely the region of space occupied at time  $t$  by the part  $\mathcal{P}$  of the body  $\mathcal{B}$ .

### 7.2.1. Balance law in integral form for a scalar physical quantity

**Definition 7.4.** Let  $\Psi = \Psi(\underline{\mathbf{x}}, t)$  be a scalar physical quantity expressed in the Eulerian framework. Then, the balance law for  $\Psi$  takes the form

$$\frac{d}{dt} \int_{\mathcal{V}_t} \Psi(\underline{\mathbf{x}}, t) dV_t = \int_{\partial\mathcal{V}_t} (\underline{\gamma} \cdot \underline{\mathbf{n}})(\underline{\mathbf{x}}, t) d(\partial V_t) + \int_{\mathcal{V}_t} \beta(\underline{\mathbf{x}}, t) dV_t \quad (7.5)$$

where  $\mathcal{V}_t$  is a material volume (see Definition 7.2) and  $\underline{\mathbf{n}}(\underline{\mathbf{x}}, t)$  is the outward unit normal vector at the point  $\underline{\mathbf{x}}$  on  $\partial\mathcal{V}_t$ . The vector field  $\underline{\gamma}(\underline{\mathbf{x}}, t)$  and the scalar field  $\beta(\underline{\mathbf{x}}, t)$  model the dynamics of  $\Psi$  through the boundary  $\partial\mathcal{V}_t$  and in the interior of  $\mathcal{V}_t$ , respectively.

To better understand the meaning of each contribution in (7.5), we denote by  $\mathcal{A}$  the total amount of  $\Psi$  in  $\mathcal{V}_t$ , namely

$$\mathcal{A}(t) := \int_{\mathcal{V}_t} \Psi(\underline{\mathbf{x}}, t) dV_t,$$

and by  $\mathcal{G}_1(t)$  and  $\mathcal{G}_2(t)$  the boundary and volume integrals on the right-hand side of (7.5), namely

$$\mathcal{G}_1(t) := \int_{\partial\mathcal{V}_t} (\underline{\gamma} \cdot \underline{\mathbf{n}})(\underline{\mathbf{x}}, t) d(\partial V_t) \quad \text{and} \quad \mathcal{G}_2(t) := \int_{\mathcal{V}_t} \beta(\underline{\mathbf{x}}, t) dV_t.$$

The balance law (7.5) can now be rewritten as

$$\frac{d}{dt} \mathcal{A}(t) = \mathcal{G}_1(t) + \mathcal{G}_2(t). \quad (7.6)$$

It is useful to notice that:

- if all the boundary contributions sum to zero, namely  $\mathcal{G}_1(t) \equiv 0$ , then the balance law (7.6) reduces to

$$\frac{d}{dt} \mathcal{A}(t) = \mathcal{G}_2(t) = \int_{\mathcal{V}_t} \beta(\underline{\mathbf{x}}, t) dV_t \quad (7.7)$$

implying that  $\mathcal{A}(t)$  increases or decreases with time depending on whether  $\mathcal{G}_2(t) > 0$  or  $\mathcal{G}_2(t) < 0$ , respectively. Thus, the scalar field  $\beta$  acts as a source or sink for the physical quantity  $\Psi$  inside the volume  $\mathcal{V}_t$  and leads to an increase or decrease of the total amount  $\mathcal{A}$  of  $\Psi$  in  $\mathcal{V}_t$ . For this reason,  $\beta$  is also known as *net production rate of  $\mathcal{A}$  per unit volume*;

- if all the volume contributions sum to zero, namely  $\mathcal{G}_2(t) \equiv 0$ , then the balance law (7.6) reduces to

$$\frac{d}{dt} \mathcal{A}(t) = \mathcal{G}_1(t) = \int_{\partial\mathcal{V}_t} (\underline{\gamma} \cdot \underline{\mathbf{n}})(\underline{\mathbf{x}}, t) d(\partial V_t) \quad (7.8)$$

implying that  $\mathcal{A}(t)$  increases or decreases with time depending on whether  $\mathcal{G}_1(t) >$

0 or  $\mathcal{G}(t)_1 < 0$ , respectively. Thus, the scalar field  $\gamma \cdot \underline{n}$  leads to a gain or a loss of the physical quantity  $\Psi$  through the boundary  $\partial\bar{\mathcal{V}}_t$  and leads to an increase or decrease of the total amount  $\mathcal{A}$  of  $\Psi$  in the interior of  $\mathcal{V}_t$ .

### 7.2.1.1. Balance of mass

As stated in Equation (7.1), under the assumptions of continuum mechanics, the mass  $M(\mathcal{P}, t)$  of any part  $\mathcal{P}$  of the body  $\mathcal{B}$  occupying the material volume  $\mathcal{V}_t \subseteq \Omega_t$  at time  $t$  can be written as

$$M(\mathcal{P}, t) = \int_{\mathcal{V}_t} \rho(\underline{x}, t) d\mathcal{V}_t. \quad (7.9)$$

Thus, in order to write the balance law for mass we need to utilize (7.5) with  $\Psi(\underline{x}, t) = \rho(\underline{x}, t)$  and  $\mathcal{A}(t) = M(\mathcal{P}, t)$ . It is important to emphasize that:

- Equation (7.5) is written on a material volume  $\mathcal{V}_t$ , meaning that we are following the same part  $\mathcal{P}$  of the body  $\mathcal{B}$  during the motion. Thus, the boundary of  $\mathcal{V}_t$  moves with the mass contained in it, thereby implying that  $\underline{\gamma} = \underline{0}$  in the case when  $\Psi(\underline{x}, t) = \rho(\underline{x}, t)$ ;
- changes of mass within the volume of  $\mathcal{V}_t$  are, in general, possible due to potential injections or subtractions of mass within  $\mathcal{V}_t$  through an external action on the system. This implies that, in general, the net production rate of mass per unit volume  $\beta \neq 0$ .

Thus, the balance of mass in integral form can be written as

$$\frac{d}{dt} \int_{\mathcal{V}_t} \rho(\underline{x}, t) d\mathcal{V}_t = \int_{\mathcal{V}_t} \beta(\underline{x}, t) d\mathcal{V}_t. \quad (7.10)$$

**Remark 7.3.** In a closed system, the net production rate of mass per unit volume is zero, thereby implying that  $\beta = 0$ . In this case, the balance law for mass reduces to the following equation for mass conservation

$$\frac{d}{dt} \int_{\mathcal{V}_t} \rho(\underline{x}, t) d\mathcal{V}_t = 0. \quad (7.11)$$

### 7.2.1.2. Balance of electric charge

As stated in Equation (7.1), under the assumptions of continuum mechanics, the electric charge  $Q(\mathcal{P}, t)$  of any part  $\mathcal{P}$  of the body  $\mathcal{B}$  occupying the material volume  $\mathcal{V}_t \subseteq \Omega_t$  at time  $t$  can be written as

$$Q(\mathcal{P}, t) = \int_{\mathcal{V}_t} \zeta(\underline{x}, t) d\mathcal{V}_t. \quad (7.12)$$

Thus, in order to write the balance law for electric charge we need to utilize (7.5) with  $\Psi(\underline{x}, t) = \zeta(\underline{x}, t)$  and  $\mathcal{A}(t) = Q(\mathcal{P}, t)$ . Since the electric charge, as well as mass, is an intrinsic property of matter and  $\mathcal{V}_t$  is a material volume, we have that  $\underline{\gamma} = \underline{0}$  also in the

case when  $\Psi(\underline{\mathbf{x}}, t) = \zeta(\underline{\mathbf{x}}, t)$ . Thus, the balance of electric charge in integral form can be written as

$$\frac{d}{dt} \int_{\mathcal{V}_t} \zeta(\underline{\mathbf{x}}, t) dV_t = \int_{\mathcal{V}_t} \pi(\underline{\mathbf{x}}, t) dV_t \quad (7.13)$$

where we utilized the symbol  $\pi(\underline{\mathbf{x}}, t)$  to denote the net production rate of electric charge per unit volume.

### 7.2.1.3. Balance of energy

The laws of thermodynamics summarized in Section 2.5 and the relationship between energy and power discussed in Section 2.4 led us to state that the time rate of change of the sum between kinetic energy  $\mathcal{K}$  and internal energy  $\mathcal{E}$  is balanced by the time rate of change of the heat  $Q$ , the power  $\Pi$  of forces acting on the system and the time rate of change of other types of energy  $\mathcal{U}_a$ , see Equation (2.35), so that we can write

$$\frac{d\mathcal{K}}{dt} + \frac{d\mathcal{E}}{dt} = \Pi_Q + \Pi + \sum_{\alpha} \Pi_{\mathcal{U}_a}. \quad (7.14)$$

Following [37, Chapter 4], the kinetic energy  $\mathcal{K}(\mathcal{P}, t)$  and the internal energy  $\mathcal{E}(\mathcal{P}, t)$  of any part  $\mathcal{P}$  of the body  $\mathcal{B}$  occupying the material volume  $\mathcal{V}_t \subseteq \Omega_t$  at time  $t$  can be written as

$$\mathcal{K}(\mathcal{P}, t) = \int_{\mathcal{V}_t} \frac{1}{2} \rho(\underline{\mathbf{x}}, t) \underline{\mathbf{v}}(\underline{\mathbf{x}}, t) \cdot \underline{\mathbf{v}}(\underline{\mathbf{x}}, t) dV_t = \int_{\mathcal{V}_t} \frac{1}{2} \rho(\underline{\mathbf{x}}, t) |\underline{\mathbf{v}}(\underline{\mathbf{x}}, t)|^2 dV_t \quad (7.15)$$

and

$$\mathcal{E}(\mathcal{P}, t) = \int_{\mathcal{V}_t} \rho(\underline{\mathbf{x}}, t) e(\underline{\mathbf{x}}, t) dV_t \quad (7.16)$$

respectively, where  $e(\underline{\mathbf{x}}, t)$  represents the internal energy per unit mass. In addition, we assume that the rates of change of heat, work and other forms of energy of any part  $\mathcal{P}$  of the body  $\mathcal{B}$  occupying the material volume  $\mathcal{V}_t \subseteq \Omega_t$  at time  $t$  can be written as:

$$\Pi_Q(\mathcal{P}, t) = \int_{\partial\mathcal{V}_t} (\underline{\mathbf{q}} \cdot \underline{\mathbf{n}})(\underline{\mathbf{x}}, t) d(\partial\mathcal{V}_t) + \int_{\mathcal{V}_t} \underline{\mathbf{r}}(\underline{\mathbf{x}}, t) dV_t \quad (7.17)$$

$$\Pi(\mathcal{P}, t) = \int_{\partial\mathcal{V}_t} (\underline{\boldsymbol{\pi}} \cdot \underline{\mathbf{n}})(\underline{\mathbf{x}}, t) d(\partial\mathcal{V}_t) + \int_{\mathcal{V}_t} \underline{\mathbf{p}}(\underline{\mathbf{x}}, t) dV_t \quad (7.18)$$

$$\Pi_{\mathcal{U}_a}(\mathcal{P}, t) = \int_{\partial\mathcal{V}_t} (\underline{\boldsymbol{\omega}} \cdot \underline{\mathbf{n}})(\underline{\mathbf{x}}, t) d(\partial\mathcal{V}_t) + \int_{\mathcal{V}_t} \underline{\mathbf{u}}(\underline{\mathbf{x}}, t) dV_t \quad (7.19)$$

respectively, where the vector fields  $\underline{\mathbf{q}}$ ,  $\underline{\boldsymbol{\pi}}$  and  $\underline{\boldsymbol{\omega}}$  have the units of  $\text{J m}^{-2} \text{ s}^{-1}$ , whereas the scalar fields  $r$ ,  $p$  and  $u$  have the units of  $\text{J m}^{-3} \text{ s}^{-1}$ . Upon setting:

$$\Psi(\underline{\mathbf{x}}, t) = \frac{1}{2}\rho(\underline{\mathbf{x}}, t)|\underline{\mathbf{v}}(\underline{\mathbf{x}}, t)|^2 + \rho(\underline{\mathbf{x}}, t)\epsilon(\underline{\mathbf{x}}, t) \quad (7.20)$$

$$\underline{\gamma}(\underline{\mathbf{x}}, t) = \underline{\mathbf{q}}(\underline{\mathbf{x}}, t) + \underline{\boldsymbol{\pi}}(\underline{\mathbf{x}}, t) + \underline{\boldsymbol{\omega}}(\underline{\mathbf{x}}, t) \quad (7.21)$$

$$\beta(\underline{\mathbf{x}}, t) = r(\underline{\mathbf{x}}, t) + p(\underline{\mathbf{x}}, t) + u(\underline{\mathbf{x}}, t) \quad (7.22)$$

we utilize (7.14) and (7.5) to write the energy balance law as

$$\begin{aligned} \frac{d}{dt} \int_{\mathcal{V}_t} \left( \frac{\rho(\underline{\mathbf{x}}, t)}{2} |\underline{\mathbf{v}}(\underline{\mathbf{x}}, t)|^2 + \rho(\underline{\mathbf{x}}, t) \epsilon(\underline{\mathbf{x}}, t) \right) d\mathcal{V}_t \\ = \int_{\partial\mathcal{V}_t} ((\underline{\mathbf{q}} + \underline{\boldsymbol{\pi}} + \underline{\boldsymbol{\omega}}) \cdot \underline{\mathbf{n}})(\underline{\mathbf{x}}, t) d(\partial\mathcal{V}_t) + \int_{\mathcal{V}_t} (r + p + u)(\underline{\mathbf{x}}, t) d\mathcal{V}_t. \end{aligned} \quad (7.23)$$

### 7.2.2. Balance laws in integral form for a vector-valued physical quantity

The balance law for a vector-valued physical quantity shares the same mathematical structure as that of Definition 7.4, where the physical quantity of interest and its net production rate are now vector fields, denoted by  $\underline{\Psi}$  and  $\underline{\beta}$ , respectively, and the boundary losses and gains are represented by a second order tensor, denoted by  $\underline{\Gamma}$  (see also [118], Chapter III, Section 5).

**Definition 7.5.** Let  $\underline{\Psi} = \underline{\Psi}(\underline{\mathbf{x}}, t)$  be a vector-valued quantity in the Eulerian framework. Then, the balance law for  $\underline{\Psi}$  takes the form

$$\frac{d}{dt} \int_{\mathcal{V}_t} \underline{\Psi}(\underline{\mathbf{x}}, t) d\mathcal{V}_t = \int_{\partial\mathcal{V}_t} (\underline{\Gamma} \underline{\mathbf{n}})(\underline{\mathbf{x}}, t) d(\partial\mathcal{V}_t) + \int_{\mathcal{V}_t} \underline{\beta}(\underline{\mathbf{x}}, t) d\mathcal{V}_t \quad (7.24)$$

where  $\mathcal{V}_t$  is a material volume (see Definition 7.2) and  $\underline{\mathbf{n}}(\underline{\mathbf{x}}, t)$  is the outward unit normal vector at the point  $\underline{\mathbf{x}}$  on  $\partial\mathcal{V}_t$ . The second-order tensor  $\underline{\Gamma}$  and the vector field  $\underline{\beta}$  model the dynamics of  $\underline{\Psi}$  through the boundary  $\partial\mathcal{V}_t$  and in the interior of  $\mathcal{V}_t$ , respectively.

#### 7.2.2.1. Balance of linear momentum

Following [118, Chapter III Section 1], the linear momentum  $\underline{\mathbf{p}}(\mathcal{P}, t)$  of any part  $\mathcal{P}$  of the body  $\mathcal{B}$  occupying the material volume  $\mathcal{V}_t \subseteq \Omega_t$  at time  $t$  can be written as

$$\underline{\mathbf{p}}(\mathcal{P}, t) = \int_{\mathcal{V}_t} \rho(\underline{\mathbf{x}}, t) \underline{\mathbf{v}}(\underline{\mathbf{x}}, t) d\mathcal{V}_t, \quad (7.25)$$

where  $\rho(\underline{\mathbf{x}}, t) \underline{\mathbf{v}}(\underline{\mathbf{x}}, t)$  represents the linear momentum per unit volume or, in other words, the density of linear momentum. As a vector-valued quantity, the balance law for the

linear momentum will be of the same form as (7.24), upon setting  $\underline{\Psi}(\underline{x}, t) = \rho(\underline{x}, t)\underline{v}(\underline{x}, t)$ , namely

$$\frac{d}{dt} \int_{\mathcal{V}_t} \rho(\underline{x}, t) \underline{v}(\underline{x}, t) d\mathcal{V}_t = \int_{\partial\mathcal{V}_t} (\underline{\underline{T}} \underline{n})(\underline{x}, t) d(\partial\mathcal{V}_t) + \int_{\mathcal{V}_t} \underline{b}(\underline{x}, t) d\mathcal{V}_t \quad (7.26)$$

where we utilized the symbols  $\underline{\underline{T}}$  and  $\underline{b}$  to denote the boundary and volumetric sources of linear momentum, respectively. It is interesting to notice that:

- the balance law (7.26) expresses the second Newton law (2.8) for the material volume  $\mathcal{V}_t$ . Indeed, upon setting

$$\underline{\underline{F}}_{\partial\mathcal{V}_t} := \int_{\partial\mathcal{V}_t} (\underline{\underline{T}} \underline{n})(\underline{x}, t) d(\partial\mathcal{V}_t) \quad \text{and} \quad \underline{\underline{F}}_{\mathcal{V}_t} := \int_{\mathcal{V}_t} \underline{b}(\underline{x}, t) d\mathcal{V}_t$$

the balance law (7.26) can be written as

$$\frac{d\underline{\underline{p}}}{dt} = \underline{\underline{F}}_{\partial\mathcal{V}_t} + \underline{\underline{F}}_{\mathcal{V}_t}$$

stating that the time rate of change of linear momentum equals the sum of all forces  $\underline{\underline{F}}_{\partial\mathcal{V}_t}$  and  $\underline{\underline{F}}_{\mathcal{V}_t}$  generated at the domain boundary and within the domain volume, respectively;

- Cauchy’s fundamental theorem allows us to identify the second-order tensor  $\underline{\underline{T}}$  in (7.26) with the *Cauchy stress tensor*, which characterizes the exchange of forces at the boundary between adjacent material volumes inside the body (see [118, Chapter III, Sections 3-4]). The vector field

$$\underline{\underline{t}}(\underline{x}, t) := (\underline{\underline{T}} \underline{n})(\underline{x}, t) \quad (7.27)$$

is called *traction* and represents the force per unit area acting at the point  $\underline{x}$  on the domain boundary with outward normal unit vector  $\underline{n}(\underline{x}, t)$ ;

- the vector field  $\underline{b}(\underline{x}, t)$  in (7.26) is the resultant of external body forces, such as gravity, per unit volume.

Let us further elaborate on the meaning of the components of the Cauchy stress tensor  $\underline{\underline{T}}$ . To this end, let us consider a material volumes  $d\mathcal{V}$  in the shape of a cube and let us consider the surfaces  $S_1, S_2$  and  $S_3$  whose normal vectors are  $\underline{n}_1 = \underline{e}_1$ ,  $\underline{n}_2 = \underline{e}_2$  and  $\underline{n}_3 = \underline{e}_3$ , respectively. Let us indicate by  $\underline{\underline{t}}^{(1)}, \underline{\underline{t}}^{(2)}$  and  $\underline{\underline{t}}^{(3)}$  the traction vectors at the boundaries  $S_1, S_2$  and  $S_3$ , respectively. Thanks to definition (7.27), we can calculate  $\underline{\underline{t}}^{(1)}$  as

$$\underline{\underline{t}}^{(1)} = \underline{\underline{T}} \underline{e}_1 = \begin{bmatrix} T_{11} & T_{12} & T_{13} \\ T_{21} & T_{22} & T_{23} \\ T_{31} & T_{32} & T_{33} \end{bmatrix} \begin{bmatrix} 1 \\ 0 \\ 0 \end{bmatrix} = \begin{bmatrix} T_{11} \\ T_{21} \\ T_{31} \end{bmatrix} = T_{11} \underline{e}_1 + T_{21} \underline{e}_2 + T_{31} \underline{e}_3. \quad (7.28)$$

Following a similar procedure, we can obtain the expression for the traction vector on the other surfaces of the infinitesimal volume  $dV$ . Summarizing, we have:

$$\underline{\underline{\mathbf{t}}}^{(1)} = T_{11} \underline{\mathbf{e}}_1 + T_{21} \underline{\mathbf{e}}_2 + T_{31} \underline{\mathbf{e}}_3 \quad (7.29)$$

$$\underline{\underline{\mathbf{t}}}^{(2)} = T_{12} \underline{\mathbf{e}}_1 + T_{22} \underline{\mathbf{e}}_2 + T_{32} \underline{\mathbf{e}}_3 \quad (7.30)$$

$$\underline{\underline{\mathbf{t}}}^{(3)} = T_{13} \underline{\mathbf{e}}_1 + T_{23} \underline{\mathbf{e}}_2 + T_{33} \underline{\mathbf{e}}_3. \quad (7.31)$$

Let us now consider an infinitesimal volume  $dW$  that is in contact with  $dV$  on the side of the surface  $S_2$ . The third Newton law, namely the action-reaction law, allows us to draw the components of the traction on the surface of  $dW$  as equal in magnitude and opposite in direction to those on the adjacent surface on  $dV$ :  $T_{22}$  represents how much the two surfaces are pushing on each other, whereas  $T_{12}$  and  $T_{32}$  represent how much the two surfaces are rubbing on each other. More rigorously, we can say that the diagonal entries of  $\underline{\underline{\mathbf{T}}}$  represent the normal stress due to *pressure*, whereas the off-diagonal entries represent the *shear stress*.

### 7.2.3. Again on Balance of energy

In the balance law (7.26), we have defined boundary and volumetric forces acting on the part  $\mathcal{P}$ . As a consequence, we can write explicitly the power  $\Pi(\mathcal{P}, t)$  introduced in (7.18) as

$$\Pi(\mathcal{P}, t) = \int_{\partial V_t} (\underline{\underline{\mathbf{T}}} \underline{\mathbf{n}})(\underline{\mathbf{x}}, t) \cdot \underline{\mathbf{v}}(\underline{\mathbf{x}}, t) d(\partial V_t) + \int_{V_t} \underline{\mathbf{b}}(\underline{\mathbf{x}}, t) \cdot \underline{\mathbf{v}}(\underline{\mathbf{x}}, t) dV_t. \quad (7.32)$$

Thus, comparing (7.32) with (7.18) we can infer that

$$\underline{\pi} \cdot \underline{\mathbf{n}} \equiv \underline{\underline{\mathbf{T}}} \underline{\mathbf{n}} \cdot \underline{\mathbf{v}} \quad \text{and} \quad \underline{p} \equiv \underline{\mathbf{b}} \cdot \underline{\mathbf{v}}. \quad (7.33)$$

Furthermore, noticing that

$$\underline{\underline{\mathbf{T}}} \underline{\mathbf{n}} \cdot \underline{\mathbf{v}} = \sum_{k,i=1}^3 (T_{ki} n_i) v_k = \sum_{k,i=1}^3 v_k T_{ki} n_i = (\underline{\mathbf{v}}^T \underline{\underline{\mathbf{T}}})^T \cdot \underline{\mathbf{n}} = \underline{\underline{\mathbf{T}}}^T \underline{\mathbf{v}} \cdot \underline{\mathbf{n}} \quad (7.34)$$

we can define  $\underline{\pi}$  as

$$\underline{\pi} \equiv \underline{\underline{\mathbf{T}}}^T \underline{\mathbf{v}}. \quad (7.35)$$

As a result, the balance law for energy can be written as

$$\begin{aligned} \frac{d}{dt} \int_{V_t} \left( \frac{\rho(\underline{\mathbf{x}}, t)}{2} |\underline{\mathbf{v}}(\underline{\mathbf{x}}, t)|^2 + \rho(\underline{\mathbf{x}}, t) \epsilon(\underline{\mathbf{x}}, t) \right) dV_t \\ = \int_{\partial V_t} ((\underline{\mathbf{q}} + \underline{\underline{\mathbf{T}}}^T \underline{\mathbf{v}} + \underline{\omega}) \cdot \underline{\mathbf{n}})(\underline{\mathbf{x}}, t) d(\partial V_t) + \int_{V_t} (\underline{\mathbf{r}} + \underline{\mathbf{b}} \cdot \underline{\mathbf{v}} + \underline{\mathbf{u}})(\underline{\mathbf{x}}, t) dV_t. \end{aligned} \quad (7.36)$$

### 7.3. Balance laws in local form

The balance laws in integral form provide identities holding for any material volume  $\mathcal{V}_t$  at every instant of time  $t$ . However, we would like to know what happens at each point of the continuum in order to investigate the local kinematics and dynamics of the system under investigation. With this aim, we need to reformulate the balance laws in local form according to the following conceptual steps:

- use a transport theorem to move the time derivative on the left-hand side of Equations (7.5) and (7.24) inside the corresponding volume integrals;
- use the divergence theorem (A.1) to write the first term on the right-hand side of Equations (7.5) and (7.24) as integrals on the volume;
- (*Eulerian form*) collect all terms under the same volume integral to obtain an integral identity of the kind

$$\int_{\mathcal{V}_t} [\text{expression}] d\mathcal{V}_t = 0. \quad (7.37)$$

Since (7.37) has to be equal to zero for any volume  $\mathcal{V}_t \subseteq \Omega_t$  expressed in the coordinate frame of the current placement, then it must be that

$$[\text{expression}] = 0 \quad \forall \underline{\mathbf{x}} \in \Omega_t, \forall t \in (0, T). \quad (7.38)$$

#### 7.3.1. Balance of mass

Applying (A.7) to (7.10) we obtain

$$\frac{d}{dt} \int_{\mathcal{V}_t} \rho(\underline{\mathbf{x}}, t) d\mathcal{V}_t = \int_{\mathcal{V}_t} \left( \frac{\partial \rho}{\partial t}(\underline{\mathbf{x}}, t) + \nabla_{\underline{\mathbf{x}}} \cdot (\rho \underline{\mathbf{v}})(\underline{\mathbf{x}}, t) \right) d\mathcal{V}_t = \int_{\mathcal{V}_t} \beta(\underline{\mathbf{x}}, t) d\mathcal{V}_t. \quad (7.39)$$

This implies that

$$\int_{\mathcal{V}_t} \left[ \frac{\partial \rho}{\partial t}(\underline{\mathbf{x}}, t) + \nabla_{\underline{\mathbf{x}}} \cdot (\rho \underline{\mathbf{v}})(\underline{\mathbf{x}}, t) - \beta(\underline{\mathbf{x}}, t) \right] d\mathcal{V}_t = 0 \quad (7.40)$$

for any material volume  $\mathcal{V}_t \subseteq \Omega_t$  and, therefore, we obtain that

$$\frac{\partial \rho}{\partial t}(\underline{\mathbf{x}}, t) + \nabla_{\underline{\mathbf{x}}} \cdot (\rho \underline{\mathbf{v}})(\underline{\mathbf{x}}, t) = \beta(\underline{\mathbf{x}}, t) \quad \forall \underline{\mathbf{x}} \in \Omega_t, \forall t \in (0, T). \quad (7.41)$$

In the case where  $\beta = 0$ , the balance of mass reduces to the following equation for *mass conservation*

$$\frac{\partial \rho}{\partial t}(\underline{\mathbf{x}}, t) + \nabla_{\underline{\mathbf{x}}} \cdot (\rho \underline{\mathbf{v}})(\underline{\mathbf{x}}, t) = 0 \quad \forall \underline{\mathbf{x}} \in \Omega_t, \forall t \in (0, T). \quad (7.42)$$

Furthermore, in the case where  $\rho$  is constant, Equation (7.42) reduces to a spatial constraint on the velocity, namely

$$\nabla_{\underline{\mathbf{x}}} \cdot \underline{\mathbf{v}}(\underline{\mathbf{x}}, t) = 0 \quad \forall \underline{\mathbf{x}} \in \Omega_t, \forall t \in (0, T). \quad (7.43)$$

### 7.3.2. Balance of electric charge

Applying (A.7) to (7.13) we obtain

$$\begin{aligned} \frac{d}{dt} \int_{\mathcal{V}_t} \zeta(\underline{\mathbf{x}}, t) d\mathcal{V}_t &= \int_{\mathcal{V}_t} \left( \frac{\partial \zeta}{\partial t}(\underline{\mathbf{x}}, t) + \nabla_{\underline{\mathbf{x}}} \cdot (\zeta \underline{\mathbf{v}})(\underline{\mathbf{x}}, t) \right) d\mathcal{V}_t \\ &= \int_{\mathcal{V}_t} \pi(\underline{\mathbf{x}}, t) d\mathcal{V}_t. \end{aligned} \quad (7.44)$$

This implies that

$$\int_{\mathcal{V}_t} \left[ \frac{\partial \zeta}{\partial t}(\underline{\mathbf{x}}, t) + \nabla_{\underline{\mathbf{x}}} \cdot (\zeta \underline{\mathbf{v}})(\underline{\mathbf{x}}, t) - \pi(\underline{\mathbf{x}}, t) \right] d\mathcal{V}_t = 0 \quad (7.45)$$

for any material volume  $\mathcal{V}_t \subseteq \Omega_t$  and, therefore, we obtain that

$$\frac{\partial \zeta}{\partial t}(\underline{\mathbf{x}}, t) + \nabla_{\underline{\mathbf{x}}} \cdot (\zeta \underline{\mathbf{v}})(\underline{\mathbf{x}}, t) = \pi(\underline{\mathbf{x}}, t) \quad \forall \underline{\mathbf{x}} \in \Omega_t, \forall t \in (0, T). \quad (7.46)$$

In the case where  $\pi = 0$ , the balance of electric charge reduces to the following equation for *electric charge conservation*

$$\frac{\partial \zeta}{\partial t}(\underline{\mathbf{x}}, t) + \nabla_{\underline{\mathbf{x}}} \cdot (\zeta \underline{\mathbf{v}})(\underline{\mathbf{x}}, t) = 0 \quad \forall \underline{\mathbf{x}} \in \Omega_t, \forall t \in (0, T). \quad (7.47)$$

### 7.3.3. Balance of energy

Applying (A.8) to (7.36) with

$$\rho\eta = \rho \left( \frac{|\underline{\mathbf{v}}|^2}{2} + e \right)$$

and applying the divergence theorem (A.1), we obtain

$$\int_{\mathcal{V}_t} \left[ \rho \frac{D}{Dt} \left( \frac{|\underline{\mathbf{v}}|^2}{2} + e \right) + \beta \left( \frac{|\underline{\mathbf{v}}|^2}{2} + e \right) \right] d\mathcal{V}_t = \int_{\mathcal{V}_t} \left[ \nabla_{\underline{\mathbf{x}}} \cdot (\underline{\mathbf{q}} + \underline{\mathbf{T}}^T \underline{\mathbf{v}} + \underline{\omega}) + r + \underline{\mathbf{b}} \cdot \underline{\mathbf{v}} + u \right] d\mathcal{V}_t. \quad (7.48)$$

Since  $\mathcal{V}_t$  is arbitrary, we obtain the following expression for the balance of energy in local form

$$\rho \frac{D}{Dt} \left( \frac{|\underline{\mathbf{v}}|^2}{2} + e \right) + \beta \left( \frac{|\underline{\mathbf{v}}|^2}{2} + e \right) = \nabla_{\underline{\mathbf{x}}} \cdot (\underline{\mathbf{q}} + \underline{\mathbf{T}}^T \underline{\mathbf{v}} + \underline{\omega}) + r + \underline{\mathbf{b}} \cdot \underline{\mathbf{v}} + u \quad (7.49)$$

holding for all  $x \in \Omega_t$  and  $t \in (0, T)$ . For the sake of convenience, let us rewrite the above expression as

$$\rho \frac{\partial e}{\partial t} + \rho (\underline{\mathbf{v}} \cdot \nabla_{\underline{\mathbf{x}}}) e + \beta e = \nabla_{\underline{\mathbf{x}}} \cdot (\underline{\mathbf{q}} + \underline{\omega}) + r + u - \mathcal{F} \quad (7.50)$$

with

$$\begin{aligned}
 \mathcal{F} &= \rho \frac{\partial}{\partial t} \frac{|\underline{\mathbf{v}}|^2}{2} + \rho (\underline{\mathbf{v}} \cdot \nabla_{\underline{\mathbf{x}}}) \frac{|\underline{\mathbf{v}}|^2}{2} + \beta \frac{|\underline{\mathbf{v}}|^2}{2} - \nabla_{\underline{\mathbf{x}}} \cdot \underline{\underline{\mathbf{T}}}^T \underline{\mathbf{v}} - \underline{\mathbf{b}} \cdot \underline{\mathbf{v}} \\
 &= \frac{\rho}{2} \sum_{i=1}^3 \frac{\partial v_i^2}{\partial t} + \frac{\rho}{2} \sum_{i,j=1}^3 v_j \frac{\partial v_i^2}{\partial x_j} + \frac{\beta}{2} \sum_{i=1}^3 v_i^2 - \sum_{i,j=1}^3 \frac{\partial}{\partial x_j} (v_i T_{ij}) - \sum_{i=1}^3 b_i v_i \\
 &= \sum_{i=1}^3 \left( \rho \frac{\partial v_i}{\partial t} + \rho \sum_{j=1}^3 v_j \frac{\partial v_i}{\partial x_j} + \frac{\beta}{2} v_i - \sum_{j=1}^3 \frac{\partial T_{ij}}{\partial x_j} - b_i \right) v_i - \sum_{i,j=1}^3 T_{ij} \frac{\partial v_i}{\partial x_j} \\
 &= \left( \rho \frac{\partial \underline{\mathbf{v}}}{\partial t} + \rho (\underline{\mathbf{v}} \cdot \nabla_{\underline{\mathbf{x}}}) \underline{\mathbf{v}} + \frac{\beta}{2} \underline{\mathbf{v}} - \nabla_{\underline{\mathbf{x}}} \cdot \underline{\underline{\mathbf{T}}} - \underline{\mathbf{b}} \right) \cdot \underline{\mathbf{v}} - \underline{\underline{\mathbf{T}}} : \nabla_{\underline{\mathbf{x}}} \underline{\mathbf{v}}. \tag{7.51}
 \end{aligned}$$

### 7.3.4. Balance of linear momentum

Applying (A.8) to each component of the vectorial equation (7.26) with  $\rho \eta = \rho v_k$ ,  $k = 1, 2, 3$ , and applying the divergence theorem (A.1), we obtain

$$\begin{aligned}
 \frac{d}{dt} \int_{\mathcal{V}_t} \rho v_k d\mathcal{V}_t &= \int_{\mathcal{V}_t} \left[ \rho \frac{\partial v_k}{\partial t} + \rho (\underline{\mathbf{v}} \cdot \nabla_{\underline{\mathbf{x}}}) v_k + \beta v_k \right] d\mathcal{V}_t \\
 &= \int_{\mathcal{V}_t} \sum_{i=1}^3 \frac{\partial T_{ki}}{\partial x_i} d\mathcal{V}_t + \int_{\mathcal{V}_t} b_k d\mathcal{V}_t \quad k = 1, 2, 3. \tag{7.52}
 \end{aligned}$$

Since  $\mathcal{V}_t$  is arbitrary, we obtain the following componentwise expression for the balance of linear momentum

$$\rho \frac{\partial v_k}{\partial t} + \rho \sum_{i=1}^3 v_i \frac{\partial v_k}{\partial x_i} + \beta v_k = \sum_{i=1}^3 \frac{\partial T_{ki}}{\partial x_i} + b_k \quad \forall \underline{\mathbf{x}} \in \Omega_t, \forall t \in (0, T), \quad k = 1, 2, 3, \tag{7.53}$$

which, in vectorial form, reads

$$\rho \frac{\partial \underline{\mathbf{v}}}{\partial t} + \rho (\underline{\mathbf{v}} \cdot \nabla_{\underline{\mathbf{x}}}) \underline{\mathbf{v}} + \beta \underline{\mathbf{v}} = \nabla_{\underline{\mathbf{x}}} \cdot \underline{\underline{\mathbf{T}}} + \underline{\mathbf{b}} \quad \forall \underline{\mathbf{x}} \in \Omega_t, \forall t \in (0, T). \tag{7.54}$$

It is interesting to notice how the term  $\beta$ , representing the net production rate of mass per unit volume, also impacts the balance of linear momentum. In the case where  $\beta = 0$ , the balance law (7.54) simplifies to

$$\rho \frac{\partial \underline{\mathbf{v}}}{\partial t} + \rho (\underline{\mathbf{v}} \cdot \nabla_{\underline{\mathbf{x}}}) \underline{\mathbf{v}} = \nabla_{\underline{\mathbf{x}}} \cdot \underline{\underline{\mathbf{T}}} + \underline{\mathbf{b}} \quad \forall \underline{\mathbf{x}} \in \Omega_t, \forall t \in (0, T). \tag{7.55}$$

The balance of linear momentum (7.54) can be written in an equivalent form, which

is also referred to as *conservative form*, as

$$\frac{\partial(\rho\underline{\mathbf{v}})}{\partial t} + \nabla_{\underline{\mathbf{x}}} \cdot (\rho\underline{\mathbf{v}} \otimes \underline{\mathbf{v}}) = \nabla_{\underline{\mathbf{x}}} \cdot \underline{\mathbf{T}} + \underline{\mathbf{b}} \quad \forall \underline{\mathbf{x}} \in \Omega_t, \forall t \in (0, T) \quad (7.56)$$

whose componentwise expression is

$$\frac{\partial(\rho v_k)}{\partial t} + \sum_{i=1}^3 \frac{\partial}{\partial x_i} (\rho v_k v_i) = \sum_{i=1}^3 \frac{\partial T_{ki}}{\partial x_i} + b_k \quad \forall \underline{\mathbf{x}} \in \Omega_t, \forall t \in (0, T), \quad k = 1, 2, 3. \quad (7.57)$$

In order to show the equivalence between (7.54) and (7.56), we observe that

$$\frac{\partial(\rho v_k)}{\partial t} + \sum_{i=1}^3 \frac{\partial}{\partial x_i} (\rho v_k v_i) = \rho \frac{\partial v_k}{\partial t} + \rho \sum_{i=1}^3 v_i \frac{\partial v_k}{\partial x_i} + v_k \left( \frac{\partial \rho}{\partial t} + \sum_{i=1}^3 \frac{\partial(\rho v_i)}{\partial x_i} \right)$$

for  $k = 1, 2, 3$ , which in vectorial form reads

$$\begin{aligned} \frac{\partial(\rho\underline{\mathbf{v}})}{\partial t} + \nabla_{\underline{\mathbf{x}}} \cdot (\rho\underline{\mathbf{v}} \otimes \underline{\mathbf{v}}) &= \rho \frac{\partial \underline{\mathbf{v}}}{\partial t} + \rho (\underline{\mathbf{v}} \cdot \nabla_{\underline{\mathbf{x}}}) \underline{\mathbf{v}} + \underline{\mathbf{v}} \left( \frac{\partial \rho}{\partial t} + \nabla_{\underline{\mathbf{x}}} \cdot (\rho\underline{\mathbf{v}}) \right) \\ &= \rho \frac{\partial \underline{\mathbf{v}}}{\partial t} + \rho (\underline{\mathbf{v}} \cdot \nabla_{\underline{\mathbf{x}}}) \underline{\mathbf{v}} + \beta \underline{\mathbf{v}}, \end{aligned}$$

where the mass balance (7.41) was used in the last step. Thus, the equivalence between (7.54) and (7.56) is proved.

### 7.3.5. Balance of angular momentum

It is possible to proof that the local form of the angular momentum balance corresponds to require that the Cauchy stress tensor  $\underline{\mathbf{T}}$  must be symmetric:

$$\underline{\mathbf{T}} = \underline{\mathbf{T}}^T \quad \forall \underline{\mathbf{x}} \in \Omega_t, \forall t \in (0, T). \quad (7.58)$$

### 7.3.6. Final formulation of the energy balance law

The balance laws for linear and angular momentum allow us to revisit and simplify Equation (7.50) for the balance of energy. Specifically, let us consider the functional

$$\mathcal{F} = \left( \rho \frac{\partial \underline{\mathbf{v}}}{\partial t} + \rho (\underline{\mathbf{v}} \cdot \nabla_{\underline{\mathbf{x}}}) \underline{\mathbf{v}} + \beta \underline{\mathbf{v}} - \nabla_{\underline{\mathbf{x}}} \cdot \underline{\mathbf{T}} - \underline{\mathbf{b}} \right) \cdot \underline{\mathbf{v}} - \underline{\mathbf{T}} : \nabla_{\underline{\mathbf{x}}} \underline{\mathbf{v}} - \frac{\beta}{2} \underline{\mathbf{v}} \cdot \underline{\mathbf{v}} \quad (7.59)$$

appearing in the integral on the right hand side of (7.50). The balance of linear momentum (7.54) guarantees that the term in the parenthesis is identically equal to zero, whereas the symmetry of  $\underline{\mathbf{T}}$  ensured by the balance of angular momentum allows us to utilize the properties of the double inner product,

to write

$$\underline{\underline{\mathbf{T}}} : \nabla_{\underline{\mathbf{x}}} \underline{\mathbf{v}} = \underline{\underline{\mathbf{T}}} : \underline{\underline{\mathbf{D}}} \quad (7.60)$$

where  $\underline{\underline{\mathbf{D}}}$  is the symmetric part of  $\nabla_{\underline{\mathbf{x}}} \underline{\mathbf{v}}$  defined as  $\underline{\underline{\mathbf{D}}} = (\nabla_{\underline{\mathbf{x}}} \underline{\mathbf{v}} + (\nabla_{\underline{\mathbf{x}}} \underline{\mathbf{v}})^T)/2$ . Thus, we can write

$$\mathcal{F} = -\underline{\underline{\mathbf{T}}} : \underline{\underline{\mathbf{D}}} - \frac{\beta}{2} \underline{\mathbf{v}} \cdot \underline{\mathbf{v}}$$

so that the energy balance in Eulerian local form finally reads

$$\rho \frac{\partial e}{\partial t} + \rho (\underline{\mathbf{v}} \cdot \nabla_{\underline{\mathbf{x}}}) e + \beta e = \nabla_{\underline{\mathbf{x}}} \cdot (\underline{\mathbf{q}} + \underline{\omega}) + r + u + \underline{\underline{\mathbf{T}}} : \underline{\underline{\mathbf{D}}} + \frac{\beta}{2} \underline{\mathbf{v}} \cdot \underline{\mathbf{v}} \quad (7.61)$$

holding for all  $\underline{\mathbf{x}} \in \Omega_t$  and  $t \in (0, T)$ . An equivalent formulation of (7.61), known also as conservative form, reads

$$\frac{\partial(\rho e)}{\partial t} + \nabla_{\underline{\mathbf{x}}} \cdot (\rho e \underline{\mathbf{v}} - \underline{\mathbf{q}} - \underline{\omega}) = r + u + \underline{\underline{\mathbf{T}}} : \underline{\underline{\mathbf{D}}} + \frac{\beta}{2} \underline{\mathbf{v}} \cdot \underline{\mathbf{v}}. \quad (7.62)$$

“Notes” — 2019/5/17 — 17:39 — page 132 — #140

## CHAPTER 8

# Homogeneous mixtures

In this chapter we introduce the concept of Homogeneous multicomponent mixture. The mixture has then modeled by deriving its balances laws.

### 8.1. Homogeneous mixtures

The following assumption serves as a starting point for the multicomponent theory:

**Assumption 8.1.** *Let the body  $\mathcal{B}$  be a homogeneous mixture of  $\Upsilon$  components, let  $\mathcal{P}$  be any part of  $\mathcal{B}$  and let  $\mathcal{V}_t$  be the current placement of  $\mathcal{P}$ . Each point in  $\mathcal{V}_t$ , indicated by the position vector  $\underline{x}$  is simultaneously occupied by  $\Upsilon$  material particles, one for each component of the mixture.*

Clearly, in the case of a body made of a single component, namely  $\Upsilon = 1$ , we fully recover the theory already developed so far. In the case of multiple components, though, the above assumption implies that *the mixture can be represented as a superposition of continuous media*. As a consequence, we can invoke the *additivity of mass*, which implies that the mass  $M(\mathcal{P}, t)$  of a given part  $\mathcal{P}$  of  $\mathcal{B}$  at time  $t$  can be written as the sum of the mass  $M_\alpha(\mathcal{P}, t)$  of each component  $\alpha$ , with  $\alpha = 1, \dots, \Upsilon$ , contained in  $\mathcal{P}$  at time  $t$ , namely

$$M(\mathcal{P}, t) = \sum_{\alpha=1}^{\Upsilon} M_\alpha(\mathcal{P}, t). \quad (8.1a)$$

Similarly, the *additivity of electric charge* implies that the electric charge  $Q(\mathcal{P}, t)$  of a given part  $\mathcal{P}$  of  $\mathcal{B}$  at time  $t$  can be written as the sum of the electric charge  $Q_\alpha(\mathcal{P}, t)$  of each component  $\alpha$ , with  $\alpha = 1, \dots, \Upsilon$ , contained in  $\mathcal{P}$  at time  $t$ , namely

$$Q(\mathcal{P}, t) = \sum_{\alpha=1}^{\Upsilon} Q_\alpha(\mathcal{P}, t). \quad (8.1b)$$

Since each component of the mixture is assumed to be modeled as a continuum, mass and electric charge of each component are assumed to be absolutely continuous as in Assumption 7.1. As a consequence, we can introduce a mass density  $\rho_\alpha$  and an electric

charge density  $\zeta_\alpha$  in such a way to write

$$M_\alpha(\mathcal{P}, t) = \int_{\mathcal{V}_t} \rho_\alpha d\mathcal{V}_t \quad \text{and} \quad Q_\alpha(\mathcal{P}, t) = \int_{\mathcal{V}_t} \zeta_\alpha d\mathcal{V}_t, \quad \alpha = 1, \dots, \Upsilon.$$

From the additivity of mass and electric charge, see Equations (8.1), it follows that

$$M(\mathcal{P}, t) = \sum_{\alpha=1}^{\Upsilon} M_\alpha(\mathcal{P}, t) = \sum_{\alpha=1}^{\Upsilon} \int_{\mathcal{V}_t} \rho_\alpha d\mathcal{V}_t = \int_{\mathcal{V}_t} \left( \sum_{\alpha=1}^{\Upsilon} \rho_\alpha \right) d\mathcal{V}_t \quad (8.2)$$

and

$$Q(\mathcal{P}, t) = \sum_{\alpha=1}^{\Upsilon} Q_\alpha(\mathcal{P}, t) = \sum_{\alpha=1}^{\Upsilon} \int_{\mathcal{V}_t} \zeta_\alpha d\mathcal{V}_t = \int_{\mathcal{V}_t} \left( \sum_{\alpha=1}^{\Upsilon} \zeta_\alpha \right) d\mathcal{V}_t. \quad (8.3)$$

Thus, we can define mass and electric charge densities for the mixture, denoted by  $\rho_m$  and  $\zeta_m$ , respectively, as

$$\rho_m(\underline{x}, t) := \sum_{\alpha=1}^{\Upsilon} \rho_\alpha(\underline{x}, t) \quad \text{and} \quad \zeta_m(\underline{x}, t) := \sum_{\alpha=1}^{\Upsilon} \zeta_\alpha(\underline{x}, t). \quad (8.4)$$

Finally, mass and electric charge of any part  $\mathcal{P}$  of the mixture at time  $t$  can be written as

$$M(\mathcal{P}, t) = \int_{\mathcal{V}_t} \rho_m d\mathcal{V}_t \quad \text{and} \quad Q(\mathcal{P}, t) = \int_{\mathcal{V}_t} \zeta_m d\mathcal{V}_t. \quad (8.5)$$

## 8.2. Balance laws for multicomponent mixtures

In the following, we will derive the balance equations for mass, linear momentum, angular momentum and energy for each single component in the mixture, in both integral and local forms. We will then obtain the balance laws for the mixture by means of the additivity principle.

### 8.2.1. Balance of mass

Let us begin with the balance of mass for the component  $\alpha$  in the mixture. Let  $\mathcal{V}_t$  be an arbitrary material volume in  $\Omega_t$ . Then, in analogy to Equation (7.10), we can write

$$\frac{d}{dt} \int_{\mathcal{V}_t} \rho_\alpha(\underline{x}, t) d\mathcal{V}_t = \int_{\mathcal{V}_t} \beta_\alpha(\underline{x}, t) d\mathcal{V}_t \quad (8.6)$$

for  $\alpha = 1, \dots, \Upsilon$ , where  $\rho_\alpha$  is the partial density of the component  $\alpha$ . Applying the Leibnitz transport theorem (A.7) with  $\Psi = \rho_\alpha$  and  $\underline{\varphi} = \underline{\varphi}_\alpha$ , we obtain the local form

of (8.6) as

$$\frac{\partial \rho_\alpha}{\partial t}(\underline{\mathbf{x}}, t) + \nabla_{\underline{\mathbf{x}}} \cdot (\rho_\alpha \underline{\mathbf{v}}_\alpha)(\underline{\mathbf{x}}, t) = \beta_\alpha(\underline{\mathbf{x}}, t) \quad \forall \underline{\mathbf{x}} \in \Omega_t, \quad \forall t \in (0, T). \quad (8.7)$$

Summing over  $\alpha$ , we obtain

$$\frac{\partial}{\partial t} \left( \sum_{\alpha=1}^Y \rho_\alpha(\underline{\mathbf{x}}, t) \right) + \nabla_{\underline{\mathbf{x}}} \cdot \left( \sum_{\alpha=1}^Y (\rho_\alpha \underline{\mathbf{v}}_\alpha)(\underline{\mathbf{x}}, t) \right) = \sum_{\alpha=1}^Y \beta_\alpha(\underline{\mathbf{x}}, t). \quad (8.8)$$

Thus, using the definition (8.4) of the mass density for the mixture and defining the velocity for the mixture as

$$\underline{\mathbf{v}}_m(\underline{\mathbf{x}}, t) := \frac{\sum_{\alpha=1}^Y \rho_\alpha(\underline{\mathbf{x}}, t) \underline{\mathbf{v}}_\alpha(\underline{\mathbf{x}}, t)}{\sum_{\alpha=1}^Y \rho_\alpha(\underline{\mathbf{x}}, t)} = \frac{\sum_{\alpha=1}^Y \rho_\alpha(\underline{\mathbf{x}}, t) \underline{\mathbf{v}}_\alpha(\underline{\mathbf{x}}, t)}{\rho_m(\underline{\mathbf{x}}, t)}, \quad (8.9)$$

we obtain the following equation for the mass balance of the mixture

$$\frac{\partial \rho_m}{\partial t}(\underline{\mathbf{x}}, t) + \nabla_{\underline{\mathbf{x}}} \cdot (\rho_m \underline{\mathbf{v}}_m)(\underline{\mathbf{x}}, t) = \beta_m(\underline{\mathbf{x}}, t) \quad \forall \underline{\mathbf{x}} \in \Omega_t, \quad \forall t \in (0, T), \quad (8.10)$$

where the net volumetric mass source for the mixture is defined as

$$\beta_m(\underline{\mathbf{x}}, t) := \sum_{\alpha=1}^Y \beta_\alpha(\underline{\mathbf{x}}, t). \quad (8.11)$$

It is interesting to observe that the velocity of the mixture defined in (8.9) can also be written as

$$\underline{\mathbf{v}}_m(\underline{\mathbf{x}}, t) = \sum_{\alpha=1}^Y c_\alpha(\underline{\mathbf{x}}, t) \underline{\mathbf{v}}_\alpha(\underline{\mathbf{x}}, t) \quad (8.12)$$

where  $c_\alpha$  is a density ratio defined as

$$c_\alpha(\underline{\mathbf{x}}, t) := \frac{\rho_\alpha(\underline{\mathbf{x}}, t)}{\rho_m(\underline{\mathbf{x}}, t)}. \quad (8.13)$$

### 8.2.2. Balance of electric charge

Let  $\mathcal{V}_t$  be an arbitrary material volume in  $\Omega_t$ . Then, in analogy to Equation (7.13), we can write

$$\frac{d}{dt} \int_{\mathcal{V}_t} \zeta_\alpha(\underline{\mathbf{x}}, t) d\mathcal{V}_t = \int_{\mathcal{V}_t} \pi_\alpha(\underline{\mathbf{x}}, t) d\mathcal{V}_t \quad (8.14)$$

for  $\alpha = 1, \dots, Y$ , where  $\zeta_\alpha$  is the partial electric charge density of the component  $\alpha$ . Applying the Leibnitz transport theorem (A.7) with  $\Psi = \zeta_\alpha$  and  $\underline{\varphi} = \underline{\varphi}_\alpha$ , we obtain the

local form of (8.14) as

$$\frac{\partial \zeta_\alpha}{\partial t}(\underline{x}, t) + \nabla_{\underline{x}} \cdot (\zeta_\alpha \underline{v}_\alpha)(\underline{x}, t) = \pi_\alpha(\underline{x}, t) \quad \forall \underline{x} \in \Omega_t, \quad \forall t \in (0, T). \quad (8.15)$$

Summing over  $\alpha$ , we obtain

$$\frac{\partial}{\partial t} \left( \sum_{\alpha=1}^{\Upsilon} \zeta_\alpha(\underline{x}, t) \right) + \nabla_{\underline{x}} \cdot \left( \sum_{\alpha=1}^{\Upsilon} (\zeta_\alpha \underline{v}_\alpha)(\underline{x}, t) \right) = \sum_{\alpha=1}^{\Upsilon} \pi_\alpha(\underline{x}, t). \quad (8.16)$$

Thus, using the definition (8.4) of the electric charge density for the mixture and defining

$$\underline{\omega}_m(\underline{x}, t) := \frac{\sum_{\alpha=1}^{\Upsilon} \zeta_\alpha(\underline{x}, t) \underline{v}_\alpha(\underline{x}, t)}{\sum_{\alpha=1}^{\Upsilon} \zeta_\alpha(\underline{x}, t)} = \frac{\sum_{\alpha=1}^{\Upsilon} \zeta_\alpha(\underline{x}, t) \underline{v}_\alpha(\underline{x}, t)}{\zeta_m(\underline{x}, t)}, \quad (8.17)$$

we obtain the following equation for the balance of electric charge of the mixture

$$\frac{\partial \zeta_m}{\partial t}(\underline{x}, t) + \nabla_{\underline{x}} \cdot (\zeta_m \underline{\omega}_m)(\underline{x}, t) = \pi_m(\underline{x}, t) \quad \forall \underline{x} \in \Omega_t, \quad \forall t \in (0, T), \quad (8.18)$$

where the net volumetric source of electric charge for the mixture is defined as

$$\pi_m(\underline{x}, t) := \sum_{\alpha=1}^{\Upsilon} \pi_\alpha(\underline{x}, t). \quad (8.19)$$

### 8.2.3. Balance of linear momentum

In analogy to what we saw for a single-component medium, defining the linear momentum of the component  $\alpha$  of the mixture as  $\underline{p}_\alpha = \rho_\alpha \underline{v}_\alpha$ , we can write

$$\frac{d}{dt} \int_{V_t} \rho_\alpha(\underline{x}, t) \underline{v}_\alpha(\underline{x}, t) dV_t = \int_{\partial V_t} \underline{T}_{\alpha} \underline{n}_{\underline{x}}(\underline{x}, t) d(\partial V_t) + \int_{V_t} \underline{b}_\alpha(\underline{x}, t) dV_t \quad (8.20)$$

where  $\underline{T}_\alpha$  is usually referred to as *partial stress tensor* of the component  $\alpha$ . The volumetric source term  $\underline{b}_\alpha$  is the resultant of external body forces and interaction forces between components acting on the component  $\alpha$  per unit volume.

Applying the transport theorem (A.7) and the divergence theorem (A.1), and utilizing the balance of mass (8.7), we obtain

$$\rho_\alpha \frac{\partial \underline{v}_\alpha}{\partial t} + \rho_\alpha (\underline{v}_\alpha \cdot \nabla_{\underline{x}}) \underline{v}_\alpha + \beta_\alpha \underline{v}_\alpha = \nabla_{\underline{x}} \cdot \underline{T}_\alpha + \underline{b}_\alpha \quad \forall \underline{x} \in \Omega_t, \quad \forall t \in (0, T) \quad (8.21)$$

whose conservative form reads

$$\frac{\partial (\rho_\alpha \underline{v}_\alpha)}{\partial t} + \nabla_{\underline{x}} \cdot (\rho_\alpha \underline{v}_\alpha \otimes \underline{v}_\alpha) = \nabla_{\underline{x}} \cdot \underline{T}_\alpha + \underline{b}_\alpha \quad \forall \underline{x} \in \Omega_t, \quad \forall t \in (0, T). \quad (8.22)$$

In order to obtain the balance of linear momentum for the mixture, we need to sum over  $\alpha$  the previous expression, thereby obtaining

$$\frac{\partial}{\partial t} \sum_{\alpha=1}^{\Upsilon} (\rho_{\alpha} \underline{\mathbf{v}}_{\alpha}) + \nabla_{\underline{\mathbf{x}}} \cdot \sum_{\alpha=1}^{\Upsilon} (\rho_{\alpha} \underline{\mathbf{v}}_{\alpha} \otimes \underline{\mathbf{v}}_{\alpha}) = \sum_{\alpha=1}^{\Upsilon} \left( \nabla_{\underline{\mathbf{x}}} \cdot \underline{\mathbf{T}}_{\alpha} + \underline{\mathbf{b}}_{\alpha} \right). \quad (8.23)$$

From the definition of density and velocity of the mixture, see (8.4) and (8.9), it follows that the first term on the left-hand side of (8.23) can be written as

$$\frac{\partial}{\partial t} \sum_{\alpha=1}^{\Upsilon} (\rho_{\alpha} \underline{\mathbf{v}}_{\alpha}) = \frac{\partial}{\partial t} (\rho_m \underline{\mathbf{v}}_m). \quad (8.24)$$

In order to deal with the second term on the left-hand side of (8.23), we introduce the relative velocity  $\underline{\mathbf{w}}_{\alpha}$  of the component  $\alpha$  with respect to the mixture, namely

$$\underline{\mathbf{w}}_{\alpha} := \underline{\mathbf{v}}_{\alpha} - \underline{\mathbf{v}}_m, \quad (8.25)$$

so that  $\underline{\mathbf{v}}_{\alpha} = \underline{\mathbf{w}}_{\alpha} + \underline{\mathbf{v}}_m$ . It is interesting to notice that (8.9) implies that

$$\rho_m \underline{\mathbf{v}}_m = \sum_{\alpha=1}^{\Upsilon} \rho_{\alpha} \underline{\mathbf{v}}_{\alpha} = \sum_{\alpha=1}^{\Upsilon} \rho_{\alpha} (\underline{\mathbf{w}}_{\alpha} + \underline{\mathbf{v}}_m) = \sum_{\alpha=1}^{\Upsilon} \rho_{\alpha} \underline{\mathbf{w}}_{\alpha} + \rho_m \underline{\mathbf{v}}_m \quad (8.26)$$

meaning that

$$\sum_{\alpha=1}^{\Upsilon} \rho_{\alpha} \underline{\mathbf{w}}_{\alpha} = 0. \quad (8.27)$$

As a consequence, we can write

$$\begin{aligned} \nabla_{\underline{\mathbf{x}}} \cdot \sum_{\alpha=1}^{\Upsilon} (\rho_{\alpha} \underline{\mathbf{v}}_{\alpha} \otimes \underline{\mathbf{v}}_{\alpha}) &= \nabla_{\underline{\mathbf{x}}} \cdot \sum_{\alpha=1}^{\Upsilon} (\rho_{\alpha} (\underline{\mathbf{w}}_{\alpha} + \underline{\mathbf{v}}_m) \otimes (\underline{\mathbf{w}}_{\alpha} + \underline{\mathbf{v}}_m)) \\ &= \nabla_{\underline{\mathbf{x}}} \cdot \sum_{\alpha=1}^{\Upsilon} (\rho_{\alpha} \underline{\mathbf{w}}_{\alpha} \otimes \underline{\mathbf{w}}_{\alpha}) + \nabla_{\underline{\mathbf{x}}} \cdot \sum_{\alpha=1}^{\Upsilon} (\rho_{\alpha} \underline{\mathbf{w}}_{\alpha} \otimes \underline{\mathbf{v}}_m) \\ &\quad + \nabla_{\underline{\mathbf{x}}} \cdot \sum_{\alpha=1}^{\Upsilon} (\rho_{\alpha} \underline{\mathbf{v}}_m \otimes \underline{\mathbf{w}}_{\alpha}) + \nabla_{\underline{\mathbf{x}}} \cdot \sum_{\alpha=1}^{\Upsilon} (\rho_{\alpha} \underline{\mathbf{v}}_m \otimes \underline{\mathbf{v}}_m) \\ &= \nabla_{\underline{\mathbf{x}}} \cdot \sum_{\alpha=1}^{\Upsilon} (\rho_{\alpha} \underline{\mathbf{w}}_{\alpha} \otimes \underline{\mathbf{w}}_{\alpha}) + \nabla_{\underline{\mathbf{x}}} \cdot \left( \left( \sum_{\alpha=1}^{\Upsilon} \rho_{\alpha} \underline{\mathbf{w}}_{\alpha} \right) \otimes \underline{\mathbf{v}}_m \right) \quad (8.28) \\ &\quad + \nabla_{\underline{\mathbf{x}}} \cdot \left( \underline{\mathbf{v}}_m \otimes \left( \sum_{\alpha=1}^{\Upsilon} \rho_{\alpha} \underline{\mathbf{w}}_{\alpha} \right) \right) + \nabla_{\underline{\mathbf{x}}} \cdot \left( \left( \sum_{\alpha=1}^{\Upsilon} \rho_{\alpha} \right) \underline{\mathbf{v}}_m \otimes \underline{\mathbf{v}}_m \right) \end{aligned}$$

which, thanks to (8.27) and the definition (8.4) of mass density of the mixture, leads

to

$$\nabla_{\underline{x}} \cdot \sum_{\alpha=1}^{\Upsilon} (\rho_{\alpha} \underline{v}_{\alpha} \otimes \underline{v}_{\alpha}) = \nabla_{\underline{x}} \cdot (\rho_m \underline{v}_m \otimes \underline{v}_m) + \nabla_{\underline{x}} \cdot \sum_{\alpha=1}^{\Upsilon} (\rho_{\alpha} \underline{w}_{\alpha} \otimes \underline{w}_{\alpha}) \quad (8.29)$$

Finally, we can rewrite (8.23) as

$$\frac{\partial}{\partial t} (\rho_m \underline{v}_m) + \nabla_{\underline{x}} \cdot (\rho_m \underline{v}_m \otimes \underline{v}_m) = \nabla \cdot \underline{\underline{T}}_m + \underline{\underline{b}}_m \quad (8.30)$$

where

$$\underline{\underline{T}}_m = \sum_{\alpha=1}^{\Upsilon} (\underline{\underline{T}}_{\alpha} - \rho_{\alpha} \underline{w}_{\alpha} \otimes \underline{w}_{\alpha}) \quad \text{and} \quad \underline{\underline{b}}_m = \sum_{\alpha=1}^{\Upsilon} \underline{\underline{b}}_{\alpha}. \quad (8.31)$$

Following the same steps as in Section 7.3.4, we can write the balance of linear momentum for the mixture in the equivalent form

$$\rho_m \frac{\partial \underline{v}_m}{\partial t} + \rho_m \underline{v}_m \cdot \nabla_{\underline{x}} \underline{v}_m + \beta_m \underline{v}_m = \nabla \cdot \underline{\underline{T}}_m + \underline{\underline{b}}_m. \quad (8.32)$$

### 8.2.4. Balance of angular momentum

Following the results of Section 7.3.5, we can write that the partial stress tensors for each component  $\alpha$  are symmetric, namely

$$\underline{\underline{T}}_{\alpha} = \underline{\underline{T}}_{\alpha}^T \quad \text{for } \alpha = 1, \dots, \Upsilon. \quad (8.33)$$

As a consequence, we have that

$$\underline{\underline{T}}_m^T = \left( \sum_{\alpha=1}^{\Upsilon} (\underline{\underline{T}}_{\alpha} - \rho_{\alpha} \underline{w}_{\alpha} \otimes \underline{w}_{\alpha}) \right)^T = \sum_{\alpha=1}^{\Upsilon} (\underline{\underline{T}}_{\alpha}^T - \rho_{\alpha} (\underline{w}_{\alpha} \otimes \underline{w}_{\alpha})^T) = \sum_{\alpha=1}^{\Upsilon} (\underline{\underline{T}}_{\alpha} - \rho_{\alpha} \underline{w}_{\alpha} \otimes \underline{w}_{\alpha}) = \underline{\underline{T}}_m.$$

which implies that the stress tensor  $\underline{\underline{T}}_m$  of the mixture is also symmetric, namely

$$\underline{\underline{T}}_m = \underline{\underline{T}}_m^T. \quad (8.34)$$

### 8.2.5. Balance of energy

Following the results of Section 7.3.3 and in particular to the equation (7.62), we can write the following balance law for each component  $\alpha$  of the mixture:

$$\frac{\partial(\rho_{\alpha} e_{\alpha})}{\partial t} + \nabla_{\underline{x}} \cdot (\rho_{\alpha} e_{\alpha} \underline{v}_{\alpha} - \underline{\underline{q}}_{\alpha} - \underline{\omega}_{\alpha}) = r_{\alpha} + u_{\alpha} + \underline{\underline{T}}_{\alpha} : \underline{\underline{D}}_{\alpha} + \frac{\beta_{\alpha}}{2} \underline{v}_{\alpha} \cdot \underline{v}_{\alpha} \quad (8.35)$$

for  $\alpha = 1, \dots, \Upsilon$ .

Thus, summing over  $\alpha$  and utilizing definition (8.31) for  $\underline{\underline{T}}_m$ , we obtain the balance

law for the energy of the mixture which reads

$$\frac{\partial(\rho_m \epsilon_m)}{\partial t} + \nabla_{\underline{x}} \cdot (\rho_m \epsilon_m \underline{v}_m - \underline{q}_m - \underline{\omega}_m) = \underline{r}_m + \underline{u}_m + \sum_{\alpha=1}^{\Upsilon} \left( \underline{\underline{T}}_{\alpha} : \underline{\underline{D}}_{\alpha} + \frac{\beta_{\alpha}}{2} \underline{v}_{\alpha} \cdot \underline{v}_{\alpha} \right)$$

where:

$$\begin{aligned} \epsilon_m &= \frac{\sum_{\alpha=1}^{\Upsilon} \rho_{\alpha} \epsilon_{\alpha}}{\rho_m}, & \underline{q}_m &= \sum_{\alpha=1}^{\Upsilon} \underline{q}_{\alpha} \\ \underline{\omega}_m &= \sum_{\alpha=1}^{\Upsilon} \underline{\omega}_{\alpha}, & \underline{r}_m &= \sum_{\alpha=1}^{\Upsilon} \underline{r}_{\alpha}, & \underline{u}_m &= \sum_{\alpha=1}^{\Upsilon} \underline{u}_{\alpha}. \end{aligned}$$

### 8.2.6. Summary of balance laws in Eulerian local form

In the case of multicomponent mixtures, we can write balance laws for each single component of the mixture and, in addition, balance laws describing the mixture as a whole. These balance laws are summarized below in their Eulerian formulation, thereby holding for all  $\underline{x} \in \Omega_t$  and  $t \in (0, T)$ .

*Balance of mass:*

$$\begin{aligned} \frac{\partial \rho_{\alpha}}{\partial t} + \nabla_{\underline{x}} \cdot (\rho_{\alpha} \underline{v}_{\alpha}) &= \beta_{\alpha}, & \alpha &= 1, \dots, \Upsilon \\ \frac{\partial \rho_m}{\partial t} + \nabla_{\underline{x}} \cdot (\rho_m \underline{v}_m) &= \beta_m \end{aligned}$$

*Balance of electric charge:*

$$\begin{aligned} \frac{\partial \zeta_{\alpha}}{\partial t} + \nabla_{\underline{x}} \cdot (\zeta_{\alpha} \underline{v}_{\alpha}) &= \pi_{\alpha}, & \alpha &= 1, \dots, \Upsilon \\ \frac{\partial \zeta_m}{\partial t} + \nabla_{\underline{x}} \cdot (\zeta_m \underline{\omega}_m) &= \pi_m \end{aligned}$$

*Balance of energy:*

$$\frac{\partial(\rho_{\alpha} \epsilon_{\alpha})}{\partial t} + \nabla_{\underline{x}} \cdot (\rho_{\alpha} \epsilon_{\alpha} \underline{v}_{\alpha} - \underline{q}_{\alpha} - \underline{\omega}_{\alpha}) = \underline{r}_{\alpha} + \underline{u}_{\alpha} + \underline{\underline{T}}_{\alpha} : \underline{\underline{D}}_{\alpha} + \frac{\beta_{\alpha}}{2} \underline{v}_{\alpha} \cdot \underline{v}_{\alpha} \quad (8.36)$$

$$\frac{\partial(\rho_m \epsilon_m)}{\partial t} + \nabla_{\underline{x}} \cdot (\rho_m \epsilon_m \underline{v}_m - \underline{q}_m - \underline{\omega}_m) = \underline{r}_m + \underline{u}_m + \sum_{\alpha=1}^{\Upsilon} \left( \underline{\underline{T}}_{\alpha} : \underline{\underline{D}}_{\alpha} + \frac{\beta_{\alpha}}{2} \underline{v}_{\alpha} \cdot \underline{v}_{\alpha} \right) \quad (8.37)$$

*Balance of linear momentum:*

$$\rho_{\alpha} \frac{\partial \underline{v}_{\alpha}}{\partial t} + \rho_{\alpha} (\underline{v}_{\alpha} \cdot \nabla_{\underline{x}}) \underline{v}_{\alpha} + \beta_{\alpha} \underline{v}_{\alpha} = \nabla_{\underline{x}} \cdot \underline{\underline{T}}_{\alpha} + \underline{\underline{b}}_{\alpha}, \quad \alpha = 1, \dots, \Upsilon$$

140 A comprehensive physically based approach to modeling in bioengineering and life sciences

$$\rho_m \frac{\partial \underline{\mathbf{v}}_m}{\partial t} + \rho_m (\underline{\mathbf{v}}_m \cdot \nabla_{\underline{\mathbf{x}}}) \underline{\mathbf{v}}_m + \beta_m \underline{\mathbf{v}}_m = \nabla_{\underline{\mathbf{x}}} \cdot \underline{\mathbf{T}}_m + \underline{\mathbf{b}}_m$$

*Balance of angular momentum:*

$$\begin{aligned}\underline{\mathbf{T}}_\alpha &= \underline{\mathbf{T}}_\alpha^T, & \alpha &= 1, \dots, \Upsilon \\ \underline{\mathbf{T}}_m &= \underline{\mathbf{T}}_m^T\end{aligned}$$

As in the case of a single component, we notice that the balance laws do not provide enough equations to determine all the unknowns of the problem. Thus, the system of the balance laws must be completed by suitable constitutive equations, as discussed in the next chapters.

## CHAPTER 9

# Axiomatic derivaton of Poisson-Nernst-Planck and Drift-Diffusion systems

The description of ion motion has been the cause of a long-time physical and mathematical debate, particularly, in the study of a very large number of charges moving under mutual influence such as the plasma matter in stars, the discharge phenomena in vacuum and in air, and electrolysis. Among the different existing approaches for the description of ion electrodynamics the most fruitful method is represented by the so called *kinetic theory*, in which the laws of statistical mechanics are applied under the assumption that ion interactions are the result of the electric and magnetic fields determined by the theory of Maxwell’s equations illustrated in Section 2.6.

In the following, we clarify how the model equations obtained by the application of the kinetic approach (*continuum description*) are analogous to those obtained by the application of the theory of mixtures in Section 8.2. This important conclusion will allow us to apply, in the context of ion electrodynamics, the theory of mixtures as an axiomatic way to derive the well known Poisson-Nernst-Planck (PNP) model widely used in biophysical applications. Another automatic by-product of this analysis is that we obtain a general framework capable of describing ion electrodynamics, as well as the behavior of a charged fluid (Section 9.4)

### 9.1. Kinetic description of ions

In this section, we study of the motion of the  $i$ -th ion species,  $i = 1, \dots, M_{ion}$ , inside a body  $\mathcal{B}$ , under the action of external and internal forces. In particular, the internal forces represent the interaction of the ions of species  $i$  with: (a) ions of the same species  $i$ ; (b) ions of species  $j$ ,  $j \neq i$ ; and (c) with the medium.

In principle, to describe the ion motion inside the geometry reported in Fig. ?? we need to apply Newton’s second law (2.8) to determine the trajectory of each ion upon prescribing its initial position and initial velocity. This approach is computationally very expensive because of the very large number of ions that move within the medium. Moreover, even if we had the necessary computational power to simulate the motion

of each individual ion, it would be extremely challenging to interpret the simulation results in terms of their impact at a larger scale.

To remedy these difficulties, it is convenient to take the point of view of *statistical mechanics* (see, e.g., [70]) and describe the ion behavior via suitable averages dictated by the kinetic theory, as discussed in the remainder of the section (see [80, Chapter 1] and [113, Section 2.3] for all the proofs and mathematical details).

To simplify the notation, in this section we omit the subscript  $i$  that identifies each ion species in the system. According to the kinetic theory, we let  $\mathbb{R}_{\underline{x}}^3$  and  $\mathbb{R}_{\underline{v}}^3$  denote the vector spaces of positions and velocities of the ion with respect to the three-dimensional Cartesian coordinate system. The position-velocity space  $\mathcal{PS} := \mathbb{R}_{\underline{x}}^3 \times \mathbb{R}_{\underline{v}}^3$  is usually referred to as *phase space*. Let  $N$  denote the number of ion, with the understood convention that  $N$  tends to  $+\infty$ , that is, the number of ions is assumed to be very large. The kinetic theory relies on the introduction of a *distribution function*  $F$  in the phase space  $\mathcal{PS}$  associated with the ensemble of  $N$  ions, so that we can write

$$F = F(\underline{x}, \underline{v}, t) \quad (\underline{x}, \underline{v}) \in \mathcal{PS}, t \in (0, T). \quad (9.1)$$

The function  $F$  is assumed to be nonnegative for all  $(\underline{x}, \underline{v}) \in \mathcal{PS}$  and  $t \in (0, T)$ , and to be sufficiently regular in  $\mathcal{PS}$ , namely at least  $L_{loc}^1(\mathcal{PS})$ , so that we can define the absolutely continuous function

$$P_B(t) = \int_{B \subseteq \mathcal{PS}} F(\underline{y}, \underline{w}, t) d\underline{y} d\underline{w} \quad t \in (0, T) \quad (9.2)$$

representing the *probability* to find the ensemble of  $N$  ions in the subset  $B$  of the phase space at each time  $t \in (0, T)$ .

**Remark 9.1.** *The relationship between the functions  $P_B$  and  $F$  in (9.2) is analogous to that between mass and mass density introduced in (7.1). There is, however, a notable difference: the integral in (9.2) is performed over the phase space, whereas in (7.1) the integral is performed over a material volume  $\mathcal{V}_t$  within the physical space.*

The Liouville postulate, also known as Liouville theorem, states that the distribution function remains constant along a ion trajectory  $(\underline{x}(t), \underline{v}(t))$  in the phase space, that is

$$\frac{d}{dt} F(\underline{x}(t), \underline{v}(t), t) = 0 \quad t \in (0, T). \quad (9.3)$$

Computing the derivative in (9.3) by means of the chain rule, we see that  $F$  satisfies the following partial differential equation in the phase space

$$\frac{\partial F}{\partial t} + \nabla_{\underline{x}} F \cdot \frac{d\underline{x}}{dt} + \nabla_{\underline{v}} F \cdot \frac{d\underline{v}}{dt} = 0 \quad (\underline{x}, \underline{v}) \in \mathcal{PS}, t \in (0, T). \quad (9.4)$$

The quantity  $\frac{d\underline{x}}{dt}$  is the ion velocity  $\underline{v}$ . The quantity  $\frac{d\underline{v}}{dt}$  is the ion acceleration that,

according to Newton’s second law, is equal to  $\underline{\mathbf{F}}/m$ , where  $\underline{\mathbf{F}}$  denotes the resultant of all forces acting on the ion, including in particular the action of the electromagnetic field  $(\underline{\mathbf{E}}, \underline{\mathbf{B}})$ .

The evolution of the distribution function  $F$  is determined by the following Cauchy problem:

$$\frac{\partial F}{\partial t} + \underline{\mathbf{v}} \cdot \nabla_{\underline{\mathbf{x}}} F + \frac{1}{m} \underline{\mathbf{F}}(\underline{\mathbf{E}}, \underline{\mathbf{B}}, \underline{\mathbf{x}}, \underline{\mathbf{v}}, t) \cdot \nabla_{\underline{\mathbf{v}}} F = 0 \quad (\underline{\mathbf{x}}, \underline{\mathbf{v}}) \in \mathcal{PS}, t \in (0, T), \quad (9.5a)$$

$$F(\underline{\mathbf{x}}, \underline{\mathbf{v}}, 0) = F_0(\underline{\mathbf{x}}, \underline{\mathbf{v}}) \quad (\underline{\mathbf{x}}, \underline{\mathbf{v}}) \in \mathcal{PS}. \quad (9.5b)$$

The electromagnetic field  $(\underline{\mathbf{E}}, \underline{\mathbf{B}})$  in (9.5a) is not, in general, a *given* function of position and time but is the result of the solution of the Maxwell equations (see Section 2.6). For this reason, the mathematical formulation to determine the distribution function in the phase space is well-known as the *Vlasov-Maxwell system*.

A complete theoretical analysis of the Vlasov-Maxwell equation system goes beyond the scope of this book and we refer to [30, 122, 32] and to [80, Section 1.3] for a detailed mathematical treatment. In the remainder of this section, we limit ourselves to illustrating the basic ideas on how to derive from the Vlasov-Maxwell system a hierarchy of continuum-based partial differential equations that constitute the historical model of ion electrodynamics within a medium under the action of external and internal forces. To this end, we make the following assumption.

**Assumption 9.1** (Existence and nonnegativity of  $F$ ). *We assume that there exists a solution  $F : \mathcal{PS} \times (0, T) \rightarrow \mathbb{R}$  to the Cauchy problem (9.5a)- (9.5b) satisfying the lower and upper bounds*

$$0 \leq F(\underline{\mathbf{x}}, \underline{\mathbf{v}}, t) \leq 1 \quad (\underline{\mathbf{x}}, \underline{\mathbf{v}}) \in \mathcal{PS}, t \in (0, T). \quad (9.6)$$

The direct solution of the kinetic equation (9.5a) is not immediately applicable to any physical problem of interest and so it is more convenient to introduce the *number density function in the position space* (shortly, number density) of the considered ensemble of  $N$  ions defined as

$$n(\underline{\mathbf{x}}, t) = \int_{\mathbb{R}_{\underline{\mathbf{v}}}^3} F(\underline{\mathbf{x}}, \underline{\mathbf{v}}, t) d\underline{\mathbf{v}} \quad \underline{\mathbf{x}} \in \mathbb{R}_{\underline{\mathbf{x}}}^3, t \in (0, T). \quad (9.7)$$

Assumption 9.1 implies that the number density  $n$  is a nonnegative absolutely continuous function, as physically expected.

**Remark 9.2.** *Definition (9.7) shows that  $n(\underline{\mathbf{x}}, t)$  is the number of ions per unit volume in a material particle occupying the infinitesimal volume  $dV_t$  located at  $\underline{\mathbf{x}}$  in the physical space at time  $t$ , in analogy to what discussed in Section 7.1. In this perspective, we are moving towards a continuum-based description of ion motion instead of following the motion of each single ion.*

**Remark 9.3.** Since Assumption 9.1 and the related Equation (9.7) hold for each of the  $M_{ion}$  ion species, we conclude that each infinitesimal volume  $dV_t$  is simultaneously occupied by the  $M_{ion}$  ion species. This situation is analogous to that described in the case of homogeneous mixtures.

In order to further develop a continuum-based description of ion motion, the kinetic theory introduces the concept of *average in the phase space* and thanks to this proceed with

the application of the so-called *method of moments* to derive a sequence of conservation laws for the spatial and temporal description of  $n$  and related conserved variables, by taking  $\xi$  equal to an algebraic polynomial of degree  $k \geq 0$ , with respect to the variable  $\underline{y}$ . We refer to [80] and [61] and references cited therein for a complete illustration and analysis of the method in the case of the zeroth order, first order and second order moments (corresponding to  $k = 0$ ,  $k = 1$  and  $k = 2$ ). In conclusion, the application of the method of moments, produces a system of balance laws holding for each ion species within a medium. Indeed, there is a strong analogy between these results obtained via the method of moments following from statistical mechanics and those obtained in Section 8.2 via the mixture theory following from continuum mechanics. In the next sections, we further elaborate this analogy.

## 9.2. From kinetic description to continuum approach via mixture theory

The key to understand the analogy between the conclusions of statistical mechanics and the axiomatic formalism adopted for the description of a multicomponent mixture lays in the relationship between the  $i$ -th ion number density  $n_i(\underline{x}, t)$  and the definition of the mass of the single component  $\alpha$  given in Section 8.1. The kinetic theory outlined in Section 9.1 showed that:

- the number density function  $n_i(\underline{x}, t)$ , for  $i = 1, \dots, M_{ion}$ , represents the averaged number of ions of the  $i$ -th species per unit volume (units  $\text{m}^{-3}$ ) contained in the infinitesimal volume  $dV_t$  located at  $\underline{x}$  at time  $t$ ;
- the number density function  $n_i(\underline{x}, t)$ , for  $i = 1, \dots, M_{ion}$ , is an absolutely continuous function in the sense of Assumption 7.1;
- the  $M_{ion}$  ion species simultaneously occupy any infinitesimal volume  $dV_t$ , thereby calling for a continuum model based on homogeneous mixtures.

Thus, utilizing the same notation as in Chapter 8, we can compute the mass  $M_\alpha$  of the ion species  $\alpha$  contained in any part  $\mathcal{P}$  of a multicomponent mixture  $\mathcal{B}$  as

$$M_\alpha(\mathcal{P}, t) := \int_{V_t} m_\alpha n_\alpha(\underline{x}, t) dV_t \quad (9.8)$$

where  $\mathcal{V}_t$  is the volume occupied by the part  $\mathcal{P}$  at time  $t$  and  $m_\alpha$  is the atomic mass of the ion component  $\alpha$  (units: Kg). Thus, the *mass density* for the ion component  $\alpha$  can be defined as

$$\rho_\alpha(\underline{\mathbf{x}}, t) := m_\alpha n_\alpha(\underline{\mathbf{x}}, t) \quad \underline{\mathbf{x}} \in \Omega_t, t \in (0, T), \quad (9.9)$$

where  $\Omega_t$  denotes the current placement of  $\mathcal{B}$ .

**Remark 9.4.** *The step that led us from the concept of number density to that of mass density apparently reduces to a trivial multiplication by the factor  $m_\alpha$ . However, relation (9.8) lends itself to a natural generalization to include atomic mass exchanges, as in the case of nuclear reactions and transitions. In such a circumstance, relation (9.8) must be written as*

$$M_\alpha(\mathcal{P}, t) := \int_{\mathcal{V}_t} m_\alpha(\underline{\mathbf{x}}, t) n_\alpha(\underline{\mathbf{x}}, t) dV_t \quad (9.10)$$

so that (9.9) becomes

$$\rho_\alpha(\underline{\mathbf{x}}, t) := m_\alpha(\underline{\mathbf{x}}, t) n_\alpha(\underline{\mathbf{x}}, t) \quad \underline{\mathbf{x}} \in \Omega_t, t \in (0, T). \quad (9.11)$$

The electric charge  $Q_\alpha$  of the component  $\alpha$  contained in any part  $\mathcal{P}$  of the multicomponent mixture  $\mathcal{B}$  can be computed as

$$Q_\alpha(\mathcal{P}, t) := \int_{\mathcal{V}_t} q z_\alpha n_\alpha(\underline{\mathbf{x}}, t) dV_t \quad (9.12)$$

where  $q z_\alpha$  is the electric charge of the ion component  $\alpha$  (units: C). Thus, the *electric charge density* for the ion component  $\alpha$  can be defined as

$$\zeta_\alpha(\underline{\mathbf{x}}, t) := q z_\alpha n_\alpha(\underline{\mathbf{x}}, t) \quad \underline{\mathbf{x}} \in \Omega_t, t \in (0, T). \quad (9.13)$$

### 9.3. Relationship between the motion of charged particles in the continuum approach and the Maxwell equations

The introduction of the electric charge density (9.13) in the context of ionic homogeneous mixtures is not a mere formal analogy with the mass density, but it has profound consequences on the mathematical description of the coupling between ion motion and electromagnetic field. The goal of this section is to clarify this crucial point.

Following Section 8.2, let us consider a homogeneous mixture made of  $\Upsilon$  components. The mass balance for each component  $\alpha$ , for  $\alpha = 1, \dots, \Upsilon$ , can be written as

$$\frac{\partial \rho_\alpha(\underline{\mathbf{x}}, t)}{\partial t} + \nabla_{\underline{\mathbf{x}}} \cdot (\rho_\alpha(\underline{\mathbf{x}}, t) \underline{\mathbf{v}}_\alpha(\underline{\mathbf{x}}, t)) = \beta_\alpha(\underline{\mathbf{x}}, t) \quad \underline{\mathbf{x}} \in \Omega_t, t \in (0, T), \quad (9.14)$$

where  $\rho_\alpha$ ,  $\underline{\mathbf{v}}_\alpha$  and  $\beta_\alpha$  represent mass density, velocity and net production rate, respectively, of the component  $\alpha$ . Thanks to the relationship between mass density and num-

ber density for ion species established by (9.11), the mass balance for each component  $\alpha$  can also be written as

$$\frac{\partial(m_\alpha n_\alpha(\underline{x}, t))}{\partial t} + \nabla_{\underline{x}} \cdot (m_\alpha n_\alpha(\underline{x}, t) \underline{v}_\alpha(\underline{x}, t)) = \beta_\alpha(\underline{x}, t) \quad \underline{x} \in \Omega_t, \quad t \in (0, T) \quad (9.15)$$

where we assumed  $m_\alpha$  to be constant. Interestingly, multiplying Equation (9.15) by  $q z_\alpha / m_\alpha$  we obtain

$$\frac{\partial(q z_\alpha n_\alpha(\underline{x}, t))}{\partial t} + \nabla_{\underline{x}} \cdot (q z_\alpha n_\alpha(\underline{x}, t) \underline{v}_\alpha(\underline{x}, t)) = \frac{q z_\alpha}{m_\alpha} \beta_\alpha(\underline{x}, t) \quad \underline{x} \in \Omega_t, \quad t \in (0, T)$$

which, thanks to the relationship between number density and electric charge density given in (9.13), leads to the following balance of electric charge

$$\frac{\partial \zeta_\alpha(\underline{x}, t)}{\partial t} + \nabla_{\underline{x}} \cdot (\zeta_\alpha(\underline{x}, t) \underline{v}_\alpha(\underline{x}, t)) = \pi_\alpha(\underline{x}, t) \quad \underline{x} \in \Omega_t, \quad t \in (0, T) \quad (9.16)$$

with

$$\pi_\alpha(\underline{x}, t) := \frac{q z_\alpha}{m_\alpha} \beta_\alpha(\underline{x}, t). \quad (9.17)$$

Following the mixture theory paradigm presented in Section 8.1, the mass density and the electric charge density characterizing the homogeneous mixture are defined as

$$\rho_m(\underline{x}, t) := \sum_{\alpha=1}^r \rho_\alpha(\underline{x}, t) \quad \text{and} \quad \zeta_m(\underline{x}, t) := \sum_{\alpha=1}^r \zeta_\alpha(\underline{x}, t) \quad (9.18)$$

and satisfy the following balance equations:

$$\frac{\partial \rho_m(\underline{x}, t)}{\partial t} + \nabla_{\underline{x}} \cdot (\rho_m(\underline{x}, t) \underline{v}_m(\underline{x}, t)) = \beta_m(\underline{x}, t) \quad \underline{x} \in \Omega_t, \quad t \in (0, T) \quad (9.19a)$$

$$\frac{\partial \zeta_m(\underline{x}, t)}{\partial t} + \nabla_{\underline{x}} \cdot (\zeta_m(\underline{x}, t) \underline{\omega}_m(\underline{x}, t)) = \pi_m(\underline{x}, t) \quad \underline{x} \in \Omega_t, \quad t \in (0, T) \quad (9.19b)$$

where we recall that:

$$\begin{aligned} \underline{v}_m(\underline{x}, t) &:= \sum_{\alpha=1}^r c_\alpha(\underline{x}, t) \underline{v}_\alpha(\underline{x}, t), & c_\alpha(\underline{x}, t) &= \frac{\rho_\alpha(\underline{x}, t)}{\rho_m(\underline{x}, t)} = \frac{m_\alpha n_\alpha(\underline{x}, t)}{\sum_{\alpha=1}^r m_\alpha n_\alpha(\underline{x}, t)} \\ \underline{\omega}_m(\underline{x}, t) &:= \sum_{\alpha=1}^r b_\alpha(\underline{x}, t) \underline{v}_\alpha(\underline{x}, t), & b_\alpha(\underline{x}, t) &= \frac{\zeta_\alpha(\underline{x}, t)}{\zeta_m(\underline{x}, t)} = \frac{q z_\alpha n_\alpha(\underline{x}, t)}{\sum_{\alpha=1}^r q z_\alpha n_\alpha(\underline{x}, t)} \\ \beta_m(\underline{x}, t) &:= \sum_{\alpha=1}^r \beta_\alpha(\underline{x}, t), & \pi_m(\underline{x}, t) &:= \sum_{\alpha=1}^r \pi_\alpha(\underline{x}, t) = \sum_{\alpha=1}^r \frac{q z_\alpha}{m_\alpha} \beta_\alpha(\underline{x}, t). \end{aligned}$$

**Remark 9.5.** For each ion species  $\alpha$ , the same transport velocity  $\underline{v}_\alpha$  appears in both balance of mass, see (9.15), and balance of electric charge, see (9.16). However, when

adding the contributions from all ion species, the resulting balance equations for the charged homogeneous mixture show different transport velocities for the mass and electric charge, which have been denoted by  $\underline{v}_m$  and  $\underline{\omega}_m$ , respectively.

The presence of an electric charge density, such as  $\zeta_m$ , generates an electromagnetic field, as illustrated mathematically by Maxwell’s equations, see Section 2.6. Let us now assume, for the sake of simplicity, that the charged homogeneous mixture under consideration is the only charged body present in the whole space. Then, the electric charge density  $\rho^{el}$  appearing on the right-hand side of (2.47) can be defined in terms of  $\zeta_m$  as

$$\rho^{el}(\underline{x}, t) = \begin{cases} \zeta_m(\underline{x}, t) & \underline{x} \in \Omega_t, t \in (0, T) \\ 0 & \text{elsewhere} \end{cases}. \quad (9.20)$$

In the typical framework of Maxwell’s equations, though, the electric charge density  $\rho^{el}$  is considered to be a datum for the system, along with the conduction current density  $\underline{J}$ . In addition, the two quantities,  $\rho^{el}$  and  $\underline{J}$ , must satisfy the compatibility condition (2.48) at every point in space and time. Thus, in particular, the compatibility condition must be verified for every  $\underline{x} \in \Omega_t$  and  $t \in (0, T)$ , where, simultaneously, the balance of electric charge (9.19b) must hold. As a consequence, we have that:

$$\rho^{el}(\underline{x}, t) = \zeta_m(\underline{x}, t) \quad \underline{x} \in \Omega_t, t \in (0, T)$$

$$\frac{\partial \rho^{el}(\underline{x}, t)}{\partial t} + \nabla_{\underline{x}} \cdot \underline{J} = 0 \quad \underline{x} \in \Omega_t, t \in (0, T)$$

$$\frac{\partial \zeta_m(\underline{x}, t)}{\partial t} + \nabla_{\underline{x}} \cdot (\zeta_m(\underline{x}, t) \underline{\omega}_m(\underline{x}, t)) = \pi_m(\underline{x}, t) \quad \underline{x} \in \Omega_t, t \in (0, T)$$

must hold simultaneously, thereby implying that

$$\nabla_{\underline{x}} \cdot \underline{J} = \nabla_{\underline{x}} \cdot (\zeta_m(\underline{x}, t) \underline{\omega}_m(\underline{x}, t)) - \pi_m(\underline{x}, t). \quad \underline{x} \in \Omega_t, t \in (0, T)$$

**Definition 9.1** (Closed system with respect to the total electric charge). A homogeneous mixture made of  $\Upsilon$  components is closed with respect to the total electric charge if  $\pi_m(\underline{x}, t) \equiv 0$ . In such a case, the conduction current density  $\underline{J}$  can be characterized as

$$\underline{J}(\underline{x}, t) = \zeta_m(\underline{x}, t) \underline{\omega}_m(\underline{x}, t), \quad (9.21a)$$

or, equivalently

$$\underline{J}(\underline{x}, t) = \sum_{\alpha=1}^{\Upsilon} q z_\alpha n_\alpha(\underline{x}, t) \underline{v}_\alpha(\underline{x}, t). \quad (9.21b)$$

In order to completely determine  $n_\alpha$ ,  $\underline{v}_\alpha$  and  $\underline{J}$  we need to invoke also the balance laws of linear momentum (and internal energy if the system is not isothermal).

#### 9.4. Ions charged fluid as an example of Homogeneous charged mixtures

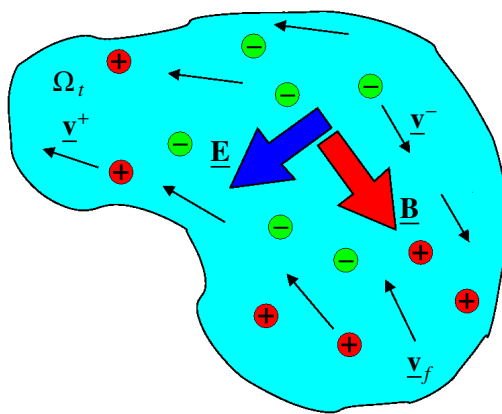


**Figure 9.1** Schematic representation of an ionic solution made of a fluid phase (light blue color) and two ion species, namely cations (red circles) and anions (green circles), so that  $M_{ion} = 2$  and  $\Upsilon = 3$ . The electromagnetic field pair ( $\underline{E}, \underline{B}$ ) is represented by the dark blue and red arrows. The fluid velocity is denoted by  $\underline{v}_f$ . The cation velocity is denoted by  $\underline{v}^+$  and the anion velocity is denoted by  $\underline{v}^-$ .

Let us consider a homogeneous mixture composed of  $M_{ion}$  ion species and one fluid solvent, see Figure 9.1, which we will refer to as *ionic solution*. Since the mixing between ions and fluid occurs at the molecular level, we can adopt the modeling framework pertaining to *homogeneous multicomponent mixtures* described in Section 8.2. Let us identify by the subscript  $\alpha$ , with  $\alpha = 1, \dots, M_{ion}$ , the ion species and by the subscript  $f$  the fluid, so that the mixture includes  $\Upsilon = M_{ion} + 1$  components. Let us assume that the mixture is isothermal, and we denote by  $\Theta$  (units: K) the system temperature.

*Ion species.* Following Sections 9.3 and 8.2, the balance laws for mass, electric charge and linear momentum for each ion species  $\alpha$ , with  $\alpha = 1, \dots, M_{ion}$ , can be written as:

$$\frac{\partial \rho_\alpha}{\partial t} + \nabla_{\underline{x}} \cdot (\rho_\alpha \underline{v}_\alpha) = \beta_\alpha \quad (9.22a)$$

$$\frac{\partial \zeta_\alpha}{\partial t} + \nabla_{\underline{x}} \cdot (\zeta_\alpha \underline{v}_\alpha) = \pi_\alpha \quad (9.22b)$$

$$\rho_\alpha \frac{\partial \underline{v}_\alpha}{\partial t} + \rho_\alpha (\underline{v}_\alpha \cdot \nabla_{\underline{x}}) \underline{v}_\alpha + \beta_\alpha \underline{v}_\alpha = \nabla \cdot \underline{\underline{T}}_\alpha + \underline{\underline{b}}_\alpha, \quad (9.22c)$$

with  $\rho_\alpha = m_\alpha n_\alpha$  and  $\zeta_\alpha = q z_\alpha n_\alpha$ , holding for  $\underline{x} \in \Omega_t$  and  $t \in (0, T)$ . For each ion component  $\alpha$  of the mixture,  $\beta_\alpha$  is the net production rate of the mass density (units:  $\text{Kg m}^{-3}\text{s}^{-1}$ ),  $\pi_\alpha = q z_\alpha \beta_\alpha / m_\alpha$  is the net production rate of the electric charge density (units:  $\text{C m}^{-3}\text{s}^{-1}$ ),  $\underline{v}_\alpha$  is the velocity field (units:  $\text{ms}^{-1}$ ),  $\underline{\underline{T}}_\alpha$  is the stress tensor (units:  $\text{Nm}^{-2}$ ) and  $\underline{\underline{b}}_\alpha$  is the force density (including forces due to external fields as well as interactions among mixture components) acting upon the ion component  $\alpha$  (units:  $\text{Nm}^{-3}$ ).

The net production rate  $\beta_\alpha$  strongly depends on the specific application. For example, in the study of biological channels, it is customary to neglect sources/sinks in the ion mass densities and set  $\beta_\alpha = 0$ , for  $\alpha = 1, \dots, M_{ion}$  (see [105, Chapter 1]). Conversely, in the study of electron and hole charge transport in semiconductors,  $\beta_\alpha$  is a nonlinear function of all the ion number densities and also of the electric field (see [113, Chapter 4]). Furthermore, when chemical reactions occur in the system under investigation, the net production rate  $\beta_\alpha$  can be described by applying the mass action law derived by Bronsted [20] and Haase [50]. Thus, for the sake of generality, in the following we will keep the net production rate indicated as  $\beta_\alpha$ .

Interestingly, relationship (9.17) implies that the characterization of the net production rate  $\beta_\alpha$  of mass density directly translates into a characterization of the net production rate  $\pi_\alpha$  of electric charge density.

To characterize the constitutive laws for  $\underline{\underline{T}}_\alpha$  and  $\underline{\underline{b}}_\alpha$  we refer to Figure 9.2, which provides a schematic representation of an ion in motion within a fluid under the action of the forces exerted by the electric field, by the fluid and by the surrounding ions. The stress tensor  $\underline{\underline{T}}_\alpha$  is typically assumed to be of the same form as that introduced for compressible viscous fluids , namely

$$\underline{\underline{T}}_\alpha = -p_\alpha \underline{\underline{I}} + \lambda_\alpha (\nabla_{\underline{x}} \cdot \underline{v}_\alpha) \underline{\underline{I}} + 2\mu_\alpha \underline{\underline{D}}(\underline{v}_\alpha) \quad (9.23)$$

where  $p_\alpha$  is the hydrostatic pressure exerted by the surrounding ions of the same species (see red arrows in Figure 9.2),  $\lambda_\alpha$  (units:  $\text{Kg m}^{-1}\text{s}^{-1}$ ) is the bulk modulus for the ion species  $\alpha$  characterizing its resistance to compression, and  $\mu_\alpha$  (units:  $\text{Kg m}^{-1}\text{s}^{-1}$ ) is the dynamic viscosity (also referred to as shear viscosity) for the ion species  $\alpha$  characterizing its internal friction (see the cyan arrows  $\underline{v}_\alpha$  and  $\underline{v}_\beta$  in Figure 9.2). Using the law of ideal gases and remember that

$$n_\alpha = \frac{nN_A}{V}, \quad (9.24)$$

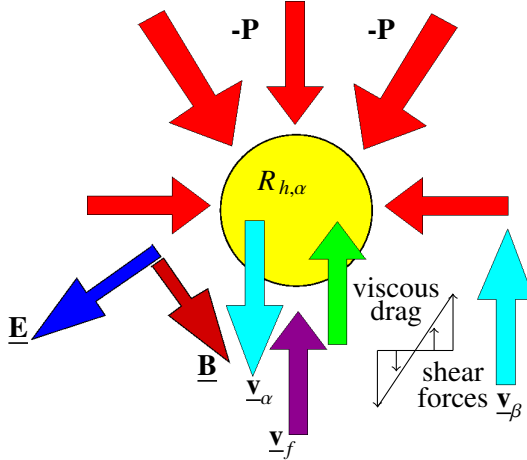


**Figure 9.2** Motion of an ion (yellow) in a fluid. The cyan arrows represent the velocity of two ion particles located at different spatial positions in the fluid. The butterfly-like diagram represents the distribution of shear forces that are exchanged between the two ions because of their different velocities. The red arrows represent the compressive stress on the ion exerted by the neighboring ions. The green arrow represents the viscous resistance of the fluid whose velocity is represented by the dark magenta arrow. The blue arrow represents the electric field whereas the red brick arrow represents the magnetic induction.

we can write

$$p_\alpha = n_a K_B \Theta, \quad (9.25)$$

where  $K_B$  is the Boltzmann constant, so that we have

$$\underline{\underline{T}}_a = -n_a K_B \Theta \underline{\underline{I}} + \lambda_a (\nabla \underline{x} \cdot \underline{v}_a) \underline{\underline{I}} + 2\mu_a \underline{\underline{D}}(\underline{v}_a). \quad (9.26)$$

**Remark 9.6.** The constitutive relation (9.26) was theoretically derived in [6] and the resulting continuum-based formulation has been numerically investigated in [12].

The force density  $\underline{\underline{b}}_a$  includes a contribution  $\underline{\underline{m}}_a$  due to the viscous drag between ions of the species  $a$  and the other components of the mixture and a contribution  $\underline{\underline{f}}_a$  due the action of the gravitational and electromagnetic fields, so that we can write

$$\underline{\underline{b}}_a = \underline{\underline{m}}_a + \underline{\underline{f}}_a. \quad (9.27)$$

The contribution  $\underline{\underline{m}}_a$  can be written in terms of the relative velocities between the

component  $\alpha$  and the other mixture components as

$$\underline{\mathbf{m}}_\alpha = - \sum_{\substack{\gamma=1 \\ \gamma \neq \alpha}}^{M_{ion}} c_{\alpha\gamma} (\underline{\mathbf{v}}_\alpha - \underline{\mathbf{v}}_\gamma) - c_{\alpha f} (\underline{\mathbf{v}}_\alpha - \underline{\mathbf{v}}_f) \quad (9.28)$$

where  $c_{\alpha\gamma}$  and  $c_{\alpha f}$ , with  $\alpha, \gamma = 1, \dots, M_{ion}$  and  $\alpha \neq \gamma$ , are nonnegative quantities representing the viscous drag coefficients among the components of the mixture. Importantly, the action-reaction principle requires that  $c_{\alpha\gamma} = c_{\gamma\alpha}$  for  $\alpha, \gamma = 1, \dots, M_{ion}$  and  $\alpha \neq \gamma$ . The contribution  $\underline{\mathbf{f}}_\alpha$  in (9.27) is expressed by means of the gravitational and Lorentz forcesto give

$$\underline{\mathbf{f}}_\alpha = \rho_\alpha \underline{\mathbf{g}} + q z_\alpha n_\alpha (\underline{\mathbf{E}} + \underline{\mathbf{v}}_\alpha \times \underline{\mathbf{B}}). \quad (9.29)$$

where  $\underline{\mathbf{g}}$  is the acceleration of gravity.

*Fluid solvent.* Similarly, for the fluid component we have:

$$\frac{\partial \rho_f}{\partial t} + \nabla_{\underline{\mathbf{x}}} \cdot (\rho_f \underline{\mathbf{v}}_f) = \beta_f \quad (9.30a)$$

$$\rho_f \frac{\partial \underline{\mathbf{v}}_f}{\partial t} + \rho_f (\underline{\mathbf{v}}_f \cdot \nabla_{\underline{\mathbf{x}}}) \underline{\mathbf{v}}_f + \beta_f \underline{\mathbf{v}}_f = \nabla \cdot \underline{\underline{\mathbf{T}}}_f + \underline{\mathbf{b}}_f, \quad (9.30b)$$

holding for  $\underline{\mathbf{x}} \in \Omega_t$  and  $t \in (0, T)$ , where  $\beta_f$  is the fluid net production rate (units:  $\text{Kg m}^{-3}\text{s}^{-1}$ ),  $\underline{\mathbf{v}}_f$  is the fluid velocity (units:  $\text{ms}^{-1}$ ),  $\underline{\underline{\mathbf{T}}}_f$  is the fluid stress tensor (units:  $\text{Nm}^{-2}$ ) and  $\underline{\mathbf{b}}_f$  is the force density acting upon the fluid component of the mixture (units:  $\text{Nm}^{-3}$ ). The fluid solvent is often composed of water, which will be described as an electrically neutral incompressible viscous fluid. Thuswe will assume

$$\rho_f = \text{given constant} > 0 \quad \text{and} \quad \beta_f = 0 \quad (9.31)$$

so that (9.30a) simply becomes

$$\nabla_{\underline{\mathbf{x}}} \cdot \underline{\mathbf{v}}_f = 0. \quad (9.32)$$

In addition, we write the fluid stress tensor in the form

$$\underline{\underline{\mathbf{T}}}_f = -p_f \underline{\mathbf{I}} + 2\mu_f \underline{\underline{\mathbf{D}}}(\underline{\mathbf{v}}_f). \quad (9.33)$$

The force density  $\underline{\mathbf{b}}_f$  comprises the action of the gravitational field and the viscous drag due to the interaction between the fluid and all the ion species, as in [35], so that we can write

$$\underline{\mathbf{b}}_f = \rho_f \underline{\mathbf{g}} - \sum_{\alpha=1}^{M_{ion}} c_{fa} (\underline{\mathbf{v}}_f - \underline{\mathbf{v}}_\alpha) \quad (9.34)$$

where the viscous drag coefficients  $c_{f\alpha}$  are equal to the  $c_{\alpha f}$ , for  $\alpha = 1, \dots, M_{ion}$ , as required by the action-reaction principle.

*Electromagnetic field.* The electromagnetic field ( $\underline{\mathbf{E}}, \underline{\mathbf{B}}$ ) appearing in (9.29) must be solved consistently with the Maxwell equations (2.44), namely:

$$\nabla \times \underline{\mathbf{E}} = -\frac{\partial \underline{\mathbf{B}}}{\partial t} \quad (9.35a)$$

$$\nabla \times \underline{\mathbf{H}} = \underline{\mathbf{J}} + \frac{\partial \underline{\mathbf{D}}}{\partial t} \quad (9.35b)$$

$$\nabla \cdot \underline{\mathbf{D}} = \rho^{el} \quad (9.35c)$$

$$\nabla \cdot \underline{\mathbf{B}} = 0. \quad (9.35d)$$

**Remark 9.7.** We remark that Maxwell’s equations hold for any  $\underline{x} \in \mathbb{R}^3$ , whereas the balance laws for the mixture hold only in  $\underline{x} \in \Omega_t$ . This is the mathematical formalization of the physical fact that moving charges generate an electromagnetic field that propagates through the whole space, thus both inside and outside the region of space  $\Omega_t$  occupied by the mixture at time  $t$ . In the study of ionic solutions, however, the main interest is the influence of the electromagnetic field on the ion motion within the mixture and so we can restrict the domain of Maxwell’s equations to  $\Omega_t$ .

Assuming that the ionic solution exhibits a linear and homogeneous behavior with respect to the electromagnetic field, we complement system (9.35) with the constitutive relationships

$$\underline{\mathbf{D}} = \varepsilon_m \underline{\mathbf{E}} \quad \text{and} \quad \underline{\mathbf{B}} = \mu_m \underline{\mathbf{H}} \quad (9.36)$$

where  $\varepsilon_m$  and  $\mu_m$  characterize the dielectric permittivity and the magnetic permeability of the mixture, respectively. In addition, as discussed in Section 9.3, we can characterize the electric charge density  $\rho^{el}$  and the conduction current density  $\underline{\mathbf{J}}$  appearing in Maxwell’s equations in terms of quantities associated with the ionic species within the mixture as

$$\rho^{el} = \zeta_m \quad \text{and} \quad \underline{\mathbf{J}} = \zeta_m \underline{\omega}_m + \underline{\phi} \quad \text{for } \underline{x} \in \Omega_t, t \in (0, T) \quad (9.37)$$

where:

$$\zeta_m = \sum_{\alpha=1}^{M_{ion}} \zeta_\alpha, \quad \underline{\omega}_m = \frac{1}{\zeta_m} \sum_{\alpha=1}^{M_{ion}} \zeta_\alpha \underline{\mathbf{v}}_\alpha \quad (9.38)$$

$$\nabla_{\underline{x}} \cdot \underline{\phi} = -\pi_m, \quad \pi_m = \sum_{\alpha=1}^{M_{ion}} \frac{q z_\alpha}{m_\alpha} \beta_\alpha. \quad (9.39)$$

**Remark 9.8.** In accordance with Definition 9.1, if the homogeneous mixture made of

$\Upsilon$  components is closed with respect to the total electric charge we can set  $\underline{\phi} = \underline{0}$  in (9.37).

*Full coupled system.* Finally, the dynamics of the ionic solution is described by the following system of partial differential equations:

$$m_\alpha \frac{\partial n_\alpha}{\partial t} + m_\alpha \nabla_{\underline{x}} \cdot (n_\alpha \underline{v}_\alpha) = \beta_\alpha \quad (9.40a)$$

$$\begin{aligned} m_\alpha n_\alpha \frac{\partial \underline{v}_\alpha}{\partial t} + m_\alpha n_\alpha (\underline{v}_\alpha \cdot \nabla_{\underline{x}}) \underline{v}_\alpha + \beta_\alpha \underline{v}_\alpha = \\ \nabla_{\underline{x}} \cdot \left[ -K_B \Theta n_\alpha \underline{\underline{I}} + \lambda_\alpha (\nabla_{\underline{x}} \cdot \underline{v}_\alpha) \underline{\underline{I}} + 2\mu_\alpha \underline{\underline{D}}(\underline{v}_\alpha) \right] \end{aligned} \quad (9.40b)$$

$$- \sum_{\substack{\gamma=1 \\ \gamma \neq \alpha}}^{M_{ion}} c_{\alpha\gamma} (\underline{v}_\alpha - \underline{v}_\gamma) - c_{\alpha f} (\underline{v}_\alpha - \underline{v}_f) + m_\alpha n_\alpha \underline{\underline{g}} + q z_\alpha n_\alpha (\underline{\underline{E}} + \mu_m \underline{v}_\alpha \times \underline{\underline{H}})$$

$$\nabla_{\underline{x}} \cdot \underline{v}_f = 0 \quad (9.40c)$$

$$\rho_f \frac{\partial \underline{v}_f}{\partial t} + \rho_f (\underline{v}_f \cdot \nabla_{\underline{x}}) \underline{v}_f + \beta_f \underline{v}_f = -\nabla_{\underline{x}} p_f + 2\mu_f \nabla_{\underline{x}} \cdot \underline{\underline{D}}(\underline{v}_f) + \rho_f \underline{\underline{g}} - \sum_{\alpha=1}^{M_{ion}} c_{\alpha f} (\underline{v}_f - \underline{v}_\alpha) \quad (9.40d)$$

$$\mu_m \frac{\partial \underline{\underline{H}}}{\partial t} = -\nabla_{\underline{x}} \times \underline{\underline{E}} \quad (9.40e)$$

$$\epsilon_m \frac{\partial \underline{\underline{E}}}{\partial t} + \sum_{\alpha=1}^{M_{ion}} (q z_\alpha n_\alpha \underline{v}_\alpha) + \underline{\phi} = \nabla_{\underline{x}} \times \underline{\underline{H}} \quad (9.40f)$$

$$\epsilon_m \nabla_{\underline{x}} \cdot \underline{\underline{E}} = \sum_{\alpha=1}^{M_{ion}} q z_\alpha n_\alpha \quad (9.40g)$$

$$\mu_m \nabla_{\underline{x}} \cdot \underline{\underline{H}} = 0 \quad (9.40h)$$

holding for  $\alpha = 1, \dots, M_{ion}$ ,  $\underline{x} \in \Omega_t$ ,  $t \in (0, T)$ . System (9.40) can be solved upon prescribing initial conditions for  $n_\alpha$ ,  $\underline{v}_\alpha$ ,  $\underline{v}_f$ ,  $\underline{\underline{E}}$  and  $\underline{\underline{H}}$ , along with suitable boundary conditions on the surfaces delimiting the region  $\Omega_t$ . It is interesting to notice that, for given  $\underline{\underline{E}}$  and  $\underline{\underline{H}}$ , the equation block (9.40a)-(9.40d) constitutes a system of  $4(M_{ion} + 1)$  scalar equations for the  $4(M_{ion} + 1)$  scalar dependent variables  $n_\alpha$ ,  $[\underline{v}_\alpha]_i$ ,  $p_f$ ,  $[\underline{v}_f]_i$ ,  $i = 1, 2, 3$ . Similarly, for given  $n_\alpha$ ,  $\underline{v}_\alpha$  and  $\beta_\alpha$ , the equation block (9.40e)-(9.40h) constitutes a system of 8 scalar equations characterizing the curl and the divergence of the electric field  $\underline{\underline{E}}$  and of the magnetic field  $\underline{\underline{H}}$  (see Section 2.6.7.2).

*Balance equations for the mixture.* Proceeding as in Section 8.2, the balance of mass for the mixture can be obtained by adding (9.30a) and (9.22a) for  $\alpha = 1, \dots, M_{ion}$ , to

write

$$\frac{\partial \rho_m}{\partial t} + \nabla_{\underline{x}} \cdot (\rho_m \underline{v}_m) = \beta_m \quad (9.41)$$

where

$$\rho_m := \rho_f + \sum_{\alpha=1}^{M_{ion}} \rho_\alpha, \quad \underline{v}_m := \frac{1}{\rho_m} \left( \rho_f \underline{v}_f + \sum_{\alpha=1}^{M_{ion}} \rho_\alpha \underline{v}_\alpha \right), \quad \beta_m = \sum_{\alpha=1}^{M_{ion}} \beta_\alpha.$$

Similarly, the balance of linear momentum for the mixture can be obtained by adding (9.30b) and (9.22c) for  $\alpha = 1, \dots, M_{ion}$  to write

$$\begin{aligned} \rho_m \frac{\partial \underline{v}_m}{\partial t} + \rho_m (\underline{v}_m \cdot \nabla_{\underline{x}}) \underline{v}_m + \beta_m \underline{v}_m &= \nabla_{\underline{x}} \cdot \left( -p_f \underline{I} + 2\mu_f \underline{\underline{D}}(\underline{v}_f) - \rho_f \underline{w}_f \otimes \underline{w}_f \right) \\ &+ \nabla_{\underline{x}} \cdot \left( -K_B \Theta \sum_{\alpha=1}^{M_{ion}} n_\alpha \underline{I} + \sum_{\alpha=1}^{M_{ion}} \lambda_\alpha (\nabla_{\underline{x}} \cdot \underline{v}_\alpha) \underline{I} + 2 \sum_{\alpha=1}^{M_{ion}} \mu_\alpha \underline{\underline{D}}(\underline{v}_\alpha) - \sum_{\alpha=1}^{M_{ion}} \rho_\alpha \underline{w}_\alpha \otimes \underline{w}_\alpha \right) \\ &+ \rho_m \underline{g} + q \sum_{\alpha=1}^{M_{ion}} z_\alpha n_\alpha (\underline{E} + \underline{v}_\alpha \times \underline{B}) \end{aligned} \quad (9.42)$$

where

$$\underline{w}_f := \underline{v}_f - \underline{v}_m \quad \text{and} \quad \underline{w}_\alpha := \underline{v}_\alpha - \underline{v}_m.$$

## 9.5. The velocity-extended Poisson-Nernst-Planck model

In this section, we show that the classic velocity-extended Poisson-Nernst-Planck model for ion electrodynamics theoretically studied in [105, 62, 111, 64] and numerically investigated in [76, 63, 75, 109, 4, 108, 81] is a special instance of the formulation studied in Section 9.4. To this end, let us make the following assumptions:

- net production terms  $\beta_\alpha = 0$  for every  $\alpha = 1, \dots, M_{ion}$ , thereby implying that the system is closed with respect to both mass and electric charge. Thus, Remark 9.8 allows us to set  $\underline{\phi} = \underline{0}$  in (9.37);
- temporal variation of the magnetic induction field  $\underline{B}$  is negligible in comparison with the spatial variation of the electric field  $\underline{E}$  (quasi-static approximation, see Remark 3.2), thereby reducing Faraday’s law (2.44a) to  $\nabla \times \underline{E} = \underline{0}$  and, as a consequence, obtaining  $\underline{E} = -\nabla_{\underline{x}} \psi$ , where  $\psi$  is the electric potential;
- contribution of the magnetic field  $\underline{H}$  is small in comparison with that of the electric field  $\underline{E}$  in the equation block (9.40e)-(9.40h), thereby allowing us to neglect the term  $\mu_m \underline{v}_\alpha \times \underline{H}$  in the right-hand side of the linear momentum balance (9.40b) and the term  $\nabla_{\underline{x}} \times \underline{H}$  in (9.40f), and to reduce Equation (9.40h) to the trivial identity  $0 = 0$ ;
- resistances to compression in the description of the ion components of the mixture

- are negligible, thereby implying  $\lambda_\alpha = 0$  for every  $\alpha = 1, \dots, M_{ion}$ ;
- shear viscous effects in the description of the ion components of the mixture are negligible, thereby implying  $\mu_\alpha = 0$  for every  $\alpha = 1, \dots, M_{ion}$ ;
- drag viscous effects among ion components of the mixture are negligible, thereby implying  $c_{\alpha\gamma=0}$  for every  $\alpha, \gamma = 1, \dots, M_{ion}$ ;
- the viscous drag coefficient  $c_{\alpha f}$  between the ion species  $\alpha$  and the fluid can be characterized using Stokes' drag theory as

$$c_{\alpha f} = 6\pi\mu_f R_{h,\alpha} n_\alpha \quad (9.43)$$

where  $\mu_f$  is the dynamic viscosity (or shear viscosity) of the fluid (units:  $\text{Kg m}^{-1}\text{s}^{-1}$ ),

$$R_{h,\alpha} = \frac{K_B\Theta}{6\pi\mu_f D_\alpha} \quad (9.44)$$

is the hydrodynamic radius of the ion species  $\alpha$  and  $D_\alpha$  is the molecular diffusion coefficient of the ion species  $\alpha$  in the fluid (units:  $\text{m}^2\text{s}^{-1}$ );

- Einstein's relation holds true, thereby implying that

$$D_\alpha = \frac{K_B\Theta}{q|z_\alpha|} \mu_\alpha^{el} \quad \alpha = 1, \dots, M_{ion}, \quad (9.45)$$

where  $\mu_\alpha^{el}$  is the *electric mobility* of the ion component  $\alpha$  of the charged mixture (units:  $\text{Vm}^{-2}\text{s}^{-1}$ );

- inertial terms are negligible for each component of the mixture, thereby implying

$$\frac{D_\alpha \underline{\mathbf{v}}_f}{Dt} = \frac{\partial \underline{\mathbf{v}}_f}{\partial t} + (\underline{\mathbf{v}}_f \cdot \nabla \underline{\mathbf{x}}) \underline{\mathbf{v}}_f = \underline{\mathbf{0}} \quad \text{and} \quad \frac{D_\alpha \underline{\mathbf{v}}_\alpha}{Dt} = \frac{\partial \underline{\mathbf{v}}_\alpha}{\partial t} + (\underline{\mathbf{v}}_\alpha \cdot \nabla \underline{\mathbf{x}}) \underline{\mathbf{v}}_\alpha = \underline{\mathbf{0}}$$

for every  $\alpha = 1, \dots, M_{ion}$ ;

- the effects of the gravitational field are negligible.

Under the above assumptions, the equation system (9.40) reduces to:

$$\frac{\partial n_\alpha}{\partial t} + \nabla \underline{\mathbf{x}} \cdot (n_\alpha \underline{\mathbf{v}}_\alpha) = 0, \quad (9.46a)$$

$$- K_B\Theta \nabla \underline{\mathbf{x}} n_\alpha + q z_\alpha n_\alpha \underline{\mathbf{E}} - c_{\alpha f} (\underline{\mathbf{v}}_\alpha - \underline{\mathbf{v}}_f) = \underline{\mathbf{0}} \quad (9.46b)$$

$$\nabla \underline{\mathbf{x}} \cdot \underline{\mathbf{v}}_f = 0 \quad (9.46c)$$

$$- \nabla \underline{\mathbf{x}} p_f + 2\mu_f \nabla \underline{\mathbf{x}} \cdot \underline{\mathbf{D}}(\underline{\mathbf{v}}_f) - \sum_{\alpha=1}^{M_{ion}} c_{\alpha f} (\underline{\mathbf{v}}_f - \underline{\mathbf{v}}_\alpha) = \underline{\mathbf{0}} \quad (9.46d)$$

$$\varepsilon_m \frac{\partial \underline{\mathbf{E}}}{\partial t} + \sum_{\alpha=1}^{M_{ion}} q z_\alpha n_\alpha \underline{\mathbf{v}}_\alpha = \underline{\mathbf{0}} \quad (9.46e)$$

$$\varepsilon_m \nabla_{\underline{x}} \cdot \underline{\mathbf{E}} = \sum_{\alpha=1}^{M_{ion}} q z_\alpha n_\alpha \quad (9.46f)$$

$$\underline{\mathbf{E}} = -\nabla_{\underline{x}} \psi. \quad (9.46g)$$

Combining (9.46b) and (9.46d), we get the following reduced balance law for the linear momentum of the fluid mixture

$$-\nabla_{\underline{x}} p_f + 2\mu_f \nabla_{\underline{x}} \cdot \underline{\mathbf{D}}(\underline{\mathbf{v}}_f) - \sum_{\alpha=1}^{M_{ion}} K_B \Theta \nabla_{\underline{x}} n_\alpha + \sum_{\alpha=1}^{M_{ion}} q z_\alpha n_\alpha \underline{\mathbf{E}} = \underline{0}. \quad (9.47)$$

Let us now rewrite the above system of equations in a more traditional form in the context of ion electrodiffusion (see, e.g., [106]). Dividing the momentum balance equation (9.46b) by the quantity  $c_{af}$  and using (9.45), we obtain the following constitutive equation for the flux density  $n_\alpha \underline{\mathbf{v}}_\alpha$  (units:  $\text{m}^{-2}\text{s}^{-1}$ ) of the ion component  $\alpha$  of the charged mixture:

$$\underline{\mathbf{f}}_\alpha := n_\alpha \underline{\mathbf{v}}_\alpha \quad \alpha = 1, \dots, M_{ion}, \quad (9.48a)$$

$$n_\alpha \underline{\mathbf{v}}_\alpha = n_\alpha \underline{\mathbf{v}}_f + \mu_\alpha^{el} \frac{z_\alpha}{|z_\alpha|} \underline{\mathbf{E}} - D_\alpha \nabla_{\underline{x}} n_\alpha \quad \alpha = 1, \dots, M_{ion}. \quad (9.48b)$$

The flux density (9.48a) is the sum of three distinct contributions:

- the convective flux density due to the drifting effect of the velocity of the fluid component on the charged particles

$$\underline{\mathbf{f}}_{\alpha,c,fl} = n_\alpha \underline{\mathbf{v}}_f;$$

- the convective flux density due to the drifting effect of the electric field on the charged particles

$$\underline{\mathbf{f}}_{\alpha,c,\underline{\mathbf{E}}} = \mu_\alpha^{el} \frac{z_\alpha}{|z_\alpha|} n_\alpha \underline{\mathbf{E}};$$

- the diffusive flux density due to the molecular ion diffusion process, described by Fick’s law

$$\underline{\mathbf{f}}_{\alpha,c,diff} = -D_\alpha \nabla_{\underline{x}} n_\alpha.$$

Combining the above results and neglecting the compatibility condition (9.46e), we obtain the following simplified system of partial differential equations that describe the mixture dynamics:

$$\frac{\partial n_\alpha}{\partial t} + \nabla_{\underline{x}} \cdot \underline{\mathbf{f}}_\alpha = 0 \quad (9.49a)$$

$$\underline{\mathbf{f}}_\alpha = n_\alpha \underline{\mathbf{v}}_f + \mu_\alpha^{el} \frac{z_\alpha}{|z_\alpha|} n_\alpha \underline{\mathbf{E}} - D_\alpha \nabla_{\underline{x}} n_\alpha, \quad (9.49b)$$

$$\nabla_{\underline{x}} \cdot \underline{\mathbf{v}}_f = 0 \quad (9.49c)$$

$$-2\mu_f \nabla_{\underline{x}} \cdot \underline{\mathbf{D}}(\underline{\mathbf{v}}_f) + \nabla_{\underline{x}} p_f = \underline{\mathbf{F}}_{ef} \quad (9.49d)$$

$$\underline{\mathbf{F}}_{ef} = - \sum_{\alpha=1}^{M_{ion}} K_B \Theta \nabla_{\underline{x}} n_\alpha + \sum_{\alpha=1}^{M_{ion}} q z_\alpha n_\alpha \underline{\mathbf{E}} \quad (9.49e)$$

$$\epsilon_m \nabla_{\underline{x}} \cdot \underline{\mathbf{E}} = q \sum_{\alpha=1}^{M_{ion}} z_\alpha n_\alpha \quad (9.49f)$$

$$\underline{\mathbf{E}} = -\nabla_{\underline{x}} \psi. \quad (9.49g)$$

We emphasize that Equation (9.49d) describes the balance of linear momentum for the *whole mixture* and not for the fluid only. System (9.49) is a set of  $4(M_{ion} + 1) + 4$  scalar differential equations in the  $4(M_{ion} + 1) + 4$  scalar dependent variables  $n_\alpha$ ,  $[\underline{\mathbf{f}}_\alpha]_i$ ,  $i = 1, 2, 3$ ,  $p_f$ ,  $(\underline{\mathbf{v}}_f)_i$ ,  $i = 1, 2, 3$ ,  $\psi$  and  $[\underline{\mathbf{E}}]_i$ ,  $i = 1, 2, 3$ . Its solution can be computed upon prescribing initial conditions for  $n_\alpha$  and  $\underline{\mathbf{v}}_f$  as well as boundary conditions for  $n_\alpha$ ,  $\underline{\mathbf{f}}_\alpha$ ,  $p_f$ ,  $\underline{\mathbf{v}}_f$ ,  $\psi$  and  $\underline{\mathbf{E}}$  on the boundary of  $\Omega_t$ .

The term  $n_\alpha \underline{\mathbf{v}}_f$  in (9.49b) and the term  $\underline{\mathbf{F}}_{ef}$  in (9.49d) express the *coupling* between ion and fluid dynamics within the charged mixture. In particular, the presence of the advective fluid velocity in (9.49b) gives to the equation system (9.49) the name of *velocity-extended Poisson-Nernst-Planck (VE-PNP) model*. We also notice that the volume force density  $\underline{\mathbf{F}}_{ef}$  in (9.49e) embodies two effects, one due to gradients in number densities of each ion species and one due to the action of the electric field.

## 9.6. The Poisson-Nernst-Planck model

The basic PNP model is obtained by completely neglecting in the VE-PNP system (9.49) the presence of the fluid component in the mixture, which gives:

$$\frac{\partial n_\alpha}{\partial t} + \nabla_{\underline{x}} \cdot \underline{\mathbf{f}}_\alpha = 0 \quad (9.50a)$$

$$\underline{\mathbf{f}}_\alpha = \mu_\alpha^{el} \frac{z_\alpha}{|z_\alpha|} n_\alpha \underline{\mathbf{E}} - D_\alpha \nabla_{\underline{x}} n_\alpha \quad (9.50b)$$

$$\epsilon_m \nabla_{\underline{x}} \cdot \underline{\mathbf{E}} = q \sum_{\alpha=1}^{M_{ion}} z_\alpha n_\alpha \quad (9.50c)$$

$$\underline{\mathbf{E}} = -\nabla_{\underline{x}} \psi. \quad (9.50d)$$

System (9.50) is a set of  $4M_{ion} + 4$  scalar equations in the  $4M_{ion} + 4$  scalar dependent variables  $n_\alpha$ ,  $[\underline{\mathbf{f}}_\alpha]_i$ ,  $i = 1, 2, 3$ ,  $\psi$  and  $[\underline{\mathbf{E}}]_i$ ,  $i = 1, 2, 3$ . Its solution can be obtained upon prescribing initial conditions for  $n_\alpha$  as well as boundary conditions for  $n_\alpha$ ,  $\psi$  and  $\underline{\mathbf{E}}$  on the boundary of  $\Omega_t$ . The PNP model (9.50) is the most widely used continuum-based approach to study the electrophysiological behavior of excitable cells and of

protein ion channels that are present on their membrane. For a complete analysis and discussion of this application we refer to [105, 13, 15, 94, 14, 63, 19, 109, 4, 108]

**Remark 9.9** (The electrochemical potential). *Replacing (9.50d) into (9.50b), collecting out  $\mu_\alpha^{el} n_\alpha z_\alpha / |z_\alpha|$  and using (9.45), we can write the ion momentum balance equation in the following equivalent form:*

$$\underline{\mathbf{f}}_\alpha = -\mu_\alpha^{el} \frac{z_\alpha}{|z_\alpha|} n_\alpha \nabla_{\underline{\mathbf{x}}} \varphi_\alpha^{ec} \quad \alpha = 1, \dots, M_{ion}, \quad (9.51a)$$

$$\varphi_\alpha^{ec} := \psi + \frac{V_{th}}{z_\alpha} \ln \left( \frac{n_\alpha}{n_{ref}} \right) \quad \alpha = 1, \dots, M_{ion}, \quad (9.51b)$$

where  $\varphi_\alpha^{ec}$  is the electrochemical potential associated with the ion species  $\alpha$ ,  $V_{th} := D_\alpha |z_\alpha| / \mu_\alpha^{el}$  is the thermal voltage (units: V) and  $n_{ref}$  is a positive constant that has the physical meaning of a reference number density. Noticeably, by inverting (9.51b) we see that in the case of the basic PNP system, the ion number densities are related to the electric and electrochemical potentials through the so-called generalized Maxwell-Boltzmann statistics

$$n_\alpha = n_{ref} \exp \left( \frac{z_\alpha (\varphi_\alpha^{ec} - \psi)}{V_{th}} \right) \quad \alpha = 1, \dots, M_{ion}. \quad (9.51c)$$

The above relation suggests that even a small variation in the distance between the electrochemical and electric potential may result into a significant variation in the ion number density. This, in turn, may therefore significantly modify the local conductivity  $\sigma_\alpha$  (units:  $\Omega m^{-1}$ ) of the  $\alpha$  ion component of the mixture, that is defined as

$$\sigma_\alpha := q |z_\alpha| \mu_\alpha^{el} n_\alpha \quad \alpha = 1, \dots, M_{ion}. \quad (9.51d)$$

**Remark 9.10** (The condensed PNP system). *By eliminating the vector variables  $\underline{\mathbf{f}}_\alpha$  and  $\underline{\mathbf{E}}$  in favor of the scalar variables  $n_\alpha$  and  $\psi$ , the PNP system (9.50) reduces to the following sets of PDEs:*

$$\frac{\partial n_\alpha}{\partial t} + \nabla \cdot \left( -\mu_\alpha^{el} \frac{z_\alpha}{|z_\alpha|} n_\alpha \nabla \psi - D_\alpha \nabla_{\underline{\mathbf{x}}} n_\alpha \right) = 0, \quad (9.52a)$$

$$\nabla_{\underline{\mathbf{x}}} \cdot (-\varepsilon_m \nabla_{\underline{\mathbf{x}}} \psi) = q \sum_{\alpha=1}^{M_{ion}} z_\alpha n_\alpha. \quad (9.52b)$$

**Remark 9.11** (The ion current density). *We associate with the flux density  $\underline{\mathbf{f}}_\alpha$ , see (9.48a), the ion current density  $\underline{\mathbf{J}}_\alpha$ ,  $\alpha = 1, \dots, M_{ion}$  defined as*

$$\underline{\mathbf{J}}_\alpha = q z_\alpha \underline{\mathbf{f}}_\alpha = q |z_\alpha| \mu_\alpha^{el} n_\alpha \underline{\mathbf{E}} - q z_\alpha D_\alpha \nabla_{\underline{\mathbf{x}}} n_\alpha. \quad (9.53a)$$

*In the definition (9.53a) we identify two contributions:*

- the drift current density due to the translational force exerted by the electric field

on the charged particles

$$\underline{\mathbf{J}}_{\alpha,drift} = q\mu_a^{el}|z_\alpha|n_a\underline{\mathbf{E}}; \quad (9.53b)$$

- the diffusive current density due to the molecular ion diffusion process, described by Fick's law

$$\underline{\mathbf{J}}_{\alpha,diff} = -qz_\alpha D_\alpha \nabla_{\underline{\mathbf{x}}} n_\alpha. \quad (9.53c)$$

The vector  $\underline{\mathbf{J}}_\alpha$  has the units of  $\text{Am}^{-2}$ . This corresponts to the Nernst-Planck definition 5.3 of the transmembrane current.

**Remark 9.12** (Thermodynamic equilibrium). We define that the ionic species  $\alpha$  is under the thermodynamic equilibrium if

$$J_\alpha(\underline{\mathbf{x}}) = 0 \quad \underline{\mathbf{x}} \in \Omega_t. \quad (9.54)$$

## 9.7. The Drift-Diffusion model for semiconductors

The PNP system for the description of ion electrodynamics that was described in Section 9.6 has used since the 50s to mathematically investigate the flow of electrons and holes in a semiconductor material. Let us consider a mixture composed by three charged components:

- electrons, whose number density will be denoted by  $n_1 = n$  and  $z_1 = -1$ ;
- holes, whose number density will be denoted by  $n_2 = p$  and  $z_2 = +1$  ;
- ionized dopant impurities, whose number density will be denoted by  $n_3 = \text{Dop}$ .

Let also assume that the net generation rate for electron and hole is not null while the ones related to the impurities remains null:

- electrons,  $b_1 = b_n$ ;
- holes,  $b_2 = b_p$  ;
- ionized dopant impurities,  $b_{\text{Dop}} = 0$ .

Electrons and holes are described as mobile charges whose velocities are denoted by  $\underline{\mathbf{v}}_n$  and  $\underline{\mathbf{v}}_p$  respectively. The ionized dopant impurities are assumed to be fixed charges within the crystalline lattice and, therefore, their velocity is equal to zero resulting in  $\underline{\mathbf{J}}_{\text{Dop}} = \underline{\mathbf{0}}$ . As a consequence the mass balance equation for the impurities ensures that the inpuity are also constant in time: so we can neglect both mass and linear momentum equation for the impurities. By multiplying times  $q$  the mass balance equations and using (9.53a) we get:

$$q \frac{\partial n}{\partial t} - \nabla_{\underline{\mathbf{x}}} \cdot \underline{\mathbf{J}}_n = qb_n \quad (9.55a)$$

$$q \frac{\partial p}{\partial t} + \nabla_{\underline{\mathbf{x}}} \cdot \underline{\mathbf{J}}_p = qb_p \quad (9.55b)$$

$$\underline{\mathbf{J}}_n = q\mu_n^{el}n\underline{\mathbf{E}} + qD_n \nabla_{\underline{\mathbf{x}}} n \quad (9.55c)$$

$$\underline{\mathbf{J}}_p = q\mu_p^{el} p \underline{\mathbf{E}} - qD_p \nabla_{\underline{x}} p \quad (9.55d)$$

$$\nabla_{\underline{x}} \cdot (\varepsilon_{sem} \underline{\mathbf{E}}) = q \text{Dop} + qp - qn \quad (9.55e)$$

$$\underline{\mathbf{E}} = -\nabla_{\underline{x}} \psi. \quad (9.55f)$$

In writing (9.55) it is understood that Dop is a given function of the spatial position  $\underline{x}$  inside the semiconductor material and that Dop does not vary with time. The DD model was proposed in the form (9.55) and analyzed for the first time in [100]. The scalar dependent variables are the electron number density  $n$ , the hole number density  $p$  and the electric potential  $\psi$ , whereas the vector-valued dependent variables are the electron and hole current densities  $\underline{\mathbf{J}}_n, \underline{\mathbf{J}}_p$  (units:  $\text{Am}^{-2}$ ) and the electric field  $\underline{\mathbf{E}}$  (units:  $\text{Vm}^{-1}$ ).

The quantity  $q \text{Dop}$  at the right-hand side of the Poisson equation (9.55e) is a given function of position and physically represents the net doping profile of the semiconductor material. We notice that, unlike the case of the ion electrodynamics model (9.50), the net charge density generation rates for electron and hole are not null and can be written as  $qb_n = q(G_n - R_n)$  and  $qb_p = q(G_p - R_p)$  (units:  $\text{Cm}^{-3}\text{s}^{-1}$ ).

The mathematical form of these rates is rather complex and for their description and physical interpretation we refer to [113, Chapter 4].

The DD system (9.55) is the most widely used mathematical modeling tool for the simulation of semiconductor devices in modern electronics technology. We refer to the books [113, 79, 80, 61, 77] for an extensive description of the physical models employed to describe the transport parameters  $\mu_n, \mu_p, D_n, D_p$ , the generation/recombination rates  $G_n, R_n, G_p$  and  $R_p$ , the net doping profile Dop, the boundary/initial conditions as well as the properties of existence and uniqueness of the solution, the convergence of the linearization solution maps and the accuracy/stability of the spatial and temporal discretization schemes that are adopted in contemporary numerical software.

**Remark 9.13** (Boltzmann distribution for electron and hole). *The application of Remark 9.9 to the DD system (9.50) leads to the Maxwell-Boltzmann statistics (9.51c) for electrons and holes:*

$$n = n_{int} \exp\left(\frac{\psi - \varphi_n}{V_{th}}\right), \quad (9.56a)$$

$$p = n_{int} \exp\left(\frac{\varphi_p - \psi}{V_{th}}\right), \quad (9.56b)$$

where the constant positive quantity  $n_{int}$  is the intrinsic concentration in the semiconductor material, physically representing the number density of electrons and holes that are available for electric conduction if  $\text{Dop}=0$  (see [89, Chapter 1]) and the electro-

chemical potential are defined as:

$$\varphi_n = \psi - V_{th} \ln \frac{n}{n_{int}}, \quad (9.57a)$$

$$\varphi_p = \psi + V_{th} \ln \frac{p}{n_{int}}, \quad (9.57b)$$

In section we will review this concept introducing the Fermi distribution that leads to the psudo-fermi potential.

**Remark 9.14** (Generalized Ohm’s law). *The electron  $\underline{\mathbf{J}}_n$  and hole  $\underline{\mathbf{J}}_p$  current density appearing in the DD system (9.55) leads to the following expressions of the current densities:*

$$\underline{\mathbf{J}}_n = \sigma_n \underline{\mathbf{E}}_n, \quad (9.58a)$$

$$\underline{\mathbf{J}}_p = \sigma_p \underline{\mathbf{E}}_p, \quad (9.58b)$$

where:

$$\underline{\mathbf{E}}_n := -\nabla_{\underline{\mathbf{x}}} \varphi_n, \quad (9.59a)$$

$$\underline{\mathbf{E}}_p := -\nabla_{\underline{\mathbf{x}}} \varphi_p, \quad (9.59b)$$

are the electrochemical fields responsible for charge motion inside the material,  $\varphi_n$ ,  $\varphi_p$  are the electron and hole electrochemical potentials, and  $\sigma_n = q\mu_n^{el}n$ ,  $\sigma_p = q\mu_p^{el}p$  are the electric conductivities of electrons and holes, respectively. Relations (9.58) can be interpreted as generalized Ohm’s laws for electrons and holes in a semiconductor material.

**Remark 9.15** (Thermodynamic equilibrium of the semiconducotor). *We define that the semiconductor occupying the space region  $\Omega_t$  is under the thermodynamic equilibrium if*

$$J_n(\underline{\mathbf{x}}) = J_p(\underline{\mathbf{x}}) = 0 \quad \underline{\mathbf{x}} \in \Omega_t. \quad (9.60)$$

**Remark 9.16** (Generation and recombinaton at thermodynamic equilibrium). *The condition of thermodynamic equilibrium in the semiconductor material corresponds also to require that the net recombination rate is equal to zero at each point of the material and at each time level*

$$G_n(\underline{\mathbf{x}}, t) - R_n(\underline{\mathbf{x}}, t) = 0 \quad \text{for } \underline{\mathbf{x}} \in \Omega_t, t \in (0, T) \quad (9.61a)$$

$$G_p(\underline{\mathbf{x}}, t) - R_p(\underline{\mathbf{x}}, t) = 0 \quad \text{for } \underline{\mathbf{x}} \in \Omega_t, t \in (0, T) \quad (9.61b)$$

“Notes” — 2019/5/17 — 17:39 — page 162 — #170

## CHAPTER 10

# The Poisson-Nernst-Planck model in 1D-framework

In this chapter we consider the PNP model illustrated in Sect. 9.6 in the case of a one-dimensional (1D) channel geometry. In particular, we derive a reduced boundary-value initial-value differential problem starting from a multi-domain partition of the intra and extracellular environments, for which appropriate boundary conditions are provided at the entrance and outlet sections of the channel. Our presentation is based on [26] to which we refer for all the biophysical details.

### 10.1. 1-D geometrical model

We illustrate in Fig. 10.1 the schematic representation of a cross-section of a biological channel, assuming rotational invariance around the channel axis ( $x$  axis) (see [26]).

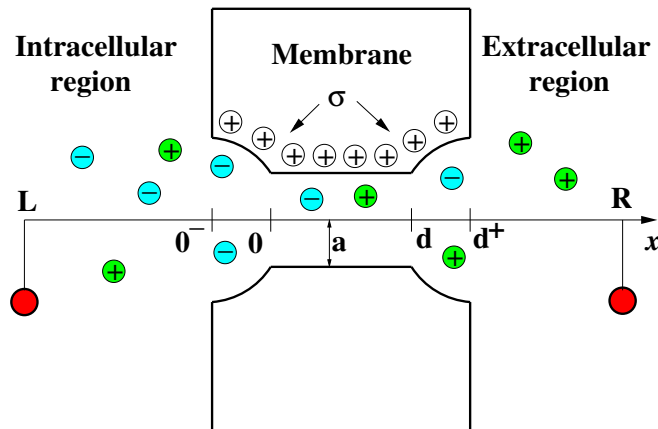


**Figure 10.1** Schematic view of the biophysical problem. Five regions can be distinguished. From left to right: intracellular bathing solution, antechamber, channel region, antechamber, bathing solution in the extracellular side. At the endpoints,  $x = 0$  and  $x = L$ , terminal contacts are marked in red color.

The red bullets at the endpoints of the domain,  $x = L$  and  $x = R$ , are the terminals of a Cellular Electrophysiology equipment, and represent the physical places where the electrical potential is fixed and the solution intra and extra-cellular concentrations are accessible to experimental measurements. Then, five spatial regions can be distinguished, ordered from left to right:

1. Region 1,  $L \leq x \leq 0^-$ : this is the bathing solution in the intracellular side.
2. Region 2,  $0^- < x \leq 0$ : this is the channel antechamber (or access region) from the intracellular side.
3. Region 3,  $0 \leq x < d$ : this is the channel region.
4. Region 4,  $d \leq x < d^+$ : this is the channel antechamber from the extracellular side.
5. Region 5,  $d^+ \leq x \leq R$ : this is the bathing solution in the extracellular side.

Finally, two kinds of charges can be identified in Fig. 10.1:

- a fixed charge density  $\sigma$  (units  $\text{Cm}^{-2}$ ) uniformly distributed over the surface of the channel;
- a mobile charge density  $\rho_{mob}$  (units  $\text{Cm}^{-3}$ ) of cations and anions that are flowing through the channel fluid under the action of electrodiffusive forces.

The mobile charge density accounts for the transmembrane current as defined in 5.20a. The surface charge density accounts for fixed ion charges that are trapped within the aminoacid structure of the protein that is located in the bilayer (porous) lipid structure constituting the cellular membrane and that unfolds the channel region. The surface charge density  $\sigma$  has the effect to modify the motion of cations and anions throughout the channel because if  $\sigma < 0$  cations are attracted while anions are repelled and the opposite occurs if  $\sigma > 0$ .

The surface charge density  $\sigma$  can be accounted for in the term  $\rho_{fix}$  at the right-hand side of the differential Gauss law (14.13d) as follows. Let  $x$  and  $x + dx$  be two points along the channel axis and let  $d\Sigma_{lat}(x) = 2\pi a(x)dx$  denote the infinitesimal lateral surface of the channel,  $a(x)$  being the value at  $x$  of the radius of the channel circular cross-section. The infinitesimal fixed charge distributed over  $d\Sigma_{lat}(x)$  is

$$dQ_\sigma(x) = \sigma(x)2\pi a(x)dx.$$

The volumetric fixed charge  $\rho_{fix}(x)$  contained in the infinitesimal volume  $dV(x) = \pi a(x)^2 dx$  is

$$dQ_V(x) = \rho_{fix}(x)\pi a(x)^2 dx$$

so that, equating the two infinitesimal charges we find

$$\rho_{fix}(x) = \frac{dQ_\sigma(x)}{\pi a^2(x)dx} = \frac{2\sigma(x)}{a(x)}.$$

Therefore, the volumetric concentration  $P(x)$  (units  $\text{m}^{-3}$ ) of fixed (or permanent) ions in the channel electrostatically equivalent to the surface concentration  $\sigma(x)/q$  (units

$\text{m}^{-2}$ ) of fixed (or permanent) ions located on the membrane lipid bilayer is

$$P(x) = \frac{\rho_{fix}(x)}{q} = \frac{2\sigma(x)}{qa(x)}. \quad (10.1)$$

## 10.2. Biophysical assumptions for 1-D framework

The endpoints of the domain,  $x = L$  and  $x = R$ , are located sufficiently far from the antechamber and channel regions, in such a way that appropriate equilibrium conditions can be applied. More importantly, the endpoints are assumed to be the physical place where the solution intra and extra-cellular electrochemical conditions are accessible to experimental measurements. Because of this, following [25, 26], we assume that at  $x = L$  and  $x = R$ :

(A1) the electric potential  $\psi$  is a known given quantity of time, so that:

$$\psi(L, t) = \psi_L(t) \quad (10.2a)$$

$$\psi(R, t) = \psi_R(t); \quad (10.2b)$$

(A2) the ion concentrations  $n_\alpha$  are known given quantities of time, so that:

$$n_\alpha(L, t) = n_{\alpha,L}(t), \quad \alpha = 1, \dots, M_{ion} \quad (10.2c)$$

$$n_\alpha(R, t) = n_{\alpha,R}(t), \quad \alpha = 1, \dots, M_{ion} \quad (10.2d)$$

where  $M_{ion} \geq 1$  is the number of ions flowing in the cellular solution. For each  $\alpha = 1, \dots, M_{ion}$ , we set  $n_{\alpha,L}^{max} = \max_{t \in [0, T]} n_{\alpha,L}(t)$  and  $n_{\alpha,R}^{max} = \max_{t \in [0, T]} n_{\alpha,R}(t)$ . The boundary values for the ion concentrations satisfy the electroneutrality constraint at each time level  $t$ :

$$\sum_{\alpha=1}^{M_{ion}} z_\alpha n_{\alpha,L}(t) = 0 \quad (10.2e)$$

$$\sum_{\alpha=1}^{M_{ion}} z_\alpha n_{\alpha,R}(t) = 0 \quad (10.2f)$$

where  $z_\alpha$  is the charge number associated with each ion species  $\alpha$  ( $z_\alpha > 0$  for cations,  $z_\alpha < 0$  for anions and  $z_\alpha = 0$  for neutral species).

We assume also that the thermodynamical equilibrium condition in the bathing regions for each ion species  $\alpha$  holds for each time level  $t$ ; this corresponds to:

(A3)

$$J_\alpha(x, t) = 0 \quad L \leq x \leq 0^-, \quad \alpha = 1, \dots, M_{ion} \quad (10.2g)$$

$$J_\alpha(x, t) = 0 \quad d^+ \leq x \leq R, \quad i = \alpha, \dots, M_{ion}. \quad (10.2h)$$

We make the following assumptions within the antechamber regions:

(A4) electroneutrality holds at the channel mouth entrances:

$$qP(0^-, t) + q \sum_{\alpha=1}^{M_{ion}} z_\alpha n_\alpha(0^-, t) = 0 \quad (10.2i)$$

$$qP(d^+, t) + q \sum_{\alpha=1}^{M_{ion}} z_\alpha n_\alpha(d^+, t) = 0; \quad (10.2j)$$

(A5) the electric potential is spatially constant:

$$\psi(x, t) = \psi(0^-, t) \quad 0^- \leq x \leq 0 \quad (10.2k)$$

$$\psi(x, t) = \psi(d^+, t) \quad d^- \leq x \leq d^+; \quad (10.2l)$$

(A6) the ion concentrations are spatially constant:

$$n_\alpha(x, t) = n_\alpha(0^-, t) \quad 0^- \leq x \leq 0 \quad \alpha = 1, \dots, M_{ion} \quad (10.2m)$$

$$n_\alpha(x, t) = n_\alpha(d^+, t) \quad d^- \leq x \leq d^+ \quad \alpha = 1, \dots, M_{ion}. \quad (10.2n)$$

### 10.3. Calculation of the Boundary conditions at channel openings

In this section, using the geometrical representation of the problem of Sect. 10.1 and the assumptions in Sect. 10.2 we derive the boundary conditions for PNP Model of Sec. 9.6 at  $x = 0$  and  $x = d$  (channel openings). Using (A3) at each time level  $t$  and the remark 9.9 we get the following

$$\varphi_\alpha^{ec}(x, t) = \text{const} =: \overline{\varphi}_{\alpha,L}^{ec}(t) \quad L \leq x \leq 0^- \quad \alpha = 1, \dots, M_{ion} \quad (10.3a)$$

$$\varphi_\alpha^{ec}(x, t) = \text{const} =: \overline{\varphi}_{\alpha,R}^{ec}(t) \quad d^+ \leq x \leq R \quad \alpha = 1, \dots, M_{ion} \quad (10.3b)$$

where  $\overline{\varphi}_{\alpha,L}^{ec}(t)$  and  $\overline{\varphi}_{\alpha,R}^{ec}(t)$ ,  $\alpha = 1, \dots, M_{ion}$ , are to be determined. Using (A2) in the equations above at  $z = L$  and  $z = R$ , respectively, and the Maxwell-Boltzmann (MB) statistics 9.51c we obtain, for each time level  $t$ , the boundary values for the electrochemical potential:

$$\overline{\varphi}_{\alpha,L}^{ec}(t) = \psi_L(t) + \frac{V_{th}}{z_\alpha} \ln \left( \frac{n_{\alpha,L}(t)}{n_{ref}} \right) \quad \alpha = 1, \dots, M_{ion} \quad (10.4a)$$

$$\overline{\varphi}_{\alpha,R}^{ec}(t) = \psi_R(t) + \frac{V_{th}}{z_\alpha} \ln \left( \frac{n_{\alpha,R}(t)}{n_{ref}} \right) \quad \alpha = 1, \dots, M_{ion}. \quad (10.4b)$$

From the previous discussion, we see that the electrochemical potentials are spatially constant in the bathing regions, but this does not necessarily mean that also the electric potential and the ion concentrations are constant in those regions. On the contrary, it is expected that these quantities experience a spatial variation in such a way that diffusive and drift current densities mutually cancel out each other to ensure the

equilibrium conditions (10.2g)-(10.2h). This means that it makes sense to introduce the voltage drops occurring across the bathing solution regions, the so-called *built-in potentials*:

$$\varphi_{bi}(0^-, t) =: \psi(L, t) - \psi(0^-, t) \quad (10.5a)$$

$$\varphi_{bi}(d^+, t) =: \psi(d^+, t) - \psi(R, t). \quad (10.5b)$$

To determine the built-in potentials we enforce the charge neutrality conditions (10.2i) and (10.2j) obtaining, at  $x = 0^-$ :

$$\begin{aligned} P(0^-) + \sum_{\alpha=1}^{M_{ion}} z_\alpha n_\alpha(0^-, t) &= P(0^-) + \sum_{\alpha=1}^{M_{ion}} z_\alpha n_{ref} \exp\left(z_\alpha \frac{(\varphi_{\alpha}^{ec}(0^-, t) - \psi(0^-, t))}{V_{th}}\right) \\ &= P(0^-) + \sum_{\alpha=1}^{M_{ion}} z_\alpha n_{ref} \exp\left(z_\alpha \frac{(\overline{\varphi}_{\alpha,L}^{ec}(t) - \psi(L, t))}{V_{th}}\right) \exp\left(z_\alpha \frac{(\psi(L, t) - \psi(0^-, t))}{V_{th}}\right) \\ &= P(0^-) + \sum_{\alpha=1}^{M_{ion}} z_\alpha n_{\alpha,L}(t) \exp\left(z_\alpha \frac{\varphi_{bi}(0^-, t)}{V_{th}}\right) = 0 \end{aligned} \quad (10.5c)$$

and similarly at  $x = d^+$ :

$$\begin{aligned} P(d^+) + \sum_{\alpha=1}^{M_{ion}} z_\alpha n_\alpha(d^+, t) &= P(d^+) + \sum_{\alpha=1}^{M_{ion}} z_\alpha n_{ref} \exp\left(z_\alpha \frac{(\varphi_{\alpha}^{ec}(d^+, t) - \psi(d^+, t))}{V_{th}}\right) \\ &= P(d^+) + \sum_{\alpha=1}^{M_{ion}} z_\alpha n_{ref} \exp\left(z_\alpha \frac{(\overline{\varphi}_{\alpha,R}^{ec}(t) - \psi(R, t))}{V_{th}}\right) \exp\left(z_\alpha \frac{(\psi(R, t) - \psi(d^+, t))}{V_{th}}\right) \\ &= P(d^+) + \sum_{\alpha=1}^{M_{ion}} z_\alpha n_{\alpha,R}(t) \exp\left(-z_\alpha \frac{\varphi_{bi}(d^+, t)}{V_{th}}\right) = 0. \end{aligned} \quad (10.5d)$$

**Remark 1.** In the particular case of the  $KCl$  solution ( $z_1 = +1$ ,  $z_2 = -1$ ) considered in [25] or in the Drift Diffusion model (9.55), equations (10.5c) and (10.5d) can be explicitly solved, to yield:

$$\begin{aligned} \varphi_{bi}(0^-, t) &= V_{th} \ln\left(\frac{-P(0^-) + \sqrt{(P(0^-))^2 + 4(n_{1,L}(t))^2}}{2n_{1,L}(t)}\right) \\ \varphi_{bi}(d^+, t) &= V_{th} \ln\left(\frac{P(d^+) + \sqrt{(P(d^+))^2 + 4(n_{1,R}(t))^2}}{2n_{1,R}(t)}\right) \end{aligned}$$

where we notice that  $n_{1,L}(t) = n_{2,L}(t)$  and  $n_{1,R}(t) = n_{2,R}(t)$ , at each time level  $t$ , because of the electroneutrality constraints (10.2e) and (10.2f).

In order to complete the characterization of the boundary values for the dependent variables of the problem we need the value of the electric potential and of the ion concentrations at the two endpoints of the channel. The potential is determined using (10.5) and (A5), which yield at each time level  $t$ :

$$\psi(0, t) = \psi(0^-, t) = \psi_L(t) - \varphi_{bi}(0^-, t) \quad (10.6a)$$

$$\psi(d, t) = \psi(d^+, t) = \psi_R(t) + \varphi_{bi}(d^+, t). \quad (10.6b)$$

To determine the ion concentrations we use (10.4a) and (10.5a) at  $x = 0$  to obtain:

$$\begin{aligned} n_\alpha(0, t) &= n_\alpha(0^-, t) = n_{ref} \exp\left(z_\alpha \frac{(\varphi_i^{ec}(0^-, t) - \psi(0^-, t))}{V_{th}}\right) \\ &= n_{ref} \exp\left(z_\alpha \frac{(\overline{\varphi}_{\alpha,L}^{ec}(t) - \psi(0^-, t))}{V_{th}}\right) \\ &= n_{ref} \exp\left(z_\alpha \frac{(\overline{\varphi}_{\alpha,L}^{ec}(t) - \psi(L, t))}{V_{th}}\right) \exp\left(z_\alpha \frac{(\psi(L, t) - \psi(0^-, t))}{V_{th}}\right) \\ &= n_{\alpha,L}(t) \exp\left(z_\alpha \frac{\varphi_{bi}(0^-, t)}{V_{th}}\right) \quad \alpha = 1, \dots, M_{ion} \end{aligned} \quad (10.7a)$$

and, similarly, (10.4b) and (10.5b) at  $x = d$  to obtain:

$$\begin{aligned} n_\alpha(d, t) &= n_\alpha(d^+, t) = n_{ref} \exp\left(z_\alpha \frac{(\varphi_\alpha^{ec}(d^+, t) - \psi(d^+, t))}{V_{th}}\right) \\ &= n_{ref} \exp\left(z_i \frac{(\overline{\varphi}_{\alpha,R}^{ec}(t) - \psi(d^+, t))}{V_{th}}\right) \\ &= n_{ref} \exp\left(z_i \frac{(\overline{\varphi}_{\alpha,R}^{ec}(t) - \psi(R, t))}{V_{th}}\right) \exp\left(z_\alpha \frac{(\psi(R, t) - \psi(d^+, t))}{V_{th}}\right) \\ &= n_{\alpha,R}(t) \exp\left(-z_\alpha \frac{\varphi_{bi}(d^+, t)}{V_{th}}\right) \quad \alpha = 1, \dots, M_{ions}. \end{aligned} \quad (10.7b)$$

## 10.4. The PNP model in 1D

Let  $T_{final} > 0$  denote the temporal duration of ion electrodiffusion into the channel. Then, the equations for the PNP model to be solved in the space-time cylinder  $Q_{T_{final}} := (0, d) \times (0, T_{final})$  read:

$$qz_\alpha \frac{\partial n_\alpha}{\partial t} + \frac{\partial J_\alpha}{\partial x} = 0 \quad \alpha = 1, \dots, M \quad (10.8a)$$

$$J_\alpha = q\mu_\alpha |z_\alpha| n_\alpha E - qz_\alpha D_\alpha \frac{\partial n_\alpha}{\partial x} \quad \alpha = 1, \dots, M_{ions} \quad (10.8b)$$

$$\frac{\partial E}{\partial x} = \frac{q}{\varepsilon} \left( \sum_{\alpha=1}^{M_{ion}} z_\alpha n_\alpha + P \right) \quad (10.8c)$$

$$E = -\frac{\partial \varphi}{\partial x} \quad (10.8d)$$

where diffusivities and electrical mobilities are related by

$$D_\alpha = \frac{\mu_\alpha V_{th}}{|z_\alpha|} \quad \alpha = 1, \dots, M_{ion}. \quad (10.9)$$

For each time  $t \in (0, T_{final})$ , the Dirichlet boundary conditions at  $x = 0$  are:

$$\psi(0, t) = \psi_L(t) - \varphi_{bi}(0^-, t) \quad (10.10a)$$

$$n_\alpha(0, t) = n_{\alpha,L}(t) \exp\left(z_\alpha \frac{\varphi_{bi}(0^-, t)}{V_{th}}\right) \quad \alpha = 1, \dots, M_{ion}, \quad (10.10b)$$

where the built-in potential at  $x = 0^-$  is determined by solving the nonlinear algebraic equation

$$P(0^-, t) + \sum_{\alpha=1}^{M_{ion}} z_\alpha n_{\alpha,L}(t) \exp\left(z_\alpha \frac{\varphi_{bi}(0^-, t)}{V_{th}}\right) = 0 \quad (10.10c)$$

whereas the boundary conditions at  $x = d$  are:

$$\psi(d, t) = \psi_R(t) + \varphi_{bi}(d^+, t) \quad (10.10d)$$

$$n_\alpha(d, t) = n_{\alpha,R}(t) \exp\left(-z_\alpha \frac{\varphi_{bi}(d^+, t)}{V_{th}}\right) \quad \alpha = 1, \dots, M_{ion}, \quad (10.10e)$$

where the built-in potential at  $x = d^+$  is determined by solving the nonlinear algebraic equation

$$P(d^+) + \sum_{\alpha=1}^{M_{ion}} z_\alpha n_{\alpha,R}(t) \exp\left(-z_\alpha \frac{\varphi_{bi}(d^+, t)}{V_{th}}\right) = 0. \quad (10.10f)$$

$$(10.10g)$$

In the above relations, the boundary data at  $x = 0$  and at  $x = d$  for  $\psi$  and  $n_\alpha$  are given, experimentally accessible, functions of time. Moreover, at time  $t = 0$  the following initial conditions are prescribed for the ion concentrations in the interior of the channel

$$n_\alpha(x, 0) = n_\alpha^0(x) \quad \alpha = 1, \dots, M_{ion} \quad (10.10h)$$

where the initial data  $n_\alpha^0$  are given positive bounded functions in  $(0, d)$ . The initial spatial distribution of the electric potential  $\psi^0 = \psi^0(x)$  for each  $x \in [0, d]$  inside the

channel can be determined by solving the Poisson equation

$$-\frac{\partial^2 \psi^0}{\partial x^2} = \frac{q}{\varepsilon} \left( \sum_{\alpha=1}^{M_{ion}} z_\alpha n_\alpha^0 + P \right) \quad \forall x \in (0, d) \quad (10.10i)$$

subject to the boundary conditions:

$$\psi^0(0) = \psi_L(0) - \varphi_{bi}(0^-, 0) \quad (10.10j)$$

$$\psi^0(d) = \psi_R(0) + \varphi_{bi}(d^+, 0). \quad (10.10k)$$

#### 10.4.1. Electrochemical potential with ions space occupation

It is possible to modify the definition of the electrochemical potential by considering the fact that ions have a non null physical dimension. This is of particular importance in the realistic application for the calculation of transmembrane currents in ionic channels when the dimension of ions is comparable with the ones of the channel. Hard Sphere theory [104, 101] is focused on the fact that two different particles or body cannot occupy the same space at the same time, considering the so called size-exclusion effect.

In [102, 103], Rosenfeld and Roth have introduced a short-range interaction term to describe this effect by an additional contribution to the definition of the electrochemical potential (9.51b). This term is composed by two parts that have different physical meaning: the first is the local correction due to electrostatic short range interactions (the long-range is already accounted with equation (9.50c)), the second is due to the volume exclusion effects. Below we sketch the procedure adopted by Rosenfeld and Roth to obtain a mathematical expression of this correction. The electrochemical hard sphere potential  $\varphi_i^{echs}$  can be calculated as:

$$\varphi_i^{echs} = \psi + \frac{k_B \Theta}{qz_\alpha} \ln \left( \frac{n_\alpha}{n_{ref}} \right) + \mu_\alpha^{ex} \quad (10.11)$$

where  $\mu_\alpha^{ex}$  is the exclusion effect potential that is the objective of the next calculation. In view of the calculation of  $\mu_\alpha^{ex}$ , we introduce generalized densities  $n_\alpha$  as the convolutions of the densities and weight functions which account for the fundamental geometrical properties of each ion. Let define  $\phi_{HS}$  as the excess of free energy density, consequently the corresponding potential can be computed as:

$$\mathcal{F}_{HS} = k_B \Theta \int \phi_{HS}(n_\beta(x')) dx' \quad (10.12)$$

where  $n_\beta$  is given by

$$n_\beta(x) = \sum_{\alpha=1}^{M_{ion}} \int n_\alpha(x') w_\alpha^{(\beta)}(x' - x) dx' \quad (10.13)$$

for  $\beta = 1, 2, 3, 4, 5, 6$  with

$$\begin{aligned} w_\alpha^{(1)}(r) &= \frac{1}{4\pi R_\alpha^2} w_\alpha^{(3)}(r) & w_\alpha^{(3)}(r) &= \delta(|r| - R_\alpha) \\ w_\alpha^{(2)}(r) &= \frac{1}{4\pi R_\alpha} w_\alpha^{(4)}(r) & w_\alpha^{(4)}(r) &= \Lambda(|r| - R_\alpha) \\ w_\alpha^{(5)}(r) &= \frac{1}{4\pi R_\alpha} w_\alpha^{(6)}(r) & w_\alpha^{(6)}(r) &= \frac{r}{|r|} \delta(|r| - R_\alpha) \end{aligned}$$

Here  $\delta$  denotes the Dirac delta function centred on the ions position and  $\Lambda$  is a unit step function such that  $\Lambda(x) = 1$  for  $x \leq 0$  and  $\Lambda(x) = 0$  for  $x > 0$ . In order to reduce the computational effort, it is possible to apply the LDA (Local Density Approximation) to determine the weights  $w_\alpha^{(\beta)}$  under the following hypotheses:

- densities are smooth:  $n_\alpha \in C^2$
- ionic radii are small:  $R_\alpha \ll 1$
- ion crowding:  $n_\alpha R_\alpha^3 = O(1)$
- $\frac{\nabla n_\alpha}{n_\alpha} = O(1) \rightarrow |\nabla n_\alpha| R_\alpha^3 = O(1)$
- $\frac{\Delta n_\alpha}{n_\alpha} = O(1) \rightarrow |\Delta n_\alpha| R_\alpha^3 = O(1)$

obtaining

$$\begin{aligned} c_1(x) &= \sum_\alpha n_\alpha(x) + \frac{1}{6} \sum_\alpha R_\alpha^2 \Delta n_\alpha(x) & c_3(x) &= 4\pi \sum_\alpha n_\alpha(x) R_\alpha^2 \\ c_2(x) &= \sum_\alpha n_\alpha(x) R_\alpha + \frac{1}{6} \sum_\alpha R_\alpha^3 \Delta n_\alpha(x) & c_4(x) &= \frac{4\pi}{3} \sum_\alpha n_\alpha(x) R_\alpha^3 \\ c_5(x) &= \frac{1}{3} \sum_\alpha \nabla n_\alpha(x) R_\alpha^2 & c_6(x) &= \frac{4\pi}{3} \sum_\alpha \nabla n_\alpha(x) R_\alpha^3 \end{aligned}$$

$$\alpha = 1, \dots, M_{ion}$$

By replacing these coefficients in Eq.(10.12) we have the final expression of the excess free energy:

$$\phi_{HS}^{LDA} = -c_1 \ln(1 - c_4) + \frac{c_2 c_3}{1 - c_4} + \frac{c_3^3}{24\pi(1 - c_4)^2}.$$

From the relation  $\mu_\alpha^{HS} = \frac{\partial \phi_{HS}^{LDA}(n_\alpha)}{\partial n_\alpha}$  the hard sphere potential is then given by:

$$\begin{aligned}\mu_{\alpha}^{HS} = & -\ln\left(1 - \frac{4\pi}{3} \sum_k n_k R_k^3\right) + 4\pi \frac{\frac{R_{\alpha}(\sum_k n_k R_k^2) + R_{\alpha}^2(\sum_k n_k R_k) + \frac{1}{3} R_{\alpha}^3(\sum_k n_k)}{1 - \frac{4\pi}{3} \sum_k n_k R_k^3}}{3} \\ & + \frac{16\pi^2}{3} \frac{\frac{R_{\alpha}^3(\sum_k n_k R_k)(\sum_k n_k R_k^2) + \frac{3}{2} R_{\alpha}^2(\sum_k n_k R_k^2)^2}{(1 - \frac{4\pi}{3} \sum_k n_k R_k^3)^2}}{9} + \frac{64\pi^3}{9} \frac{R_{\alpha}^3(\sum_k n_k R_k^2)^3}{(1 - \frac{4\pi}{3} \sum_k n_k R_k^3)^3}\end{aligned}\quad (10.14)$$

## CHAPTER 11

# The Poisson-Nernst-Planck model of ion pumps and exchangers

This chapter provides a description of the principal functions of ion pumps and exchangers that are ubiquitous in the human body. Their mathematical modeling is based on the Velocity-extended Poisson-Nernst-Planck model, equipped with proper constitutive relations to characterize the body force acting on the ionic solution due to the presence of several types of ions in the pore.

### 11.1. Ion pumps and exchangers

In this section we provide a short description of the biochemical activity of four important ion pumps and exchangers that are present in the human body. In particular, we will emphasize the types of ions involved in the transport and the consequence of such transport on the balance of electric charge.

#### 11.1.1. The sodium-potassium ATPase pump

The sodium-potassium ( $\text{Na}^+ \text{-K}^+$ ) ATPase pump plays a fundamental role in cellular biology as it is present in the membrane of every cell in any living biological system. The ATPase enzyme causes the hydrolysis of one molecule of ATP and produces the necessary energy to expel three  $\text{Na}^+$  ions, while allowing two  $\text{K}^+$  ions to enter. This process is not electrically neutral as it entails an outflux of three positive charged particles of sodium and an influx of only two positive charged particles of potassium. The ion outflux and influx are schematically represented in Figure 11.1.

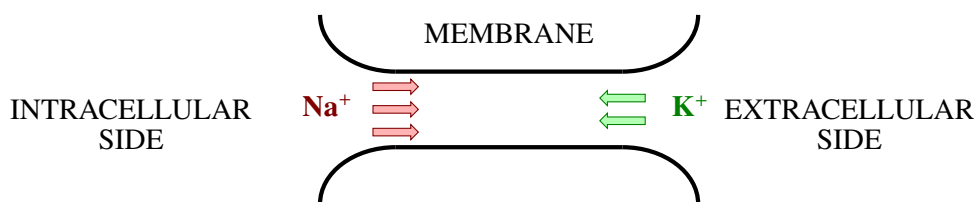


**Figure 11.1** Schematic representation of the  $\text{Na}^+ \text{-K}^+$ -ATPase pump. The stoichiometric ratio is 3 : 2, since there is an outflux of three  $\text{Na}^+$  ions and an influx of two  $\text{K}^+$  ions.

### 11.1.2. The calcium-sodium exchanger

The calcium-sodium ( $\text{Ca}^{++}$ - $\text{Na}^+$ ) exchanger is activated when calcium accumulates inside the cell above a certain threshold, that is usually around 1 mM. This pump entails the influx of three  $\text{Na}^+$  ions and an outflux of one  $\text{Ca}^{++}$  ion. This process is not electrically neutral as three positive sodium ions enter the cell whereas only one positive calcium ion exits the cell. The ion outflux and influx are schematically represented in Figure 11.2.

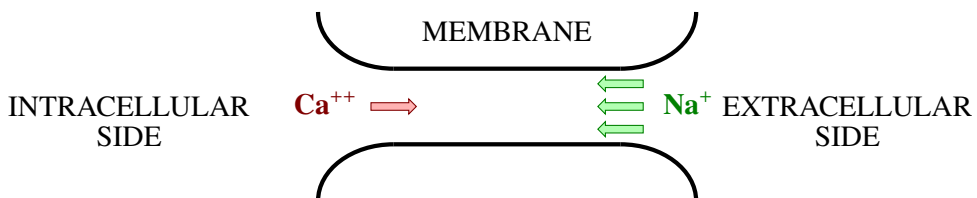


**Figure 11.2** Schematic representation of the  $\text{Ca}^{++}$ - $\text{Na}^+$  exchanger. The stoichiometric ratio is 3 : 1, since there is an influx of three  $\text{Na}^+$  ions and an outflux of one  $\text{Ca}^{++}$  ion.

### 11.1.3. The chloride-bicarbonate exchanger

The chloride-bicarbonate ( $\text{Cl}^-$ - $\text{HCO}_3^-$ ) exchanger involves the movement of negative ions. Carbonic anhydrase is an enzyme that mediates the transport of bicarbonate to maintain the homeostatic balance of carbonate across the cell membrane. More precisely, carbonic anhydrase favors the splitting of one molecule of  $\text{H}_2\text{CO}_3$  into a positive  $\text{H}^+$  ion and a negative  $\text{HCO}_3^-$  ion. Then, the  $\text{HCO}_3^-$  ion exits the cell through the anion channel with an exchange of a chlorine ion  $\text{Cl}^-$  that enters the cell. The balance of this exchanger is electrically neutral because for every negative charged  $\text{HCO}_3^-$  leaving the cell there is a negative charged  $\text{Cl}^-$  ion entering the cell. The ion outflux and influx are schematically represented in the top panel of Figure 11.3.

### 11.1.4. The sodium-proton exchanger

The sodium-proton ( $\text{Na}^+$ - $\text{H}^+$ ) exchanger is strictly correlated with the activity of the  $\text{Cl}^-$ - $\text{HCO}_3^-$  exchanger. A positive  $\text{H}^+$  ion resulting from the splitting reaction of one molecule of  $\text{H}_2\text{CO}_3$  exits the cell with an exchange of one  $\text{Na}^+$  ion entering the cell. Thus, this exchanger is electrically neutral. The ion outflux and influx are schematically represented in the bottom panel of Figure 11.3.

## 11.2. The mathematical model of ion pumps and exchangers

Several physical microscopical mechanisms concur to determine the macroscopic and measurable variables of ion transport through protein pores in the cell membrane. Specif-

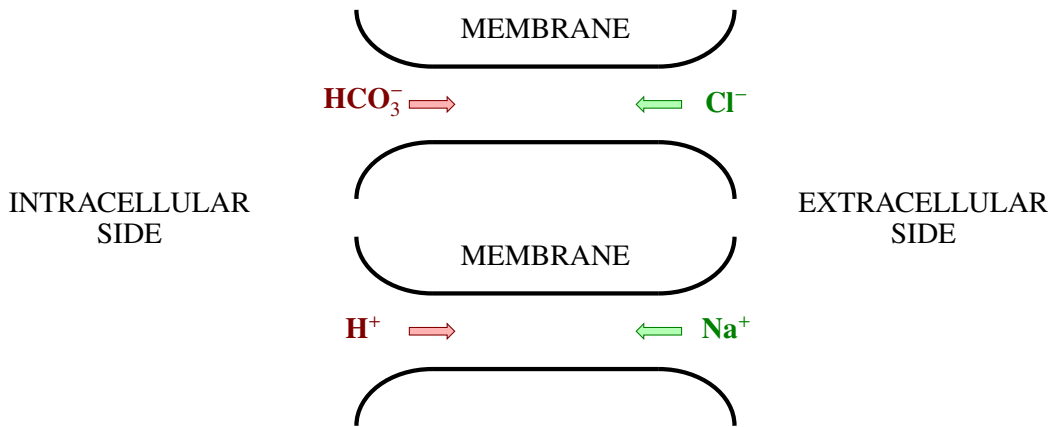


**Figure 11.3** Schematic representation of the  $\text{Cl}^-$ - $\text{HCO}_3^-$  exchanger (top panel) and of the  $\text{Na}^+$ - $\text{H}^+$  exchanger (bottom panel). The stoichiometric ratio of the  $\text{Cl}^-$ - $\text{HCO}_3^-$  exchanger is 1 : 1, since there is an influx of one  $\text{Cl}^-$  ion and an outflux of one  $\text{HCO}_3^-$  ion. The stoichiometric ratio of the  $\text{Na}^+$ - $\text{H}^+$  exchanger is also 1:1, since there is an influx of one  $\text{Na}^+$  ion and an outflux of one  $\text{H}^+$  ion.

ically, in order to build a mathematical model for ion pumps and exchangers, we need to account for the following mechanisms:

- *interaction among multiple ion species and aqueous fluid*: this mechanism is determined by the fact that ions in the intra- and extracellular environments can be thought of as charged solute particles inside an aqueous fluid. Mathematically, this mechanism is described by means of the homogeneous charged mixture approach presented in Section 9.4. We will refer to the ionic solution flowing inside the protein pore as *intrapore fluid*;
- *external driving force*: this mechanism may be due to the hydrolysis of ATP, as in the  $(\text{Na}^+ - \text{K}^+)$  pump, or to other reactions that establish electrochemical gradients of specific ion species inside or outside the cell, as in the other exchangers considered here. The mathematical description of this mechanism is still subject of ongoing research in applied mathematics and biology. In this chapter, we will account for this mechanism by imposing given values for ion flux densities of selected species as boundary conditions, as discussed in Section 11.2.2;
- *electric field formation*: this mechanism is determined by the mutual interaction among ions moving inside the protein pore and their interaction with the permanent electric charge density distributed on the pore surface. Mathematically, the mechanism is described by the Poisson equation (9.49f), supplied by appropriate boundary conditions at the inlet and outlet sections of the pore and on its external surface;

- *ion diffusion and drift*: this mechanism is determined by the superposition of a diffusion process driven by ion concentration gradients along the pore and of a drift process driven by the force exerted by the electric field on each ion. Mathematically, the mechanism is described by the Nernst-Planck equation (9.49b), supplied by appropriate initial conditions inside the pore and by appropriate boundary conditions at the inlet and outlet sections of the pore and on its external surface;
- *fluid motion*: this mechanism is determined by the volume force density that is exerted by the ions moving inside the fluid. Mathematically, the mechanism is described by the time-dependent Stokes equations with a force term for the intrapore fluid (9.49c)- (9.49e), supplied by appropriate initial conditions inside the pore and by appropriate boundary conditions at the inlet and outlet sections of the pore and on its external surface.

The aforementioned physical microscopical mechanisms are combined in the velocity-extended Poisson-Nernst-Planck model (9.49) (shortly, VE-PNP), complemented by proper initial and boundary conditions, which will be described in Section 11.2.2.

### 11.2.1. Geometrical description of the problem

Protein pores have very complex geometries, which oftentimes changes dynamically, in order to achieve specific biological functions. In this chapter, we will adopt the idealized geometry reported in Figure 11.4, which is based on the biophysical settings analyzed in [26, 25].

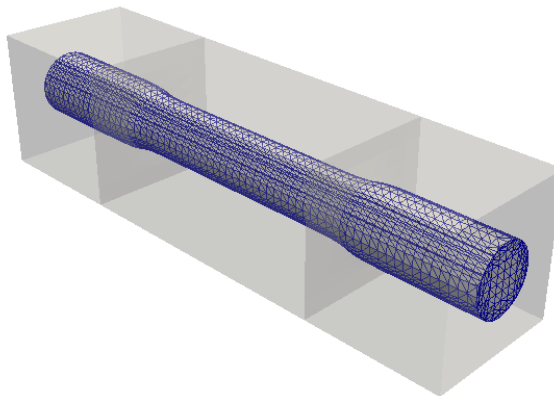


**Figure 11.4** Computational domain for the simulation of the ion pumps and exchangers reported in this chapter. The protein pore is represented by a cylinder with a cross section that varies along its axis to include the pore antichambers in the inlet and outlet regions. The gray-shaded volume represents a portion of the environment external to the pore that is considered for a proper evaluation of the electric field.

The protein pore is represented by a cylinder with a cross section that varies along its axis to include the pore antichambers in the inlet and outlet regions. The cylinder is contained in a parallelepiped representing a portion of the environment external to the pore, which is considered for a proper evaluation of the electric field. The parallelepiped is composed by the union of two cubes of side equal to 2.5nm containing the antichambers and by a central parallelepiped of length equal to 5nm containing the inner pore, so that the total length is equal to 10nm. The radius of the cylinder varies along the pore axis, ranging from the value of 0.6nm in the pore antichambers to the value of 0.4nm in the inner pore. The full domain has been partitioned in tetrahedrons as reported in Figure 11.4, where the discretization of the parallelepiped surrounding the cylinder is not shown for sake of visual clarity.

Since we are treating a wide variety of ion exchangers, as well as the presence of a large number of ion species in each protein pore, to help the clarity of the discussion we report in Figure 11.5 a two-dimensional cross-section of the pore geometry presented in Figure 11.4 and identify the various regions of the domain with the corresponding labels for the ease of reference. The region to the left with respect to sideA is the intracellular site whereas the region to the right with respect to sideB is the extracellular site.

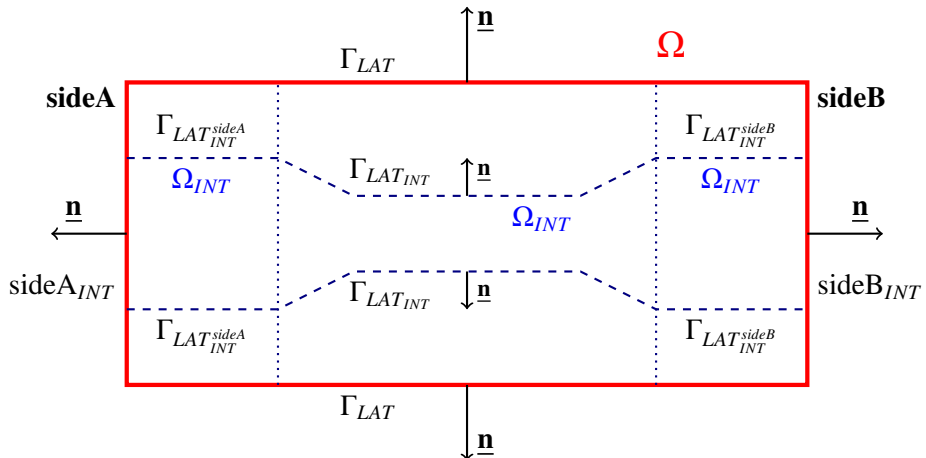


**Figure 11.5** Two-dimensional cross-section of the pore geometry and boundary labels for the simulation of ion pumps and exchangers.

Referring to the notation of Figure 11.5, in the remainder of the section, the VEPNP equations (9.49a)-(9.49b) and the Stokes system (9.49c)-(9.49d) are solved only inside the cylinder  $\Omega_{INT}$  whereas the Poisson equation (9.49f) (9.49g)) is solved in the whole domain  $\Omega$ . For a detailed discussion of the analytical properties of the model

equations (9.49) and of the numerical methods used for their discretization we refer to [108].

### 11.2.2. Boundary and initial conditions

The VE-PNP system adopted in this chapter for the mathematical description of ion transport through protein pores necessitates boundary and initial conditions to complete the Poisson problem for the electric field, the Nerst-Planck problem for the ion drift-diffusion and the Stokes problem for the motion of the intrapore fluid. The conditions are specified in the next sections.

#### 11.2.2.1. Boundary conditions for the Poisson equation

Let  $\gamma := \Gamma_{LAT_{INT}^{sideA}} \cup \Gamma_{LAT_{INT}^{sideB}} \cup \Gamma_{LAT_{INT}}$  denote the two-dimensional surface separating the pore region from the surrounding environment region, as depicted in Figure 11.5. An electric charge density is often present on the inner pore surface  $\gamma$ , which is due to the chemical structural properties of the protein constituting the pore. Thus, we need to account for possible jumps of the electric displacement  $\underline{\mathbf{D}} = \epsilon_m \underline{\mathbf{E}}$  across that interface.

For a given vector-valued function  $\underline{\tau} : \Omega \rightarrow \mathbb{R}^3$  we define the jump of  $\underline{\tau}$  across the surface  $\gamma$  as

$$[\![\underline{\tau}]\!]_\gamma := (\underline{\tau}|_{\Omega \setminus \Omega_{INT}}|_\gamma - \underline{\tau}|_{\Omega_{INT}}|_\gamma) \cdot \underline{\mathbf{n}},$$

whereas for a given scalar-valued function  $\phi : \Omega \rightarrow \mathbb{R}$  we define the jump of  $\phi$  across the surface  $\gamma$  as

$$[\![\phi]\!]_\gamma := \phi|_{\Omega \setminus \Omega_{INT}}|_\gamma \underline{\mathbf{n}} - \phi|_{\Omega_{INT}}|_\gamma \underline{\mathbf{n}}.$$

We notice that the jump of a vector-valued function is a scalar function whereas the jump of a scalar-valued function is a vector-valued function.

For all  $t \in I_T$ , we consider the following boundary conditions for the Poisson equation (9.49f)-(9.49g):

$$\psi = 0 \quad \text{on } sideA_{int} \times I_T \quad (11.1a)$$

$$\underline{\mathbf{D}} \cdot \underline{\mathbf{n}} = 0 \quad \text{on } \Gamma_{LAT} \cup sideB \cup sideA \cup sideB_{int} \times I_T \quad (11.1b)$$

$$[\![\underline{\mathbf{D}}]\!]_\gamma = h_\gamma \quad \text{on } \gamma \times I_T \quad (11.1c)$$

$$[\![\psi]\!]_\gamma = 0 \quad \text{on } \gamma \times I_T, \quad (11.1d)$$

where

$$h_\gamma = \begin{cases} \sigma_{fixed} & \text{on } \Gamma_{LAT_{INT}} \times I_T \\ 0 & \text{on } \Gamma_{LAT_{INT}^{sideA}} \cup \Gamma_{LAT_{INT}^{sideB}} \times I_T. \end{cases} \quad (11.1e)$$

Condition (11.1a) has the scope of introducing a reference value for the calculation of

the electrostatic potential drop across the cell membrane. Condition (11.1b) expresses the biological fact that the aforementioned potential drop is caused solely by the ion charge distribution within the pore because no external bias is applied. The quantity  $\sigma_{fixed}$  (unit:  $\text{C m}^{-2}$ ) in (11.1e) is a given distribution of superficial permanent charge density that mathematically represents the electric charge contained in the aminoacid structure of the protein surrounding the ion channel. We notice that the interface condition (11.1d) expresses the physical fact that the electric potential is a continuous function across  $\gamma$ . Conversely, the interface condition (11.1c) expresses the physical fact that the normal component of the electric displacement is discontinuous across the pore lateral surface because of the presence of the aminoacid fixed charge density  $\sigma_{fixed}$ . Determining precise values for  $\sigma_{fixed}$  is far from trivial, and it typically requires a fine calibration procedure to guarantee the correct functionality of the specific ion pump/exchanger under consideration. Table 11.1 reports the values of  $\sigma_{fixed}$  that have been utilized for the simulation of the pump/exchangers considered in [? ], but they can be adapted to a different application.

Pump/exchanger	$\sigma_{fixed} [\text{C cm}^{-2}]$
sodium-potassium pump	$-1 \cdot 10^{10}$
calcium-sodium exchanger	$-6 \cdot 10^{11}$
chloride-bicarbonate exchanger	$+3.9 \cdot 10^{11}$
sodium-proton exchanger	$-2.65 \cdot 10^{12}$

Table 11.1 Values of the fixed charge density  $\sigma_{fixed}$ .

### 11.2.2.2. Boundary and initial conditions for the Nernst-Planck equations

Multiple ion species are simultaneously present in each pore. In the following, we will assume that sodium, potassium, chloride and bicarbonate ions are present in each pump/exchanger. In addition, calcium ions will be included in the calcium-sodium exchanger and protons will be included in the sodium-proton exchanger.

In Section 11.2, we mentioned that the external driving force that govern the activity of ion pumps/exchangers would be incorporated in the mathematical model via suitable boundary conditions for the ion flux densities. In accordance with the biochemical functions of each pump/exchanger reviewed in Section 11.1, we impose the following conditions:

- *sodium-potassium pump*: a flux density  $g_{\text{Na}^+}$  entering the pore from the intracellular side and a flux density  $g_{\text{K}^+}$  entering the pore from the extracellular side;

- *calcium-sodium exchanger*: a flux density  $g_{\text{Na}^+}$  entering the pore from the extracellular side and a flux density  $g_{\text{Ca}^{++}}$  entering the pore from the intracellular side;
- *chloride-bicarbonate exchanger*: a flux density  $g_{\text{Cl}^-}$  entering the pore from the extracellular side and a flux density  $g_{\text{HCO}_3^-}$  entering the pore from the intracellular side;
- *sodium-proton exchanger*: a flux density  $g_{\text{H}^+}$  entering the pore from the intracellular side and a flux density  $g_{\text{Na}^+}$  entering the pore from the extracellular side.

The specific values for the flux densities  $g_{\text{Na}^+}$ ,  $g_{\text{K}^+}$ ,  $g_{\text{Ca}^{++}}$ ,  $g_{\text{Cl}^-}$ ,  $g_{\text{HCO}_3^-}$  and  $g_{\text{H}^+}$  have been selected in such a way that the stoichiometric ratios:

$$r_{\text{Na}^+-\text{K}^+} := \frac{g_{\text{K}^+}}{g_{\text{Na}^+}}, \quad (11.2a)$$

$$r_{\text{Ca}^{++}-\text{Na}^+} := \frac{g_{\text{Ca}^{++}}}{g_{\text{Na}^+}}, \quad (11.2b)$$

$$r_{\text{Cl}^--\text{HCO}_3^-} := \frac{g_{\text{Cl}^-}}{g_{\text{HCO}_3^-}}, \quad (11.2c)$$

$$r_{\text{H}^+-\text{Na}^+} := \frac{g_{\text{H}^+}}{g_{\text{Na}^+}}, \quad (11.2d)$$

are compatible with the expected activity of each specific pump/exchanger, as reviewed in Section 11.1, namely:

$$r_{\text{Na}^+-\text{K}^+} := 3 : 2, \quad (11.3a)$$

$$r_{\text{Ca}^{++}-\text{Na}^+} := 1 : 3, \quad (11.3b)$$

$$r_{\text{Cl}^--\text{HCO}_3^-} := 1 : 1; \quad (11.3c)$$

$$r_{\text{H}^+-\text{Na}^+} := 1 : 1. \quad (11.3d)$$

### 11.2.2.3. Boundary and initial conditions for the Stokes system

The calculation of the velocity of the intrapore fluid, is made possible by solving the Stokes system (9.49c)- (9.49d). We assume that (1) the intrapore fluid adheres to the channel wall; (2) no external pressure drop is applied across the pore; (3) the intrapore fluid is at the rest when the pump is not active. As a consequence, we adopt the following boundary and initial conditions:

$$\underline{\mathbf{u}} = \mathbf{0} \quad \text{on } \gamma \times I_T \quad (11.4a)$$

$$\underline{\mathbf{T}} \underline{\mathbf{n}} = \mathbf{0} \quad \text{on } \text{side}A_{int} \cup \text{side}B_{int} \times I_T \quad (11.4b)$$

$$\underline{\mathbf{u}}(\underline{\mathbf{x}}, 0) = \mathbf{0} \quad \text{in } \Omega_{INT}. \quad (11.4c)$$

### 11.2.3. The volumetric force acting on the intrapore fluid

In Section 9.4, we utilized a constitutive relationship (9.49e) originally proposed by Stratton to characterize the volumetric force density  $\underline{\mathbf{F}}_{ef}$  on the right-hand side of the linear momentum balance equation (9.49d). The Stratton formulation is widely adopted in the modeling description of electrokinetic phenomena, but it is not the only one proposed in the literature to characterize  $\underline{\mathbf{F}}_{ef}$ . In the context of ion pumps in cell membranes, the following characterization of  $\underline{\mathbf{F}}_{ef}$  can be used:

$$\underline{\mathbf{F}}_{ef} = \sum_{\alpha=1}^{M_{ion}} \underline{\mathbf{F}}_{\alpha}, \quad (11.5a)$$

where

$$\underline{\mathbf{F}}_{\alpha} = qz_{\alpha}n_{\alpha} \underline{\mathbf{E}}_{\alpha}^{ec} - k_{osm} \nabla n_{\alpha} \quad \alpha = 1, \dots, M_{ion}. \quad (11.5b)$$

The first term on the right-hand side of (11.5b) represents the volume force density due to a generalized electrochemical field  $\underline{\mathbf{E}}_{\alpha}^{ec}$ . Assuming that  $\underline{\mathbf{E}}_{\alpha}^{ec}$  is a gradient field, we have:

$$\underline{\mathbf{E}}_{\alpha}^{ec} = -\nabla \psi_{\alpha}^{ec} \quad \alpha = 1, \dots, M_{ion}, \quad (11.6)$$

where  $\psi_{\alpha}^{ec}$  is the generalized electrochemical potential associated with the  $\alpha$ -th species as defined in (9.51b). The generalized electrochemical field is the result of the superposed effect of passive drift due to the electric field (e), the diffusion mechanism associated with chemical concentration gradient (c). The second term on the right-hand side of (11.5b) represents the volume force density due to an osmotic concentration gradient according to the parameter  $k_{osm} = k_{osm,\alpha}k_B\theta$  (units: Nm). The value of  $k_{osm}$  is considered a characteristic property of the single pump/exchanger and a typical value is reported in Table 11.2. Relation (11.5b) is referred to henceforth as electrochemical model including an osmotic force (eck).

Pump/exchanger	$k_{osm}$
sodium-potassium pump	$4.1 \cdot 10^{-19}$
calcium-sodium exchanger	$3.95 \cdot 10^{-19}$
chloride-bicarbonate exchanger	$24 \cdot 10^{-19}$
sodium-proton exchanger	$4 \cdot 10^{-19}$

**Table 11.2** Values of the electrochemical osmotic parameter  $k_{osm}$  for each pump/exchanger. The units of  $k_{osm}$  are N m.

“Notes” — 2019/5/17 — 17:39 — page 182 — #190

# CHAPTER 12

## The Drift Diffusion model

In this chapter we consider the Drift Diffusion model illustrated in Sect. 9.7 in view of the application to the Semiconductor device physics.

### 12.1. Fermi distribution and Thermal equilibrium

In this section we introduce some physical aspects related to the semiconductor physics that are fundamental for the correct physical interpretation of the Drift Diffusion model. Since the most used material in the fabrication of semiconductor devices technology is silicon, the following description is based on this material choice but can be easily extended considering any other type of semiconductor material

#### 12.1.1. Intrinsic semiconductor

In a silicon crystal each atom has four valence electrons to share with its four neighboring atoms. The valence electrons are shared in a paired configuration called covalent bond. In a solid semiconductor energy levels of electrons are grouped into bands separated by regions of not allowed energy, the so-called forbidden gaps. The highest energy band completely filled by electrons at 0[K] is called *valence band* ( $E_V$ ), the next band is called *conduction band* ( $E_C$ ).

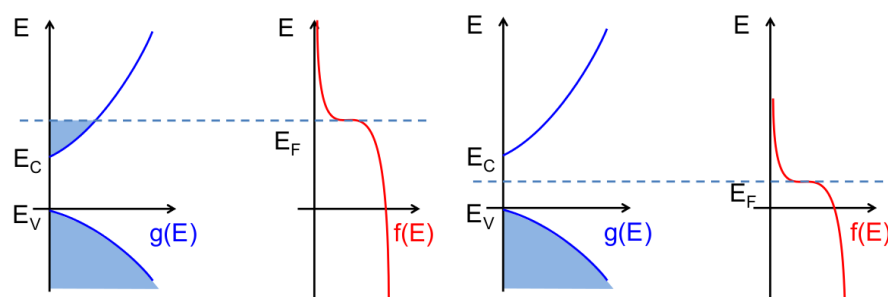


**Figure 12.1** Two typical examples of state density occupation ( $g(E)$ ) and probability distribution ( $f(E)$ ).

In silicon the band gap is 1.11 [eV] [16, 89], so at room temperature a small fraction of the electrons are excited into the conduction band, leaving behind vacancies (called *holes*) in the valence band. In contrast, an insulator has a much larger forbidden gap making room-temperature conduction virtually impossible, while metals have partially filled conduction bands even at absolute zero temperature, making them excellent conductors at any temperature. A suitable formulation of the electron concentration in the conduction band is given by the following integral

$$n = \int_{E_c}^{\infty} g(E)f(E) dE \quad (12.1)$$

where  $g(E)dE$  represents the number of electronic states per unit volume with an energy between  $E$  and  $E + dE$  in the conduction band and  $f(E)$  is the *Fermi-Dirac distribution function*, which gives the probability that an electronic state at energy  $E$  is occupied by an electron

$$f_D(E) = \frac{1}{1 + \exp\left(\frac{E - E_f}{k_B\Theta}\right)}. \quad (12.2)$$

In (12.2)  $k_B = 1.38 \times 10^{-23} [J/K]$  is Boltzmann’s constant,  $\Theta$  is the absolute temperature and  $E_f$  is the *Fermi level*. 12.1 shows the state density occupation  $g(E)$  and the probability distribution  $f(E)$  for a metal and a semiconductor. In order to obtain an analytic formula for the state density occupation  $g(E)$  that it will be used in the semiconductor model, we can consider the so-called parabolic approximation of the conduction band [97]

$$E = E_c + \frac{\hbar^2}{2m_e^*} k^2 \quad (12.3)$$

where  $\hbar = h/2\pi$  and  $h = 6.63 \times 10^{-34} [J s]$  is Planck’s constant,  $m_e^*$  the electron effective mass,  $E_c$  the minimum value of the conduction band and  $k$  the wavenumber. Applying (12.3), the conduction band density of states can be calculated as

$$g(E) = \frac{m_e^* \sqrt{2m_e^*(E - E_c)}}{\pi^2 \hbar^3}. \quad (12.4)$$

where (12.1) is a Fermi integral of order 1/2 and need to be evaluated numerically.

**Definition 12.1** (Fermi energy Level). *The Fermi level ( $E_f$ ) is the energy at which the probability of occupation of an energy state by an electron is equal to 1/2.*

In most cases, when the thermal energy is at least several times  $k_B\Theta$  above or below the Fermi level (non degenerate semiconductor), equation (12.2) can be approximated by the Maxwell-Boltzmann statistics, which reads as follows:

$$f_D(E) \simeq f_{MB}(E) = \begin{cases} \exp\left(-\frac{E - E_f}{k_B\Theta}\right) & E \gg E_f \\ 1 - \exp\left(-\frac{E_f - E}{k_B\Theta}\right) & E \ll E_f. \end{cases} \quad (12.5)$$

The Fermi level concept plays an essential role for the equilibrium of a semiconductor system. In fact one possible definition of thermal equilibrium in this context is

**Definition 1** (Thermal equilibrium in semiconductor). In a semiconductor at thermal equilibrium the Fermi level is constant at each point of the material and at each time level, in mathematical terms

$$E_f(\mathbf{x}, t) = \bar{E}_f \quad \forall \mathbf{x} \in \Omega \quad \forall t \quad (12.6)$$

for a suitable constant  $\bar{E}_f$ .

Replacing (12.5) and (12.4) into (12.1) we get:

$$n = N_c \exp\left(-\frac{E_c - \bar{E}_f}{k_B\Theta}\right). \quad (12.7)$$

Using the similar procedure the hole concentration  $p$  in the valence band is given by:

$$p = N_v \exp\left(-\frac{\bar{E}_f - E_v}{k_B\Theta}\right). \quad (12.8)$$

where  $N_c$  and  $N_v$  are the *effective density of states* while  $E_c$  is the minimum value of the valence band and  $E_v$  is the maximum value of the valence band.

**Definition 12.2** (Intrinsic semiconductor). A semiconductor is said to be intrinsic if  $n = p$ .

In an intrinsic semiconductor the *intrinsic Fermi level*  $E_i$  can be calculated by (12.7) and (12.8) as:

$$E_i = E_f = \frac{E_c + E_v}{2} - \frac{k_B\Theta}{2} \ln\left(\frac{N_c}{N_v}\right). \quad (12.9)$$

By replacing (12.9) in (12.7) we obtain the intrinsic carrier concentration  $n_i = n = p$ :

$$n_i = \sqrt{N_c N_v} \exp\left(-\frac{E_g}{2k_B\Theta}\right) \quad (12.10)$$

where  $E_g = E_c - E_v$  is defined to be the semiconductor energy gap.

**Remark 12.1.** Since the thermal energy,  $k_B\Theta$  is much smaller than the usual semiconductor bandgap  $E_g$ , the intrinsic Fermi level is very close to the midgap value  $E_{midgap} = E_g/2$ . In the case of silicon, at  $T = 300$  K, the value of the energy gap is  $E_g = 1.12$  eV and the value of the effective density of states is  $N_c = 2.8 \cdot 10^{25} \text{ m}^{-3}$  and  $N_v = 1.04 \cdot 10^{25} \text{ m}^{-3}$  (the difference to being ascribed to the fact that the effective mass for electrons and holes is not the same), from which relation (12.9) yields

$$E_F = 0.56 - \frac{0.02589}{2} \cdot 0.9904 = (0.56 - 0.0128) \text{ eV.}$$

The energy shift from midgap is thus about 2.3% so that in the case of an intrinsic semiconductor made of silicon it is a reasonable approximation to set

$$E_F := E_i = \frac{E_g}{2} \quad (12.11)$$

where  $E_i$  is called, for notational coherence, intrinsic Fermi level.

Equations (12.7) and (12.8) can be written in terms of the intrinsic carrier density ( $n_i$ ) and energy ( $E_i$ ) as:

$$n = n_i \exp\left(\frac{E_f - E_i}{k_B\Theta}\right) \quad (12.12)$$

$$p = n_i \exp\left(\frac{E_i - E_f}{k_B\Theta}\right). \quad (12.13)$$

**Definition 12.3** (Mass action law). At the Thermal equilibrium the mass action law holds

$$np = n_i^2. \quad (12.14)$$

The analysis of the work principles of devices can be effectively done by the band diagram (12.2), which summarizes the information presented above.

### 12.1.2. Extrinsic semiconductor

At room temperature an intrinsic semiconductor has an extremely low free-carrier concentration, therefore, its resistivity is very high. In order to improve the conductivity of the semiconductor, impurities atoms are added in the material. This introduces additional energy levels in the forbidden gap: the impurities are easily ionized adding either electrons to the conduction band or holes to the valence band, in such a way that

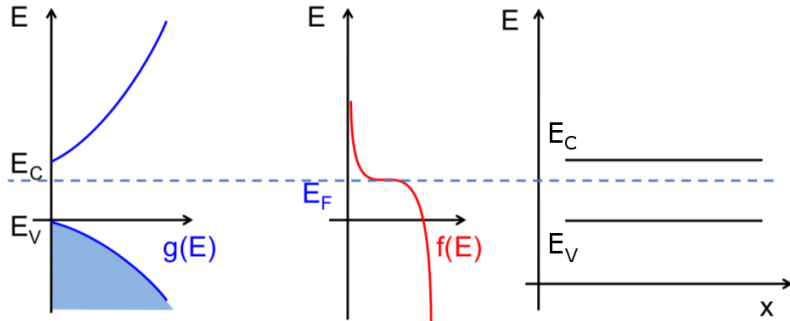


Figure 12.2 Construction of the band diagram.

the electrical conductivity is dominated by the type and concentration of the impurity atoms. Two are the types of impurities which are electrically active: those from column V of the Periodic Table such as arsenic or phosphorus, and those from column III such as boron or indium. The thermal energy at room temperature is sufficient to ionize the impurities and free the extra electron to the conduction band (column V) or accept an electron from valence band (column III). Column V impurities are called *donors*; they become positively charged when ionized. Silicon material doped with column-V impurities or donors is called *n-type* silicon. Column III impurities are called *acceptors*: they become negatively charged when ionized. Silicon material doped with column-III impurities or acceptors is called *p-type* silicon. A p-type or an n-type is named as *extrinsic* silicon. In terms of the energy-band diagram, donors add allowed electron states in the bandgap close to the conduction-band edge, while acceptors add allowed states just above the valence-band edge. The Fermi level in n-type silicon moves up towards the conduction band while in p-type silicon it moves down towards the valence band. This behaviour is presented in the band diagrams of 12.3.

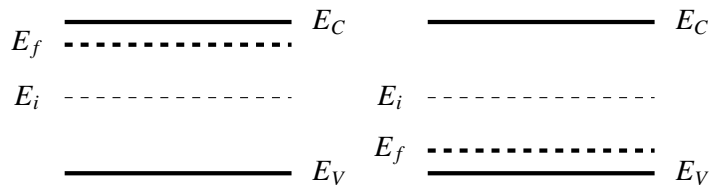


Figure 12.3 Band diagrams of extrinsic silicon for (12.21) and (12.22).

The position of the Fermi level depends on both the ionization energy and the concentration of dopants. For the sake of simplicity we consider that at room temperature all impurities are ionized ( $N_d = N_d^+$  and  $N_a = N_a^-$ ). For an n-type material with a donor

impurity concentration,  $N_d$ , the charge neutrality condition requires that

$$n = N_d^+ + p \quad (12.15)$$

where  $N_d^+$  is the density of ionized donors. Similarly for a p-type material with acceptor impurity concentration  $N_a$  we have

$$p = N_a^- + n. \quad (12.16)$$

Since the magnitude of impurities is in the range of  $10^{16} \div 10^{20} [\text{cm}^{-3}]$ , and intrinsic carrier concentration in the order of  $10^{10} [\text{cm}^{-3}]$ , we can approximate the carrier concentrations as:

$$n \simeq N_d^+, \quad p \simeq \frac{n_i^2}{N_d^+} \quad (\text{n-type}) \quad (12.17)$$

$$p \simeq N_a^-, \quad n \simeq \frac{n_i^2}{N_a^-} \quad (\text{p-type}). \quad (12.18)$$

Replacing (12.17) in (12.7) and (12.8) in (12.15) and (12.16) and solving the corresponding algebraic equation, we have:

$$E_c - E_f = k_B \Theta \ln \left( \frac{N_c}{N_d^+} \right) \quad (12.19)$$

$$E_f - E_v = k_B \Theta \ln \left( \frac{N_v}{N_a^-} \right). \quad (12.20)$$

Equations (12.19) and (12.20) can be written in a more useful form using (12.12) and (12.13) (for  $n_i$  and  $E_i$ ):

$$E_f - E_i = k_B \Theta \ln \left( \frac{N_d^+}{n_i} \right) \quad (12.21)$$

$$E_i - E_f = k_B \Theta \ln \left( \frac{N_a^-}{n_i} \right). \quad (12.22)$$

**Remark 12.2.** *The distance between the Fermi level and the intrinsic Fermi level is a logarithmic function of doping concentration.*

### 12.1.3. Carrier densities at nonequilibrium condition

In semiconductor devices a nonequilibrium condition is often possible: the densities of one or both types of carriers depart from their equilibrium as given by (12.12) and (12.13). In particular, the minority carrier concentration can be easily overwhelmed by the injection from neighboring regions. Under these circumstances, while

electrons and holes are in local equilibrium with themselves, they are not in equilibrium with each other. In order to extend the relationship between Fermi level and densities discussed above, we can introduce different Fermi levels for electrons and holes. They are called *quasi Fermi levels* defined as:

$$E_{fn} = E_i + k_B\Theta \ln\left(\frac{n}{n_i}\right) \quad (12.23)$$

$$E_{fp} = E_i - k_B\Theta \ln\left(\frac{p}{n_i}\right). \quad (12.24)$$

Considering the well known relation between electrostatic potential and energy  $\psi = -E/q$ , (12.23) and (12.24) can be written as:

$$n = n_i \exp\left(\frac{\psi_i - \varphi_n}{k_B\Theta/q}\right) \quad (12.25)$$

$$p = n_i \exp\left(\frac{\varphi_p - \psi_i}{k_B\Theta/q}\right) \quad (12.26)$$

where  $\varphi_n$  and  $\varphi_p$  are the quasi Fermi potential levels and  $\psi_i$  is the midgap potential level, while  $q = 1.602e^{-19}[C]$  is the elementary charge.

**Remark 12.3.** *In non equilibrium conditions, the quasi Fermi levels have the same physical meaning in terms of the state occupancy as the Fermi level, therefore the electron (hole) density in the conduction band can be calculated using  $E_{fn}$  ( $E_{fp}$ ).*

$$E_c = E_{fn} + k_B\Theta \ln\left(\frac{N_c}{N_d^+}\right) \quad (12.27)$$

$$E_v = E_{fp} - k_B\Theta \ln\left(\frac{N_v}{N_a^-}\right). \quad (12.28)$$

## 12.2. Geometrical model and boundary conditions

Let us consider the device domain as the union of two open disjoint subsets,  $\Omega_{Si}$  (doped silicon part), and  $\Omega_{ox}$  (oxide part), such that their intersection  $\partial\Omega_{Si} \cap \partial\Omega_{ox} = \Gamma_{int}$  is the interface. The oxide region  $\Omega_{ox}$  is assumed to be a perfect insulator so that:

$$\begin{aligned} n &= p = 0 \\ \mathbf{J}_n &= \mathbf{J}_p = \mathbf{0}. \end{aligned} \quad (12.29)$$

The device boundary  $\partial\Omega$  is divided into two disjoint subsets:  $\partial\Omega_c$  and  $\partial\Omega_a$ . The subset  $\partial\Omega_c$  includes the so called *ohmic contacts* (with ohmic contacts we define every

electrical terminal of the device on which the external input voltages are applied). Ohmic contacts are assumed to be *ideal*, they are equipotential surfaces and no voltage drop occurs at the interface between the contact and the neighbouring domain. This is well represented by suitable Dirichlet boundary conditions, therefore in the following we set  $\partial\Omega_c = \Gamma_D$  and enforce:

$$\psi = \varphi_D \quad (12.30)$$

$$n = n_D \quad \text{on } \Gamma_D \quad (12.31)$$

$$p = p_D \quad (12.32)$$

We point that in the case of a perfect insulator domain, (12.30) reduces to the only condition on the electrostatic potential.

Artificial boundaries ( $\partial\Omega_a$ ) are needed in order to obtain a self-contained simulation domain. On these boundaries no electric and current flux is exchanged with the surrounding environment, this fact being well represented by homogeneous Neumann boundary conditions ( $\partial\Omega_a = \Gamma_N$ ):

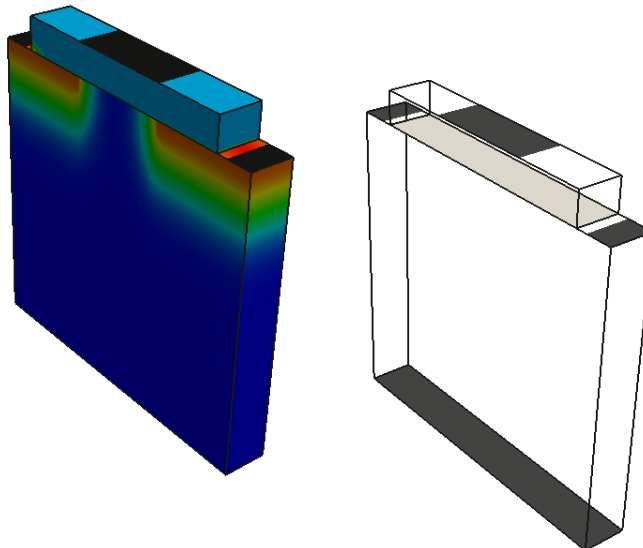


**Figure 12.4** (a) MOS device with net dopant concentration distributed according to a gaussian profile and  $\Gamma_D$  colored in black. The oxide layer is colored in light blue. (b) Outline of the MOS device with  $\Gamma_{int}$  in light gray.

$$\mathbf{D} \cdot \mathbf{n} = 0 \quad (12.33)$$

$$\mathbf{J}_n \cdot \mathbf{n} = 0 \quad \text{on } \Gamma_N \quad (12.34)$$

$$\mathbf{J}_p \cdot \mathbf{n} = 0 \quad (12.35)$$

where  $\mathbf{n}$  is the outward unit normal vector defined over  $\partial\Omega$ . As we noted before on  $\partial\Omega_{ox} \cap \Gamma_N$  condition (12.33) is reduced to the first equation. When oxide is present, the silicon boundaries for continuity equations become

$$\Gamma_{D,Si} = \Gamma_D \cap \partial\Omega_{Si} \quad (12.36)$$

$$\Gamma_{N,Si} = \Gamma_N \cap \partial\Omega_{Si} \cup \Gamma_{int}. \quad (12.37)$$

Fig.12.4 shows an example of boundary setting for a MOS device: in 12.2 contacts are colored in black and in 12.2 with light gray we indicate the interface between oxide and silicon. Thermodynamical equilibrium and charge neutrality are the physical characteristic of an ideal contact. These conditions correspond to the following algebraic system for  $n_D$  and  $p_D$ :

$$\begin{cases} p_D n_D &= n_i^2 \\ p_D - n_D + N_D^+ - N_A^- &= 0 \end{cases}. \quad (12.38)$$

Solving 12.38 on  $\Gamma_{D,Si}$  we have:

$$n_D = \frac{D + \sqrt{D^2 + 4n_i^2}}{2} \quad (12.39)$$

$$p_D = \frac{-D + \sqrt{D^2 + 4n_i^2}}{2} \quad (12.40)$$

where  $D := N_D^+ - N_A^-$  is the net doping concentration. Furthermore at each contact, the quasi Fermi potential levels of silicon are aligned with the external applied voltage  $V_{ext}$

$$\varphi_n = \varphi_p = V_{ext}. \quad (12.41)$$

where  $\varphi_f = -E_f/q$  is the unique quasi Fermi potential level defined at the contacts. As a consequence, we can easily determine potential condition on  $\Gamma_{D,Si}$  using (12.12) and (12.13)

$$\varphi_D = V_{ext} + V_{th} \ln \left( \frac{n_D}{n_i} \right) \quad \text{n-type} \quad (12.42)$$

$$\varphi_D = V_{ext} - V_{th} \ln \left( \frac{p_D}{n_i} \right) \quad \text{p-type.} \quad (12.43)$$

When  $\Omega_{ox} \neq \emptyset$  we set  $\varphi_D$  equal to the external applied voltage on  $\Gamma_D/\Gamma_{D,Si}$ .

### 12.3. Physical model for mobility and Recombination and generation terms

In this section, we describe the principal models used to represent in mathematical form electrical mobilities and recombination/generation mechanisms for electron and hole in the Drift Diffusion system (9.55). As stated in remark 9.14, mobility represents the relation between electron (hole) current density and Electric field. As described in sec 12.1 the electron (hole) are travelling inside the crystal so they are subjected to a number of scattering events with the other electrons (holes), the crystal lattice, the surface. A detailed mathematical description of these events at the atomic scale is not affordable so effective description can be adopted to include in the Drift diffusion system.

#### 12.3.1. Carrier Mobility

In remark 9.14 we have discussed the generalized Ohm’s law and the fundamental role played by mobilities  $\mu_n^{el}$  and  $\mu_p^{el}$  in characterizing the conductivity properties. A great effort has to be made for their modeling to include the most (even if not all) the phenomena occurring at the microscopic scale. In the following we skip the subscript  $n$  and  $p$  and the upscript  $el$ ; in the following tables we report the value of the parameters appearing in the different formula for electron and hole.

#### Lattice Scattering

Semiconductor materials can be described as perfect crystalline structures where the defects are completely ionized and occupy lattice positions. At temperatures different from the 0 K crystal lattice vibrates, generating *phonons*. These phonons are responsible for the scattering with the carriers travelling in the crystal. Increasing temperature will cause more scattering to occur, hence degrading mobility. In order to model the phonon scattering effect the following expression has been proposed [124]:

$$\mu_L = \mu_0 \left( \frac{\Theta}{\Theta_0} \right)^{-\beta} \quad (12.44)$$

where  $\mu_0$  is the reference mobility and  $\beta$  a properly fitted parameter at  $\Theta_0 = 300 K$ . Parameter values for electron and hole, are reported in Tab. 12.1.

Parameter	Electrons	Holes	Unit of Measure
$\mu_0$	1417.0	470.5	$cm^2V^{-1}s^{-1}$
$\beta$	2.5	2.2	

 Table 12.1 Phonon scattering - parameter values at  $\Theta_0 = 300 K$ 

### Ionized Impurity Scattering

The presence of ions, used for obtain  $n/p$ -type region in an extrinsic semiconductor, is responsible for degrading the carrier mobilities: the charged nuclei break the regularity of the silicon lattice, introducing local perturbations to the electrostatic potential, thus interfering with the carrier trajectories.

A model for this phenomenon was proposed by Masetti et al. in [125] and can be expressed as follows:

$$\mu_{LI} = \mu_{min1} \exp\left(-\frac{P_c}{N_{tot}}\right) + \frac{\mu_L - \mu_{min2}}{1 + \left(\frac{N_{tot}}{C_r}\right)^\alpha} - \frac{\mu_1}{1 + \left(\frac{C_s}{N_{tot}}\right)^\beta} \quad (12.45)$$

where  $\mu_L$  is the carrier mobility calculated by taking into account the sole lattice scattering (namely, using (12.44)), while  $N_{tot}$  is the sum of acceptor and donor densities,  $N_{tot} = N_{tot}(\mathbf{x}) = N_D^+(\mathbf{x}) + N_A^-(\mathbf{x})$ . Values for the other parameters are reported in Tab. 12.2.

### High-Field Carrier Velocity Saturation

The presence of an electric field accelerates the mobile charges, thus their velocities increase, but speed values cannot grow indefinitely. From a physical point of view, once the maximum value has been reached, the carrier extra energy is emitted under the form of optical phonons. To avoid unfeasible carrier velocities when  $|\mathbf{E}| \rightarrow \infty$ , an upper bound must be provided. Mathematically, we require that:

$$\lim_{|\mathbf{E}| \rightarrow \infty} \mu|\mathbf{E}| = v_{sat} < +\infty.$$

The Canali model [126] is a very common choice for implementing the aforementioned specification:

$$\mu = \frac{\mu_{low}}{\left[1 + \left(\frac{\mu_{low} F_{drive}}{v_{sat}}\right)^\beta\right]^{1/\beta}} \quad (12.46)$$

Parameter	Electron	Hole	Unit of Measure
$\mu_{min1}$	52.2	44.9	$cm^2V^{-1}s^{-1}$
$\mu_{min2}$	52.2	0	$cm^2V^{-1}s^{-1}$
$\mu_1$	43.4	29.0	$cm^2V^{-1}s^{-1}$
$P_c$	0	$9.23 \times 10^{16}$	$cm^3$
$C_r$	$9.68 \times 10^{16}$	$2.23 \times 10^{17}$	$cm^3$
$C_s$	$3.43 \times 10^{20}$	$6.10 \times 10^{20}$	$cm^3$
$\alpha$	0.680	0.719	
$\beta$	2.0	2.0	

Table 12.2 Ionized impurities scattering - parameter values

where  $\mu_{low}$  is the low-field mobility,  $F_{drive}$  is the carrier driving force (that will be discussed in Sect. 12.3.4), while  $v_{sat}$  and  $\beta$  are given by

$$v_{sat} = v_0 \exp\left(\frac{300}{\Theta}\right)^{\nu_{exp}}, \quad \beta = \beta_0 \left(\frac{\Theta}{300}\right)^{\beta_{exp}}. \quad (12.47)$$

All parameter values are reported in Tab. 12.3.

Parameter	Electron	Hole	Unit of Measure
$v_0$	$1.07 \times 10^7$	$8.37 \times 10^6$	$cms^{-1}$
$\nu_{exp}$	0.87	0.52	
$\beta_0$	1.109	1.213	
$\beta_{exp}$	0.66	0.17	

Table 12.3 Canali model - parameter values

**Remark 12.4.** There exist a number of other mobility models in the modern approach to the simulation of the semiconductor devices that take into account other microscopic phenomena such as the scattering with the Si/SiO<sub>2</sub> interface, the Coulomb scattering, the polycrystalline structure and many others. All this model can be combined together using Mathiessen’s rule as explain below.

### Combining Mobility Models

To describe the carrier travelling as the result of different mechanisms, we need to assume appropriate combining rules. At low electric field the distinct contributions are assembled using the *Mathiessen rule*:

$$\mu = \left( \frac{1}{\mu_1} + \cdots + \frac{1}{\mu_N} \right)^{-1}. \quad (12.48)$$

The global mobility is thus computed as the harmonic average of the various mechanisms taking place during carrier motion. In conditions of high electric field, once the low-field mobility has been determined using Matthiessen's rule, the resulting mobility is calculated by choosing a proper high-field model.

In conclusion, we can outline the process of characterizing carrier mobility as:

- compute the constant mobility (12.44)
- evaluate the Masetti model (12.45) and other possible scattering mechanisms
- combining the models using (12.48)
- apply the high field saturation using Canali model (12.46).

#### 12.3.2. Generation-Recombination Phenomena

In thermodynamic equilibrium no net generation or recombination process can take place: in a typical semiconductor device under working conditions, this assumption obviously does not hold, then a non-zero generation (G) or recombination (R) rate must be calculated. It is possible to use a general expression  $R(n, p)$  (units:  $\text{cm}^{-3}\text{s}^{-1}$ ) to evaluate the terms at the right and side in the (9.55a) and (9.55b) given by:

$$R(n, p) = -(G_{n,p} - R_{n,p}) = (pn - n_i^2)F(n, p) \quad (12.49)$$

where the first term expresses the fact that, at equilibrium, the resulting rate must be null, while the scalar function  $F(n, p)$  has to be provided according to the effect that has to be modeled whose parameters depends if considering electron or hole. When different mechanisms are present it is possible to assemble the models just adding all together.

#### Shockley-Read-Hall Recombination

In indirect bandgap semiconductors, such as silicon, the most relevant phenomenon is the trap assisted generation-recombination, in which carriers can move from valence to conduction band and viceversa. Even if, in principle, carriers can jump up or down directly, the possibility of having enough energy is extremely small (band minima and maxima are misaligned). Trap states placed in the forbidden gap allow the particle

momentum to change, hence making the transition possible. These spurious energy levels are generated by lattice imperfections -*deep defect levels*- that can significantly increase when dopants are inserted.

The global mechanism can be decomposed in the following two processes:

- an electron in the conduction band relaxes to the valence band via a trap state and there neutralizes a hole ( $R_{SRH}$ );
- a hole in the valence band jumps into the conduction band via a trap state and there recombines with an electron ( $G_{SRH}$ ).

To derive the Shockley-Read-Hall formula for the function  $F_{SRH}$  we refer to [89]

$$F_{SRH}(n, p) = \frac{1}{\tau_{n,0}(n + \bar{n}) + \tau_{p,0}(p + \bar{p})} \quad (12.50)$$

with

$$\bar{n} = n_i \exp\left(\frac{E_t - E_i}{k_B\Theta}\right), \quad \bar{p} = n_i \exp\left(\frac{E_i - E_t}{k_B\Theta}\right) \quad (12.51)$$

Parameters  $\tau_{n,0}$  and  $\tau_{p,0}$  are the carrier lifetimes (units:  $s^{-1}$ ), while the value  $E_t$  represents the energy level (units: eV) of the trap state. The maximum recombination rate occurs when  $E_t = E_i$  (i.e. when the trap is placed on the intrinsic Fermi level) and typical values for carrier lifetimes lie in the range spanning  $\mu s$  to  $ms$ , as reported in Tab. 12.4.

Parameter	Electron	Hole	Unit of Measure
$\tau_{n(p),0}$	$1.0 \times 10^{-5}$	$3.0 \times 10^{-6}$	$s$
$E_t$	0.0	0.0	eV

Table 12.4 Shockley-Read-Hall model - parameter values.

### Auger Recombination

The Auger recombination is a three-particle process in which electron-hole pairs recombine in band-to-band transitions, giving the excess of energy to another electron or hole, that eventually will lose its energy by colliding with the lattice, hence relaxing to the bottom of the proper band.

Four different situations can occur:

- $R_{Au}^{2n,1p}$ , where high-energy electron in the conduction band recombines with a hole in valence band, releasing the excess energy to another electron in the conduction band;

- $G_{Au}^{2n,1p}$ , where an electron in the valence band jumps into the conduction band acquiring the required energy from a higher energy electron in the conduction band, consequently leaving a hole in the valence band;
- $R_{Au}^{2p,1n}$ , is the same as the  $R_{Au}^{2n,1p}$  recombination, but the roles of electrons and holes are exchanged;
- $G_{Au}^{2p,1n}$ , is the same as the  $G_{Au}^{2n,1p}$  generation, but the roles of electrons and holes are exchanged.

The whole process is quantitatively expressed by the function:

$$F_{Au}(n, p) = \Gamma_n n + \Gamma_p p \quad (12.52)$$

in which  $\Gamma_n$  and  $\Gamma_p$  take the name of Auger coefficients and represent the proper event probability. Their values are reported in Tab. 12.5. Substituting the expression of  $F_{Au}$  in (12.49) leads to the polynomial terms  $n^2p$  and  $p^2n$ , highlighting the three-particle interaction needed for the phenomenon to happen.

As a final note we point out that, being the Auger coefficients usually very small, the Auger effect becomes relevant only in case of very high dopant concentration.

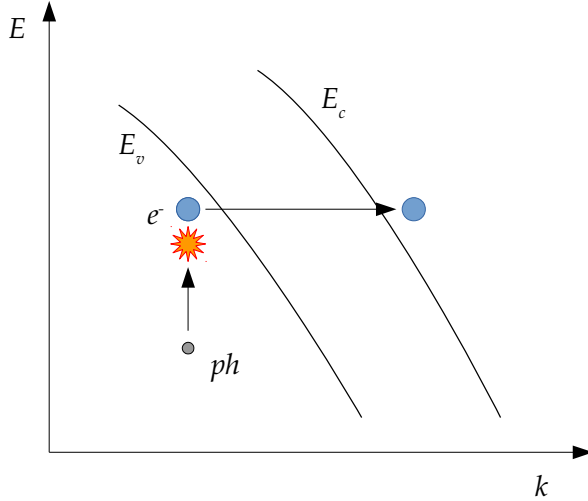
Parameter	Electron	Hole	Unit of Measure
$\Gamma$	$2.9 \times 10^{-31}$	$1.028 \times 10^{-31}$	$cm^6 s^{-1}$

Table 12.5 Auger model - parameter values

### Phonon-assisted Tunneling

Under certain circumstances -such as high potential drops across small intervals or narrow  $p$ - $n$  junctions with high doping concentrations- the resulting energy bands exhibit a steep gradient. In these scenarios, the distance between bands gets considerably reduced and the small spatial gap allows the wavefunctions of electrons in valence and conduction to overlap, hence making a transition possible. Even though no extra energy is required to perform the transition, a change in the particle momentum is required; this occurs via a phonon collision, as shown in Fig. 12.5.

In his work, Schenk [127] rigorously derives an expression for the phonon-assisted



**Figure 12.5** Representation of the phonon-assisted tunneling effect in the  $E$ - $k$  plane: colliding with the phonon ( $ph$ ), the electron ( $e^-$ ) is able to move from the valence to the conduction band crossing the forbidden gap.

tunneling and obtains a result that, coherently with equation (12.49), reads as:

$$R(n, p) = \frac{AF^{\frac{7}{2}}}{(n + n_i)(p + n_i)} \times \left[ \frac{(F_{cr}^\pm)^{-\frac{3}{2}} \exp\left(-\frac{F_{cr}^\pm}{F}\right)}{\exp\left(-\frac{\hbar\omega_{ph}}{k_B\Theta}\right) - 1} + \frac{(F_{cr}^\pm)^{-\frac{3}{2}} \exp\left(-\frac{F_{cr}^\pm}{F}\right)}{1 - \exp\left(-\frac{\hbar\omega_{ph}}{k_B\Theta}\right)} \right] \quad (12.53)$$

where we have denoted by  $F$  the electric field magnitude  $|\mathbf{E}|$ , while  $F_{cr}^\pm$  is the critical field strength and is given by

$$F_{cr}^\pm = B(E_{gap} \pm \hbar\omega_{ph}) , \quad (12.54)$$

the quantity  $\hbar\omega_{ph}$  being the acoustic phonon energy. The other parameters are summarized in Tab. 12.6. The upper sign in (12.53) and (12.54) refers to tunneling generation ( $np < n_i^2$ ), while the lower one to recombination ( $np > n_i^2$ ). We note that the mathematical form of the Phonon-assisted-tunneling is different from the generic formula we have introduced in (12.49) but this mechanism can be considered by adding its contribution to the other mechanisms.

### Impact ionization

Parameter	Value	Unit of Measure
$A$	$8.977 \times 10^{20}$	s
$B$	$2.14667 \times 10^7$	eV
$\hbar\omega_{ph}$	18.6	meV

Table 12.6 Schenk model - parameter values.

If the electric field magnitude is high, carriers can acquire enough kinetic energy to generate an electron-hole pair by breaking a lattice bond when a collision occurs. The three particles can in turn generate additional pairs by impacting other atoms and ionizing them as well, causing an avalanche generation effect.

Models describing impact ionization phenomena assume a slightly different form than (12.49). The generic expression relies on Chynoweth’s law [128]:

$$F_{II} = \alpha_n(F_{drive})n|\mathbf{v}_n| + \alpha_p(F_{drive})p|\mathbf{v}_p|. \quad (12.55)$$

Coefficients  $\alpha_n$  and  $\alpha_p$  can be interpreted as the probability for unit length for an electron or hole to collide with an atom and to ionize it. Among the various possibilities, we choose the Van Overstraeten-De Man model [129], which gives:

$$\alpha_\nu(F_{drive}) = \gamma a_\nu \exp\left(-\frac{\gamma b_\nu}{F_{drive}}\right) \quad \nu = n, p \quad (12.56)$$

with

$$\gamma = \frac{\tanh\left(\frac{\hbar\omega_{op}}{2k_B\Theta_0}\right)}{\tanh\left(\frac{\hbar\omega_{op}}{2k_B\Theta}\right)}. \quad (12.57)$$

The quantity  $\hbar\omega_{op}$  is the optical phonon energy, while the scalar value  $F_{drive}$  is the avalanche field, that can be set as either equal to the quasi Fermi potential gradient or the electric field component parallel to the current density (see Sect. 12.3.4). Parameter values are reported in Tab. 12.7 where they assume a different value depending on the intensity of the electric field.

### 12.3.3. Bandgap Narrowing and Intrinsic Concentration

As many other quantities, such as the mobility values previously treated, the energy bandgap is affected by temperature. Even though the nature of this phenomenon still presents unclarified points (especially at low temperature), it is believed that this de-

Parameter	Electron	Hole	Valid Range	Unit of Measure
$E_0$	$4.0 \times 10^5$	$4.0 \times 10^5$		$Vcm^{-1}$
$a_{high}$	$7.03 \times 10^5$	$6.71 \times 10^5$	$E_0 \div 6.0 \times 10^5$	$cm^{-1}$
$a_{low}$	$7.03 \times 10^5$	$1.582 \times 10^6$	$1.75 \times 10^5 \div E_0$	$cm^{-1}$
$b_{high}$	$1.231 \times 10^6$	$1.693 \times 10^6$	$E_0 \div 6.0 \times 10^5$	$Vcm^{-1}$
$b_{low}$	$1.231 \times 10^6$	$2.036 \times 10^6$	$1.75 \times 10^5 \div E_0$	$Vcm^{-1}$
$\hbar\omega_{op}$	0.063	0.063		eV

Table 12.7 Van Overstraeten-De Man model - parameter values

pendence arises from two different effects:

- a shift in the relative position of conduction and valence bands due to lattice dilatation/compression;
- a change induced by electron-phonon interaction;

It can be shown that the bandgap is related with temperature through:

$$\Delta E_{gap} \propto \Theta^2 \quad \text{for } \Theta \ll \Theta_D \quad (12.58)$$

$$\Delta E_{gap} \propto \Theta \quad \text{for } \Theta \gg \Theta_D \quad (12.59)$$

$\Theta_D$  being the material *Debye temperature*. According to (12.58) and (12.59), Varshni [130], proposed the following expression:

$$E_{gap}(T) = E_{gap}(0) - \frac{\alpha \Theta^2}{\Theta + \beta} \quad (12.60)$$

where  $E_{gap}(0)$  is the bandgap energy at 0 K, and  $\alpha$  and  $\beta$  are properly fitted parameters (values for silicon are reported in Tab. 12.8).

Parameter	Value	Unit of Measure
$E_{gap}(0)$	1.1696	eV
$\alpha$	$4.74 \times 10^{-4}$	$eVk^{-1}$
$\beta$	636	K

Table 12.8 Thermal bandgap model - parameter values.

Intrinsic concentration also depends on temperature and not only through the energy gap, but also by means of the effective density of states  $N_C$  and  $N_V$

$$n_i = \sqrt{N_C(\Theta)N_V(\Theta)} \exp\left(-\frac{E_{gap}}{2k_B\Theta}\right). \quad (12.61)$$

A possibility for expliciting the temperature dependence is represented by the following expressions:

$$N_C(\Theta) = 2\left(\frac{2\pi m_e^* k_B \Theta}{h^2}\right)^{\frac{3}{2}} = N_C(300K)\left(\frac{\Theta}{300K}\right)^{\frac{3}{2}}, \quad (12.62)$$

$$N_V(\Theta) = 2\left(\frac{2\pi m_h^* k_B \Theta}{h^2}\right)^{\frac{3}{2}} = N_V(300K)\left(\frac{\Theta}{300K}\right)^{\frac{3}{2}}. \quad (12.63)$$

A second approach is to consider the expression of the effective mass. For electrons we have:

$$m_e^* = 6^{\frac{2}{3}} (m_l m_t^2)^{\frac{2}{3}}, \quad (12.64)$$

$$\frac{m_t}{m_0} = a \frac{E_{gap}(0)}{E_{gap}(\Theta)} \quad (12.65)$$

and  $N_C$  becomes

$$N_C(T) = N_{C,0} \left(\frac{m_e^*(\Theta)}{m_0}\right)^{\frac{2}{3}} \left(\frac{\Theta}{300K}\right)^{\frac{2}{3}}. \quad (12.66)$$

For the holes, the effective mass expression is:

$$\frac{m_h^*}{m_0} = \frac{a + b\Theta + c\Theta^2 + d\Theta^3 + e\Theta^4}{1 + f\Theta + g\Theta^2 + h\Theta^3 + i\Theta^4} \quad (12.67)$$

and the resulting density of states is

$$N_V(\Theta) = N_{V,0} \left(\frac{m_h^*(\Theta)}{m_0}\right)^{\frac{2}{3}} \left(\frac{\Theta}{300K}\right)^{\frac{2}{3}}. \quad (12.68)$$

Parameter values are shown in Tab. 12.9 for electrons and Tab. 12.10 for holes.

#### 12.3.4. Driving Force

In some of the models discussed in the previous paragraph, the driving force has been mentioned as the force that drive the physical mechanism but it has not been specified. Two are the main approaches for the calculation of the driving force:

- the gradient of quasi-Fermi potential

$$F_{drive,\nu} = |\nabla \varphi_\nu| \quad \nu = n, p \quad (12.69)$$

Parameter	Value	Unit of Measure
$m_0$	$9.109 \times 10^{-31}$	$kg$
$m_l$	$0.9163m_0$	$Kg$
$a$	0.1905	
$N_{C,0}$	$2.5094 \times 10^{19}$	$cm^{-3}$
$N_C(300K)$	$2.89 \times 10^{19}$	$cm^{-3}$

**Table 12.9** Electron effective mass and density of states in conduction band - parameter values.

Parameter	Value	Unit of Measure
$m_0$	$9.109 \times 10^{-31}$	$kg$
$a$	0.4435870	
$b$	$0.3609528 \times 10^{-2}$	$K^{-1}$
$c$	$0.1173515 \times 10^{-3}$	$K^{-2}$
$d$	$0.1263218 \times 10^{-5}$	$K^{-3}$
$e$	$0.3025581 \times 10^{-8}$	$K^{-4}$
$f$	$0.4683382 \times 10^{-2}$	$K^{-1}$
$g$	$0.2286895 \times 10^{-3}$	$K^{-2}$
$h$	$0.7469271 \times 10^{-6}$	$K^{-3}$
$i$	$0.1727481 \times 10^{-8}$	$K^{-4}$
$N_{V,0}$	$2.5094 \times 10^{19}$	$cm^{-3}$
$N_V(300K)$	$3.14 \times 10^{19}$	$cm^{-3}$

Table 12.10 Hole effective mass and density of states in conduction band - parameter values.

- the electric field component parallel to the current density

$$F_{drive,v} = \frac{\mathbf{E} \cdot \mathbf{J}_v}{|\mathbf{J}_v|} \quad v = n, p \quad (12.70)$$

where  $F_{drive,v}$  indicates the carrier driving force for electron or hole. The choice of the approach to model the driving force significantly affects the performance of a numerical simulation and the model results.

## CHAPTER 13

# Numerical Discretization and Solution Algorithms of the Drift Diffusion system

The Drift-Diffusion model (9.55) is a highly nonlinear system of PDEs, induced in particular by the physical models introduced in chapter 12. An analytical solution is possible only under strong simplifications and/or in particular device operation, so that an accurate numerical approach is required to treat the simulation of realistic situation. In this chapter we describe the most used methodologies adopted for addressing the solution of the equations (9.55e) (9.55a) and (9.55b) in their stationary form.

### 13.1. Abstract Newton’s Method

Let us consider a generic abstract form of a non linear boundary value problem

$$\mathcal{N}(U) + \sigma U = f \quad \text{in } \Omega \tag{13.1a}$$

$$\mathcal{B}_{\partial\Omega}(U) = 0 \quad \text{on } \partial\Omega. \tag{13.1b}$$

In the nonlinear partial differential equation (13.1a),  $U : \Omega \rightarrow \mathbb{R}$  represents the dependent variable,  $\mathcal{N}$  is the nonlinear differential operator acting on the space independent variable,  $\sigma = \gamma/\Delta t + \kappa$  and  $f$  is a given source term. In (13.1b),  $\mathcal{B}_{\partial\Omega} : \partial\Omega \rightarrow \mathbb{R}$  is (in general) a nonlinear operator representing the boundary conditions that are enforced on the dependent variable  $U$  on  $\partial\Omega$ .

Now we would like to extend the Newton method to the iterative solution of (13.1); to do that, we denote by  $V$  the Hilbert space in which we seek the solution of (13.1) and endow  $V$  with the norm  $\|\cdot\|_V$ . Then, we set

$$G(U) := \mathcal{N}(U) + \sigma U - f, \tag{13.2}$$

and we consider the following nonlinear abstract problem associated with the nonlinear differential operator  $G : V \rightarrow V$ : find  $U \in V$  such that

$$G(U) = 0. \tag{13.3}$$

The abstract Newton method for the iterative solution of problem (13.3) reads:

given  $U^{(0)} \in V$ , for all  $j \geq 0$  until convergence, solve the following *linearized problem*:

$$G'(U^{(j)})\delta U^{(j)} = -G(U^{(j)}) \quad \text{Solve step} \quad (13.4a)$$

$$U^{(j+1)} = U^{(j)} + \delta U^{(j)} \quad \text{Update step.} \quad (13.4b)$$

In order to extend the Newton’s Method to an abstract setting, we need introduce the generalization of the function derivative  $f'(x)$ .

**Definition 13.1** (The Frèchet derivative). *The Frèchet derivative of the nonlinear operator  $G$ , evaluated at  $v \in V$*

$$\begin{aligned} G' : \quad V &\rightarrow L(V; V) \\ v &\rightarrow G'(v) \end{aligned} \quad (13.5)$$

is defined through the following limit

$$G'(v) := \lim_{\eta \rightarrow 0} \frac{G(v + \eta w) - G(v)}{\eta} \quad \forall w \in V. \quad (13.6)$$

**Remark 13.1.** From Definition 13.1, we see that  $G'(\cdot)$  is a linear operator from  $V$  into  $L(V; V)$ , the set of real-valued linear continuous functionals from  $V$  into  $V$ . The Frèchet derivative  $G'(v)$  acts on the generic element  $w$  belonging to the normed function space  $V$ , exactly as  $g'(x)$  is a linear operator from the domain of  $g$  into  $\mathbb{R}$ .

**Example 13.1** (Frèchet derivative of a linear operator). Let us compute the Frèchet derivative of  $G(\cdot) = \nabla_{\underline{x}} \cdot (-K \nabla_{\underline{x}}(\cdot))$ , where  $K : \Omega \rightarrow \mathbb{R}$  is a strictly positive given continuously differentiable function. We have

$$\begin{aligned} G'(v) &= \lim_{\eta \rightarrow 0} \frac{\nabla_{\underline{x}} \cdot (-K \nabla_{\underline{x}}(v + \eta w)) - \nabla_{\underline{x}} \cdot (-K \nabla_{\underline{x}} v)}{\eta} \\ &= \lim_{\eta \rightarrow 0} \frac{\nabla_{\underline{x}} \cdot (-K \nabla_{\underline{x}}(\eta w))}{\eta} = \nabla_{\underline{x}} \cdot (-K \nabla_{\underline{x}} w) \equiv G(w) \end{aligned}$$

which shows that the Frèchet derivative of a linear operator coincides with the operator itself.

**Example 13.2** (Frèchet derivative of a semilinear operator). Let us compute the Frèchet derivative of the semilinear operator  $G(\cdot) = \nabla_{\underline{x}} \cdot (-K \nabla_{\underline{x}}(\cdot)) + f(\underline{x}, \cdot)$ , where  $f$  is a given function (in general nonlinearly depending on  $u$ ) continuously differentiable with re-

spect to the second argument. We have

$$\begin{aligned} G'(v) &= \lim_{\eta \rightarrow 0} \frac{\nabla_{\underline{x}} \cdot (-K \nabla_{\underline{x}}(v + \eta w)) + f(\underline{x}, v + \eta w) - \nabla_{\underline{x}} \cdot (-K \nabla_{\underline{x}} v) - f(\underline{x}, v)}{\eta} \\ &= \nabla_{\underline{x}} \cdot (-K \nabla_{\underline{x}} w) + \lim_{\eta \rightarrow 0} \frac{f(\underline{x}, v + \eta w) - f(\underline{x}, v)}{\eta} \\ &= \nabla_{\underline{x}} \cdot (-K \nabla_{\underline{x}} w) + \frac{\partial f}{\partial u}(\underline{x}, v)w. \end{aligned}$$

**Theorem 13.1** (Local convergence theorem for the abstract Newton Method). *Let  $U^* \in V$  be a solution of problem (13.3). Assume that  $G'$  is Lipschitz continuous in the ball  $\mathcal{B}(U^*; R)$ , i.e., that there exists  $K_L > 0$  such that*

$$\|G'(v) - G'(z)\|_{L(V; V)} \leq K_L \|v - z\|_V \quad \forall v, z \in \mathcal{B}(U^*; R), \quad v \neq z,$$

where  $\|\cdot\|_{L(V; V)}$  is the norm on  $L(V; V)$ . Then, there exists  $R' > 0$ , with  $R' \leq R$ , such that for all  $U^{(0)} \in \mathcal{B}(U^*; R')$  the sequence  $\{U^{(j)}\}$  generated by (13.4) converges quadratically to  $U^*$ . This means that there exists  $C > 0$  such that, for a suitable  $j_0 \geq 0$  we have

$$\|U^* - U^{(j+1)}\|_V \leq C \|U^* - U^{(j)}\|_V^2 \quad \forall j \geq j_0. \quad (13.7)$$

**Remark 13.2.** Theorem 13.1 tells us that the Newton method converges very rapidly, provided to start sufficiently close to the zero  $U^* \in V$  of  $G$ . In particular, the assumption that  $G'$  is locally Lipschitz continuous in the ball  $\mathcal{B}(U^*; R)$  is the abstract request corresponding to the request that  $g \in C^2(I_\alpha)$  for the standard Newton Method.

## 13.2. Gummel Map iteration algorithm

Originally proposed [131], the Gummel map algorithm is an iterative method used to solve (9.55e) (9.55a) and (9.55b) in stationary conditions, i.e negleting the time derivative term. The solving procedure is outlined in Algorithm 13.1.

In 13.1 the nonlinearity is limited to the sole Poisson equation (9.55a), whereas the continuity equations for electron and hole are solved in a linearized form as described below.

### 13.2.1. Non Linear Poisson Equation

In equation (9.55a): we replace the electron and hole concentrations with the Maxwell-Boltzmann statistics (12.25) and (12.26) with  $\varphi_i = \psi$  the electrostaic potential, obtaining

$$G(\psi) = \nabla_{\underline{x}} \cdot (-\varepsilon \nabla_{\underline{x}} \psi) - q n_i \left( \exp\left(\frac{\varphi_p - \psi}{V_{th}}\right) - \exp\left(\frac{\psi - \varphi_n}{V_{th}}\right) \right) - qD = 0. \quad (13.8)$$

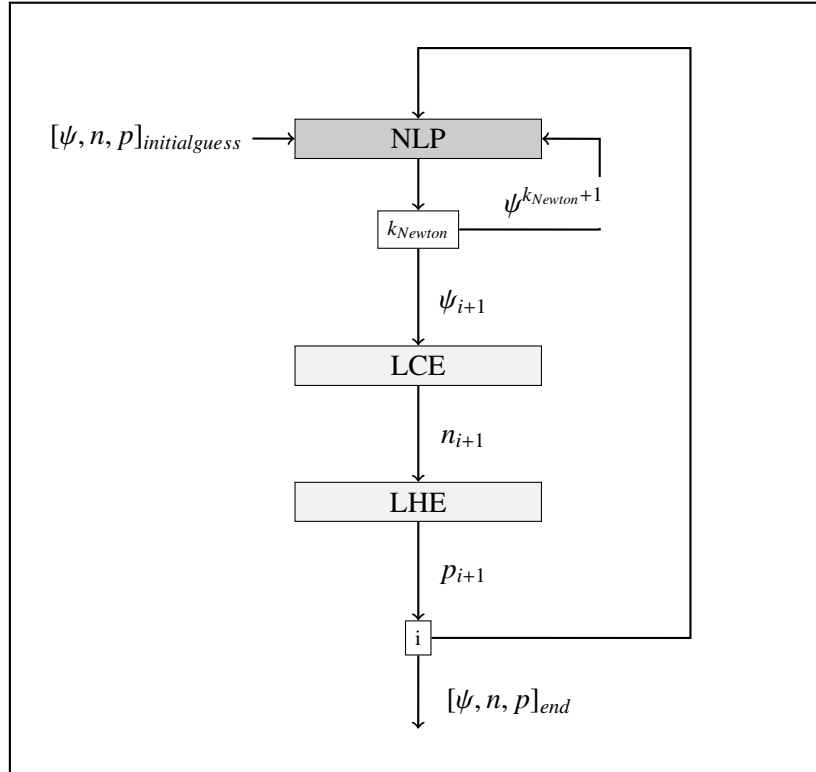


Figure 13.1 Flow chart of Gummel algorithm.

In order to solve non linear Poisson equation (13.8) we use the abstract form of the Newton method (see section 13.1) with the operator  $G$  defined in (13.8). The calculated Frechét derivative is given by:

$$G'(\psi)\delta\psi = -\nabla_{\underline{x}} \cdot (\varepsilon \nabla_{\underline{x}} \delta\psi) + \frac{qn_i}{V_{th}} \left( \exp\left(\frac{\varphi_p - \psi}{V_{th}}\right) + \exp\left(\frac{\psi - \varphi_n}{V_{th}}\right) \right) \delta\psi \quad (13.9)$$

The Newton method applied to the solution of the non linear Poisson equation reads:

$$\begin{cases} \nabla_{\underline{x}} \cdot (-\varepsilon \nabla_{\underline{x}} \delta\psi^k) + \sigma^k \delta\psi^k = -f^k & \text{in } \Omega \\ \delta\psi^k = 0 & \text{on } \Gamma_D \\ \nabla_{\underline{x}} \delta\psi^k \cdot \mathbf{n} = 0 & \text{on } \Gamma_N \\ \psi^{k+1} = \psi^k + \delta\psi^k \end{cases} \quad (13.10)$$

where

$$\sigma^k = \begin{cases} \frac{qn_i}{V_{th}} \left( \exp\left(\frac{\varphi_p - \psi^k}{V_{th}}\right) + \exp\left(\frac{\psi^k - \varphi_n}{V_{th}}\right) \right) & \text{in } \Omega_{Si} \\ 0 & \text{in } \Omega_{ox} \end{cases} \quad (13.11)$$

and

$$f^k = \begin{cases} \nabla \cdot (-\varepsilon \nabla_{\underline{x}} \psi^k) - qn_i \left( \exp\left(\frac{\varphi_p - \psi^k}{V_{th}}\right) - \exp\left(\frac{\psi^k - \varphi_n}{V_{th}}\right) \right) - qD & \text{in } \Omega_{Si} \\ \nabla \cdot (-\varepsilon \nabla_{\underline{x}} \varphi^k) & \text{in } \Omega_{ox} \end{cases} \quad (13.12)$$

**Remark 13.3.** We note that the plain application of the Newton method to solve the Non Linear Poisson in semiconductor application overestimate the correction step. This phenomenon is frequently indicated as overshoot and can be solved simply limiting the size of the update  $\delta\psi$  determined by Newtons method. This method is known as the damping.

### 13.2.1.1. Updating the Electrostatic potential within the Gummel map

The electrostatic potential is updated within the Gummel map using the obtained solution of equation (13.8)

$$\psi^i = \psi^{\bar{k}}$$

where  $i$  indicates the Gummel map iteration, while  $\bar{k}$  is the index of Newton's algorithm at which the convergence criterion is satisfied.

### 13.2.2. Linearized continuity equations

The linearization of (9.55a) and (9.55b) is obtained by two steps (see [132]):

- including the electrostatic potential as calculated by the solution of (13.8)  $\psi^i$
- computing the rate  $R(n, p)$  (12.49), using the solution from the previous iteration obtaining:

$$\begin{aligned} R_n^i &= (n^i p^{i-1} - n_i^2) F(n^{i-1}, p^{i-1}) && \text{for electron,} \\ R_p^i &= (n^{i-1} p^i - n_i^2) F(n^{i-1}, p^{i-1}) && \text{for hole.} \end{aligned}$$

where  $i$  indicates the present Gummel iteration. Considering the other generation mechanism not included in the definition of  $R(n, p)$  their linearization is performed adopthing the same approach.

Using the two steps, we get the Linearized Electron Continuity (LEC) and Linearized Hole Conitnuity (LHC), from the equations (9.55a) and (9.55b) respectively:

$$\nabla_{\underline{x}} \cdot (qn^i \mu_n \nabla_{\underline{x}} \psi^i - qD_n \nabla_{\underline{x}} n^i) = -qR_n^i \quad \text{in } \Omega_{Si}$$

$$\begin{aligned} \text{(LEC)} \quad n^i &= n_D && \text{on } \Gamma_{D,Si} \\ \nabla_{\underline{x}} n^i \cdot \mathbf{n} &= 0 && \text{on } \Gamma_{N,Si} \end{aligned} \quad (13.13)$$

and

$$\begin{aligned} \text{(LHC)} \quad \nabla_{\underline{x}} \cdot (-qp^i \mu_p \nabla_{\underline{x}} \psi^i - qD_p \nabla_{\underline{x}} p^i) &= -qR_p^i && \text{in } \Omega_{Si} \\ p^i &= p_D && \text{on } \Gamma_{D,Si} \\ \nabla_{\underline{x}} p^i \cdot \mathbf{n} &= 0 && \text{on } \Gamma_{N,Si} \end{aligned} \quad (13.14)$$

It is useful to split the R/G term in equations (13.13) and (13.14) to highlights the reaction term:

$$\nabla_{\underline{x}} \cdot (+qn^i \mu_n \nabla_{\underline{x}} \psi^i - qD_n \nabla_{\underline{x}} n^i) + q\sigma_n^{i-1} n^i = qf_n^{i-1} \quad (13.15)$$

$$\nabla_{\underline{x}} \cdot (-qp^i \mu_p \nabla_{\underline{x}} \psi^i - qD_p \nabla_{\underline{x}} p^i) + q\sigma_p^{i-1} p^i = qf_p^{i-1} \quad (13.16)$$

where

$$\begin{aligned} \sigma_n^{i-1} &= p^{i-1} F(n^{i-1}, p^{i-1}) & \sigma_p^{i-1} &= n^{i-1} F(n^{i-1}, p^{i-1}) \\ f_n^{i-1} &= n_i^2 F(n^{i-1}, p^{i-1}) & f_p^{i-1} &= n_i^2 F(n^{i-1}, p^{i-1}) \end{aligned}$$

Equations (13.13) and (13.14) are solved sequentially providing the carrier densities  $n$  and  $p$  needed to recompute the quasi-Fermi potentials  $\varphi_n$  and  $\varphi_p$ , within (13.8), using (12.25) and (12.26). Then, the Gummel map iteration counter is increased and the procedure continues until convergence.

**Remark 13.4.** It is interesting to notice that the algebraic counterpart of the above procedure for the evaluation of R/G term corresponds to the Jacobi iterative method for linear systems. Another possible approach is to use the latest computed electron density ( $n^i$ ) in (13.16), instead of the previous one ( $n^{i-1}$ ), leading to a Gauss-Seidel method.

### 13.2.3. Convergence evaluation

The monitoring of the Gummel map convergence is based on two possible choice

- The first approach is based on the residual of (13.8) and on the difference between the solutions of (13.13) and (13.14) of two successive iteration using a suitable norms, as:

$$\begin{aligned} \|G(\psi^k)\|_{L^2} &< tol_{NLP}, \\ \|\psi^i - \psi^{i-1}\|_{L^\infty} + \|n^i - n^{i-1}\|_{L^\infty} + \|p^i - p^{i-1}\|_{L^\infty} &< tol_{GM}. \end{aligned}$$

where  $tol_{NLP}$  and  $tol_{GM}$  are positive predefined tolerances.

- The second approach is based on the evaluation of the difference between the pseu-

dopotential as calculated by two successive iteration using a suitable norms, as:

$$\|\phi_n^i - \phi_n^{i-1}\|_{L^\infty} + \|phi_p^i - \phi_p^{i-1}\|_{L^\infty} < tol_{GM}.$$

With the above choices, it has been proved in [62] that the Gummel map algorithm converges to the exact solution of the Drif-Diffusion with a linear rate. Regardless such theoretical results, in practice the method often exhibits a higher convergence rate (superlinear).

**Remark 13.5.** *The Gummel map is not the only viable choice for solving the stationary Drift-Diffusion system, another common approach is the so called fully coupled Newton algorithm as explained in 13.3. Albeit the latter one attains a convergence rate substantially higher (quadratic), the former one still has a few non negligible advantages:*

- less computational requirements, because at each iteration 3 linear systems of dimension  $N_{dof}^2$  have to be solved instead of a system of dimension  $(3N_{dof})^2$ ;
- avoiding the estimation of the initial guess, which is an extremely valuable feature especially in a 3D context, where the problem of finding a good initial guess is often non trivial.

### 13.3. Fully Coupled Newton algorithm

An alternative approach to the solution of the stationary form of the Drift-Diffusion model (9.55) is the fully coupled Netwon's algorithm. let us write the Drift-Diffusion model (9.55) as:

$$\mathbf{F}(\mathbf{U}) = \mathbf{0} \quad (13.17)$$

where

$$\mathbf{U} := [\psi, n, p]^T, \quad \mathbf{F}(\mathbf{U}) := \begin{bmatrix} F_1(\mathbf{U}) \\ F_2(\mathbf{U}) \\ F_3(\mathbf{U}) \end{bmatrix} \quad (13.18)$$

having set:

$$\begin{aligned} F_1(\mathbf{U}) &= \nabla_{\underline{x}} \cdot (-\varepsilon \nabla_{\underline{x}} \psi) - q(p - n + D) \\ F_2(\mathbf{U}) &= \nabla_{\underline{x}} \cdot (q\mu_n n \nabla_{\underline{x}} \psi - qD_n \nabla_{\underline{x}} n) + qR \\ F_3(\mathbf{U}) &= \nabla_{\underline{x}} \cdot (-q\mu_p p \nabla_{\underline{x}} \psi - qD_p \nabla_{\underline{x}} p) + qR. \end{aligned}$$

Applying the generalization of the abstract Newton method to a vector operator

$\mathbf{F}(\mathbf{U})$  we get the following Jacobian matrix

$$\begin{bmatrix} F'_{1,\psi} & F'_{1,n} & F'_{1,p} \\ F'_{2,\psi} & F'_{2,n} & F'_{2,p} \\ F'_{3,\psi} & F'_{3,n} & F'_{3,p} \end{bmatrix} \begin{bmatrix} \delta\psi \\ \delta n \\ \delta p \end{bmatrix} = \begin{bmatrix} -F_1(\psi, n, p) \\ -F_2(\psi, n, p) \\ -F_3(\psi, n, p) \end{bmatrix}. \quad (13.19)$$

**Remark 13.6.** Each row of the above matrix need to be discretized using the FEM. Denoting by  $N_{dof}$  the number of degrees of freedom (dofs) to represent  $\delta\psi$ ,  $\delta n$  and  $\delta p$  we see that the structure of the discrete problem associated with (13.19) is the following linear algebraic system

$$\begin{bmatrix} \mathbf{K}_{1,\psi} & \mathbf{K}_{1,n} & \mathbf{K}_{1,p} \\ \mathbf{K}_{2,\psi} & \mathbf{K}_{2,n} & \mathbf{K}_{2,p} \\ \mathbf{K}_{3,\psi} & \mathbf{K}_{3,n} & \mathbf{K}_{3,p} \end{bmatrix} \begin{bmatrix} \delta\psi \\ \delta n \\ \delta p \end{bmatrix} = \begin{bmatrix} -\mathbf{F}_1(\psi, n, p) \\ -\mathbf{F}_2(\psi, n, p) \\ -\mathbf{F}_3(\psi, n, p) \end{bmatrix} \quad (13.20)$$

where each matrix  $\mathbf{K}$  is a block of size  $N_{dof} \times N_{dof}$ . This implies that at every iteration step we have to solve a linear problem of  $3 \times N_{dof}$  variables. Moreover, to ensure convergence of the Newton iterative process, it is important to provide a very good initial guess vector  $[\psi^0, n^0, p^0]$ . Because the problem variables have different orders of magnitude and the Jacobian matrix is often quite ill-conditioned, appropriate scaling and balancing techniques are needed in order to avoid problems associated with round-off error.

### 13.4. Weak Formulation of the Drift Diffusion system

In order to numerically solve the Gummel map algorithm 13.2 we proceed to derive the weak formulation for each of the equations in 13.1. Let introduce the Sobolev space  $H^1(\Omega)$  defined as:

$$H^1(\Omega) = \{v \in L^2(\Omega) : \|\nabla v\|_{L^2(\Omega)} < \infty\}$$

and the associated subspace  $H_{0,\Gamma_D}^1(\Omega)$  composed by functions vanishing on the boundary  $\Gamma_D \subseteq \partial\Omega$ :

$$H_{0,\Gamma_D}^1(\Omega) = \{v \in H^1(\Omega) : v|_{\Gamma_D} = 0\}.$$

#### 13.4.1. Weak form of the Nonlinear Poisson Equation

In order to obtain the weak form of (13.10) let us multiply by a test function  $v \in V = H_{0,\Gamma_D}^1(\Omega)$  and integrating on the whole domain we obtain equation (13.10):

$$\int_{\Omega} \nabla_{\underline{x}} \cdot (-\varepsilon \nabla_{\underline{x}} \delta \psi^k) v \, d\Omega + \int_{\Omega} \sigma^k \delta \psi^k v \, d\Omega = \int_{\Omega} f^k v \, d\Omega.$$

Applying Green’s theorem to the first term, we get:

$$\begin{aligned} \int_{\Omega} \nabla_{\underline{x}} \cdot (-\varepsilon \nabla_{\underline{x}} \delta \psi^k) v \, d\Omega &= \int_{\Omega} \varepsilon \nabla_{\underline{x}} \delta \psi^k \nabla v \, d\Omega - \int_{\partial\Omega} \varepsilon \nabla_{\underline{x}} \delta \psi^k \cdot \mathbf{n} v \, d\Gamma \\ &= \int_{\Omega} \varepsilon \nabla_{\underline{x}} \delta \psi^k \nabla_{\underline{x}} v \, d\Omega - \int_{\Gamma_D} \varepsilon \nabla_{\underline{x}} \delta \psi^k \cdot \mathbf{n} v \, d\Gamma - \int_{\Gamma_N} \varepsilon \nabla_{\underline{x}} \delta \psi^k \cdot \mathbf{n} v \, d\Gamma \\ &= \int_{\Omega} \varepsilon \nabla_{\underline{x}} \delta \psi^k \nabla v \, d\Omega \end{aligned}$$

where we have used the fact that functions in  $H_{0,\Gamma_D}^1(\Omega)$  have null trace on  $\Gamma_D$  and the homogeneous Neumann boundary conditions. The weak formulation for the generic Newton iteration of the nonlinear Poisson equation reads: Find  $\delta \varphi^k \in V$  s.t.:

$$a^k(\delta \varphi^k, v) = L^k(v) \quad \forall v \in V \quad (13.21)$$

where  $a^k : V \times V \mapsto \mathbb{R}$  and  $L^k : V \mapsto \mathbb{R}$  are defined as

$$\begin{aligned} a^k(u, v) &= \int_{\Omega} \varepsilon \nabla u \nabla v \, d\Omega + \int_{\Omega} \sigma^k u v \, d\Omega, \\ L^k(v) &= \int_{\Omega} -f^k v \, d\Omega. \end{aligned}$$

#### 13.4.1.1. Well-posedness analysis

Let assume the following additional properties:

- $0 < \varepsilon_m \leq \varepsilon(x) \leq \varepsilon_M$  a.e. in  $\Omega$ ;
- $\sigma^k \in L^\infty(\Omega)$  and  $\sigma^k > 0$  a.e. in  $\Omega$   $\forall k > 0$ ;
- $f^k \in L^2(\Omega)$   $\forall k > 0$ .

Using the above properties, it is possible to proof:

- Continuity of  $a^k(\cdot, \cdot)$

$$|a^k(u, v)| \leq (\varepsilon_M + c_P^2 \|\sigma^k\|_{L^\infty(\Omega)}) \|u\|_V \|v\|_V \quad \forall u, v \in V$$

- Coercivity of  $a^k(\cdot, \cdot)$

$$a^k(u, u) \geq \varepsilon_m \|u\|_V^2 \quad \forall u \in V$$

- Continuity of  $L^k$

$$|L^k(v)| \leq c_P \|f^k\|_{L^2(\Omega)} \|v\|_V \quad \forall v \in V$$

where  $c_P$  is the Poincaré constant associated with the domain  $\Omega$ .

The Lax-Milgram hypothesis (see section A.3) are satisfied, hence the well-posedness of each Newton iteration in the Non Linear Poisson is proved.

### 13.4.2. Weak form of the Linearized Electron Continuity equation

In this section we address the weak formulation of the Linearized Electron Continuity Equation (13.15); the weak form for the Linearized Hole Continuity Equation (13.16) can be obtained in similar way. Equation (13.15) can be rewritten as a diffusion-advection-reaction (DAR) problem in conservative form:

$$\begin{cases} \nabla_{\underline{x}} \cdot (-D_n \nabla_{\underline{x}} n) + \nabla_{\underline{x}} \cdot (\mathbf{a}_n^i n) + \sigma_n^{i-1} n = f_n^{i-1} & \text{in } \Omega_{S_i} \\ n^i = n_D & \text{on } \Gamma_{D,S_i} \\ \nabla_{\underline{x}} n^i \cdot \mathbf{n} = 0 & \text{on } \Gamma_{N,S_i} \end{cases} \quad (13.22)$$

where the transport coefficient  $\mathbf{a}_n^i$  is defined as:

$$\mathbf{a}_n^i = \mu_n \nabla_{\underline{x}} \psi^i .$$

We multiply the first equation in (13.22) by a test function  $v \in V = H_{0,\Gamma_{D,S_i}}^1(\Omega_{S_i})$  (note that the domain and the Dirichlet boundary have been changed according to the considerations made in section 12.2) and integrate over the domain  $\Omega_{S_i}$ . The weak form of LCE reads as: Find  $n^i \in V = H_{0,\Gamma_{D,S_i}}^1(\Omega_{S_i})$  s.t.:

$$a_i(n^i, v) = L_i(v) \quad \forall v \in V \quad (13.23)$$

where  $a^i : V \times V \mapsto \mathbb{R}$  and  $L^i : V \mapsto \mathbb{R}$  are defined as

$$\begin{aligned} a^i(u, v) &= \int_{\Omega_{S_i}} D_n \nabla_{\underline{x}} u \nabla_{\underline{x}} v \, d\Omega - \int_{\Omega_{S_i}} \beta_n^i u \cdot \nabla_{\underline{x}} v \, d\Omega + \int_{\Omega_{S_i}} \sigma_n^i u v \, d\Omega , \\ L^i(v) &= \int_{\Omega_{S_i}} f_n^i v \, d\Omega . \end{aligned}$$

#### 13.4.2.1. Well-posedness analysis

To proof the well-posedness of (13.23) it is useful to introduce the Slotboom variable  $u_n$ :

$$u_n := n_i \exp\left(-\frac{\varphi_n}{V_{th}}\right) \quad (13.24)$$

which implies

$$n = \exp\left(\frac{\psi}{V_{th}}\right) u_n .$$

Notice that

$$\nabla_{\underline{x}} u_n = \exp\left(-\frac{\psi}{V_{th}}\right) \nabla n - \exp\left(-\frac{\psi}{V_{th}}\right) \frac{n}{V_{th}} \nabla_{\underline{x}} \psi$$

and using Einstein relation (9.45), we get

$$\nabla_{\underline{x}} \cdot \left( -D_n \exp\left(\frac{\psi}{V_{th}}\right) \nabla_{\underline{x}} u_n \right) = \nabla_{\underline{x}} \cdot \left( -D_n \nabla_{\underline{x}} n + \mu_n n \nabla_{\underline{x}} \psi \right).$$

Replacing the Slotboom variable into (13.22) we get:

$$\begin{cases} \nabla_{\underline{x}} \cdot \left( -D_n \exp\left(\frac{\psi}{V_{th}}\right) \nabla_{\underline{x}} u_n \right) + \sigma_n^{i-1} \exp\left(\frac{\psi}{V_{th}}\right) u_n = f_n^{i-1} & \text{in } \Omega_{S_i} \\ u_n = n_D \exp\left(-\frac{\psi}{V_{th}}\right) & \text{on } \Gamma_{D,S_i} \\ \nabla_{\underline{x}} u_n \cdot \mathbf{n} = 0 & \text{on } \Gamma_{N,S_i} \end{cases} \quad (13.25)$$

By multiplying the first equation in (13.25) by a test function  $v \in V = H_{0,\Gamma_{D,S_i}}^1(\Omega_{S_i})$  and integrate over the domain  $\Omega_{S_i}$  the weak formulation associated to (13.25) reads as Find  $u_n^i \in V = H_{0,\Gamma_{D,S_i}}^1(\Omega_{S_i})$  s.t.:

$$\tilde{a}_i(u_n^i, v) = \tilde{L}_i(v) \quad \forall v \in V \quad (13.26)$$

where  $\tilde{a}^i : V \times V \mapsto \mathbb{R}$  and  $\tilde{L}^i : V \mapsto \mathbb{R}$  are defined as

$$\begin{aligned} \tilde{a}^i(u, v) &= \int_{\Omega_{S_i}} D_n \exp\left(\frac{\psi}{V_{th}}\right) \nabla_{\underline{x}} u \nabla v \, d\Omega + \int_{\Omega_{S_i}} \sigma_n^i \exp\left(\frac{\psi}{V_{th}}\right) u v \, d\Omega, \\ \tilde{L}^i(v) &= \int_{\Omega_{S_i}} f_n^i v \, d\Omega = L^i(v). \end{aligned}$$

We will furthermore require that  $\forall i > 0$ :

- $0 < d_m \leq D_n \exp\left(\frac{\psi}{V_{th}}\right) \leq d_M$  a.e. in  $\Omega_{S_i}$ ;
- $\sigma_n^i \exp\left(\frac{\psi}{V_{th}}\right) \in L^\infty(\Omega_{S_i})$  and  $\sigma_n^i \geq 0$  a.e. in  $\Omega_{S_i}$ ;
- $f_n^i \in L^2(\Omega_{S_i})$ .

Using the same arguments in 13.4.1, it is possible to prove that the hypothesis of the Lax-Milgram theorem (see section A.3) are verified:

- Continuity of  $\tilde{a}^i(\cdot, \cdot)$

$$|\tilde{a}^i(u, v)| \leq \left( d_M + c_P^2 \left\| \sigma_n^i \exp\left(\frac{\psi}{V_{th}}\right) \right\|_{L^\infty(\Omega_{S_i})} \right) \|u\|_V \|v\|_V \quad \forall u, v \in V$$

- Coercivity of  $\tilde{a}^i(\cdot, \cdot)$

$$\tilde{a}^i(u, u) \geq d_m \|u\|_V^2 \quad \forall u \in V$$

- Continuity of  $\tilde{L}^i$

$$|\tilde{L}^i(v)| \leq c_P \|f\|_{L^2(\Omega)} \|v\|_V \quad \forall v \in V$$

Having proved that (13.26) is uniquely solvable, the existence and uniqueness of the solution  $n^i$  of (13.23) immediately follows from relation (13.24).

### 13.5. Finite Element Approximation of Non Linear Poisson equation

Let  $\{\mathcal{T}_h\}_{h>0}$  be a family of simplicial partitions of  $\Omega$  such that  $\cup_{K \in \mathcal{T}_h} K = \bar{\Omega}_h \sim \bar{\Omega}$  where, for simplicity, we assume that the approximating domain,  $\bar{\Omega}_h$ , coincides exactly with the original one,  $\Omega$  (i.e.,  $\Omega$  is a polyhedron). The positive parameter  $h$  represents the maximum simplex diameter:

$$h := \max_{K \in \mathcal{T}_h} h_K, \quad h_K = \max_{\mathbf{x}, \mathbf{y} \in K} |\mathbf{x} - \mathbf{y}|.$$

Furthermore we assume that the following *regularity condition* holds for each grid  $\mathcal{T}_h$ : there exists a positive constant  $\delta$  such that

$$\frac{h_K}{\rho_K} \leq \delta \quad \forall K \in \mathcal{T}_h \quad (13.27)$$

where  $\rho_K$  is the *sphericity* of  $K$  (namely, the diameter of the inscribed hypersphere). In order to numerically solve the generic Newton iteration of the Nonlinear Poisson problem (13.21), we discretize the Sobolev space  $V = H_{\Gamma_D}^1(\Omega)$  with linear finite elements, namely the space of continuous piecewise linear functions over  $\mathcal{T}_h$ :

$$V_h = X_h^1(\Omega) = \{v_h \in C^0(\Omega) : v_h|_K \in \mathbb{P}_1(K), \forall K \in \mathcal{T}_h\}. \quad (13.28)$$

We can state the finite element formulation of problem (13.21) as follows: Find  $\delta\psi_h^k \in V_h \cap H_{\Gamma_D}^1(\Omega)$  s.t.:

$$a^k(\delta\psi_h^k, v_h) = L^k(v_h) \quad \forall v_h \in V_h \quad (13.29)$$

Exploiting the usual Lagrangian basis  $\{\varphi_j\}_{j=1}^{N_h}$ , where  $N_h = \dim(X_h^1(\Omega))$ , we can write each element of  $X_h^1(\Omega)$  in the following way:

$$v_h(x) = \sum_{j=1}^{N_h} v_j \varphi_j(x). \quad (13.30)$$

Therefore, equation (13.29) becomes:

$$\sum_{j=1}^{N_h} \delta\psi_j^k a^k(\varphi_j, \varphi_i) = L^k(\varphi_i) \quad \forall i \in \{1, \dots, N_h\}.$$

This leads to the algebraic counterpart of problem (13.29), which reads as: Find  $\delta\psi^k \in \mathbb{R}^{N_h}$  s.t.:

$$\mathbf{A}^k \delta\psi^k = \mathbf{b}^k \quad (13.31)$$

where  $\mathbf{A}^k \in \mathbb{R}^{N_h \times N_h}$  and  $\mathbf{b}^k \in \mathbb{R}^{N_h}$  are defined as

$$\begin{aligned} [\mathbf{A}^k]_{i,j} &= a^k(\varphi_j, \varphi_i), \\ [\mathbf{b}^k]_i &= L^k(\varphi_i). \end{aligned}$$

Expanding the expression for the matrix coefficients

$$[\mathbf{A}^k]_{i,j} = [\mathbf{S}^k]_{i,j} + [\mathbf{N}^k]_{i,j} = \int_{\Omega} \varepsilon \nabla_{\underline{x}} \varphi_i \nabla_{\underline{x}} \varphi_j d\Omega + \int_{\Omega} \sigma^k \varphi_i \varphi_j d\Omega$$

we can recognize the two separate contributions of the *stiffness matrix*  $\mathbf{S}^k$  and the *mass matrix*  $\mathbf{N}^k$  to the global matrix.

“Notes” — 2019/5/17 — 17:39 — page 216 — #224

## CHAPTER 14

# Modeling of advanced non-volatile memory devices

In this chapter we consider the modeling of advance memory device obtained by extending the Drift-Diffusion and Poisson-Nernst-Planck models in more general context.

### 14.1. Introduction on semiconductor memory devices

The semiconductor memory devices are divided into two branches, both based on the complementary metal-oxide-semiconductor (CMOS) technology:

- the volatile memories, that lose the data content when the power supply is turned off. They provide fast writing and reading capabilities. Among them static random access memories (SRAM), or high density, dynamic random access memories (DRAM);
- the nonvolatile memories, that have the capability to keep the data content even without power supply. This kind of memory functions as *storage* for data and program codes and not as memory for running computer program codes, due to less efficient read and write performances with respect to the volatile ones.

#### 14.1.1. Basic concepts of nonvolatile memories

Let us assume that by a programming operation we are able to inject a charge distribution  $\rho_{net}(x)$  in the gate insulator of a MOS structure (Fig. 14.1). This charge distribution causes a shift in the gate voltage needed to maintain the flatband condition, which means a shift in the device threshold voltage given by [135]:

$$\Delta V_t = -\frac{1}{\epsilon_{ox}} \int_0^{t_{ox}} x \rho_{net}(x) dx = -\frac{1}{C_{ox}} \int_0^{t_{ox}} \frac{x}{t_{ox}} \rho_{net}(x) dx \quad (14.1)$$

where  $x = 0$  is the gate-oxide interface and  $x = t_{ox}$  is the oxide-silicon interface. The injected charge is trapped in the gate insulator with a retention time of years, without the need of a power supply. For electron injection in an nMOSFET,  $\Delta V_t$  is positive, i.e., the threshold voltage increases from  $V_{t,low}$  to  $V_{t,high}$  after charge injection (Fig. 14.2). Hence, once a proper charge amount and a corresponding  $\Delta V_t$  is defined, it is

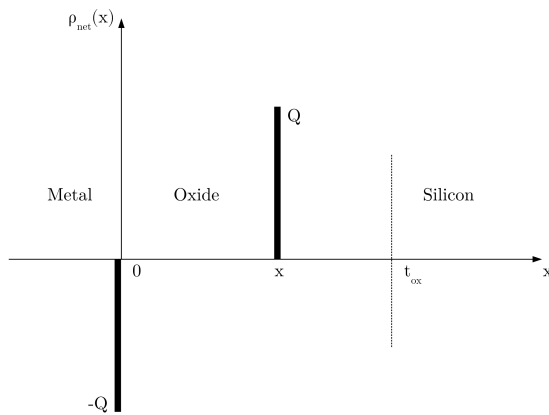


**Figure 14.1** Schematic illustrating a sheet charge of areal density  $Q$  within the oxide layer of an MOS capacitor biased at flat-band condition.

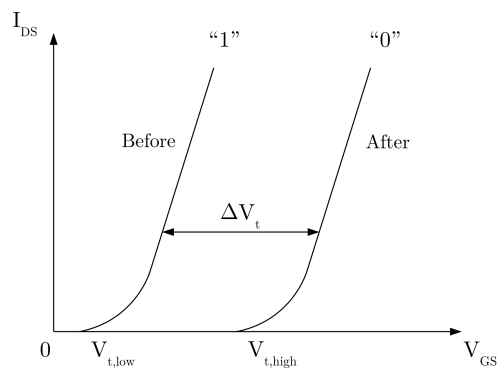


**Figure 14.2** Schematic illustrating the threshold voltage shift from  $V_{t,low}$  to  $V_{t,high}$  after charge injection.

possible to fix a reading voltage between  $V_{t,low}$  and  $V_{t,high}$  in such a way that the current of the non programmed cell is very high (typically in the range of tens of  $nA$ ), while the current of the programmed cell is much lower than  $nA$ . In this way, it is possible to define the logical state 1 as no stored electron charge and large reading current and the logical state 0 as stored electron charge and zero reading current (Fig. 14.3). The

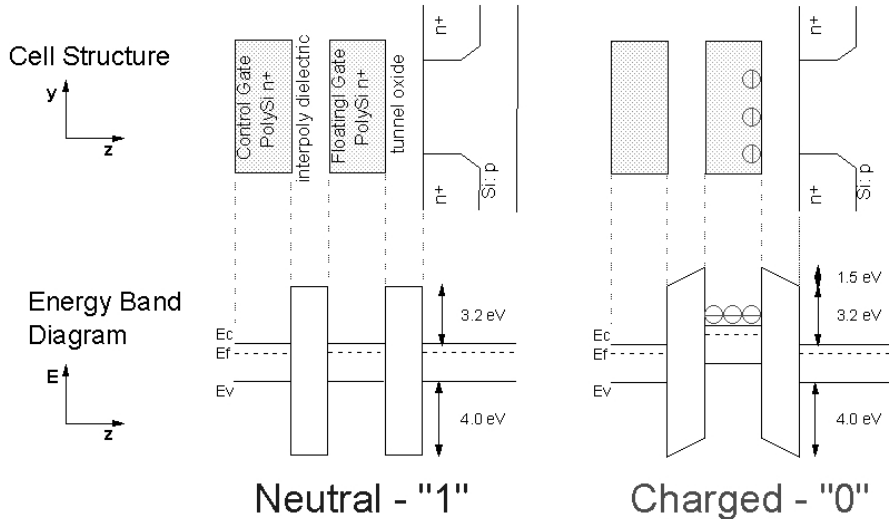


**Figure 14.3** Schematic energy band diagram referred to a *floating gate* MOSFET structure [133].

problem of writing a cell corresponds to the physical problem of forcing an electron above or across an energy barrier. The energy barrier for electron injection into  $SiO_2$  is  $3.1\text{ eV}$ , significantly lower than that for hole,  $4.6\text{ eV}$ . As a result, MOSFET-based non-volatile devices usually employ electrons instead of holes for memory programming. The main physical mechanisms used to write a memory cell are [133]:

- the channel hot electron (CHE) mechanism, where electrons gain enough energy to pass the silicon-oxide energy barrier, thanks to the electric field in the transistor channel between source and drain. In fact, the electron energy distribution presents a tail in the high energy side that can be modulated by the longitudinal electric field.
- The photoelectric effect, where electrons gain enough energy to surmount the barrier thanks to the interaction with a photon with energy larger than the barrier itself. For  $SiO_2$ , this corresponds to UV radiation. This mechanism was originally used in EPROMs to erase the entire device.
- The FowlerNordheim electron tunneling mechanism, that is a quantum-mechanical tunnel process. The tunneling of electrons from the silicon conduction band through a triangular energy into the oxide conduction band, is induced by a strong electric field (in the range of  $8 - 10\text{ MV/cm}$ ) across a thin oxide (typically  $10\text{ nm}$ ).

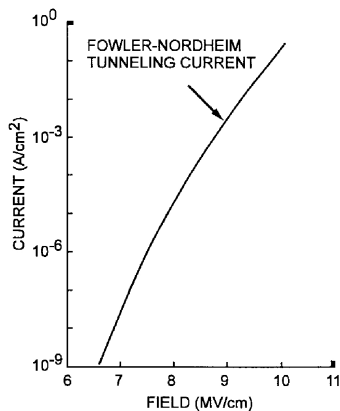


**Figure 14.4** Fowler-Nordheim tunneling current density as a function of electric field in oxide [134].

### 14.1.2. Emerging memories

The concept expressed in section 14.1.1 has been extended to a variety of different possible future (and present) new architecture and mememory concepts: [136]:

- the charge-trap memory replaces the polysilicon material with a dielectric trapping material (i.e. silicon nitride  $Si_3N_4$ )
- the resistive switching memory (RRAM or ReRAM) [137] [138], that is a kind of memory based on the ability of some dielectric material in a metal-insulator-metal (MIM) structure to switch between a high resistive state to a low resistive one, due to an electrically induced formation of a conductive path;
- the ferroelectric memory (FeRAM), that is a kind of memory that codes data by electrical alteration of the polarization direction;
- the phase-change memory (PCM) [139], that is based on the use of *chalcogenide* materials, displaying two stable phases with different electrical resistivity: a high-resistance amorphous phase and a low-resistance poly-crystalline phase;
- the spin-transfer-torque RAM (STT-RAM), that is an advanced type of magnetoresistive RAM (MRAM) in which the spin of the electrons is flipped using a spin-polarized current [140];
- carbon-based resistive memories [141], that consists of an electrode/carbon/electrode capacitor structure, whose resistance can be changed by appropriate current pulses. One of the proposed switching mechanism is the creation and destruction of conductive  $sp^2$ -bonds in an otherwise insulating carbon matrix consisting of  $sp^3$ -bonds.

## 14.2. Modeling of Charge Trap memory devices

This kind of memory devices is today the real alternative to the traditionally approach used to realize the non-volatile memory devices such as the NAND-FLASH.

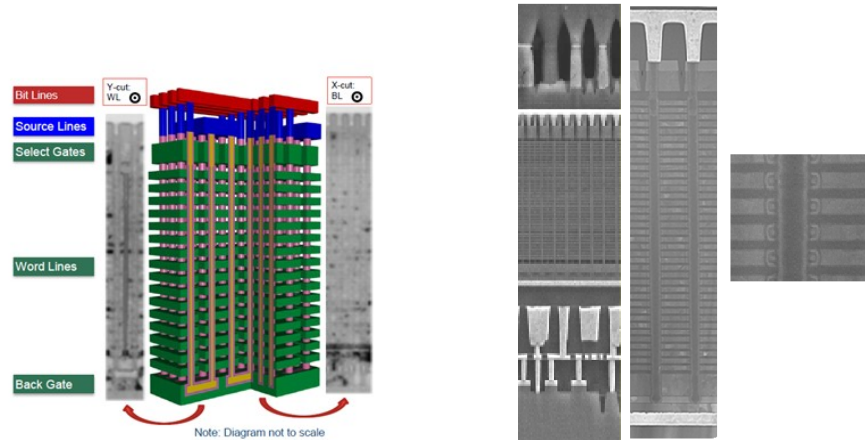


**Figure 14.5** 3DNAND devices in the market are based on continuous storage node (charge trap) and on the discrete storage node (PolySi). [166] [165]

The injected charge used to modify the threshold voltage has been trapped in the traps center of the trapping material. The physical mechanism that occurs at the traps level are describe below:

- (1a) Trap-mediated charge capture by an unoccupied trap
  - (2a) Trap-mediated charge capture by an occupied trap
  - (3a) Band-mediated charge capture by an unoccupied trap
  - (4a) Band-mediated charge capture by an occupied trap
  - (5a) Direct tunneling emission from trap into semiconductor/metal CB/VB
  - (6a) Poole-Frenkel (PF) thermionic emission from trap towards nitride CB/VB
- Several other physical mechanisms occur at the level of nitride CB and VB once charges have been injected by tunneling into them:
- (1b) Charge tunneling injection and emission at the nitride interfaces
  - (2b) Charge transport
  - (3b) Shockley-Read-Hall (SRH) R/G
  - (4b) Direct tunneling emission from band into semiconductor/metal CB/VB
  - (5b) Intraband R/G [(3a), (4a), (6a)].

**Remark 14.1.** Henceforth we assume that charge transport in the conduction and valence bands (2b) is the result of drift and diffusion forces. This choice allows us

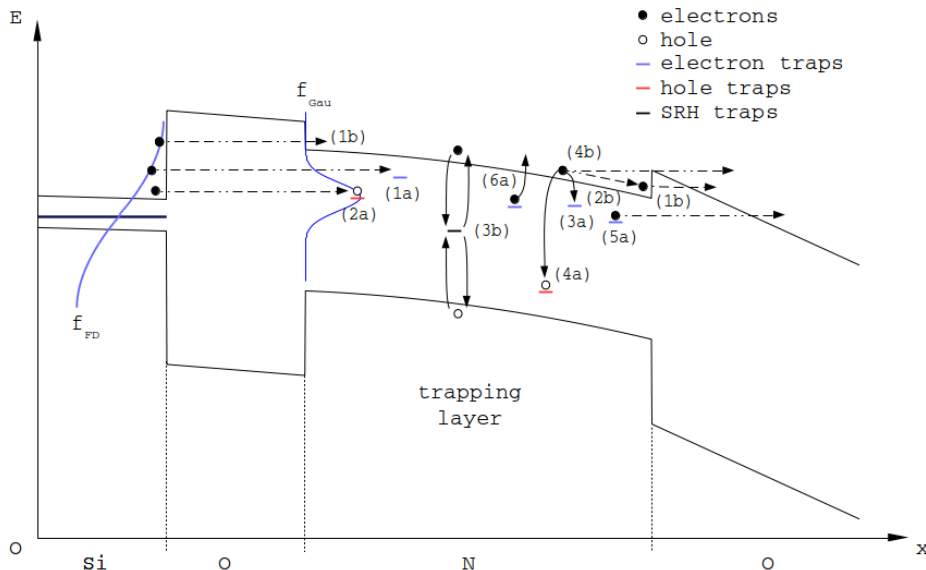


**Figure 14.6** Schematic representation of the band diagram of a SONOS structure. The gate contact on the rightmost side of the diagram is not reported. The mechanisms involved in the electron trapping and detrapping dynamics are illustrated.  $f_{FD}$  is the Fermi-Dirac energy distribution for electrons in the silicon substrate whereas  $f_{Gau}$  is the Gaussian energy distribution of electron traps.

*to employ the mathematical modeling and computational framework traditionally employed in the study of silicon-based devices.*

#### 14.2.1. Mathematical model

The trapped charge dynamics is described by the following equations:

$$\begin{aligned} \frac{\partial n_T}{\partial t} = & \frac{1}{q} (|J_n|\sigma_n + J_{B-T,n}\sigma_{T,n}) (N_{T,n} - n_T) \\ & - (e_n + \frac{1}{q}|J_p|\sigma_r + J_{B-T,p}\sigma_{rd})n_T \end{aligned} \quad (14.2a)$$

$$\begin{aligned} \frac{\partial p_T}{\partial t} = & \frac{1}{q} (|J_p|\sigma_p + J_{B-T,p}\sigma_{T,p}) (N_{T,p} - p_T) \\ & - (e_p + \frac{1}{q}|J_n|\sigma_r + J_{B-T,n}\sigma_{rd})p_T \end{aligned} \quad (14.2b)$$

$N_{T,n}$  and  $N_{T,p}$  being the electron and hole trap densities in the nitride,  $n_T$  and  $p_T$  the trapped electron and hole densities,  $\mathbf{J}_n$  and  $\mathbf{J}_p$  the Drift-Diffusion current densities as expressed in (14.5e) and (14.5f),  $J_{B-T,n}$  and  $J_{B-T,p}$  the tunneling current densities from substrate and gate to traps. Each aforementioned current density is characterized by a different cross section  $\sigma$  [ $cm^2$ ]. Finally,  $e_n$  and  $e_p$  are the emissivity functions for electrons and holes, to be specified later.

We point out that the terms proportional to the free trap densities ( $N_{T,n} - n_T$ ) and ( $N_{T,p} - p_T$ ) describe either band mediated trapping mechanisms ( $|\mathbf{J}_n| \sigma_n$  for electrons and  $|\mathbf{J}_p| \sigma_p$  for holes) or direct capture of an injected carrier in a free trap site ( $J_{B-T,n} \sigma_{T,n}$  for electrons and  $J_{B-T,p} \sigma_{T,p}$  for holes). On the other hand, the terms proportional to the trapped carrier densities  $n_T$  and  $p_T$  model all the mechanisms that cause a decrement of such densities: emission from trap ( $e_n$  and  $e_p$ ), trap mediated recombination of an electron with a captured hole ( $|\mathbf{J}_p| \sigma_r$  and  $J_{B-T,p} \sigma_{rd}$ ) and trap mediated recombination of a hole with a captured electron ( $|\mathbf{J}_n| \sigma_r$  and  $J_{B-T,n} \sigma_{rd}$ ).

Moreover, we remark that  $N_{T,n}$  and  $N_{T,p}$ ,  $e_n$  and  $e_p$  are constant functions of space and time but depend on the energy level of the trap centers that follow a gaussian distribution around the average value  $\bar{E}_T$  and with variance  $fwhh$ :

$$G(E) = \frac{1}{fwhh \sqrt{2\pi}} \exp\left(-\frac{1}{2}\left(\frac{E - \bar{E}_T}{fwhh}\right)^2\right). \quad (14.3)$$

The trapped carrier densities and the current densities are functions of space and time and depend also on the energy level. On the other hand  $\sigma_{T,n}$ ,  $\sigma_{T,p}$ ,  $\sigma_r$  are constant functions in space, time and energy. The emissivity functions must be carefully determined on the basis of the different possible ways a carrier can be emitted from a trap. In our framework we assume that the total emissivity coefficient  $e_{n,p}$  is the result of the combination of two processes: thermal ionization (Poole-Frenkel model [142]) and trap-to-band tunneling. The expression for the total emissivity coefficient, valid for both electrons and holes, is:

$$e_{n,p} = \nu_{th,n:p} P_{th,n:p} + \xi \nu_{T-B,n:p} P_{T-B,n:p} \quad (14.4a)$$

where  $P_{th,n:p}$  and  $P_{T-B,n:p}$  are the thermal and the tunneling emission probability from a trap, and  $\nu_{th,n:p}$ ,  $\nu_{T-B,n:p}$  are the corresponding attempt-to-escape frequencies. The thermal emission coefficient is calculated according to [143]:

$$P_{th,n:p} = \exp\left(-\frac{E_{T,n:p} - \beta |\mathbf{E}|^\gamma}{K_B \Theta}\right) \quad \beta = \sqrt{\frac{q^3}{\pi \epsilon_0 \epsilon_{hf}}} \quad (14.4b)$$

where  $E_{T,n:p}$  is the (positive) trap energy position with respect to the trapping layer conduction band for electrons or valence band for holes,  $K_B$  is the Boltzmann constant,  $\Theta$  the device temperature and  $\epsilon_{hf}$  high frequency relative dielectric constant of silicon

nitride. The term  $\beta|\mathbf{E}|^\gamma$  accounts for the barrier reduction in presence of an electric field.

It is reasonable to assume that, when the free carrier density approaches the density of states in the trapping layer, which we express with  $N_{c:v,T}$ , the emission from trap is practically inhibited. We account for this fact in the mathematical model by introducing the term

$$\xi = 1/\{1 + \exp[(u_{n:p} - N_{c:v,T})/\omega]\} \quad (14.4c)$$

as  $\xi \rightarrow 0$  when  $n - N_c \gg \omega$ ,  $\omega$  being a numerical parameter.

The tunneling probability from trap to semiconductor conduction band is calculated modifying the approach presented in [144] by considering the trap-to-band transmission coefficient in the WKB approximation:

$$P_{T-B,n:p} = TC(E_{T,n:p}). \quad (14.4d)$$

The adopted model for charge transport in the conduction and valence bands represents an extension of Arnett’s system [145] to a 2D framework, with the addition of the hole contribution. The two-carrier transport model takes the cue from the work presented in [146]. The basic equations for charge transport in nitride represent an adaptation of the *Drift-Diffusion* approach for an amorphous layer:

$$\nabla \cdot \mathbf{E} = \frac{q}{\epsilon}(p - n + p_T - n_T) \quad (14.5a)$$

$$\frac{\partial n}{\partial t} - \frac{1}{q} \nabla \cdot \mathbf{J}_n = \bar{G}_n - \bar{R}_n \quad (14.5b)$$

$$\frac{\partial p}{\partial t} + \frac{1}{q} \nabla \cdot \mathbf{J}_p = \bar{G}_p - \bar{R}_p \quad (14.5c)$$

$$\mathbf{E} = -\nabla\psi \quad (14.5d)$$

$$\mathbf{J}_n = qn\mu_n \mathbf{E} + qD_n \nabla n \quad (14.5e)$$

$$\mathbf{J}_p = qp\mu_p \mathbf{E} - qD_p \nabla p \quad (14.5f)$$

$$\bar{G}_n = e_{th,n} n_T + \bar{G}_{SRH} \quad (14.5g)$$

$$\bar{R}_n = \frac{1}{q} |\mathbf{J}_n| (\sigma_n(N_{T,n} - n_T) + \sigma_r p_T) + \nu_{B-B,n} TC_{B-B,n} n + \bar{R}_{SRH} \quad (14.5h)$$

$$\bar{G}_p = e_{th,p} p_T + \bar{G}_{SRH} \quad (14.5i)$$

$$\bar{R}_p = \frac{1}{q} |\mathbf{J}_p| (\sigma_p(N_{T,p} - p_T) + \sigma_r n_T) + \nu_{B-B,p} TC_{B-B,p} p + \bar{R}_{SRH}. \quad (14.5j)$$

In the *Poisson* equation (14.13d),  $\epsilon$  is the material dielectric constant,  $n$  and  $p$  are the free electron and hole volume densities in the conduction and valence band of the nitride, respectively, whereas  $n_T$  and  $p_T$  the trapped electron and hole volume densi-

ties. In the continuity equations (14.5b), (14.5c),  $\mathbf{J}_n$  and  $\mathbf{J}_p$  are the current densities for electrons and holes, where  $\mu_n$  and  $\mu_p$  are the electron and hole mobilities and  $D_n$  and  $D_p$  the electron and hole diffusion coefficients, obtained by Einstein relation. The functions  $\bar{R}_n$  and  $\bar{R}_p$  are the recombination rates for electrons and holes due to trapping and detrapping processes whereas  $\bar{G}_n$  and  $\bar{G}_p$  are the generation rates for electrons and holes due to trapping and detrapping processes. Finally, the functions  $\bar{R}_{SRH}$  and  $\bar{G}_{SRH}$  are the recombination and generation rates associated with the two-particle Shockley-Read-Hall process schematically indicated by (3b) in Figure 14.6. System (14.5) is closed by the proper initial and boundary conditions. The initial conditions are:

$$n(\mathbf{x}, 0) = n^0(\mathbf{x}), \quad p(\mathbf{x}, 0) = p^0(\mathbf{x}) \quad \forall \mathbf{x} \in \Omega \quad (14.6a)$$

$$n_T(\mathbf{x}, 0) = n_T^0(\mathbf{x}), \quad p_T(\mathbf{x}, 0) = p_T^0(\mathbf{x}) \quad \forall \mathbf{x} \in \Omega, \quad (14.6b)$$

where  $n^0$ ,  $p^0$ ,  $n_T^0$  and  $p_T^0$  are nonnegative given functions of space.

For equation (14.13d) we enforce a nonhomogeneous Dirichlet boundary condition:

$$\psi(\mathbf{x}, t) = \psi^0(\mathbf{x}, t) \quad \forall \mathbf{x} \in \partial\Omega \quad (14.7a)$$

where we indicate with  $\partial\Omega$  the trapping layer boundary. Boundary conditions for (14.5b), (14.5c) represent a delicate modeling issue since their characterization depends on the memory cell operation, i.e. on the bias conditions applied to the cell. If carriers are physically injected into an interface  $\Gamma_{in}$  on which a positive outward unit normal  $\mathbf{n}$  is defined, we apply a nonhomogeneous Neumann boundary condition (Fig. 14.7):

$$\mathbf{J}(\mathbf{x}, t) \cdot \mathbf{n}(\mathbf{x}) = J_{WKB}(\mathbf{x}, t) \quad \forall \mathbf{x} \in \Gamma_{in} \quad (14.7b)$$

where the flux density  $\mathbf{J}$  is such that  $\mathbf{J}_n = -q\mathbf{J}$  and  $\mathbf{J}_p = q\mathbf{J}$  whereas  $J_{WKB}$  is the tunneling current density. This is the case of electrons injected through the oxide by means of tunneling, from the substrate into the trapping layer during program, the case of holes injected from the substrate into the trapping layer during erase, and the case of electrons back injected from the gate into the trapping layer in erase. It may be possible to have injection of holes and electrons into the trapping layer even in the retention of the programmed and the erased state, respectively, especially for high threshold voltage values.

Instead, if an outward flux of carriers from the trapping layer boundary  $\Gamma_{out}$  physically exists, we use a Robin boundary condition (Fig. 14.7):

$$\mathbf{J}(\mathbf{x}, t) \cdot \mathbf{n}(\mathbf{x}) = \alpha(\mathbf{x}, t)u(\mathbf{x}, t) \quad \forall \mathbf{x} \in \Gamma_{out} \quad (14.7c)$$

where  $\mathbf{J}$  is the previously mentioned flux density,  $u(\mathbf{x}, t) = n$  for electrons and  $u(\mathbf{x}, t) = p$  for holes, and the coefficient  $\alpha(\mathbf{x}, t)$  physically represents an escape velocity [cm/s].

This mathematical treatment allow the description of the outward electron flux from the trapping layer conduction band toward the gate in program, the outward hole flux from the trapping layer valence band toward the gate in erase, and the outward flux of electrons and holes toward both the electrodes in the retention of the programmed and the erased state respectively.

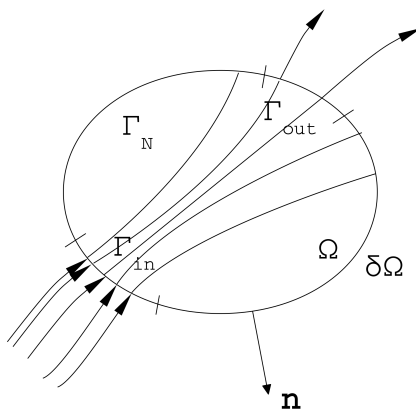


**Figure 14.7** Domain and boundary conditions. The inward and outward fluxes are represented by means of streamlines.  $\Omega$  is the trapping layer,  $\partial\Omega$  its boundary,  $\Gamma_{in}$  and  $\Gamma_{out}$  the input and output interfaces, respectively.

Mobility in an amorphous layer is typically related to the continuous trapping and detrapping dynamics. Since we have already included these two mechanisms in our model by means of the net recombination terms  $\bar{R}_{n,p}-\bar{G}_{n,p}$ , it is more convenient to adopt a constant mobility model, with values included in a range  $10^{-4} \leq \mu_{n,p} \leq 10^{-2}$ . In making this approximation we are neglecting any dependence on the electric field and on temperature.

Example of the simulation obtained with the mathematical model are reported in Fig. 14.8.

### 14.3. Modeling of Mass Transport in PCM device

Electrical and chemical properties of amorphous semiconductors were firstly investigated during the late 1950s, leading to the discovery of the existence of reversible switching effects [147]. From 1990s, research was focused on an amorphous alloy containing Germanium (Ge), Antimony (Sb) and Tellurium (Te), giving the basis for the phase change technology used nowadays. The first area of development is rewritable optical data storage, where three generations of products - compact disks

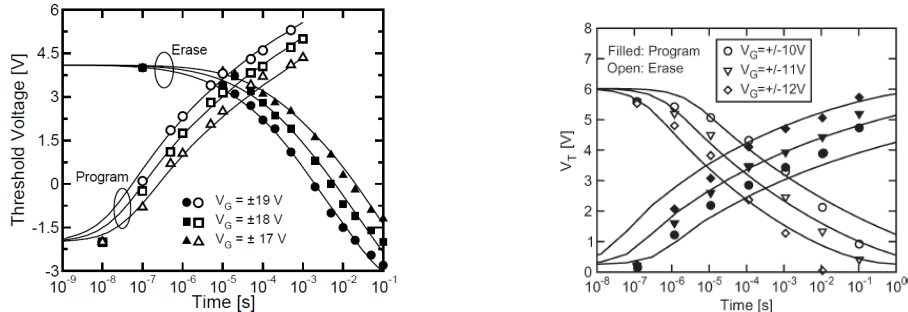


**Figure 14.8** Simulation results compared with experimental data obtained with the mathematical modeling of the Charge Trap memory. [168] [167]

(CD), digital versatile disks (DVD) and Blue-ray disks (BD) - have already been developed, and have totally overperformed the previous magneto-optical supports. In this technology the information storage relies on reversible phase transition obtained with a heating laser pulse, and on the different reflectance between the two phases, that can be read with a low power optical probing pulse.

Since the transition is also characterized by a huge electrical resistive change, the same material has been proposed for semiconductor memories, associating the stored information with the high and low resistance values. In this case, however, the phase change must be electrically induced, usually by Joule heating; as in optical devices, no energy is required to store the information because both states are stable in normal conditions, so the result is a non-volatile memory. It is only in the past 10-15 years that advances in material and device technology have made possible for phase change memories to be in competition with more established technologies such as Flash and DRAM, and the growth of reports on PCM shows how much interest they are attracting worldwide (fig. 14.9). The PCM cell is conceptually a tunable resistor, and its conventional structure is shown in figure 14.10a: one electrode is placed over the GST layer, and the other one is connected to it through a metallic pillar, the heater.

Set and reset state of PCM refer to low and high resistance states, respectively. As fabricated, the phase change material is in the crystalline, low resistance state, due to the processing temperature that is sufficient to allow crystallization; in this case, the resistance of the cell is mainly determined by the heater. The transition to the reset state is thermally induced: when voltage is applied between the top and the bottom electrode, the heater forces high current density and therefore, through Joule heating, high temperature is reached in the active area of the device. If the electrical pulse is large and short enough, the programming region is firstly melted and then quenched rapidly, preventing GST to crystallize, and leaving it in the amorphous state. This amorphous

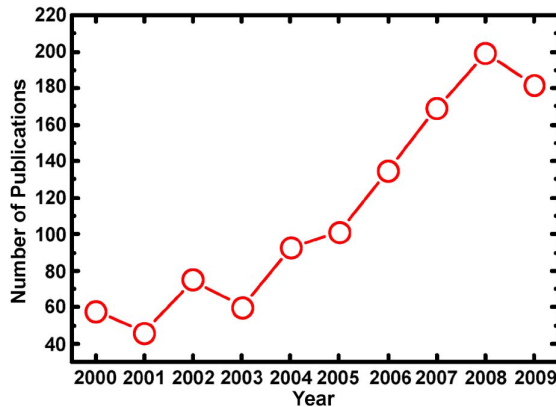


**Figure 14.9** Number of publications on PCM. Data obtained by searching the IEEE Xplore with PCM related keywords.

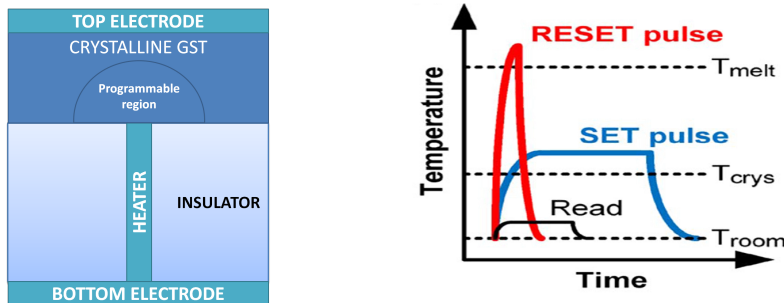


**Figure 14.10** (a) Cross section schematic of the conventional PCM cell. (b) PCM cell programming and reading is implemented with electrical pulses of different length and intensity, which bring the active layer to appropriate temperatures.

region is in series with the heater and the remaining crystalline region of the PCM material, but it gives the principal contribution to global cell resistance because of its high value. At this point, to go back to the set state, a medium amplitude pulse is applied for a time period long enough to let the programming region crystallize. Finally, a short low pulse is used to read the resistance of the cell, so that the programming state is not influenced (fig. 14.10b). Fig. 14.11 shows the experimental electrical current-voltage characteristics of a PCM device with GST in both amorphous and crystalline states. The large resistance contrast can be noticed in the different slope of the curves, at least before a peculiar voltage value called *threshold voltage* ( $V_{th}$ ) is reached.

Indeed, at this voltage a particular phenomenon occurs, called *threshold switching*, visible in the characteristics as the part of the curve with a S-shape backdrop. If a voltage higher than  $V_{th}$  is applied for a longer time than the crystallization time, the

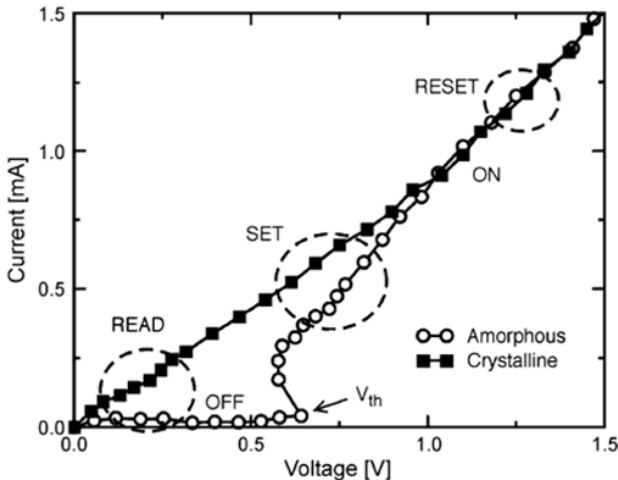


**Figure 14.11** IV characteristics of a PCM cell crystalline and amorphous state [148]. Note how the amorphous state remains highly resistive below  $V_{th}$ , then switches to low resistance.

memory changes its state. Threshold switching is a fundamental mechanism for the set process, because it allows the flow of high current through the amorphous region, without needing very high electrical fields. When the PCM is in the reset state, the resistance of the cell is too high to allow the current flow needed for Joule heating and crystallization; threshold switching lowers the resistance of the phase change material and enables set programming. Despite the fundamental role of the threshold switching effect, the physical nature of this conductance variation is yet to be fully explored. It has been firstly ascribed to a thermal breakdown in the amorphous film [149]: when the temperature sufficiently rises, a huge thermal generation of carriers takes place, and the voltage drop can thus decrease while maintaining a high current density. More recently, it was proposed that this effect is not related to a thermal breakdown, but is a pure electronic phenomenon, related to the balance between a strong Shockley-Read-Hall recombination through trap levels and a generation mechanism driven by electric field and carrier densities [150].

Clearly, there are also some disadvantages in the operation of a PCM cell

- the power consumption due to the reset pulse, which needs to be really intense to let GST reach melting temperature. Mitigation is possible by working on the geometrical structure of the cell to reach better performance, as well as choosing surrounding materials with adequate thermal and electrical conductivity.
- the programming time is another limitation, since the set pulse must be quite long to assure full crystallization of the previously amorphous region.

PCM operation strongly depends on the physical properties of the active material,

that must fulfill some specific requirements (table 14.1). Almost any material - including metals, semiconductors, insulators - can exist in amorphous or crystalline state, but this is not enough to make it a good choice.

<i>Required properties of phase change material</i>	<i>Specification</i>
High-speed phase transition	Induced by nanosecond laser or voltage pulse
Long thermal stability	Several decades at room temperature
Large optical change	For rewritable optical storage
Large resistance change	For non-volatile electronic storage
Large number of reversible transitions	More than $10^5$ cycles

Table 14.1 Required properties of phase change materials.

Phase change materials are the heart of PCM technology, and some years of research were necessary to find the appropriate alloys, despite the fact that the basic ideas were already available in 1960s. Nowadays, the preferred solutions are semiconducting or semimetallic alloys containing elements of group VI of the periodic table (*chalcogenides*), excluding oxygen. Their performance can be tuned by changing the alloy stoichiometry, by adopting proper doping, or moving to non-chalcogenide phase change compositions, but  $\text{Ge}_2\text{Sb}_2\text{Te}_5$  (GST) is still considered a reference material for phase change storage. In the following sections, we are going to illustrate its main structural, electrical and thermal features.

Material structure is the core of all GST features, since the phase determines all other aspects such as conductivity and reflectivity. As said before, at low temperature GST can exist in two different states, crystalline or amorphous, and over melting temperature it becomes liquid (fig. 14.12). Melting breaks the previous material structure, increasing the disorder in the atomic layout; instead, the way the material is cooled down from liquid phase decides if it will be amorphous or crystalline in the end.

The high conductive GST state is a polycrystalline state with face centered cubic lattice (f.c.c.), and grains that closely resemble the rock-salt structure typical of NaCl. As can be seen from figure 14.13, sixfold coordinated Tellurium atoms (light blue) occupy one lattice site, while the second lattice site is filled randomly by a Germanium or Antimony atom (dark blue).

Due to the stoichiometry of  $\text{Ge}_2\text{Sb}_2\text{Te}_5$ , one position of the basic sublattice remains unoccupied, leading to a 20% of vacancies. Vacancies are essential for the energy stability of the structure [151], and are responsible for *p*-type conduction, because the Te atoms surrounding the vacancies attract and remove delocalized electrons from the valence band [154]. Since the crystalline phase shows a long-range structural order,

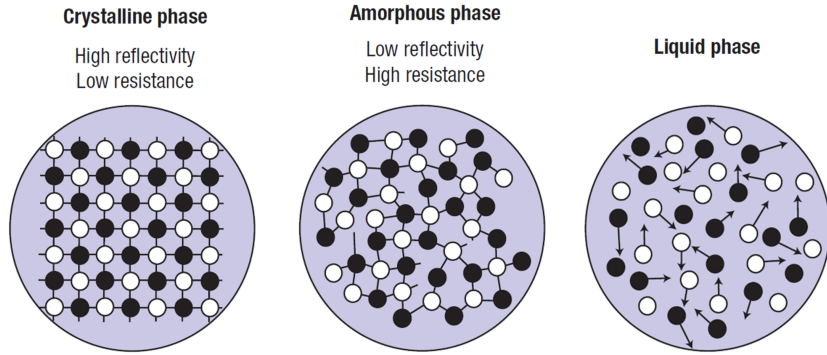


Figure 14.12 Schematic of atomic structure in GST different phases.

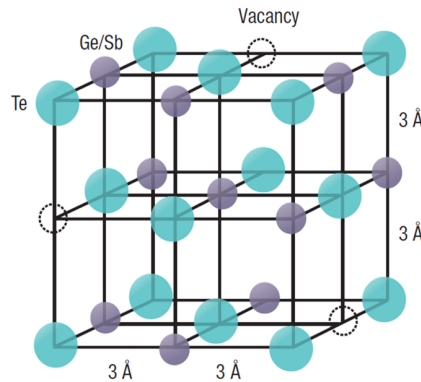


Figure 14.13 Schematic image of the crystal structure of the f.c.c. crystalline phase of  $\text{Ge}_2\text{Sb}_2\text{Te}_5$ .

the treatment of the electronic states can be done according to the Bloch Theorem.

Crystalline state is characterized by an energy gap of 0.5 eV, and in the band diagram (fig. 14.14a), near to the valence band, vacancies are represented as acceptor-like traps.

During the phase transition, this long-range structural order disappears, although a short-range order still exists, given from a covalently bonded structure that is locally similar to the crystalline one. Due to the rapidity of phase transitions and the great number of switching operations demonstrated on prototype devices [155], it has been assumed that there is not a sensible variation of atomic position during the phase change, but just the rearrangement of some bonds. The idea is that rigid blocks are built in a crystal lattice, and that during melting the interblocks bonds break, while inside the blocks atoms still remain connected, even more weakly. The result is a

partially disordered structure with increased volume.

Structural defects are numerous in amorphous state, and give rise to elevate concentrations of localized states in the energy gap, and cause the Fermi level to be set in the middle. Usually, amorphous GST is modeled as a *classic semiconductor*, with *localized states represented as donor or acceptor-like traps* (fig. 14.14b).

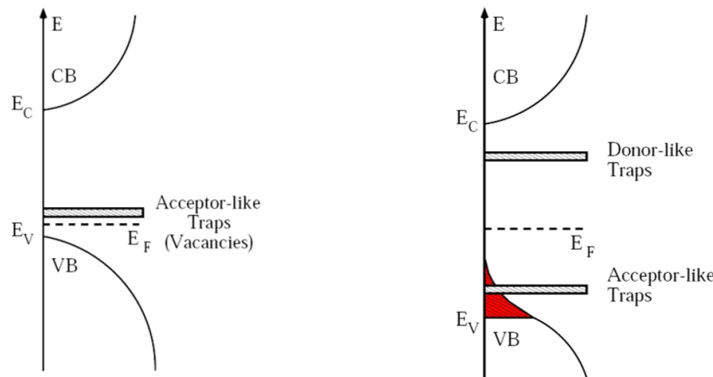


Figure 14.14 (a) Band diagram for crystalline phase. (b) Band diagram for amorphous phase.

In the following table are indicated the values commonly used in simulations to represent the band diagram for GST.

	<i>Crystalline GST</i>	<i>Amorphous GST</i>
$E_{gap}[eV]$	0.5	0.7
$N_C[cm^{-3}]$	$2.5 \cdot 10^{19}$	$2.5 \cdot 10^{19}$
$N_V[cm^{-3}]$	$2.5 \cdot 10^{19}$	$10^{20}$
Vacancies [ $cm^{-3}$ ]	$2.5 \cdot 10^{19}$	-
Localized states [ $cm^{-3}eV^{-1}$ ]	-	$10^{21}$
Donor traps [ $cm^{-3}$ ]	-	$10^{17}-10^{20}$
Acceptor traps [ $cm^{-3}$ ]	-	$10^{17}-10^{20}$

Table 14.2 Typical parameter values for crystalline and amorphous GST band diagram.

Phase change materials have a large electrical contrast, with a difference that can reach five orders of magnitude for some materials (fig. 14.15).

Electrical conduction in the crystalline phase can be described with *the drift-diffusion*

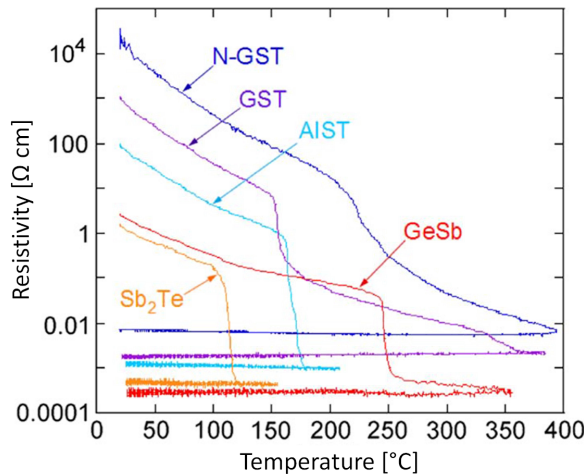


**Figure 14.15** Resistivity as a function of temperature for different phase change materials. Each 50nm-film, initially amorphous, was heated at 1 K/s until crystallization temperature is reached, then cooled with the same rate. High resistivity is shown for the amorphous material, and it decreases during the cycle; resistivity remains low during the cooling, as the films remain crystalline.

behaviour of a doped semiconductor . Figure 14.16 shows the IV characteristic of a PCM cell with GST in crystalline phase.

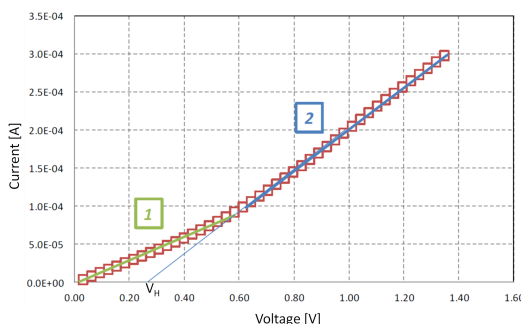


Figure 14.16 IV characteristic of a PCM cell in the set state (crystalline).

The presence of two different trends can be noticed, depending on the voltage value. For low applied voltages we have the low-fields ohmic behaviour, a linear trend with a differential resistance  $dV/dI$  given by the series of the crystalline active layer and the rest of the device structure, such as heater and contacts. Crystalline GST has a conductivity of nearly 30 S/cm and its expression has the typical temperature

dependence of semiconductors:

$$\sigma = \sigma_0 \exp \frac{E_A^c}{kT}$$

where  $E_A^c$  is the conduction activation energy for the crystalline phase ( $\approx 0.02 \text{ eV}$ ).

This trend is maintained until GST starts to melt, because the material in liquid phase has lower resistivity, resulting in a superlinear form of the characteristic. At high fields, a linear trend is restored, because most of GST is melt and the heater resistance dominates the series; however, this means that the differential resistance is lower than at low fields, so the IV curve has a greater slope. The intersection point between the horizontal axis and the linear interpolation of high-fields trend gives the potential drop on melt GST  $V_H$ .

Different behaviours can be noticed in electrical conduction of amorphous GST too, as evidenced by the IV characteristic for this phase (fig. 14.17).

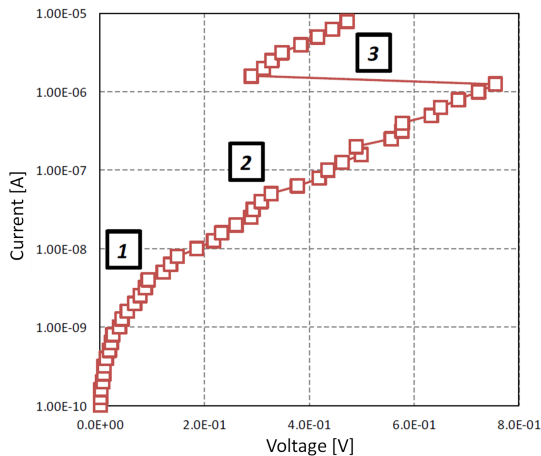
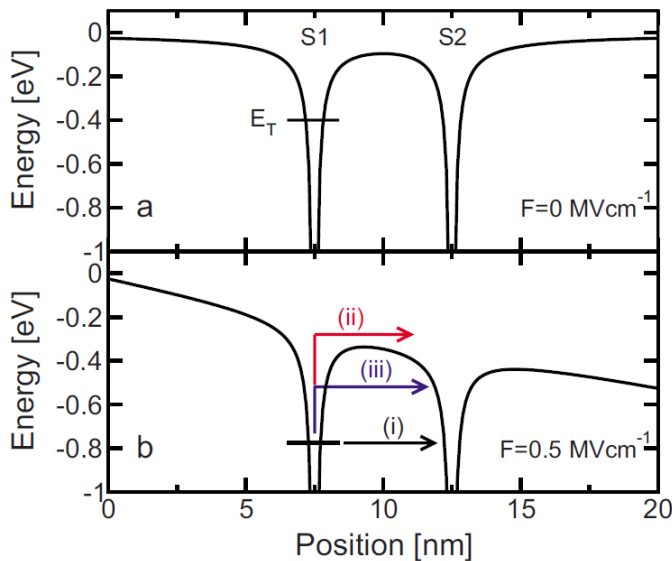


Figure 14.17 IV characteristic of a PCM cell in the reset state (amorphous).

At low fields, as for crystalline state, an ohmic trend is shown, with high resistance due to the amorphous structure. For higher applied voltages, but still lower than the threshold switching value  $V_{th}$  (subthreshold zone), the current dependence becomes exponential, and the differential resistance decreases, until it reaches zero at  $V_{th}$ . This is the value at which the threshold switching phenomenon occurs, which consists in an increase of conductivity and allows a more intense current for lower applied voltages. This causes a snap-back in the IV characteristic with negative differential resistance. Now, the higher current brings amorphous GST to higher temperatures, and the crystallization/melting process can take place. However, threshold switching is a reversible

process, and if the voltage is removed quickly the cell returns to the amorphous state without memory switching.

Several models regarding threshold switching have been proposed so far [147, 149, 150], however, a thermally-assisted hopping conduction mechanism is able to explain this phenomenon in agreement with the electron transport model for amorphous chalcogenides, but also involving only high-field effects, thus allowing to extend this interpretation to other materials.



**Figure 14.18** Profile of the electron potential energy along the minimum path between localized states S1 and S2, with electric field  $F = 0$  (top) and  $0.5 \text{ MV}/\text{cm}$  (bottom). Schematic of the electron transport processes via localized states: (i) tunneling through the energy barrier at  $E_T$ , (ii) thermal (PF) emission over the energy barrier and (iii) thermally assisted tunneling through the energy barrier at an energy  $E > E_T$ .

Fig. 14.18 schematically shows the band structure of the amorphous phase, the potential energy wells resulting from the donor-like trap states. Carriers can pass from a trap to an adjacent one by pure tunneling, Poole-Frenkel thermal emission, thermally-assisted tunneling, and qualitative evaluations indicate that these last two are the more important contributions. They are responsible for thermally-assisted hopping conduction, that is exponentially enhanced by the electric field: as applied voltage increases, the lowering of one side of the barriers gives rise to a preferred direction for hopping, leading to a growth of the current. When the threshold voltage is reached, the electron distribution evolves to a non-equilibrium condition, with the occupation of states closer to the band edge. Carriers in these states have higher mobility, and

cause exponential rise of the conductivity [158].

Thermal stress is responsible for melting and solidification of GST. Its melting temperature  $T_m$  is about 890 K. If molten GST is subject to fast cooling, it freezes without crystallizing, and becomes an undercooled liquid that transforms into a glass at temperatures lower than the glass transition temperature  $T_g$  ( $\approx 670$  K). The glass transition temperature is defined as the temperature corresponding to the appearance of discontinuities of some important material properties such as specific volume, thermal expansion coefficient, specific heat, viscosity. If an amorphous sample is kept at a temperature between  $T_g$  and  $T_m$  for a certain amount of time, it will crystallize, starting with the nucleation of small crystallites that subsequently grow; this is usually a long process, and crystallization time is usually one of the most limiting time constants in PCM operations.

With regard to other more specific thermal features such as thermal conductivity and thermal capacity, their values are reported in table 14.3; they are similar for both phases and quite small, thus indicative of a quick reaction to thermal variations during programming operations.

	<i>Crystalline GST</i>	<i>Amorphous GST</i>
Thermal conductivity [ $Wcm^{-1}K^{-1}$ ]	0.005	0.002
Thermal capacity [ $Jcm^{-3}K^{-1}$ ]	1.25	1.25

Table 14.3 Numerical values of GST thermal parameters.

#### 14.3.1. Mathematical model for the atomic migration

The general model of atomic migration describes the variation of the concentration of each chemical species as the result of different physical mechanisms. Neglecting any kind of generation/recombination mechanisms a general expression for the flux of atoms of the species  $\alpha$  with  $\alpha = 1, \dots, M_{ion}$   $\mathbf{f}_{n_\alpha}$  in the presence of an electric field  $\mathbf{E}$ , a gradient of concentration  $n_\alpha$ , the gradient of the temperature  $\Theta$  and of a contribution of a stress-migration, as investigated in [152] as a sum of the corresponding terms

$$\mathbf{f}_{n_\alpha} = K_{1,\alpha} \nabla n_\alpha + K_{2,\alpha} \mathbf{E} + K_{3,\alpha} \nabla \Theta + K_{4,\alpha} \nabla \sigma \quad (14.8)$$

where the parameters  $K_{i,\alpha}$ ,  $i = 1, 2, 3, 4$ , represent phenomenological coefficients of each contribution for the species  $\alpha$ ,  $\mathbf{E}$  the electric field,  $\Theta$  the temperature and  $\sigma$  is the mechanical stress. The first contribution is due to the gradient of the concentration: a diffusing substance flows from regions at high concentration to a region at

low concentration; the flux is proportional to the concentration gradient. Fick’s law of diffusion describes this aspect as

$$\mathbf{f}_{n_\alpha}^{diff} = -D_\alpha \nabla n_\alpha$$

where  $D_\alpha$  is the diffusion coefficient [ $m^2/s$ ] that is supposed to have an Arrhenius form

$$D_\alpha = D_{0,\alpha} \exp\left(-\frac{E_{A,\alpha}}{K_B \Theta}\right) \quad (14.9)$$

where  $D_{0,\alpha}$  is the pre-exponential diffusion coefficient [ $m^2/s$ ],  $E_{A,\alpha}$  the activation energy that characterizes the diffusion mechanism [eV],  $K_B$  the Boltzmann constant [eV/K] and  $\Theta$  the temperature [K]. Since the diffusion of constituent atoms depends on the  $\text{Ge}_2\text{Sb}_2\text{Te}_5$  phase, different values of  $D_{0,\alpha}$  and  $E_{A,\alpha}$  are assigned, in the following way:

$$(D_{0,\alpha}, E_{A,\alpha})(\mathbf{x}, t) = \begin{cases} (D_{0,\alpha}, E_{A,\alpha})^{lt} & \Theta(\mathbf{x}, t) < \Theta_g \\ (D_{0,\alpha}, E_{A,\alpha})^{cry} & \Theta_g \leq \Theta(\mathbf{x}, t) < \Theta_m \text{ and phase is crystalline} \\ (D_{0,\alpha}, E_{A,\alpha})^{amo} & \Theta_g \leq \Theta(\mathbf{x}, t) < \Theta_m \text{ and phase is amorphous} \\ (D_{0,\alpha}, E_{A,\alpha})^{mol} & \Theta(\mathbf{x}, t) \geq \Theta_m \text{ and molten phase} \end{cases}$$

where  $\Theta_g$  is the glass temperature and  $\Theta_m$  the melting temperature. The second contribution is due to the electromigration driving force, which is derived from the presence of the applied electrical field  $\mathbf{E}$  [V/m]

$$\mathbf{F} = z_\alpha q \mathbf{E}$$

where  $q$  is the elementary charge [C] and  $z_\alpha$  a dimensionless quantity called effective charge number, which is intended to describe both the partial ionization of the species and the effect of the wind force on atoms. The flow of charged particles under the effect of an electric field is what occurs in electric conduction; hence the force is given by

$$\mathbf{f}_{n_\alpha} = \mu_\alpha n_\alpha \mathbf{E}$$

where  $\mu_\alpha$  is the atomic mobility [ $m^2 V^{-1} s^{-1}$ ]. Considering that Einstein relation holds, the model for atomic transport due to electromigration is finally

$$\mathbf{f}_{n_\alpha}^{em} = -\frac{D_\alpha z_\alpha q}{K_B \Theta} n_\alpha \nabla \varphi.$$

The third contribution is due to thermomigration, which is a phenomenon observed in mixtures of mobile particles, that exhibit a response to the presence of a temperature gradient. It is generally assumed that the thermodiffusive drift velocity depends linearly on the  $\nabla \Theta / \Theta$  ratio [153]. Therefore the expression of the associated atomic

flux can be written as

$$\mathbf{f}_{n\alpha}^{tm} = -D_\alpha \alpha^{tm} n_\alpha \nabla \ln\left(\frac{\Theta}{\Theta_0}\right)$$

where  $\Theta_0 = 300K$  is a reference temperature. The dimensionless term  $\alpha^{tm}$  is defined for each species  $\alpha$  and it is called thermomigration coefficient; it regulates the intensity and the direction of the atomic flow, with respect to the temperature gradient.

Another contribution is due to phase separation, which is the tendency of atoms to segregate at the hot/cold side of the liquid/solid interface. The simplest formulation for the phase segregation force involves the gradient of a generic field  $\Phi$  describing the local phase of the material:  $\mathbf{F}_{segr} = \beta \nabla \Phi$ . In [156], the generic field is related to the temperature, hence  $\Phi = \ln(\Theta/\Theta_0)$  is taken.  $\beta$  is a temperature dependent coefficient that activates this contribution only in a narrow range of temperature  $\Theta_1 \leq \Theta_m \leq \Theta_2$  around melting temperature  $\Theta_m$ . We can write the atomic flow contribution due to phase separation as

$$\mathbf{J}^{sep} = -D_\alpha \beta(\Theta) n_\alpha \nabla \ln\left(\frac{\Theta}{\Theta_0}\right)$$

and

$$\beta(\Theta) = \begin{cases} 0 & \Theta < \Theta_1 \\ \bar{\beta}(\Theta) & \Theta_1 \leq \Theta \leq \Theta_2 \\ 0 & \Theta > \Theta_2 \end{cases} \quad (14.10)$$

Using the above approach it is possible to incorporate the phase transition into thermo-migration term.

This last force in (14.8) can be intended as a restoring force or as a pressure due to the variation of the concentrations of the chemical species: its effect is, in some way, to contrast the tendency of atoms to move, undergoing high electrical and thermal stress; to calculate the contribution due to this effect we assume that the driving force is of the form of

$$\mathbf{F} = -\omega \nabla \sigma$$

where  $\omega$  is the atomic volume of the material<sup>1</sup> and  $\sigma$  the mechanical stress [Pa], given by

$$\sigma = B \frac{\sum_\alpha (n_\alpha - n_\alpha^{in})}{\sum_\alpha n_\alpha^{in}} \quad (14.11)$$

<sup>1</sup>In the case of Ge<sub>2</sub>Sb<sub>2</sub>Te<sub>5</sub> we assume that the atomic volume of all species is identical and equal to 3.33 · 10<sup>-23</sup> cm<sup>-3</sup>.

being  $B$  the effective bulk modulus [ $\text{Pa}$ ] (that can be assumed also as a model parameter) and  $n_\alpha^{in}$  is the initial concentration of the chemical species  $\alpha$  [ $\text{m}^{-3}$ ]. So we may formalize the stress migration by introducing the flux due to mechanical-stress as

$$\mathbf{f}_{\mathbf{n}_\alpha}^{sm} = -\frac{D_\alpha}{K_B \Theta} n_\alpha \omega \nabla \sigma \quad (14.12)$$

Now we can describe the mass transport model as follows. Let  $\Omega$  be the domain of our problem. We impose homogeneous Neumann boundary conditions over the whole boundary of  $\Omega$  (because we want to keep the atoms confined in the domain). Since the total atomic density and the ratio of each constituent should be the same in all  $\Omega$ , a uniform concentration for all species is assumed as initial condition.

The model reads:

*assuming that the temperature profile  $\Theta = \Theta(\mathbf{x}, t)$ , the electrostatic potential profile  $\psi = \psi(\mathbf{x}, t)$  and the material phase are known quantities for each  $\mathbf{x} \in \Omega$  and for each time  $t \in [0, t_f]$ , find for each atomic species  $\alpha = 1, \dots, M_{ion}$  the concentration  $n_\alpha = n_\alpha(\mathbf{x}, t)$  such that:*

$$\left\{ \begin{array}{ll} \frac{\partial n_\alpha}{\partial t} + \operatorname{div} \mathbf{f}_{\mathbf{n}_\alpha} = 0 & \text{in } \Omega, 0 < t < t_f \\ \mathbf{f}_{\mathbf{n}_\alpha} = -D_\alpha (\nabla n_\alpha + \frac{z_\alpha q}{K_B \Theta} n_\alpha \nabla \psi + \Gamma_\alpha n_\alpha \nabla \ln(\frac{\Theta}{\Theta_0}) + \frac{n_\alpha \omega}{K_B \Theta} \nabla \sigma) & \text{in } \Omega, 0 < t < t_f \\ \sigma = B \frac{\sum_\alpha (n_\alpha - n_\alpha^{in})}{\sum_\alpha n_\alpha^{in}} & \\ \mathbf{f}_{\mathbf{n}_\alpha} \cdot \mathbf{n} = 0 & \text{on } \partial\Omega, 0 < t < t_f \\ n_\alpha(\mathbf{x}, 0) = \bar{n}_\alpha & \text{in } \Omega \end{array} \right.$$

where  $\Gamma_\alpha = \alpha_\alpha^{tm} + \beta_\alpha(\Theta)$ , and the coefficient  $D_\alpha$  and  $\beta_\alpha$  are expressed in Eq. (14.9) and (14.10) respectively.

**Remark 14.2.** This system is very similar to the PNP model introduced of section 9.6 in which other force acting of the system are considered.

In Fig. 14.19 a comparison between the model results and experimental characterization is reported.

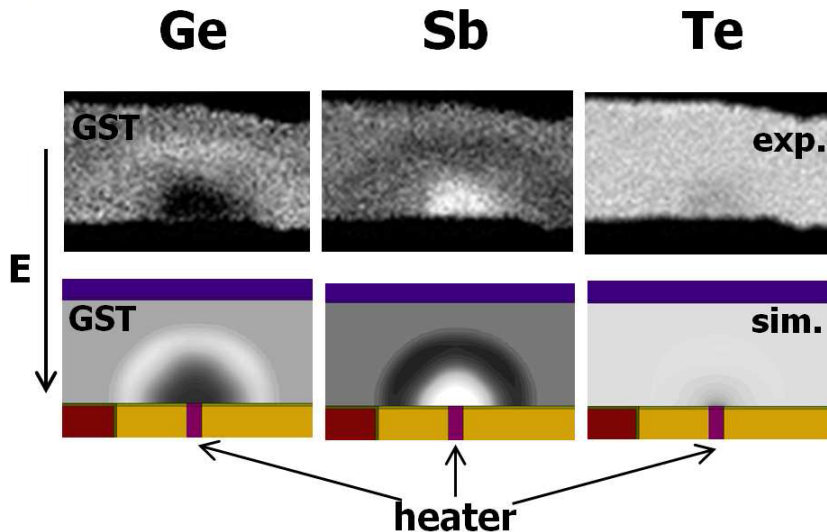


**Figure 14.19** Comparison between the simulation obtained with the atomic migration model and the experiments [157]

#### 14.4. Modeling of Conductive Bridge RAM device

The basic idea of a resistive memory is to use an electrically switchable resistance element to store the information: the two logical states (SET and RESET) of a bit correspond to different values of the cell resistance such as the random access memory (ReRAM). ReRAMs rely on the electrochemical dissolution and deposition of an active electrode metal to perform the resistive switching operation. They demonstrate a high potential for scalability, and a decisive advantage is also the fast read, write and erase speed at low voltages and operating currents. The basic ReRAM cell is a metal-ion conductor-metal (MIM) system, composed of an insulating or resistive material 'I' (solid electrolyte) sandwiched between two (possibly different) electron conductors 'M'. The two electrodes have different characteristics: one is made of an electrochemically active electrode (AE) metal, such as Ag, Cu, or Ni, the other one is an electrochemically inert counter (CE), such as Pt, Ir, W, or Au. Figure 14.20 schematically shows the principle of operation of a ReRAM memory cell. The distinguishing feature of ReRAM devices is that the active electrode is composed of a metal that can be easily electrochemically dissolved into, and conducted through, the ion conducting layer (I), whereas the counter electrode cannot. In the initial high resistance state (OFF-state) of the cell no electrodeposit of the AE metal M is present on the inert electrode or in the electrolyte (Fig. 14.20(A)). A SET, or programming, process occurs if a sufficiently positive bias voltage is applied to the active electrode allowing the dissolution of the

AE metal M through the electrolyte. Then, chemical reactions occur involving M and the free electrons of the electrolyte or the inert electrode (Fig. 14.20(B)). Finally the metal is deposited at the surface of the CE (Fig. 14.20 (C)) and precipitated in the electrolyte. Hence, the SET process can be summarized as follows:

- anodic dissolution of the metal M according to the reaction



where  $M^{z+}$  represents the metal cations in the solid electrolyte thin film

- migration of the  $M^{z+}$  cations across the solid electrolyte thin film under the action of a high electric field;
- reduction and electro-crystallization of M on the surface of the inert electrode according to the cathodic deposition reaction

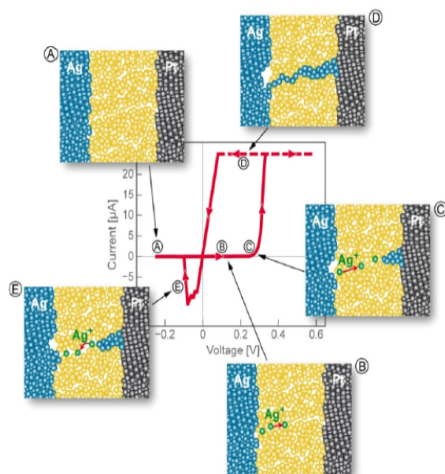
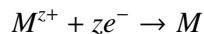


Figure 14.20 Schematic of the steps of the SET(A-D) and RESET (E) operations of RRAM cell

The three processes outlined above lead to the formation of an agglomerate of metal percentiles connecting the two electrodes (Fig. 14.20 (D)). After the metal filament has grown sufficiently far to make an electronic contact to the opposite electrode, the cell has switched to the ON-state (Fig. 14.20 (D)). The cell retains the ON-state unless a sufficient voltage of opposite polarity is applied and the electrochemical dissolution of the metal filament RESETs the cell (Fig. 14.20 (E)) to its initial OFF-state (Fig. 14.20 (A)). The process of the filament formation involves the kinetics of the

electrode reactions at both electrodes, i.e. dissolution of the M electrode and deposition of M metal on the inert counter electrode. Depending on the type of solid material used to ensure the ionic transport, the kinetics of the ionic movement may play a crucial role instead of the electrode kinetics. It is evident that these processes must be considered carefully in order to physically describe the cell operation. Therefore, let us analyze the main electrical evidences and the physics behind the filament formation. A fundamental characteristic of ReRAM cells is that their SET speed depends strongly on voltage. From the operation principles we know that a cell in its high-resistance (OFF) state can be SET to a low-resistance (ON) state by applying appropriate programming or write voltage pulses  $V_{wr}$ . The write voltage  $V_{wr}$  should be in the range of a few hundred mV to few V. The length of the write voltage pulses  $t_{wr}$  is desired to be below 100 ns in order to compete with the present devices. As we can see in Fig. 14.21 the time required to SET a ReRAM cell increases exponentially as the voltage is reduced toward zero [159].

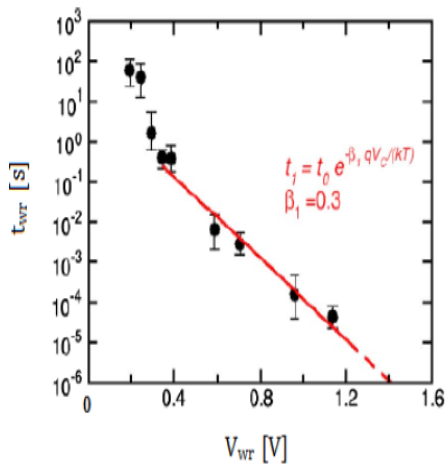


Figure 14.21 Exponential dependance of the SET speed on the SET voltage [159].

Fig. 14.22 shows measured  $I - V$  characteristics of a ReRAM device. The SET-state resistance decreases and the RESET current increases for increasing compliance current, that is the maximum current during SET operation [160]. The monotonic decrease of the SET-state resistance with the maximum current that is allowed to flow through the device during SET, shown in Fig. 14.23, is one of the fundamental characteristics of ReRAMs ([161] [162] [163]). This means that it is possible to build different low resistive states allowing multi-bit programming. Moreover, it seems that

this resistance variation is directly correlated with the spatial dimension of the filament. The abrupt variation of the resistance in ReRAMs is due to the formation of a metallic filament within the cell. Thus the process of filament formation and rupture is still in the primary focus of interest in the physical comprehension of the devices operation. First of all, the filamentary nature of the resistive switching effect is widely accepted and up to now no reasonable alternative has been suggested [159].

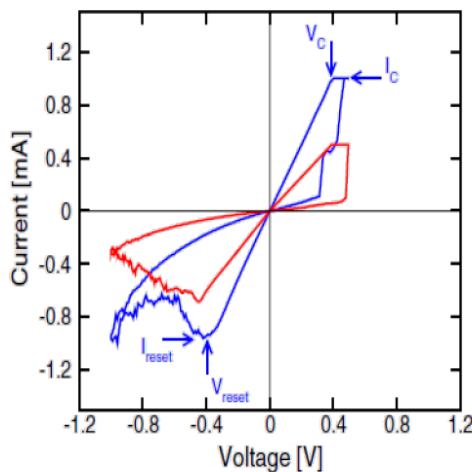


Figure 14.22 Typical  $I - V$  curves of an RRAM device [160]

However just few direct observations of a complete metal filament in a vertical cell has been published to date. The arguments supporting the formation of metal filament are:

- the drastic change in the conductivity (resistance)
- the possibility to vary the SET resistance (i.e. the filament thickness) by the applied current
- the fact that in most cases the resistance does not scale with the electrode diameter
- the observation that the resistive switching effect occurs only with soluble active electrodes (Ag, Cu) but not with noble metals.

We have already described the formation of the filament, now, considering the RESET operation, we wonder where the bridging metal filament connecting the two electrodes will start to dissolve. Since the active metal is present at both electrodes and forms the bridge, the answer to this question is not obvious. During the RESET operation, negative voltage polarity is applied to the active electrode and a positive polarity is applied to the counter electrode. Besides an electronic current across the metallic

bridge, there is an electrochemical current through the electrolyte which is supported by the electrochemical dissolution of the metal M at sites of positive potential, and by the metal M deposition at sites of negative potential at the surface of the metal.

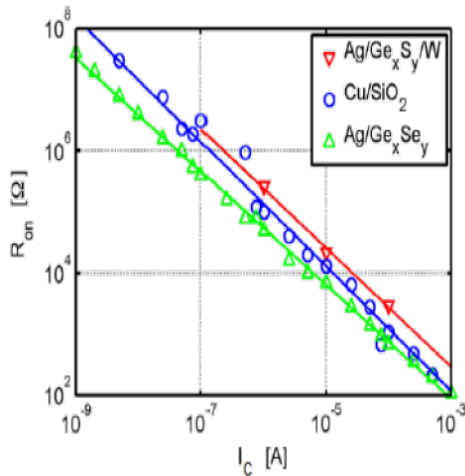


**Figure 14.23** Power law dependence of the ON-State resistance  $R_{ON}$  on the maximum current SET  $I_c$  [161]

Electric fields simulations [164] show that the RESET process starts by dissolution of the metal M at the connective neck formed between the M dendrite and the planar counter electrode, i.e., at the position at which the metal filament first touched the CE during the SET process 14.24. As previously mentioned, the dimension of the filament is not constant in space. It is very likely that the expansion of the metallic filament within the electrolyte causes a large mechanical stress in the ReRAM cell. The stress will depend on the thickness of the metallic filament. To avoid this stress, the metal filament needs to grow in nanopores of the ion conductor. Alternatively, some stress may be released by the formation of the metal filament at the interface of the ion conductor and a neighboring phase. From this brief description it is clear that the key points for ReRAMs modeling are:

- electron transport
- ion transport mechanisms
- chemical reactions
- thermal process
- mechanical stress phenomena.

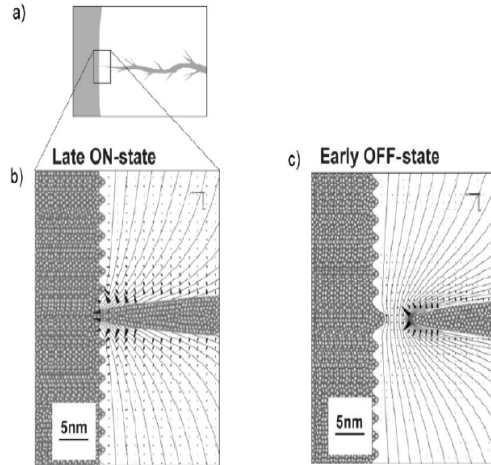


**Figure 14.24** Field simulation of the front-most Ag filament touching the Ag electrode shown in a cross-section during the RESET process a) location b) late ON state c) early OFF state. The lines are the equipotential lines, the black triangles shows the direction and strength of the electric field.

#### 14.4.1. Mathematical model

In this section we illustrate the physics based model and relative equations, able to describe the CBRAM device in all of the operation conditions: forming, reading, reset and set.

Fig 14.25 shows the ideal device with lables needed to explain the mathematical and numerical approach. CBRAM cell is formed by the Top (TE) and Bottom (BE) metal electrode, the Reservoir as a chemical reserve, and the active part of the device made by Oxide and Electrolyte both of them treated as dielectric.

CBRAM cell is described as a charged multi-species system, including electrons, moving in a material medium under a combined effect of electrical, thermal and chemical forces. In equation system (14.13) we report the fundamental conservation laws that express mass and linear momentum balance.

$$q \frac{\partial n}{\partial t} - \operatorname{div}(qD_n \nabla n - q\mu_n n \nabla \psi) = qR_{el} \quad (14.13a)$$

$$qz_\alpha \frac{\partial n_\alpha}{\partial t} - \operatorname{div}(qz_\alpha D_\alpha \nabla n_\alpha - q|z_\alpha| n_\alpha \mu_\alpha \nabla \psi) = qR_{chem} \quad (14.13b)$$

$$\frac{\partial \rho c \Theta}{\partial t} - \operatorname{div}(k \nabla \Theta) = Q_{term} \quad (14.13c)$$

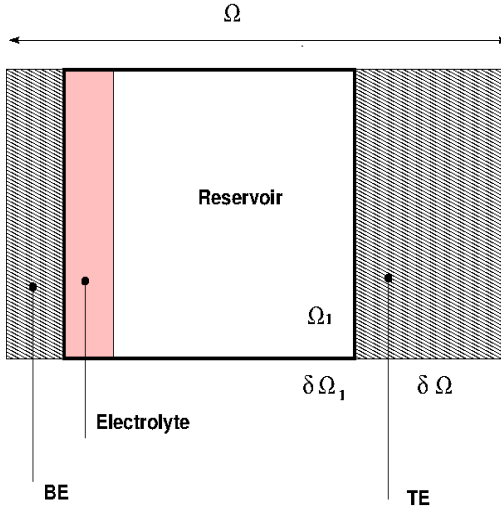


Figure 14.25 CBRAM device schematic

$$\operatorname{div}(\varepsilon \mathbf{E}) = -qn + q \sum z_\alpha n_\alpha \quad (14.13d)$$

Eq. (14.13a) is describing electrons conservation law (i.e. classical drift-diffusion model in semiconductor), where  $q$  is the electronic charge,  $\mu_n$  the electron mobility,  $D_n$  the electron diffusivity,  $R_{el}$  the net recombination/generation term resulting from the different chemistry/electronic processing and  $\psi$  the electrostatic potential. Eq. (14.13b) is the diffusion/advection/reaction equation for the  $\alpha$ -th chemical species where  $z_\alpha$  is the chemical charge,  $\mu_\alpha$  the chemical mobility,  $D_\alpha$  the chemical diffusivity and  $R_{chem}$  the net recombination/generation term resulting from the different chemical reactions. Eq. (14.13c) is the energy balance equation in the system, where  $\rho$  and  $c$  are the mass density and specific heat of the medium,  $k$  the thermal conductivity and  $Q_{term}$  the net heat production rate (limited to Joule-heat in this application). Eq. (14.13d) is the generalize Poisson equation expressing Gauss’ law in differential form, where  $q$  is the electron charge and  $\varepsilon$  the dielectric permittivity of the medium. Eq. (14.13c) and (14.13d) are solved in  $\Omega$  domain with boundary condition applied to  $\delta\Omega$ ; while eq. (14.13a) and eq. (14.13b) are solved in  $\Omega_1$  domain with boundary labeled by  $\delta\Omega_1$ . Each of (14.13) system equation requires proper boundary conditions that can be written in a compact way as:

$$\eta F(u) \cdot v = \gamma(\delta u - \bar{u}) \quad (14.14)$$

where  $F(u)$  is the term under divergence operator - the flux - of different variables  $u = n, n_\alpha, T, E$ ,  $v$  the out-normal direction of border surface,  $\eta, \gamma, \delta$  parameter able to chose the desidered condition (Diriclet, Neumann, Robin) and  $\bar{u}$  the value or the

flux of the variable at the border  $\delta\Omega$  or  $\delta\Omega_1$ . In eq. (14.13a) mixed boundary condition are used: for the injecting electrode (BE in forming and reading, TE in reset) Not-Omogeneous Neumann condition are applied by calculating the inward current flux with WKB model; at the correspond other electrode Robin condition is applied to consider the possible recombination effect at the dielectric(reservoir)/metal interface. In eq. (14.13b) omogeneus Neumann condition is used to ensure chemical mass conservation inside the cell. In eq. (14.13c) and (14.13d) simple Dirichlet condition applied to thermode and contact respectively is used to fix the temperature and the bias in the device. In eq. (14.13a) and (14.13c) we assume holding the generalized Eistein relation. The form of the  $R_{el}$  is given by the following equation:

$$R_{el} = \sum R_{\alpha,chem} \quad (14.15)$$

where the term  $\sum R_{\alpha,chem}$  in (14.15) will be discussed later. The chemical species involved in CBRAM cell are assumed to be different charge states of  $Cu$  atoms. As simplest approach we have considered only neutral  $Cu$  and its single positive ion  $Cu^+$ . The redox processing is given by the following reaction (14.16)



This reaction is resulting in two equations of type (14.13b) one for each  $Cu$  charge state where the net generation/recombination term becomes of the form of:

$$R_{chem} = \pm(k_b[Cu] - k_f[Cu^+] \frac{n}{n_0}) \quad (14.17)$$

where  $k_f$  the chemical reaction velocity for the forward reaction (right-arrow in eq. (14.16)) and  $k_b$  the ones for the backward reaction (left-arrow in eq. (14.16)), + is for equation involving  $Cu^+$  and – for  $Cu$ .

To simulate the precipitation phenomena and agglomerate formation of the metal state,  $Cu$  is assumed to be immobile at room temperature by setting appropriate value of its diffusivity coefficient: this assumption seems valid also when the reset kinetics is considered. Reaction velocities are chosen to be an Arrhenius-type expression with the reaction barrier lowered or increased (+ for forward and – for backward reaction) by the projection of the electric field  $F_{Je}$  in the direction of the electron current ( $\vartheta$  fitting parameter)

$$k_{f,b} = k_{f,b} \exp\left(\frac{-E_{f,b} \pm \vartheta F_{Je}}{k_B \Theta}\right) \quad (14.18)$$

A field dependant mobility model has been introduced for the charged chemical

species  $Cu^+$  while for  $Cu$  simple Arrhenius model is used. Considering holding Eistein relation the diffusivities of the involved chemical species become:

$$D_{Cu} = D_{0,Cu} \exp\left(\frac{-E_{a,Cu}}{k_B \Theta}\right) \quad (14.19a)$$

$$D_{Cu^+} = D_{0,Cu^+} \exp\left(\frac{-E_{a,Cu^+} + \beta |F_{Je}|}{k_B \Theta}\right) \quad (14.19b)$$

where  $\beta$  is a fitting parameter and  $F_{Je}$  the electric field in the direction of the electron current.

$Cu$  precipitation in the metallic form causes a variation in the electrical conduction resulting in cell current modulation from High to Low Resistance State. Three are the main physical properties responsible for that: electron affinity and band-gap, electron. The first two regulate the injected electron current density, the third the electric field in the cell and the last one the thermal transport velocity. Electron affinity  $E_{wf}$ , band-gap  $E_{gap}$ , and electrical conductivity  $\sigma$  are calculated based on eq. (14.20):

$$E_{wf} = E_{wf,0} - (E_{wf,Cu_m} - E_{wf,0})\left(\frac{Cu}{Cu_m}\right)^\alpha \quad (14.20a)$$

$$E_{gap} = E_{gap,0}\left(1 - \frac{Cu}{Cu_m}\right)^\alpha \quad (14.20b)$$

$$\sigma = \sigma_m\left(\frac{Cu}{Cu_m}\right)^\gamma + \varepsilon\varepsilon_{vacuum} \quad (14.20c)$$

where 0-index is referred to the un-metalized material, while m-index to the  $Cu$  metal phase.  $\alpha$  and  $\gamma$  are the metallization strength coefficient describing how fast is the transition between the not-metal and the metal behavior for band profile and electric field. All equations in (14.20) are calculated locally (i.e. in each of the device mesh points) allowing a possible not-uniformity processing in the cell.

## APPENDIX A

# Elements of mathematics and numerics

### A.1. Theorems of vector calculus

In this section we provide a summary of the main theoretical results that are needed to manipulate the integrals of differential operators applied to vector and tensor fields inside a given volume and/or on a given surface in the three-dimensional space.

#### A.1.1. The divergence theorem

In vector calculus, the divergence theorem, also known as Gauss’ theorem or Ostrogradsky’s theorem, is a fundamental result that relates the flow of a vector field through a surface (that is, the flux) to the behavior of the vector field inside the surface. More precisely, the divergence theorem states that the outward flux of a vector field through a closed surface is equal to the volume integral of the divergence of the vector field over the region inside the surface. Intuitively, it states that the sum of all sources minus the sum of all sinks gives the net flow of the vector field out of the region.

*Mathematical Statement.* Suppose that  $\Omega \subset \mathbb{R}^n$  is compact and has a piecewise smooth boundary  $\partial\Omega$ . If  $\underline{\mathbf{u}}$  is a continuously differentiable vector field defined on  $\mathbb{W}$ , with  $\overline{\Omega} \subset \mathbb{W}$ , then we have

$$\int_{\Omega} \nabla_{\underline{x}} \cdot \underline{\mathbf{u}} d\Omega = \int_{\partial\Omega} \underline{\mathbf{u}} \cdot \underline{\mathbf{n}} d(\partial\Omega). \quad (\text{A.1})$$

In components, this identity can be written as

$$\int_{\Omega} \left( \sum_{i=1}^n \frac{\partial u_i}{\partial x_i}(\underline{x}) \right) d\Omega = \int_{\partial\Omega} \left( \sum_{i=1}^n u_i(\underline{x}) n_i(\underline{x}) \right) d(\partial\Omega) \quad (\text{A.2})$$

where  $\underline{\mathbf{n}}$  is the outward unit normal vector at  $\underline{x}$  on  $\partial\Omega$ . When applied to tensor fields, the theorem can be written as the vectorial identity

$$\int_{\Omega} \nabla_{\underline{x}} \cdot \underline{\underline{\mathbf{T}}} d\Omega = \int_{\partial\Omega} \underline{\underline{\mathbf{T}}} \cdot \underline{\mathbf{n}} d(\partial\Omega). \quad (\text{A.3})$$

In components, this identity can be written as

$$\int_{\Omega} \left( \sum_{j=1}^n \frac{\partial T_{ij}}{\partial x_j}(\underline{\mathbf{x}}) \right) d\Omega = \int_{\partial\Omega} \left( \sum_{j=1}^n T_{ij}(\underline{\mathbf{x}}) n_j(\underline{\mathbf{x}}) \right) d(\partial\Omega), \quad i = 1, \dots, n. \quad (\text{A.4})$$

**Definition A.1** (Flux of a vector and of a tensor field). *The quantity on the right-hand side of (A.1) is the flux of the vector field  $\underline{\mathbf{u}}$  across the  $n - 1$ -dimensional surface  $\partial\Omega$ . Analogously, the quantity on the right-hand side of (A.3) is the flux of the tensor field  $\underline{\mathbf{T}}$  across the  $n - 1$ -dimensional surface  $\partial\Omega$ .*

**Exercise A.1.** *Given a scalar field  $f$  and a vector field  $\underline{\mathbf{u}}$  defined on  $\mathbb{W}$ , with  $\overline{\Omega} \subset \mathbb{W} \subset \mathbb{R}^n$ , show that*

$$\int_{\Omega} f \nabla_{\underline{\mathbf{x}}} \cdot \underline{\mathbf{u}} d\Omega = - \int_{\Omega} \underline{\mathbf{u}} \cdot \nabla_{\underline{\mathbf{x}}} f d\Omega + \int_{\partial\Omega} f \underline{\mathbf{u}} \cdot \underline{\mathbf{n}} d(\partial\Omega). \quad (\text{A.5})$$

Proof. Utilizing the relationship in (??) and the divergence theorem (A.1) we can write

$$\int_{\Omega} f \nabla_{\underline{\mathbf{x}}} \cdot \underline{\mathbf{u}} d\Omega = \int_{\Omega} (-\underline{\mathbf{u}} \cdot \nabla_{\underline{\mathbf{x}}} f + \nabla_{\underline{\mathbf{x}}} \cdot (f \underline{\mathbf{u}})) d\Omega = - \int_{\Omega} \underline{\mathbf{u}} \cdot \nabla_{\underline{\mathbf{x}}} f d\Omega + \int_{\partial\Omega} f \underline{\mathbf{u}} \cdot \underline{\mathbf{n}} d(\partial\Omega).$$

Of course, we are implicitly assuming that  $f$ ,  $\underline{\mathbf{u}}$  and  $\Omega$  are regular enough for the above operations to make sense.

### A.1.2. The Stokes theorem

In vector calculus, the Stokes theorem is a fundamental result that relates the flux of the curl of a vector field across a given surface in the three-dimensional space with the behavior of the vector field along the line constituting the boundary of the surface. More precisely, the Stokes theorem states that the outward flux of the curl of a vector field through a closed surface is equal to the circulation of the vector field along the boundary of the surface. Intuitively, the Stokes theorem is the generalization of Green’s theorem from circulation in a planar region to circulation along a surface.

*Mathematical Statement.* Suppose that  $S$  is an open bounded surface of  $\mathbb{R}^3$  whose boundary is the piecewise smooth line  $\Gamma$ . The outward unit normal vector to  $S$  is  $\underline{\mathbf{n}}$  whereas  $\underline{\mathbf{t}}$  is the unit tangent vector to  $\Gamma$ ,  $\underline{\mathbf{t}}$  and  $\underline{\mathbf{n}}$  being oriented according to the right-hand rule. If  $\underline{\mathbf{u}}$  is a continuously differentiable vector field defined on  $W$ , with  $\overline{S} \subset W$ , then we have

$$\int_S (\nabla \times \underline{\mathbf{u}}) \cdot \underline{\mathbf{n}} dS = \oint_{\Gamma} \underline{\mathbf{u}} \cdot \underline{\mathbf{t}} d\ell \quad (\text{A.6})$$

where  $\underline{\mathbf{t}} d\ell$  is the infinitesimal arclength vector-valued measure along  $\Gamma$ .

**Definition A.2** (Circulation of a vector field). *The quantity on the right-hand side of (A.6) is the circulation of the vector field  $\underline{\mathbf{u}}$  along the line  $\Gamma$  constituting the boundary of a given surface  $S$  in  $\mathbb{R}^3$ .*

### A.1.3. Leibnitz transport theorem

Let us consider again the case of a scalar field  $\Psi = \Psi(\underline{x}, t)$  defined on  $\mathcal{V}_t \times (0, T)$  where  $\mathcal{V}_t$  is a material domain. Let  $\underline{x}$  is the position vector of a material particle in  $\mathcal{V}_t$  and  $\underline{v}$  the Eulerian velocity, the *Leibnitz transport theorem* is

$$\frac{d}{dt} \int_{\mathcal{V}_t} \Psi(\underline{x}, t) d\mathcal{V}_t = \int_{\mathcal{V}_t} \left( \frac{\partial \Psi}{\partial t}(\underline{x}, t) + \nabla_{\underline{x}} \cdot (\Psi \underline{v})(\underline{x}, t) \right) d\mathcal{V}_t \quad (\text{A.7})$$

### A.1.4. Reynolds transport theorem

Using the balance of mass in local form, we can derive a special form of the Leibnitz transport theorem in the case where the scalar function  $\Psi$  is written in the form  $\Psi(\underline{x}, t) = \rho(\underline{x}, t) \eta(\underline{x}, t)$ , where  $\rho(\underline{x}, t)$  is the mass density and  $\eta(\underline{x}, t)$  is a scalar field. We have

$$\frac{d}{dt} \int_{\mathcal{V}_t} \rho \eta d\mathcal{V}_t = \int_{\mathcal{V}_t} \left( \rho \frac{\partial \eta}{\partial t} + \rho \underline{v} \cdot \nabla_{\underline{x}} \eta \right) d\mathcal{V}_t + \int_{\mathcal{V}_t} \beta \eta d\mathcal{V}_t, \quad (\text{A.8})$$

which, using the definition of material derivative, can be also written as

$$\frac{d}{dt} \int_{\mathcal{V}_t} \rho \eta d\mathcal{V}_t = \int_{\mathcal{V}_t} \rho \frac{D\eta}{Dt} d\mathcal{V}_t + \int_{\mathcal{V}_t} \beta \eta d\mathcal{V}_t. \quad (\text{A.9})$$

## A.2. Numerical solution of ordinary differential equations

In a wide number of applications of computational biology (see [67] and references cited therein), the mathematical model is expressed by an ordinary differential equation or by a system of ordinary differential equations. For this reason in this section we address the issue of the numerical discretization of *Ordinary Differential Equations and Systems (ODEs)*. For a more extensive theoretical analysis of this topic we refer to [98], Chapter 11 and to [45].

### A.2.1. The Cauchy problem

In this section we shortly provide the mathematical definitions of an initial value problem. Let  $t_0$  and  $T > 0$  be given quantities and  $t$  denote the independent coordinate, having usually, but non necessarily being limited to, the physical meaning of the time variable. Setting  $I_T := (t_0, t_0 + T)$ , for a given  $y_0 \in \mathbb{R}$ , the *Cauchy problem* consists of finding the real-valued function  $y = y(t) : I_T \rightarrow \mathbb{R}$  such that:

$$\frac{dy}{dt}(t) = f(t, y(t)) \quad t \in I_T \quad (\text{A.10a})$$

$$y(t_0) = y_0. \quad (\text{A.10b})$$

Equation (A.10b) is the *initial condition*. The following definition extends Definition ?? to the case of a function of two variables, such as  $f = f(t, y)$ .

**Definition A.3.** *The function  $f$  is uniformly Lipschitz continuous with respect to the argument  $y$  if there exists a positive constant  $L$  such that*

$$|f(t, y_1) - f(t, y_2)| \leq L|y_1 - y_2| \quad \forall t \in I_T, \quad \forall y_1, y_2 \in \mathbb{R}. \quad (\text{A.11})$$

**Theorem A.1.** *Assume that  $f$  is uniformly Lipschitz continuous with respect to  $y$ . Then, there exists a unique solution  $y \in C^1(I_T)$  of the Cauchy problem and such solution depends continuously on the data  $I_T$ ,  $f$  and  $y_0$ .*

In the remainder of the section we always assume that the Cauchy problem is uniquely solvable.

## A.2.2. Numerical approximation: general concepts

Applying the fundamental theorem of calculus, we get

$$y(t_a) = y(t_b) + \int_{t_a}^{t_b} f(\tau, y(\tau)) d\tau \quad \forall t_a, t_b \in I_T. \quad (\text{A.12a})$$

Unfortunately, except for simple cases, the closed form evaluation of the integral in (A.12a) is not possible, so that a *numerical approximation* of  $y(t)$  is in order. With this aim, we assume for simplicity that  $T$  is finite and construct a partition of  $I_T$  into the union of  $M_T \geq 1$  subintervals  $I_n := (t_{n-1}, t_n)$  of uniform width  $\Delta t = T/M_T$  such that  $t_n = t_0 + n\Delta t$ ,  $n = 0, 1, \dots, M_T$ . Then, we write  $y_n := y(t_n)$  and consider the quantity  $u_n$  as the *approximation* of  $y_n$  computed by the (yet unspecified) numerical scheme. The *discretization error* is defined as

$$e_n := y_n - u_n \quad n = 0, \dots, M_T. \quad (\text{A.12b})$$

### A.2.2.1. The Forward and Backward Euler methods

The simplest method that can be thought of for the numerical approximation of the Cauchy problem can be derived from the integral form (A.12a) as follows. Set  $t_a = t_n$  and  $t_b = t_{n+1}$ ,  $n = 0, 1, \dots, M_T - 1$ . Then, the *Forward Euler method* (FE) is defined as:

$$u_{n+1} = u_n + \Delta t f(t_n, u_n) \quad n = 0, \dots, M_T - 1 \quad (\text{A.13a})$$

$$u_0 = y_0. \quad (\text{A.13b})$$

We notice that the scheme is obtained upon using the following one-point quadrature rule for the approximation of the integral in (A.12a)

$$\int_{t_n}^{t_{n+1}} f(\tau, y(\tau)) d\tau \simeq \Delta t f(t_n, u_n) \quad n = 0, \dots, M_T - 1. \quad (\text{A.13c})$$

Of course, based on a similar argument, we can introduce the following alternative approach, known as the *Backward Euler method* (BE):

$$u_{n+1} = u_n + \Delta t f(t_{n+1}, u_{n+1}) \quad n = 0, \dots, M_T - 1 \quad (\text{A.13d})$$

$$u_0 = y_0. \quad (\text{A.13e})$$

We notice that the scheme is obtained upon using the following one-point quadrature rule for the approximation of the integral in (A.12a)

$$\int_{t_n}^{t_{n+1}} f(\tau, y(\tau)) d\tau \simeq \Delta t f(t_{n+1}, u_{n+1}) \quad n = 0, \dots, M_T - 1. \quad (\text{A.13f})$$

**Theorem A.2** (Convergence of the BE and FE schemes). *There exists a positive constant  $C$  independent of  $\Delta t$  such that the following error estimate holds for both FE and BE difference methods*

$$|e_n| \leq C \Delta t \quad n = 0, \dots, M_T. \quad (\text{A.13g})$$

Based on Theorem A.2 and Definition (1.7) it turns out that both FE and BE schemes converge with order  $p = 1$  with respect to  $\Delta t$ . However, a remarkable difference appears by inspection of the difference formulae (A.13a) and (A.13d). The forward Euler scheme is an *explicit* method because the solution at time  $t_{n+1}$  can be explicitly computed once  $u_n$  is known. The backward Euler scheme is an *implicit* method because the solution at time  $t_{n+1}$  can be computed only by solving the (generally nonlinear) equation

$$g(u_{n+1}) = 0 \quad n = 0, \dots, M_T - 1 \quad (\text{A.13h})$$

where the (generally nonlinear) function  $g$  is given by

$$g(x) = x - u_n - \Delta t f(t_{n+1}, x) \quad n = 0, \dots, M_T - 1. \quad (\text{A.13i})$$

Thus, despite the two schemes enjoy the same accuracy, their computational cost is quite different, that of the backward scheme being significantly larger than that of the forward scheme.

### A.2.2.2. The $\theta$ -method

In this section we introduce a generalization of the two approaches considered in Section A.2.2.1 for the solution of the Cauchy problem. Let  $\theta \in [0, 1]$  be a given parameter. The  $\theta$ -method for the numerical discretization of the Cauchy problem (A.10) computes  $\{u_n\}_{n=0}^{M_T}$  through the following formulae:

$$u_{n+1} = u_n + \theta \Delta t f(t_{n+1}, u_{n+1}) + (1 - \theta) \Delta t f(t_n, u_n) \quad n = 0, \dots, M_T - 1 \quad (\text{A.14a})$$

$$u_0 = y_0. \quad (\text{A.14b})$$

The FE and BE methods illustrated in Section A.2.2.1 are special cases of (A.14) and correspond to taking  $\theta = 0$  and  $\theta = 1$ , respectively. We notice that all the methods obtained from (A.14) for  $\theta \neq 0$  are implicit, the only explicit one being the FE method. Setting  $\theta = 1/2$  we obtain the so-called *Crank-Nicolson (CN) method* (also well-known as *trapezoidal integration* method (TI)), that computes  $\{u_n\}_{n=0}^{M_T}$  through the following formulae:

$$u_{n+1} = u_n + \frac{1}{2}\Delta t [f(t_n, u_n) + f(t_{n+1}, u_{n+1})] \quad n = 0, \dots, M_T - 1 \quad (\text{A.15a})$$

$$u_0 = y_0. \quad (\text{A.15b})$$

**Theorem A.3** (Convergence of the  $\theta$ -method). *There exists a positive constant  $C$  independent of  $\Delta t$  such that the following error estimate holds for the  $\theta$ -method*

$$|e_n| \leq C\Delta t^{p(\theta)} \quad n = 0, \dots, M_T \quad (\text{A.16})$$

where

$$p(\theta) = \begin{cases} 2 & \text{if } \theta = \frac{1}{2} \\ 1 & \text{if } \theta \neq \frac{1}{2}. \end{cases}$$

Theorem A.3 shows that the CN method *has a second order* convergence rate with respect to  $\Delta t$  whereas both FE and BE methods converge to the exact solution with first order rate with respect to  $\Delta t$ . This indicates that, for  $\Delta t$  sufficiently small, the CN scheme is far more accurate than the FE and BE methods.

### A.2.2.3. The absolute stability

The (apparently negative) feature of being implicit turns out to be an important benefit when the issue of stability is addressed. This requires to study the behaviour of the solution of the Cauchy problem for  $t \rightarrow +\infty$ . For this purpose, for a given  $\lambda > 0$ , we consider the following *linear* initial value problem:

$$\frac{dy}{dt} = -\lambda y \quad t > 0 \quad (\text{A.17a})$$

$$y(0) = 1 \quad (\text{A.17b})$$

whose exact solution is

$$y(t) = e^{-\lambda t}. \quad (\text{A.18})$$

The exact solution of (A.17) enjoys the property of *vanishing for long times*, namely

$$\lim_{t \rightarrow +\infty} y(t) = 0. \quad (\text{A.19})$$

**Definition A.4.** *A numerical method used to solve (A.17) is said to be absolutely*

stable if

$$\lim_{n \rightarrow +\infty} |u_n| = 0. \quad (\text{A.20})$$

From the above definition we immediately see that (A.20) is the discrete counterpart of (A.19). Absolute stability is a fundamental property when we are interested in the analysis of the solution of the problem for long times, so that it is highly desirable to have the freedom of taking a *large* time step to avoid an excessive computational effort.

Let us now verify whether or not the FE, BE and CN schemes are able to represent numerically the asymptotic behaviour of the linear Cauchy problem in a manner that is *independent* of the value of the temporal discretization parameter  $\Delta t$ .

Applying recursively the FE discretization (A.13c) to (A.17) the following representation formula for the numerical solution at time  $t_n$ ,  $n \geq 0$ , is obtained

$$u_n^{FE} = (1 - \lambda \Delta t)^n \quad n \geq 0. \quad (\text{A.21})$$

It is clear that in order the sequence  $\{|u_n^{FE}|\}_{n \geq 0}$  to tend to zero as  $n$  increases we must have

$$|1 - \lambda \Delta t| < 1$$

that is,  $\Delta t$  must satisfy the following constraint

$$0 < \Delta t < \Delta t_{lim} \quad \Delta t_{lim} := \frac{2}{\lambda}. \quad (\text{A.22})$$

Thus, the use of an explicit scheme gives rise to a *conditional* absolute stability. In particular, the inequality (A.22) tells us that the larger  $\lambda$  the smaller the time step to avoid divergence of the solution as time increases.

Applying recursively the BE discretization (A.13f) to (A.17) the following representation formula for the numerical solution at time  $t_n$ ,  $n \geq 0$ , is obtained

$$u_n^{BE} = \frac{1}{(1 + \lambda \Delta t)^n} \quad n \geq 0. \quad (\text{A.23})$$

Inspecting (A.23) we see that

$$\lim_{n \rightarrow +\infty} |u_n^{BE}| = 0$$

*irrespective* of the value of  $\Delta t$ . This is exactly the best case scenario according to our previous request on the choice of the time step, because the computational cost associated with (A.23) remains substantially unchanged whatever is the value of  $\lambda$ . The BE discretization is said to be *unconditionally absolutely stable*. We also notice that  $u_n^{BE} > 0$  for every  $n \geq 0$ . This property reflects on the discrete level the fact that the exact solution  $y_n > 0$  for every  $n \geq 0$ .

Applying recursively the CN discretization (A.15) to (A.17) the following representation formula for the numerical solution at time  $t_n$ ,  $n \geq 0$ , is obtained

$$u_n^{CN} = \left( \frac{1 - \lambda \frac{\Delta t}{2}}{1 + \lambda \frac{\Delta t}{2}} \right)^n \quad n \geq 0. \quad (\text{A.24})$$

As in the case of the BE method, inspecting (A.24) we see that

$$\lim_{n \rightarrow +\infty} |u_n^{CN}| = 0$$

irrespective of the value of  $\Delta t$ . Therefore, also the CN discretization is unconditionally absolutely stable.

#### A.2.2.4. The case of systems of ODEs

The models and the analysis of the previous sections can be straightforwardly extended to deal with the case of a system of ODEs:

$$\frac{d\underline{\mathbf{y}}}{dt} = \underline{\mathbf{f}}(t, \underline{\mathbf{y}}(t)) \quad t \in I_T \quad (\text{A.25a})$$

$$\underline{\mathbf{y}}(t_0) = \underline{\mathbf{y}}_0. \quad (\text{A.25b})$$

Now,  $\underline{\mathbf{y}}$  is the vector-valued dependent variable

$$\underline{\mathbf{y}}(t) = [y_1(t), y_2(t), \dots, y_N(t)]^T \quad (\text{A.25c})$$

where  $N \geq 1$  is the number of components, while  $\underline{\mathbf{y}}_0 = [y_{0,1}, y_{0,2}, \dots, y_{0,N}]^T \in \mathbb{R}^N$  is the vector of initial conditions. Again, under the assumption that (A.25a)- (A.25b) is uniquely solvable, its numerical approximation can be obtained by applying the  $\theta$ -method:

$$\underline{\mathbf{u}}_{n+1} = \underline{\mathbf{u}}_n + \theta \Delta t \underline{\mathbf{f}}(t_{n+1}, \underline{\mathbf{u}}_{n+1}) + (1 - \theta) \Delta t \underline{\mathbf{f}}(t_n, \underline{\mathbf{u}}_n) \quad n = 0, \dots, M_T - 1 \quad (\text{A.25da})$$

$$\underline{\mathbf{u}}_0 = \underline{\mathbf{y}}_0. \quad (\text{A.25db})$$

As in the case of the scalar Cauchy problem, by setting  $\theta = 0$  in (A.25da) we obtain the FE scheme for systems of ODEs:

$$\underline{\mathbf{u}}_{n+1} = \underline{\mathbf{u}}_n + \Delta t \underline{\mathbf{f}}(t_n, \underline{\mathbf{u}}_n) \quad n = 0, \dots, M_T - 1 \quad (\text{A.25e})$$

$$\underline{\mathbf{u}}_0 = \underline{\mathbf{y}}_0, \quad (\text{A.25f})$$

whereas setting  $\theta = 1$  in (A.25da) we obtain the BE scheme for systems of ODEs:

$$\underline{\mathbf{u}}_{n+1} = \underline{\mathbf{u}}_n + \Delta t \underline{\mathbf{f}}(t_{n+1}, \underline{\mathbf{u}}_{n+1}) \quad n = 0, \dots, M_T - 1 \quad (\text{A.25g})$$

$$\underline{\mathbf{u}}_0 = \underline{\mathbf{y}}_0, \quad (\text{A.25h})$$

and, finally, by setting  $\theta = 1/2$  in (A.25da) we obtain the CN scheme for systems of

ODEs:

$$\underline{\mathbf{u}}_{n+1} = \underline{\mathbf{u}}_n + \frac{1}{2}\Delta t [\underline{\mathbf{f}}(t_n, \underline{\mathbf{u}}_n) + \underline{\mathbf{f}}(t_{n+1}, \underline{\mathbf{u}}_{n+1})] \quad n = 0, \dots, M_T - 1 \quad (\text{A.25i})$$

$$\underline{\mathbf{u}}_0 = \underline{\mathbf{y}}_0. \quad (\text{A.25j})$$

Analogous considerations hold for the accuracy and stability of the above three schemes as those exposed in the previous sections.

### A.3. The Lax-Milgram Lemma

Let  $V$  be a Hilbert space (see Section ??) endowed with the norm  $\|\cdot\|_V$ . Suppose we are given a *bilinear form* (see Definition ??)

$$B(u, w) : V \times V \rightarrow \mathbb{R}$$

and a linear functional (see Definition ??)

$$F(w) : V \rightarrow \mathbb{R}$$

that satisfy the following properties:

**Continuity of  $B$**  There exists a positive constant  $M$  such that

$$|B(u, w)| \leq M\|u\|_V\|w\|_V \quad \forall u, w \in V; \quad (\text{A.5a})$$

**Coercivity of  $B$**  There exists a positive constant  $\beta_c$  such that

$$B(u, u) \geq \beta_c\|u\|_V^2 \quad \forall u \in V; \quad (\text{A.5b})$$

**Continuity of  $F$**  There exists a positive constant  $\Lambda$  such that

$$|F(w)| \leq \Lambda\|w\|_V \quad \forall w \in V. \quad (\text{A.5c})$$

Then, the following result can be proved.

**Theorem A.4 (Lax-Milgram Lemma).** *Assume that the bilinear form  $B$  and the linear functional  $F$  satisfy the three conditions (A.5). Then, the abstract problem find  $u \in V$  such that*

$$B(u, w) = F(w) \quad \forall w \in V, \quad (\text{A.6})$$

*admits a unique solution for which the following a priori estimate holds*

$$\|u\|_V \leq \frac{\Lambda}{\beta_c} \quad (\text{A.7})$$

The a priori estimate (A.7) actually represents a *stability* estimate for the mathematical model (A.6), in the sense of continuous dependence on data expressed by Definition 1.2.

“Notes” — 2019/5/17 — 17:39 — page 258 — #266

1. Data Science at NIH: Big Data to Knowledge (BD2K). <https://commonfund.nih.gov/bd2k>. Accessed: 2017-01-14.
2. ICON-ESM MPI-M’s next-generation Earth system model. <https://www.mpimet.mpg.de/en/communication/news/focus-on-overview/icon-earth-system-model/>.
3. S. Aggarwal, A. Qamar, V. Sharma, and A. Sharma. Abdominal aortic aneurysm: A comprehensive review. *Experimental & Clinical Cardiology*, 16(1):11, 2011.
4. P. Airoldi, A. G. Mauri, R. Sacco, and J. W. Jerome. Three-dimensional numerical simulation of ion nanochannels. *Journal of Coupled Systems and Multiscale Dynamics*, 3(1):57–65, 2015.
5. J. E. Anderson and D. C. Chang. Using electronic health records for surgical quality improvement in the era of big data. *JAMA Surg.*, 150(1):24–29, 2015.
6. A. M. Anile and S. Pennisi. Thermodynamic derivation of the hydrodynamical model for charge transport in semiconductors. *Phys. Rev. B*, 46:13186–13193, 1992.
7. M. Armbrust, A. Fox, R. Griffith, A. D. Joseph, R. Katz, A. Konwinski, G. Lee, D. Patterson, A. Rabkin, I. Stoica, and M. Zaharia. A view of cloud computing. *Commun. ACM*, 53(4):50–58, apr 2010.
8. F. Assous, P. Degond, E. Heintze, P. Raviart, and J. Segre. On a finite-element method for solving the three-dimensional maxwell equations. *Journal of Computational Physics*, 109(2):222 – 237, 1993.
9. F. Assous, P. Degond, E. Heintze, P. Raviart, and J. Segre. On a finite-element method for solving the three-dimensional Maxwell equations. *Journal of Computational Physics*, 109(2):222 – 237, 1993.
10. I. Babuska, K.-M. Liu, and R. Tempone. Solving stochastic partial differential equations based on the experimental data. *Mathematical Models and Methods in Applied Sciences*, 13(03):415–444, 2003.
11. A. Baicus. History of polio vaccination. *World journal of virology*, 1(4):108, 2012.
12. L. Ballestra, S. Micheletti, and R. Sacco. Semiconductor device simulation using a viscous-hydrodynamic model. *Computer Methods in Applied Mechanics and Engineering*, 191(47):5447 – 5466, 2002.
13. V. Barcilon. Ion flow through narrow membrane channels: part I. *SIAM J. Appl. Math.*, 52(5):1391–1404, 1992.
14. V. Barcilon, D. Chen, R. S. Eisenberg, and J. W. Jerome. Qualitative properties of steady-state Poisson-Nernst-Planck systems: perturbation and simulation study. *SIAM J. Appl. Math.*, 57(3):631–648, 1997.
15. V. Barcilon, R. S. Eisenberg, and D. P. Chen. Ion flow through narrow membrane channels: part II. *SIAM J. Appl. Math.*, 52(5):1405–1425, 1992.
16. S. Ben G. and S. Banerjee. *Solid State electronic Devices*. New Jersey: Prentice Hall, 2000.
17. S. Bobbio and E. Gatti. *Elementi di elettromagnetismo*. Programma di mat. fisica elettronica. Bollati Boringhieri, 1984.
18. D. Boffi, F. Brezzi, and M. Fortin. *Mixed Finite Element Methods and Applications*. Springer Series in Computational Mathematics. Springer Berlin Heidelberg, 2013.
19. M. Brera, J. W. Jerome, Y. Mori, and R. Sacco. A conservative and monotone mixed-hybridized finite element approximation of transport problems in heterogeneous domains. *Computer Methods in Applied Mechanics and Engineering*, 199(41-44):2709 – 2720, 2010.
20. J. N. Bronsted. Zur theorie der chemischen reaktionsgeschwindigkeit. *Z. Phys. Chem.*, 102(2):169–207, 1922.
21. C. Cancelli and T. Pedley. A separated-flow model for collapsible-tube oscillations. *Journal of Fluid Mechanics*, 157:375–404, 1985.
22. S. Čanić, J. Tambača, G. Guidoboni, A. Mikelić, C. J. Hartley, and D. Rosenstrauch. Modeling viscoelastic behavior of arterial walls and their interaction with pulsatile blood flow. *SIAM Journal on Applied Mathematics*, 67(1):164–193, 2006.
23. J. Caprioli and A. L. Coleman. Intraocular pressure fluctuation: a risk factor for visual field progression at low intraocular pressures in the advanced glaucoma intervention study. *Ophthalmology*, 115(7):1123–1129, 2008.

24. S. Cassani. *Blood circulation and aqueous humor flow in the eye: multi-scale modeling and clinical applications*. PhD thesis, Purdue University, 2016.
25. D. P. Chen and R. S. Eisenberg. Charges, currents, and potentials in ionic channels of one conformation. *Biophysical journal*, 64(5):1405–1421, 1993.
26. D. P. Chen and R. S. Eisenberg. Flux, coupling, and selectivity in ionic channels of one conformation. *Biophysical journal*, 65:727–746, 1993.
27. H. Cheng and W. J. Lederer. Calcium sparks. *Physiol Rev*, 88(4):1491–1545, 2008.
28. D. E. Contois. Kinetics of bacterial growth: relationship between population density and specific growth rate of continuous cultures. *J Gen Microbiol*, 1959, 21, pp 40–50, 1959.
29. G. W. De Young and J. Keizer. A single-pool inositol 1,4,5-trisphosphate-receptor-based model for agonist-stimulated oscillations in Ca<sup>2+</sup> concentration. *Proceedings of the National Academy of Sciences*, 89(20):9895–9899, 1992.
30. P. Degond and H. Neunzert. Local existence of solutions of the Vlasov-Maxwell equations and convergence to the Vlasov-Poisson equations for infinite light velocity. *Mathematical Methods in the Applied Sciences*, 8:533 – 558, 1986.
31. C. Desoer and E. Kuh. *Basic circuit theory*. McGraw Hill international editions: Electrical and electronic engineering series. McGraw-Hill, 1969.
32. R. J. Diperna and P. L. Lions. Global weak solutions of vlasov-maxwell systems. *Communications on Pure and Applied Mathematics*, 42(6):729–757, 1989.
33. P. A. M. Dirac. Quantised singularities in the electromagnetic field,. *Proceedings of the Royal Society of London A: Mathematical, Physical and Engineering Sciences*, 133(821):60–72, 1931.
34. P. A. M. Dirac. The theory of magnetic poles. *Phys. Rev.*, 74:817–830, Oct 1948.
35. B. Eisenberg, Y. Hyon, and C. Liu. Energy variational analysis of ions in water and channels: Field theory for primitive models of complex ionic fluids. *The Journal of Chemical Physics*, 133(10):104104, 2010.
36. S. I. Ellenbroek and J. Van Rheenen. Imaging hallmarks of cancer in living mice. *Nature Reviews Cancer*, 14(6):406–418, 2014.
37. A. C. Eringen. Mechanics of continua. *Huntington, NY, Robert E. Krieger Publishing Co.*, 1980. 606 p., 1, 1980.
38. G. B. Ermentrout and D. H. Terman. *Mathematical Foundations of Neuroscience*. Springer, 1st edition. edition, 2010.
39. E. Fermi and A. Scotti. *Termodinamica*. Programma di mat. fisica elettronica. Bollati Boringhieri, 1972.
40. F. Fiorani. Leonardo da vinci: Experience, experiment and design. *Renaissance Quarterly*, 61(3):921–923, 2008.
41. L. Formaggia, A. Quarteroni, and A. Veneziani, editors. *Cardiovascular Mathematics: Modeling and Simulation of the Circulatory System*. Springer-Verlag, Italy, 2009.
42. A. B. Frakt, , and S. D. Pizer. The promise and perils of big data in health care. *Am J Manag Care*, 22(2):98–99, 2016.
43. P. Fromherz. Neuroelectronics interfacing: Semiconductor chips with ion channels, nerve cells and brain. In R. Weise, editor, *Nanoelectronics and Information Technology*, pages 781–810. Wiley-VCH, Berlin, 2003.
44. V. Girault and P. Raviart. *Finite element methods for Navier-Stokes equations: theory and algorithms*. Springer series in computational mathematics. Springer-Verlag, 1986.
45. I. Gladwell. Numerical solution of ordinary differential equations (I. f. shampine). *SIAM Review*, 37(1):122–123, 1995.
46. A. E. Green and W. Zerna. *Theoretical elasticity*. Courier Corporation, 1992.
47. J. B. Grotberg and O. E. Jensen. Biofluid mechanics in flexible tubes. *Annual Review of Fluid Mechanics*, 36(1):121, 2004.
48. C. N.-T. G. S. Group et al. Comparison of glaucomatous progression between untreated patients with normal-tension glaucoma and patients with therapeutically reduced intraocular pressures. *American journal of ophthalmology*, 126(4):487–497, 1998.
49. G. Guidoboni, A. Harris, S. Cassani, J. Arciero, B. Siesky, A. Amireskandari, L. Tobe, P. Egan,

- I. Januleviciene, and J. Park. Intraocular pressure, blood pressure, and retinal blood flow autoregulation: a mathematical model to clarify their relationship and clinical relevance. *Investigative ophthalmology & visual science*, 55(7):4105–4118, 2014.
50. R. Haase. Reaction rate, activities, and affinities. *Z. Phys. Chem. Neue Folge*, 128:225–228, 1981.
  51. J. Hadfield, M. J. Plank, and T. David. Modeling secondary messenger pathways in neurovascular coupling. *Bull Math Biol.* 2013 Mar;75(3):428–43. doi: 10.1007/s11538-013-9813-x., 2013.
  52. A. Heijl, M. C. Leske, B. Bengtsson, L. Hyman, B. Bengtsson, and M. Hussein. Reduction of intraocular pressure and glaucoma progression: results from the early manifest glaucoma trial. *Archives of ophthalmology*, 120(10):1268–1279, 2002.
  53. N. Higham. *Accuracy and Stability of Numerical Algorithms*. Society for Industrial and Applied Mathematics, second edition, 2002.
  54. B. Hille. *Ionic Channels of Excitable Membranes*. Sinauer Associates, Inc., Sunderland, MA, 2001.
  55. A. Hodgkin and A. Huxley. Currents carried by sodium and potassium ions through the membrane of the giant axon of *loligo*. *Journal of Physiology*, 116:449–472, 1952.
  56. A. Hodgkin and A. Huxley. A quantitative description of membrane current and its application to conduction and excitation in nerve. *Journal of Physiology*, 117:500–544, 1952.
  57. S. A. Hughes. *Physical models and laboratory techniques in coastal engineering*, volume 7. World Scientific, 1993.
  58. G. W. Imbens and D. B. Rubin. *Causal inference in statistics, social, and biomedical sciences*. Cambridge University Press, 2015.
  59. M. Indirli, M. Forni, A. Martelli, B. Spadoni, A. Dusi, C. Alessandri, A. Bertocchi, R. Cami, A. Baratta, A. Procaccio, B. Carpani, P. Clemente, and M. Mucciarella. Development and application of innovative anti-seismic systems for the protection of cultural heritage: New achievements of ENEA. In *Conference Proceedings of the 2002 ASME-Pressure Vessel and Piping Conference, 14th International Symposium on Seismic, Shock and Vibration Isolation*, volume 2, 08 2002. Vancouver, BC, Canada, August 5–9, 2002.
  60. J. Jackson. *Classical Electrodynamics*. Wiley, 23 edition, 1998.
  61. J. W. Jerome. *Analysis of charge transport: a mathematical study of semiconductor devices*. Springer-Verlag, 1996.
  62. J. W. Jerome. Analytical approaches to charge transport in a moving medium. *Transport Theory and Statistical Physics*, 31:333–366, 2002.
  63. J. W. Jerome, B. Chini, M. Longaretti, and R. Sacco. Computational modeling and simulation of complex systems in bio-electronics. *Journal of Computational Electronics*, 7(1):10–13, 2008.
  64. J. W. Jerome and R. Sacco. Global weak solutions for an incompressible charged fluid with multi-scale couplings: Initial-boundary value problem. *Nonlinear Analysis*, 71:e2487–e2497, 2009.
  65. A. Jüngel. *Transport Equations for Semiconductors*. Springer Berlin Heidelberg, Berlin, Heidelberg, 2009.
  66. J. Keener and J. Sneyd. *Mathematical Physiology I: Cellular Physiology*. Springer, 2009.
  67. J. P. Keener and J. Sneyd. *Mathematical Physiology*. Springer, New York, 1998.
  68. J. W. Kiel, M. Hollingsworth, R. Rao, M. Chen, and H. A. Reitsamer. Ciliary blood flow and aqueous humor production. *Progress in Retinal and Eye Research*, 30(1):1 – 17, 2011.
  69. N. A. Kudryashov and I. L. Chernyavskii. Numerical simulation of the process of autoregulation of the arterial blood flow. *Izvestiya Rossiiskoi Akademii Nauk, Mekhanika Zhidkosti i Gaza*, Vol. 43, No. 1, pp. 3856., 2008.
  70. L. Landau and E. Lifshitz. *Statistical Physics*. Number v. 5 in Course of Theoretical Physics. Elsevier Science, 2013.
  71. P. D. Lax and R. D. Richtmyer. Survey of the stability of linear finite difference equations. *Comm. Pure Appl. Math.*, 9:267–293, 1956.
  72. M. C. Leske. Open-angle glaucomaan epidemiologic overview. *Ophthalmic epidemiology*, 14(4):166–172, 2007.
  73. M. C. Leske, A. Heijl, L. Hyman, B. Bengtsson, L. Dong, Z. Yang, E. Group, et al. Predictors of long-term progression in the early manifest glaucoma trial. *Ophthalmology*, 114(11):1965–1972, 2007.

74. Y.-X. Li and J. Rinzel. Equations for InsP<sub>3</sub> receptor-mediated [Ca<sup>2+</sup>]i oscillations derived from a detailed kinetic model: A Hodgkin-Huxley like formalism. *Journal of Theoretical Biology*, 166(4):461 – 473, 1994.
75. M. Longaretti, B. Chini, J. W. Jerome, and R. Sacco. Electrochemical modeling and characterization of voltage operated channels in nano-bio-electronics. *Sensor Letters*, 6(1):49–56, 2008.
76. M. Longaretti, G. Marino, B. Chini, J. W. Jerome, and R. Sacco. Computational models in nano-bioelectronics: Simulation of ionic transport in voltage operated channels. *Journal of Nanoscience and Nanotechnology*, 8(7):3686–3694, 2008.
77. M. Lundstrom. *Fundamentals of Carrier Transport, Edition 2*. University Press, Cambridge, 2009.
78. G. Magonette. Development and application of large-scale continuous pseudo-dynamic testing techniques. *Philosophical Transactions of the Royal Society of London A: Mathematical, Physical and Engineering Sciences*, 359(1786):1771–1799, 2001.
79. P. Markowich. *The Stationary Semiconductor Device Equations*. Springer-Verlag, Wien-New York, 1986.
80. P. Markowich, C. Ringhofer, and C. Schmeiser. *Semiconductor Equations*. Springer-Verlag, 1990.
81. A. G. Mauri, L. Sala, P. Airoldi, G. Novielli, R. Sacco, S. Cassani, G. Guidoboni, B. A. Siesky, and A. Harris. Electro-fluid dynamics of aqueous humor production: simulations and new directions. *Journal for Modeling in Ophthalmology*, 2:48–58, 2016.
82. J. C. Maxwell. *A Treatise on Electricity and Magnetism*:, volume 1. Cambridge University Press, Cambridge, 001 1873.
83. J. C. Maxwell. *A Treatise on Electricity and Magnetism*:, volume 2. Cambridge University Press, Cambridge, 001 1873.
84. R. A. Millikan. On the elementary electrical charge and the avogadro constant. *Phys. Rev.*, 2:109–143, Aug 1913.
85. C. B. Mills. *Designing with Models: A Studio Guide to Architectural Process Models*. John Wiley & Sons, 2011.
86. K. A. Milton. Theoretical and experimental status of magnetic monopoles. *Rept. Prog. Phys.*, 69:1637–1712, 2006.
87. G. E. Moore. Cramming more components onto integrated circuits. *Electronics*, 38(8), 1965. 4pp.
88. Y. Mori. *A Three-Dimensional Model of Cellular Electrical Activity*. PhD thesis, New York University, 2006.
89. R. Muller and T. Kamins. *Device Electronics for Integrated Circuits*. Wiley, 2002. 3rd Ed.
90. D. C. Musch, B. W. Gillespie, P. R. Lichter, L. M. Niziol, N. K. Janz, and C. S. Investigators. Visual field progression in the collaborative initial glaucoma treatment study: the impact of treatment and other baseline factors. *Ophthalmology*, 116(2):200–207, 2009.
91. not available. Ieee standard for binary floating-point arithmetic. *ANSI/IEEE Std 754-1985*, pages 0\_1–, 1985.
92. J. T. Oden, I. Babuska, F. Nobile, Y. Feng, and R. Tempone. Theory and methodology for estimation and control of errors due to modeling, approximation, and uncertainty. *Computer Methods in Applied Mechanics and Engineering*, 194(2):195 – 204, 2005.
93. J. T. Oden and S. Proudhomme. Control of modeling error in calibration and validation processes for predictive stochastic models. *International Journal for Numerical Methods in Engineering*, 87(1-5):262–272, 2011.
94. J. H. Park and J. W. Jerome. Qualitative properties of steady-state Poisson-Nernst-Planck systems: mathematical study. *SIAM J. Appl. Math.*, 57(3):609–630, 1997.
95. T. J. Pedley, B. S. Brook, and R. S. Seymour. Blood pressure and flow rate in the giraffe jugular vein. *Philosophical Transactions of the Royal Society of London B: Biological Sciences*, 351(1342):855–866, 1996.
96. M. L. Petersen and M. J. van der Laan. Causal models and learning from data: integrating causal modeling and statistical estimation. *Epidemiology (Cambridge, Mass.)*, 25(3):418, 2014.
97. R. F. Pierret and G. W. Neudeck. *Advanced Semiconductor Fundamentals*, volume 6. Prentice Hall.
98. A. Quarteroni, R. Sacco, and F. Saleri. *Numerical Mathematics*, volume 37 of *Texts in Applied Mathematics*. Springer, 2007.

99. W. V. Roosbroeck. Theory of the flow of electrons and holes in germanium and other semiconductors. *The Bell System Technical Journal*, 29:560 – 607, 1950.
100. W. V. Roosbroeck. Theory of the flow of electrons and holes in germanium and other semiconductors. *The Bell System Technical Journal*, 29(4):560–607, Oct 1950.
101. Y. Rosenfeld. Free-energy model for the inhomogeneous hard-sphere fluid mixture and density-functional theory of freezing. *Phys. Rev. Lett.*, 63:980–983, Aug 1989.
102. Y. Rosenfeld, M. Schmidt, H. Lowen, and P. Tarazona. Fundamental-measure free energy density functional theory for hard spheres: Dimensional crossover and freezing. *Phys. Rev. E*, 55:4245–4263, 1997.
103. R. Roth. Introduction to density functional theory of classical systems: Theory and applications. Lecture Notes, November 2006. ITAP, Universitaet Stuttgart and Max-Planck-Institut fur Metallforschung, Stuttgart Germany.
104. R. Roth, R. Evans, A. Lang, and G. Kahl. Fundamental measure theory for hard-sphere mixtures revisited: the white bear version. *Journal of Physics: Condensed Matter*, 14(46):12063, 2002.
105. I. Rubinstein. *Electrodiffusion of Ions*. SIAM, Philadelphia, PA, 1990.
106. I. Rubinstein. *Electrodiffusion of Ions*. SIAM, 1990.
107. M. Ruiz Estrada, S. Lai, and M. Umemoto. A simulation of a mega-earthquake in Malaysia: Kuala Lumpur and Penang area. 05 2018.
108. R. Sacco, P. Airoldi, A. G. Mauri, and J. W. Jerome. Three-dimensional simulation of biological ion channels under mechanical, thermal and fluid forces. *Applied Mathematical Modelling*, 43:221 – 251, 2017.
109. R. Sacco, F. Mangani, and J. W. Jerome. Modeling and simulation of thermo-fluid-electrochemical ion flow in biological channels. *Mol. Based Math. Biol.*, 3:78–111, 2015.
110. L. Sala, F. Salerni, and M. Szopos. Mathematical modeling of the cerebrospinal fluid flow and its interactions. In G. Guidoboni, A. Harris, and R. Sacco, editors, *Mathematical Modeling of Ocular Fluid Dynamics: From Theory to Clinical Applications*, Modeling and Simulation in Science, Engineering, and Technology. Springer-Birkhauser (New York), 2018.
111. M. Schmuck. Analysis of the Navier-Stokes-Nernst-Planck-Poisson system. *Mathematical Models and Methods in Applied Sciences*, 19(6):993–1015, 2009.
112. G. Scovazzi and T. J. R. Hughes. Lecture notes on continuum mechanics on arbitrary moving domains. Technical report, Sandia National Laboratories, 2007. Report 2007-6312P.
113. S. Selberherr. *Analysis and Simulation of Semiconductor Devices*. Springer-Verlag, 1984.
114. A. H. Shapiro. Steady flow in collapsible tubes. *Journal of Biomechanical Engineering*, 99(3):126–147, 1977.
115. B. Siesky, A. Harris, N. Kheradiya, C. Rospigliosi, L. McCranor, and R. Ehrich. The clinical significance of vascular factors in glaucoma. *Journal of Current Glaucoma Practice*, 2:12–17, 2007.
116. R. D. Simoni, R. L. Hill, and M. Vaughan. The discovery of insulin: the work of frederick banting and charles best. *Journal of Biological Chemistry*, 277(26):e15–e15, 2002.
117. Y.-C. Tham, S.-H. Lim, P. Gupta, T. Aung, T. Y. Wong, and C.-Y. Cheng. Inter-relationship between ocular perfusion pressure, blood pressure, intraocular pressure profiles and primary open-angle glaucoma: the singapore epidemiology of eye diseases study. *British Journal of Ophthalmology*, pages bjophthalmol–2017, 2018.
118. C. Truesdell. A first course in rational continuum mechanics. *Pure and applied mathematics*, 71:3–375, 1991.
119. G. Ullah, P. Jung, and A. H. Cornell-Bell. Anti-phase calcium oscillations in astrocytes via inositol (1, 4, 5)-trisphosphate regeneration. *Cell Calcium*. 2006 Mar;39(3):197-208., 2005.
120. Z. Wang, M. Tymianski, O. T. Jones, and M. Nedergaard. Impact of cytoplasmic calcium buffering on the spatial and temporal characteristics of intercellular calcium signals in astrocytes. *J. Neurosci.*, 17(19):7359–7351, 1997.
121. J. Wilkinson. *Rounding Errors in Algebraic Processes*. Prentice-Hall, Englewood Cliffs, New York, 1963.
122. S. Wollman. Local existence and uniqueness theory of the vlasov-maxwell system. *Journal of*

- Mathematical Analysis and Applications*, 127(1):103 – 121, 1987.
123. M. W. Zemansky and R. H. Dittman. *Heat and Thermodynamics*. McGraw-Hill Science/Engineering/Math, 1996.
  124. C. Lombardi. A physically based mobility model for numerical simulation of nonplanar devices. *IEEE Transactions on Computer-Aided Design*, 7:1164–1171, 1988.
  125. G. Masetti and M. Severi. Modeling of carrier mobility against carrier concentration in arsenic-, phosphorus-, and boron-doped silicon. *IEEE Transactions on Electron Devices*, 7:764–769, 1983.
  126. C. Canali. Electron and hole drift velocity measurements in silicon and their empirical relation to electric field and temperature. *IEEE Transactions on Electron Devices*, 22:1045–1047, 1975.
  127. A. Schenk. Rigorous theory and simplified model of the band-to-band tunneling in silicon. *Solid-State Electronics*, 36(1):19–34, 1993.
  128. A. G. Chynoweth. Ionization rates for electrons and holes in silicon. *Physical Review*, 109:1537–1540, 1958.
  129. R. van Overstraeten and H. de Man. Measurement of the ionization rates in diffused silicon p-n junctions. *Solid-State Electronics*, 13:583–608, 1970.
  130. Y. P. Varshni. Temperature dependence of the energy gap in semiconductors. *Physica*, 34(1):149–154, 1967.
  131. H. K. Gummel. A self-consistent iterative scheme for one-dimensional steady state transistor calculations. *Electron Devices*, pages 455–465, 1964.
  132. J. W. Jerome. *Analysis of Charge Transport*. Springer, 1996.
  133. R. Bez, E. Camerlenghi, A. Modelli, and A. Visconti *Introduction to flash memory* Proceedings of the IEEE, vol. 91, no. 4, pp. 489–502, 2003.
  134. P. Pavan, R. Bez, P. Olivo, and E. Zanoni, Flash memory cells-an overview Proceedings of the IEEE, vol. 85, no. 8, pp. 1248–1271, 1997.
  135. Y. Taur and T. H. Ning, *Fundamentals of modern VLSI devices* Cambridge university press, 2013.
  136. [http://www.itrs2.net/itrs\\_reports.html](http://www.itrs2.net/itrs_reports.html).
  137. I. Baek, M. Lee, S. Seo, M. Lee, D. Seo, D.-S. Suh, J. Park, S. Park, H. Kim, I. Yoo, et al., *Highly scalable nonvolatile resistive memory using simple binary oxide driven by asymmetric unipolar voltage pulses* Electron Devices Meeting, 2004. IEDM Technical Digest. IEEE International, pp. 587–590, IEEE, 2004.
  138. I. Baek, D. Kim, M. Lee, H.-J. Kim, E. Yim, M. Lee, J. Lee, S. Ahn, S. Seo, J. Lee, *Multi-layer cross-point binary oxide resistive memory (oxram) for post-nand storage application* IEEE International Electron Devices Meeting, 2005. IEDM Technical Digest, pp. 750–753, IEEE, 2005.
  139. S. Lai, *Current status of the phase change memory and its future* Electron Devices Meeting, 2003. IEDM’03 Technical Digest. IEEE International, pp. 10–1, IEEE, 2003.
  140. K. Wang, J. Alzate, and P. K. Amiri, *Low-power non-volatile spintronic memory: Stt-ram and beyond* Journal of Physics D: Applied Physics, vol. 46, no. 7, p. 074003, 2013.
  141. W. Koelmans, T. Bachmann, F. Zipoli, A. Ott, C. Dou, A. Ferrari, O. Cojocaru-Miredin, S. Zhang, C. Scheu, M. Wuttig, et al., *Carbon-based resistive memories* Memory Workshop (IMW), 2016 IEEE 8th International, pp. 1–4, IEEE, 2016.
  142. J. Frenkel, *On pre-breakdown phenomena in insulators and electronic semi-conductors* Physical Review 54 (8) (1938) 647.
  143. S. Manzini, *Electronic processes in silicon nitride*, Journal of Applied Physics 62 (8) (1987) 3278–3284.
  144. S. Makram-Ebeid, M. Lannoo, *Quantum model for phonon-assisted tunnel ionization of deep levels in a semiconductor* Phys. Rev. B 25 (1982) 6406–6424.
  145. P. C. Arnett, *Transient conduction in insulators at high fields* Journal of Applied Physics 46 (12) (1975) 5236–5243.
  146. A.G.Mauri et al. *Comprehensive numerical simulation of threshold-voltage transients in nitride memories* Solid-State Electronics 56 (1) (2011) 23 – 30.
  147. S. R. Ovshinsky. *Reversible electrical switching phenomena in disordered structures*. Phis. Rev. Lett. 21, 1450 (1968).
  148. H. S. P. Wong, S. Raoux, S. Kim, J. Liang, J. P. Reifenberg, B. Rajendran, M. Asheghi, K. E.

- Goodson. *Phase change memory*. Proceedings of the IEEE, 98(12), 2201-2227 (2010).
149. A. E. Owen, J. M. Robertson *Electronic conduction and switching in chalcogenide glasses*. IEEE Trans. Electron Devices, 20, 105 (1973).
  150. D. Adler, M. S. Shur, M. Silver, S. R. Ovshinsky. *Threshold switching in chalcogenide-glass thin films*. J. Appl. Phys. 51, 3289 (1980).
  151. M. Wuttig, N. Yamada. *Phase change materials for rewritable data storage*. Nature Materials, 6, 824-832 (2007).
  152. Tang, T.-Y., Cho, J.-Y., Park, Y.-J. and Joo, Y.-C. *Driving forces for elemental demixing of GeSbTe in phase-change memory: Computational study to design a durable device*. Current Applied Physics; 2013
  153. Novielli, G. *Development of physical and numerical models for mass transport in phase change materials*. Master Degree Thesis; 2013
  154. A.Pirovano, A.L. Lacaita, A. Benvenuti, F. Pellizzer, R. Bez. *Electronic switching in phase-change memories*. IEEE Transaction on Electron Devices, 51, 452-459 (2004).
  155. S. Lai, T. Lowrey. *OUM - A 180 nm nonvolatile memory cell element technology for stand alone and embedded applications*. IEEE International Electron Devices Meeting 2001.
  156. Janek, J., Korte, C. and Lidiard, A. B. *Thermodiffusion in ionic solids - model experiments and theory in book Thermal nonequilibrium phenomena in fluid mixtures*; . Springer, 2002.
  157. Novielli, G. and Ghetti, A. and Varesi, E. and Mauri, A. G. and Sacco, R. *Atomic migration in phase change materials*. Electron Devices Meeting (IEDM), 2013 IEEE International, pp 22.3.1-22.3.4
  158. D. Ielmini. *Threshold switching mechanism by high-field energy gain in the hopping transport of chalcogenide glasses*. Physical Review B, 78, 035308 (2008).
  159. I. Valov, R. Waser, J.R. Jamenson, M.N. Kozicki *Electrochemical metalization memories - fundamentals application, prospects*. nanotechnology, 22 2011.
  160. Ielmini, D. *Filamentary switching model in RRAM for time, energy and scaling projections*. IEEE IEDM Tech. Dig. 409-412, 2011.
  161. Kozicki, M. N., Gopalan, C., Balakrishnan M., Park, M., Mitkova, M. *Non-volatile memory based on solid electrolytes NVMTS*. Proc. Non-Volatile Memory Technology Symp., 10, 2004.
  162. Schindler, C., Thermadam, S. C. P., Waser, R., Kozicki, M. N. *Bipolar and unipolar resistive switching in Cu-doped SiO<sub>2</sub>*. IEEE Trans. Electron Devices, 54, 2007.
  163. Kund, M., Beitel, G., Pinnow, C. U., Rohr, T., Schumann, J., Symanczyk, R., Ufert, K. D., Muller, G. *Conductive bridging RAM (CBRAM): An emerging non-volatile memory technology scalable to sub 20nm*. IEDM Techn. Dig., 754-757, 2005.
  164. R.Waser,R. Dittman, G. Staikov, K. Szot *Redox-Based Resistive Switching Memories -Nanoionic Mechanism, Prospects and Challenges*. Adv.Material, 21, 2632-2663, 2009.
  165. A.Klein SanDisk - Flash Memory Summit. 2015.
  166. K.Parat and K.Dennison IEEE IEDM, 2015.
  167. S. M. Amoroso, C. M. Compagnoni, A. Mauri, A. Maconi, A. S. Spinelli, and A. L.Lacaita, *Semi-analytical model for the transient operation of gate-all-around charge-trap memories*. IEEE Transactions on Electron Devices, vol. 58, no. 9, pp. 3116–3123, 2011.
  168. A. Mauri, S. Amoroso, C. M. Compagnoni, A. Maconi, and A. S. Spinelli, *Comprehensive numerical simulation of threshold-voltage transients in nitride memories*. Solid-State Electronics, vol. 56, no. 1, pp. 23–30, 2011.

“Notes” — 2019/5/17 — 17:39 — page 266 — #274

1. Data Science at NIH: Big Data to Knowledge (BD2K). <https://commonfund.nih.gov/bd2k>. Accessed: 2017-01-14.
2. ICON-ESM MPI-M’s next-generation Earth system model. <https://www.mpimet.mpg.de/en/communication/news/focus-on-overview/icon-earth-system-model/>.
3. S. Aggarwal, A. Qamar, V. Sharma, and A. Sharma. Abdominal aortic aneurysm: A comprehensive review. *Experimental & Clinical Cardiology*, 16(1):11, 2011.
4. P. Airoldi, A. G. Mauri, R. Sacco, and J. W. Jerome. Three-dimensional numerical simulation of ion nanochannels. *Journal of Coupled Systems and Multiscale Dynamics*, 3(1):57–65, 2015.
5. J. E. Anderson and D. C. Chang. Using electronic health records for surgical quality improvement in the era of big data. *JAMA Surg.*, 150(1):24–29, 2015.
6. A. M. Anile and S. Pennisi. Thermodynamic derivation of the hydrodynamical model for charge transport in semiconductors. *Phys. Rev. B*, 46:13186–13193, 1992.
7. M. Armbrust, A. Fox, R. Griffith, A. D. Joseph, R. Katz, A. Konwinski, G. Lee, D. Patterson, A. Rabkin, I. Stoica, and M. Zaharia. A view of cloud computing. *Commun. ACM*, 53(4):50–58, apr 2010.
8. F. Assous, P. Degond, E. Heintze, P. Raviart, and J. Segre. On a finite-element method for solving the three-dimensional maxwell equations. *Journal of Computational Physics*, 109(2):222 – 237, 1993.
9. F. Assous, P. Degond, E. Heintze, P. Raviart, and J. Segre. On a finite-element method for solving the three-dimensional Maxwell equations. *Journal of Computational Physics*, 109(2):222 – 237, 1993.
10. I. Babuska, K.-M. Liu, and R. Tempone. Solving stochastic partial differential equations based on the experimental data. *Mathematical Models and Methods in Applied Sciences*, 13(03):415–444, 2003.
11. A. Baicus. History of polio vaccination. *World journal of virology*, 1(4):108, 2012.
12. L. Ballestra, S. Micheletti, and R. Sacco. Semiconductor device simulation using a viscous-hydrodynamic model. *Computer Methods in Applied Mechanics and Engineering*, 191(47):5447 – 5466, 2002.
13. V. Barcilon. Ion flow through narrow membrane channels: part I. *SIAM J. Appl. Math.*, 52(5):1391–1404, 1992.
14. V. Barcilon, D. Chen, R. S. Eisenberg, and J. W. Jerome. Qualitative properties of steady-state Poisson-Nernst-Planck systems: perturbation and simulation study. *SIAM J. Appl. Math.*, 57(3):631–648, 1997.
15. V. Barcilon, R. S. Eisenberg, and D. P. Chen. Ion flow through narrow membrane channels: part II. *SIAM J. Appl. Math.*, 52(5):1405–1425, 1992.
16. S. Ben G. and S. Banerjee. *Solid State electronic Devices*. New Jersey: Prentice Hall, 2000.
17. S. Bobbio and E. Gatti. *Elementi di elettromagnetismo*. Programma di mat. fisica elettronica. Bollati Boringhieri, 1984.
18. D. Boffi, F. Brezzi, and M. Fortin. *Mixed Finite Element Methods and Applications*. Springer Series in Computational Mathematics. Springer Berlin Heidelberg, 2013.
19. M. Brera, J. W. Jerome, Y. Mori, and R. Sacco. A conservative and monotone mixed-hybridized finite element approximation of transport problems in heterogeneous domains. *Computer Methods in Applied Mechanics and Engineering*, 199(41-44):2709 – 2720, 2010.
20. J. N. Bronsted. Zur theorie der chemischen reaktionsgeschwindigkeit. *Z. Phys. Chem.*, 102(2):169–207, 1922.
21. C. Cancelli and T. Pedley. A separated-flow model for collapsible-tube oscillations. *Journal of Fluid Mechanics*, 157:375–404, 1985.
22. S. Čanić, J. Tambiča, G. Guidoboni, A. Mikelić, C. J. Hartley, and D. Rosenstrauch. Modeling viscoelastic behavior of arterial walls and their interaction with pulsatile blood flow. *SIAM Journal on Applied Mathematics*, 67(1):164–193, 2006.
23. J. Caprioli and A. L. Coleman. Intraocular pressure fluctuation: a risk factor for visual field progression at low intraocular pressures in the advanced glaucoma intervention study. *Ophthalmology*, 115(7):1123–1129, 2008.

24. S. Cassani. *Blood circulation and aqueous humor flow in the eye: multi-scale modeling and clinical applications*. PhD thesis, Purdue University, 2016.
25. D. P. Chen and R. S. Eisenberg. Charges, currents, and potentials in ionic channels of one conformation. *Biophysical journal*, 64(5):1405–1421, 1993.
26. D. P. Chen and R. S. Eisenberg. Flux, coupling, and selectivity in ionic channels of one conformation. *Biophysical journal*, 65:727–746, 1993.
27. H. Cheng and W. J. Lederer. Calcium sparks. *Physiol Rev*, 88(4):1491–1545, 2008.
28. D. E. Contois. Kinetics of bacterial growth: relationship between population density and specific growth rate of continuous cultures. *J Gen Microbiol*, 1959, 21, pp 40–50, 1959.
29. G. W. De Young and J. Keizer. A single-pool inositol 1,4,5-trisphosphate-receptor-based model for agonist-stimulated oscillations in Ca<sup>2+</sup> concentration. *Proceedings of the National Academy of Sciences*, 89(20):9895–9899, 1992.
30. P. Degond and H. Neunzert. Local existence of solutions of the Vlasov-Maxwell equations and convergence to the Vlasov-Poisson equations for infinite light velocity. *Mathematical Methods in the Applied Sciences*, 8:533 – 558, 1986.
31. C. Desoer and E. Kuh. *Basic circuit theory*. McGraw Hill international editions: Electrical and electronic engineering series. McGraw-Hill, 1969.
32. R. J. Diperna and P. L. Lions. Global weak solutions of vlasov-maxwell systems. *Communications on Pure and Applied Mathematics*, 42(6):729–757, 1989.
33. P. A. M. Dirac. Quantised singularities in the electromagnetic field,. *Proceedings of the Royal Society of London A: Mathematical, Physical and Engineering Sciences*, 133(821):60–72, 1931.
34. P. A. M. Dirac. The theory of magnetic poles. *Phys. Rev.*, 74:817–830, Oct 1948.
35. B. Eisenberg, Y. Hyon, and C. Liu. Energy variational analysis of ions in water and channels: Field theory for primitive models of complex ionic fluids. *The Journal of Chemical Physics*, 133(10):104104, 2010.
36. S. I. Ellenbroek and J. Van Rheenen. Imaging hallmarks of cancer in living mice. *Nature Reviews Cancer*, 14(6):406–418, 2014.
37. A. C. Eringen. Mechanics of continua. *Huntington, NY, Robert E. Krieger Publishing Co.*, 1980. 606 p., 1, 1980.
38. G. B. Ermentrout and D. H. Terman. *Mathematical Foundations of Neuroscience*. Springer, 1st edition. edition, 2010.
39. E. Fermi and A. Scotti. *Termodinamica*. Programma di mat. fisica elettronica. Bollati Boringhieri, 1972.
40. F. Fiorani. Leonardo da vinci: Experience, experiment and design. *Renaissance Quarterly*, 61(3):921–923, 2008.
41. L. Formaggia, A. Quarteroni, and A. Veneziani, editors. *Cardiovascular Mathematics: Modeling and Simulation of the Circulatory System*. Springer-Verlag, Italy, 2009.
42. A. B. Frakt, , and S. D. Pizer. The promise and perils of big data in health care. *Am J Manag Care*, 22(2):98–99, 2016.
43. P. Fromherz. Neuroelectronics interfacing: Semiconductor chips with ion channels, nerve cells and brain. In R. Weise, editor, *Nanoelectronics and Information Technology*, pages 781–810. Wiley-VCH, Berlin, 2003.
44. V. Girault and P. Raviart. *Finite element methods for Navier-Stokes equations: theory and algorithms*. Springer series in computational mathematics. Springer-Verlag, 1986.
45. I. Gladwell. Numerical solution of ordinary differential equations (I. f. shampine). *SIAM Review*, 37(1):122–123, 1995.
46. A. E. Green and W. Zerna. *Theoretical elasticity*. Courier Corporation, 1992.
47. J. B. Grotberg and O. E. Jensen. Biofluid mechanics in flexible tubes. *Annual Review of Fluid Mechanics*, 36(1):121, 2004.
48. C. N.-T. G. S. Group et al. Comparison of glaucomatous progression between untreated patients with normal-tension glaucoma and patients with therapeutically reduced intraocular pressures. *American journal of ophthalmology*, 126(4):487–497, 1998.
49. G. Guidoboni, A. Harris, S. Cassani, J. Arciero, B. Siesky, A. Amireskandari, L. Tobe, P. Egan,

- I. Januleviciene, and J. Park. Intraocular pressure, blood pressure, and retinal blood flow autoregulation: a mathematical model to clarify their relationship and clinical relevance. *Investigative ophthalmology & visual science*, 55(7):4105–4118, 2014.
50. R. Haase. Reaction rate, activities, and affinities. *Z. Phys. Chem. Neue Folge*, 128:225–228, 1981.
  51. J. Hadfield, M. J. Plank, and T. David. Modeling secondary messenger pathways in neurovascular coupling. *Bull Math Biol.* 2013 Mar;75(3):428–43. doi: 10.1007/s11538-013-9813-x., 2013.
  52. A. Heijl, M. C. Leske, B. Bengtsson, L. Hyman, B. Bengtsson, and M. Hussein. Reduction of intraocular pressure and glaucoma progression: results from the early manifest glaucoma trial. *Archives of ophthalmology*, 120(10):1268–1279, 2002.
  53. N. Higham. *Accuracy and Stability of Numerical Algorithms*. Society for Industrial and Applied Mathematics, second edition, 2002.
  54. B. Hille. *Ionic Channels of Excitable Membranes*. Sinauer Associates, Inc., Sunderland, MA, 2001.
  55. A. Hodgkin and A. Huxley. Currents carried by sodium and potassium ions through the membrane of the giant axon of *loligo*. *Journal of Physiology*, 116:449–472, 1952.
  56. A. Hodgkin and A. Huxley. A quantitative description of membrane current and its application to conduction and excitation in nerve. *Journal of Physiology*, 117:500–544, 1952.
  57. S. A. Hughes. *Physical models and laboratory techniques in coastal engineering*, volume 7. World Scientific, 1993.
  58. G. W. Imbens and D. B. Rubin. *Causal inference in statistics, social, and biomedical sciences*. Cambridge University Press, 2015.
  59. M. Indirli, M. Forni, A. Martelli, B. Spadoni, A. Dusi, C. Alessandri, A. Bertocchi, R. Cami, A. Baratta, A. Procaccio, B. Carpani, P. Clemente, and M. Mucciarella. Development and application of innovative anti-seismic systems for the protection of cultural heritage: New achievements of ENEA. In *Conference Proceedings of the 2002 ASME-Pressure Vessel and Piping Conference, 14th International Symposium on Seismic, Shock and Vibration Isolation*, volume 2, 08 2002. Vancouver, BC, Canada, August 5–9, 2002.
  60. J. Jackson. *Classical Electrodynamics*. Wiley, 23 edition, 1998.
  61. J. W. Jerome. *Analysis of charge transport: a mathematical study of semiconductor devices*. Springer-Verlag, 1996.
  62. J. W. Jerome. Analytical approaches to charge transport in a moving medium. *Transport Theory and Statistical Physics*, 31:333–366, 2002.
  63. J. W. Jerome, B. Chini, M. Longaretti, and R. Sacco. Computational modeling and simulation of complex systems in bio-electronics. *Journal of Computational Electronics*, 7(1):10–13, 2008.
  64. J. W. Jerome and R. Sacco. Global weak solutions for an incompressible charged fluid with multi-scale couplings: Initial-boundary value problem. *Nonlinear Analysis*, 71:e2487–e2497, 2009.
  65. A. Jüngel. *Transport Equations for Semiconductors*. Springer Berlin Heidelberg, Berlin, Heidelberg, 2009.
  66. J. Keener and J. Sneyd. *Mathematical Physiology I: Cellular Physiology*. Springer, 2009.
  67. J. P. Keener and J. Sneyd. *Mathematical Physiology*. Springer, New York, 1998.
  68. J. W. Kiel, M. Hollingsworth, R. Rao, M. Chen, and H. A. Reitsamer. Ciliary blood flow and aqueous humor production. *Progress in Retinal and Eye Research*, 30(1):1 – 17, 2011.
  69. N. A. Kudryashov and I. L. Chernyavskii. Numerical simulation of the process of autoregulation of the arterial blood flow. *Izvestiya Rossiiskoi Akademii Nauk, Mekhanika Zhidkosti i Gaza*, Vol. 43, No. 1, pp. 3856., 2008.
  70. L. Landau and E. Lifshitz. *Statistical Physics*. Number v. 5 in Course of Theoretical Physics. Elsevier Science, 2013.
  71. P. D. Lax and R. D. Richtmyer. Survey of the stability of linear finite difference equations. *Comm. Pure Appl. Math.*, 9:267–293, 1956.
  72. M. C. Leske. Open-angle glaucomaan epidemiologic overview. *Ophthalmic epidemiology*, 14(4):166–172, 2007.
  73. M. C. Leske, A. Heijl, L. Hyman, B. Bengtsson, L. Dong, Z. Yang, E. Group, et al. Predictors of long-term progression in the early manifest glaucoma trial. *Ophthalmology*, 114(11):1965–1972, 2007.

74. Y.-X. Li and J. Rinzel. Equations for InsP<sub>3</sub> receptor-mediated [Ca<sup>2+</sup>]i oscillations derived from a detailed kinetic model: A Hodgkin-Huxley like formalism. *Journal of Theoretical Biology*, 166(4):461 – 473, 1994.
75. M. Longaretti, B. Chini, J. W. Jerome, and R. Sacco. Electrochemical modeling and characterization of voltage operated channels in nano-bio-electronics. *Sensor Letters*, 6(1):49–56, 2008.
76. M. Longaretti, G. Marino, B. Chini, J. W. Jerome, and R. Sacco. Computational models in nano-bioelectronics: Simulation of ionic transport in voltage operated channels. *Journal of Nanoscience and Nanotechnology*, 8(7):3686–3694, 2008.
77. M. Lundstrom. *Fundamentals of Carrier Transport, Edition 2*. University Press, Cambridge, 2009.
78. G. Magonette. Development and application of large-scale continuous pseudo-dynamic testing techniques. *Philosophical Transactions of the Royal Society of London A: Mathematical, Physical and Engineering Sciences*, 359(1786):1771–1799, 2001.
79. P. Markowich. *The Stationary Semiconductor Device Equations*. Springer-Verlag, Wien-New York, 1986.
80. P. Markowich, C. Ringhofer, and C. Schmeiser. *Semiconductor Equations*. Springer-Verlag, 1990.
81. A. G. Mauri, L. Sala, P. Airoldi, G. Novielli, R. Sacco, S. Cassani, G. Guidoboni, B. A. Siesky, and A. Harris. Electro-fluid dynamics of aqueous humor production: simulations and new directions. *Journal for Modeling in Ophthalmology*, 2:48–58, 2016.
82. J. C. Maxwell. *A Treatise on Electricity and Magnetism*:, volume 1. Cambridge University Press, Cambridge, 001 1873.
83. J. C. Maxwell. *A Treatise on Electricity and Magnetism*:, volume 2. Cambridge University Press, Cambridge, 001 1873.
84. R. A. Millikan. On the elementary electrical charge and the avogadro constant. *Phys. Rev.*, 2:109–143, Aug 1913.
85. C. B. Mills. *Designing with Models: A Studio Guide to Architectural Process Models*. John Wiley & Sons, 2011.
86. K. A. Milton. Theoretical and experimental status of magnetic monopoles. *Rept. Prog. Phys.*, 69:1637–1712, 2006.
87. G. E. Moore. Cramming more components onto integrated circuits. *Electronics*, 38(8), 1965. 4pp.
88. Y. Mori. *A Three-Dimensional Model of Cellular Electrical Activity*. PhD thesis, New York University, 2006.
89. R. Muller and T. Kamins. *Device Electronics for Integrated Circuits*. Wiley, 2002. 3rd Ed.
90. D. C. Musch, B. W. Gillespie, P. R. Lichter, L. M. Niziol, N. K. Janz, and C. S. Investigators. Visual field progression in the collaborative initial glaucoma treatment study: the impact of treatment and other baseline factors. *Ophthalmology*, 116(2):200–207, 2009.
91. not available. Ieee standard for binary floating-point arithmetic. *ANSI/IEEE Std 754-1985*, pages 0\_1–, 1985.
92. J. T. Oden, I. Babuska, F. Nobile, Y. Feng, and R. Tempone. Theory and methodology for estimation and control of errors due to modeling, approximation, and uncertainty. *Computer Methods in Applied Mechanics and Engineering*, 194(2):195 – 204, 2005.
93. J. T. Oden and S. Proudhomme. Control of modeling error in calibration and validation processes for predictive stochastic models. *International Journal for Numerical Methods in Engineering*, 87(1-5):262–272, 2011.
94. J. H. Park and J. W. Jerome. Qualitative properties of steady-state Poisson-Nernst-Planck systems: mathematical study. *SIAM J. Appl. Math.*, 57(3):609–630, 1997.
95. T. J. Pedley, B. S. Brook, and R. S. Seymour. Blood pressure and flow rate in the giraffe jugular vein. *Philosophical Transactions of the Royal Society of London B: Biological Sciences*, 351(1342):855–866, 1996.
96. M. L. Petersen and M. J. van der Laan. Causal models and learning from data: integrating causal modeling and statistical estimation. *Epidemiology (Cambridge, Mass.)*, 25(3):418, 2014.
97. R. F. Pierret and G. W. Neudeck. *Advanced Semiconductor Fundamentals*, volume 6. Prentice Hall.
98. A. Quarteroni, R. Sacco, and F. Saleri. *Numerical Mathematics*, volume 37 of *Texts in Applied Mathematics*. Springer, 2007.

99. W. V. Roosbroeck. Theory of the flow of electrons and holes in germanium and other semiconductors. *The Bell System Technical Journal*, 29:560 – 607, 1950.
100. W. V. Roosbroeck. Theory of the flow of electrons and holes in germanium and other semiconductors. *The Bell System Technical Journal*, 29(4):560–607, Oct 1950.
101. Y. Rosenfeld. Free-energy model for the inhomogeneous hard-sphere fluid mixture and density-functional theory of freezing. *Phys. Rev. Lett.*, 63:980–983, Aug 1989.
102. Y. Rosenfeld, M. Schmidt, H. Lowen, and P. Tarazona. Fundamental-measure free energy density functional theory for hard spheres: Dimensional crossover and freezing. *Phys. Rev. E*, 55:4245–4263, 1997.
103. R. Roth. Introduction to density functional theory of classical systems: Theory and applications. Lecture Notes, November 2006. ITAP, Universitaet Stuttgart and Max-Planck-Institut fur Metallforschung, Stuttgart Germany.
104. R. Roth, R. Evans, A. Lang, and G. Kahl. Fundamental measure theory for hard-sphere mixtures revisited: the white bear version. *Journal of Physics: Condensed Matter*, 14(46):12063, 2002.
105. I. Rubinstein. *Electrodiffusion of Ions*. SIAM, Philadelphia, PA, 1990.
106. I. Rubinstein. *Electrodiffusion of Ions*. SIAM, 1990.
107. M. Ruiz Estrada, S. Lai, and M. Umemoto. A simulation of a mega-earthquake in Malaysia: Kuala Lumpur and Penang area. 05 2018.
108. R. Sacco, P. Airoldi, A. G. Mauri, and J. W. Jerome. Three-dimensional simulation of biological ion channels under mechanical, thermal and fluid forces. *Applied Mathematical Modelling*, 43:221 – 251, 2017.
109. R. Sacco, F. Mangani, and J. W. Jerome. Modeling and simulation of thermo-fluid-electrochemical ion flow in biological channels. *Mol. Based Math. Biol.*, 3:78–111, 2015.
110. L. Sala, F. Salerni, and M. Szopos. Mathematical modeling of the cerebrospinal fluid flow and its interactions. In G. Guidoboni, A. Harris, and R. Sacco, editors, *Mathematical Modeling of Ocular Fluid Dynamics: From Theory to Clinical Applications*, Modeling and Simulation in Science, Engineering, and Technology. Springer-Birkhauser (New York), 2018.
111. M. Schmuck. Analysis of the Navier-Stokes-Nernst-Planck-Poisson system. *Mathematical Models and Methods in Applied Sciences*, 19(6):993–1015, 2009.
112. G. Scovazzi and T. J. R. Hughes. Lecture notes on continuum mechanics on arbitrary moving domains. Technical report, Sandia National Laboratories, 2007. Report 2007-6312P.
113. S. Selberherr. *Analysis and Simulation of Semiconductor Devices*. Springer-Verlag, 1984.
114. A. H. Shapiro. Steady flow in collapsible tubes. *Journal of Biomechanical Engineering*, 99(3):126–147, 1977.
115. B. Siesky, A. Harris, N. Kheradiya, C. Rospigliosi, L. McCranor, and R. Ehrich. The clinical significance of vascular factors in glaucoma. *Journal of Current Glaucoma Practice*, 2:12–17, 2007.
116. R. D. Simoni, R. L. Hill, and M. Vaughan. The discovery of insulin: the work of frederick banting and charles best. *Journal of Biological Chemistry*, 277(26):e15–e15, 2002.
117. Y.-C. Tham, S.-H. Lim, P. Gupta, T. Aung, T. Y. Wong, and C.-Y. Cheng. Inter-relationship between ocular perfusion pressure, blood pressure, intraocular pressure profiles and primary open-angle glaucoma: the singapore epidemiology of eye diseases study. *British Journal of Ophthalmology*, pages bjophthalmol–2017, 2018.
118. C. Truesdell. A first course in rational continuum mechanics. *Pure and applied mathematics*, 71:3–375, 1991.
119. G. Ullah, P. Jung, and A. H. Cornell-Bell. Anti-phase calcium oscillations in astrocytes via inositol (1, 4, 5)-trisphosphate regeneration. *Cell Calcium*. 2006 Mar;39(3):197-208., 2005.
120. Z. Wang, M. Tymianski, O. T. Jones, and M. Nedergaard. Impact of cytoplasmic calcium buffering on the spatial and temporal characteristics of intercellular calcium signals in astrocytes. *J. Neurosci.*, 17(19):7359–7351, 1997.
121. J. Wilkinson. *Rounding Errors in Algebraic Processes*. Prentice-Hall, Englewood Cliffs, New York, 1963.
122. S. Wollman. Local existence and uniqueness theory of the vlasov-maxwell system. *Journal of*

- Mathematical Analysis and Applications*, 127(1):103 – 121, 1987.
123. M. W. Zemansky and R. H. Dittman. *Heat and Thermodynamics*. McGraw-Hill Science/Engineering/Math, 1996.
  124. C. Lombardi. A physically based mobility model for numerical simulation of nonplanar devices. *IEEE Transactions on Computer-Aided Design*, 7:1164–1171, 1988.
  125. G. Masetti and M. Severi. Modeling of carrier mobility against carrier concentration in arsenic-, phosphorus-, and boron-doped silicon. *IEEE Transactions on Electron Devices*, 7:764–769, 1983.
  126. C. Canali. Electron and hole drift velocity measurements in silicon and their empirical relation to electric field and temperature. *IEEE Transactions on Electron Devices*, 22:1045–1047, 1975.
  127. A. Schenk. Rigorous theory and simplified model of the band-to-band tunneling in silicon. *Solid-State Electronics*, 36(1):19–34, 1993.
  128. A. G. Chynoweth. Ionization rates for electrons and holes in silicon. *Physical Review*, 109:1537–1540, 1958.
  129. R. van Overstraeten and H. de Man. Measurement of the ionization rates in diffused silicon p-n junctions. *Solid-State Electronics*, 13:583–608, 1970.
  130. Y. P. Varshni. Temperature dependence of the energy gap in semiconductors. *Physica*, 34(1):149–154, 1967.
  131. H. K. Gummel. A self-consistent iterative scheme for one-dimensional steady state transistor calculations. *Electron Devices*, pages 455–465, 1964.
  132. J. W. Jerome. *Analysis of Charge Transport*. Springer, 1996.
  133. R. Bez, E. Camerlenghi, A. Modelli, and A. Visconti *Introduction to flash memory* Proceedings of the IEEE, vol. 91, no. 4, pp. 489–502, 2003.
  134. P. Pavan, R. Bez, P. Olivo, and E. Zanoni, Flash memory cells-an overview Proceedings of the IEEE, vol. 85, no. 8, pp. 1248–1271, 1997.
  135. Y. Taur and T. H. Ning, *Fundamentals of modern VLSI devices* Cambridge university press, 2013.
  136. [http://www.itrs2.net/itrs\\_reports.html](http://www.itrs2.net/itrs_reports.html).
  137. I. Baek, M. Lee, S. Seo, M. Lee, D. Seo, D.-S. Suh, J. Park, S. Park, H. Kim, I. Yoo, et al., *Highly scalable nonvolatile resistive memory using simple binary oxide driven by asymmetric unipolar voltage pulses* Electron Devices Meeting, 2004. IEDM Technical Digest. IEEE International, pp. 587–590, IEEE, 2004.
  138. I. Baek, D. Kim, M. Lee, H.-J. Kim, E. Yim, M. Lee, J. Lee, S. Ahn, S. Seo, J. Lee, *Multi-layer cross-point binary oxide resistive memory (oxram) for post-nand storage application* IEEE International Electron Devices Meeting, 2005. IEDM Technical Digest, pp. 750–753, IEEE, 2005.
  139. S. Lai, *Current status of the phase change memory and its future* Electron Devices Meeting, 2003. IEDM’03 Technical Digest. IEEE International, pp. 10–1, IEEE, 2003.
  140. K. Wang, J. Alzate, and P. K. Amiri, *Low-power non-volatile spintronic memory: Stt-ram and beyond* Journal of Physics D: Applied Physics, vol. 46, no. 7, p. 074003, 2013.
  141. W. Koelmans, T. Bachmann, F. Zipoli, A. Ott, C. Dou, A. Ferrari, O. Cojocaru-Miredin, S. Zhang, C. Scheu, M. Wuttig, et al., *Carbon-based resistive memories* Memory Workshop (IMW), 2016 IEEE 8th International, pp. 1–4, IEEE, 2016.
  142. J. Frenkel, *On pre-breakdown phenomena in insulators and electronic semi-conductors* Physical Review 54 (8) (1938) 647.
  143. S. Manzini, *Electronic processes in silicon nitride*, Journal of Applied Physics 62 (8) (1987) 3278–3284.
  144. S. Makram-Ebeid, M. Lannoo, *Quantum model for phonon-assisted tunnel ionization of deep levels in a semiconductor* Phys. Rev. B 25 (1982) 6406–6424.
  145. P. C. Arnett, *Transient conduction in insulators at high fields* Journal of Applied Physics 46 (12) (1975) 5236–5243.
  146. A.G.Mauri et al. *Comprehensive numerical simulation of threshold-voltage transients in nitride memories* Solid-State Electronics 56 (1) (2011) 23 – 30.
  147. S. R. Ovshinsky. *Reversible electrical switching phenomena in disordered structures*. Phis. Rev. Lett. 21, 1450 (1968).
  148. H. S. P. Wong, S. Raoux, S. Kim, J. Liang, J. P. Reifenberg, B. Rajendran, M. Asheghi, K. E.

- Goodson. *Phase change memory*. Proceedings of the IEEE, 98(12), 2201-2227 (2010).
149. A. E. Owen, J. M. Robertson *Electronic conduction and switching in chalcogenide glasses*. IEEE Trans. Electron Devices, 20, 105 (1973).
  150. D. Adler, M. S. Shur, M. Silver, S. R. Ovshinsky. *Threshold switching in chalcogenide-glass thin films*. J. Appl. Phys. 51, 3289 (1980).
  151. M. Wuttig, N. Yamada. *Phase change materials for rewritable data storage*. Nature Materials, 6, 824-832 (2007).
  152. Tang, T.-Y., Cho, J.-Y., Park, Y.-J. and Joo, Y.-C. *Driving forces for elemental demixing of GeSbTe in phase-change memory: Computational study to design a durable device*. Current Applied Physics; 2013
  153. Novielli, G. *Development of physical and numerical models for mass transport in phase change materials*. Master Degree Thesis; 2013
  154. A.Pirovano, A.L. Lacaita, A. Benvenuti, F. Pellizzer, R. Bez. *Electronic switching in phase-change memories*. IEEE Transaction on Electron Devices, 51, 452-459 (2004).
  155. S. Lai, T. Lowrey. *OUM - A 180 nm nonvolatile memory cell element technology for stand alone and embedded applications*. IEEE International Electron Devices Meeting 2001.
  156. Janek, J., Korte, C. and Lidiard, A. B. *Thermodiffusion in ionic solids - model experiments and theory in book Thermal nonequilibrium phenomena in fluid mixtures*; . Springer, 2002.
  157. Novielli, G. and Ghetti, A. and Varesi, E. and Mauri, A. G. and Sacco, R. *Atomic migration in phase change materials*. Electron Devices Meeting (IEDM), 2013 IEEE International, pp 22.3.1-22.3.4
  158. D. Ielmini. *Threshold switching mechanism by high-field energy gain in the hopping transport of chalcogenide glasses*. Physical Review B, 78, 035308 (2008).
  159. I. Valov, R. Waser, J.R. Jamenson, M.N. Kozicki *Electrochemical metalization memories - fundamentals application, prospects*. nanotechnology, 22 2011.
  160. Ielmini, D. *Filamentary switching model in RRAM for time, energy and scaling projections*. IEEE IEDM Tech. Dig. 409-412, 2011.
  161. Kozicki, M. N., Gopalan, C., Balakrishnan M., Park, M., Mitkova, M. *Non-volatile memory based on solid electrolytes NVMTS*. Proc. Non-Volatile Memory Technology Symp., 10, 2004.
  162. Schindler, C., Thermadam, S. C. P., Waser, R., Kozicki, M. N. *Bipolar and unipolar resistive switching in Cu-doped SiO<sub>2</sub>*. IEEE Trans. Electron Devices, 54, 2007.
  163. Kund, M., Beitel, G., Pinnow, C. U., Rohr, T., Schumann, J., Symanczyk, R., Ufert, K. D., Muller, G. *Conductive bridging RAM (CBRAM): An emerging non-volatile memory technology scalable to sub 20nm*. IEDM Techn. Dig., 754-757, 2005.
  164. R.Waser,R. Dittman, G. Staikov, K. Szot *Redox-Based Resistive Switching Memories -Nanoionic Mechanism, Prospects and Challenges*. Adv.Material, 21, 2632-2663, 2009.
  165. A.Klein SanDisk - Flash Memory Summit. 2015.
  166. K.Parat and K.Dennison IEEE IEDM, 2015.
  167. S. M. Amoroso, C. M. Compagnoni, A. Mauri, A. Maconi, A. S. Spinelli, and A. L.Lacaita, *Semi-analytical model for the transient operation of gate-all-around charge-trap memories*. IEEE Transactions on Electron Devices, vol. 58, no. 9, pp. 3116–3123, 2011.
  168. A. Mauri, S. Amoroso, C. M. Compagnoni, A. Maconi, and A. S. Spinelli, *Comprehensive numerical simulation of threshold-voltage transients in nitride memories*. Solid-State Electronics, vol. 56, no. 1, pp. 23–30, 2011.

“Notes” — 2019/5/17 — 17:39 — page 274 — #282

1. Data Science at NIH: Big Data to Knowledge (BD2K). <https://commonfund.nih.gov/bd2k>. Accessed: 2017-01-14.
2. ICON-ESM MPI-M’s next-generation Earth system model. <https://www.mpimet.mpg.de/en/communication/news/focus-on-overview/icon-earth-system-model/>.
3. S. Aggarwal, A. Qamar, V. Sharma, and A. Sharma. Abdominal aortic aneurysm: A comprehensive review. *Experimental & Clinical Cardiology*, 16(1):11, 2011.
4. P. Airoldi, A. G. Mauri, R. Sacco, and J. W. Jerome. Three-dimensional numerical simulation of ion nanochannels. *Journal of Coupled Systems and Multiscale Dynamics*, 3(1):57–65, 2015.
5. J. E. Anderson and D. C. Chang. Using electronic health records for surgical quality improvement in the era of big data. *JAMA Surg.*, 150(1):24–29, 2015.
6. A. M. Anile and S. Pennisi. Thermodynamic derivation of the hydrodynamical model for charge transport in semiconductors. *Phys. Rev. B*, 46:13186–13193, 1992.
7. M. Armbrust, A. Fox, R. Griffith, A. D. Joseph, R. Katz, A. Konwinski, G. Lee, D. Patterson, A. Rabkin, I. Stoica, and M. Zaharia. A view of cloud computing. *Commun. ACM*, 53(4):50–58, apr 2010.
8. F. Assous, P. Degond, E. Heintze, P. Raviart, and J. Segre. On a finite-element method for solving the three-dimensional maxwell equations. *Journal of Computational Physics*, 109(2):222 – 237, 1993.
9. F. Assous, P. Degond, E. Heintze, P. Raviart, and J. Segre. On a finite-element method for solving the three-dimensional Maxwell equations. *Journal of Computational Physics*, 109(2):222 – 237, 1993.
10. I. Babuska, K.-M. Liu, and R. Tempone. Solving stochastic partial differential equations based on the experimental data. *Mathematical Models and Methods in Applied Sciences*, 13(03):415–444, 2003.
11. A. Baicus. History of polio vaccination. *World journal of virology*, 1(4):108, 2012.
12. L. Ballestra, S. Micheletti, and R. Sacco. Semiconductor device simulation using a viscous-hydrodynamic model. *Computer Methods in Applied Mechanics and Engineering*, 191(47):5447 – 5466, 2002.
13. V. Barcilon. Ion flow through narrow membrane channels: part I. *SIAM J. Appl. Math.*, 52(5):1391–1404, 1992.
14. V. Barcilon, D. Chen, R. S. Eisenberg, and J. W. Jerome. Qualitative properties of steady-state Poisson-Nernst-Planck systems: perturbation and simulation study. *SIAM J. Appl. Math.*, 57(3):631–648, 1997.
15. V. Barcilon, R. S. Eisenberg, and D. P. Chen. Ion flow through narrow membrane channels: part II. *SIAM J. Appl. Math.*, 52(5):1405–1425, 1992.
16. S. Ben G. and S. Banerjee. *Solid State electronic Devices*. New Jersey: Prentice Hall, 2000.
17. S. Bobbio and E. Gatti. *Elementi di elettromagnetismo*. Programma di mat. fisica elettronica. Bollati Boringhieri, 1984.
18. D. Boffi, F. Brezzi, and M. Fortin. *Mixed Finite Element Methods and Applications*. Springer Series in Computational Mathematics. Springer Berlin Heidelberg, 2013.
19. M. Brera, J. W. Jerome, Y. Mori, and R. Sacco. A conservative and monotone mixed-hybridized finite element approximation of transport problems in heterogeneous domains. *Computer Methods in Applied Mechanics and Engineering*, 199(41-44):2709 – 2720, 2010.
20. J. N. Bronsted. Zur theorie der chemischen reaktionsgeschwindigkeit. *Z. Phys. Chem.*, 102(2):169–207, 1922.
21. C. Cancelli and T. Pedley. A separated-flow model for collapsible-tube oscillations. *Journal of Fluid Mechanics*, 157:375–404, 1985.
22. S. Čanić, J. Tambiča, G. Guidoboni, A. Mikelić, C. J. Hartley, and D. Rosenstrauch. Modeling viscoelastic behavior of arterial walls and their interaction with pulsatile blood flow. *SIAM Journal on Applied Mathematics*, 67(1):164–193, 2006.
23. J. Caprioli and A. L. Coleman. Intraocular pressure fluctuation: a risk factor for visual field progression at low intraocular pressures in the advanced glaucoma intervention study. *Ophthalmology*, 115(7):1123–1129, 2008.

24. S. Cassani. *Blood circulation and aqueous humor flow in the eye: multi-scale modeling and clinical applications*. PhD thesis, Purdue University, 2016.
25. D. P. Chen and R. S. Eisenberg. Charges, currents, and potentials in ionic channels of one conformation. *Biophysical journal*, 64(5):1405–1421, 1993.
26. D. P. Chen and R. S. Eisenberg. Flux, coupling, and selectivity in ionic channels of one conformation. *Biophysical journal*, 65:727–746, 1993.
27. H. Cheng and W. J. Lederer. Calcium sparks. *Physiol Rev*, 88(4):1491–1545, 2008.
28. D. E. Contois. Kinetics of bacterial growth: relationship between population density and specific growth rate of continuous cultures. *J Gen Microbiol*, 1959, 21, pp 40–50, 1959.
29. G. W. De Young and J. Keizer. A single-pool inositol 1,4,5-trisphosphate-receptor-based model for agonist-stimulated oscillations in Ca<sup>2+</sup> concentration. *Proceedings of the National Academy of Sciences*, 89(20):9895–9899, 1992.
30. P. Degond and H. Neunzert. Local existence of solutions of the Vlasov-Maxwell equations and convergence to the Vlasov-Poisson equations for infinite light velocity. *Mathematical Methods in the Applied Sciences*, 8:533 – 558, 1986.
31. C. Desoer and E. Kuh. *Basic circuit theory*. McGraw Hill international editions: Electrical and electronic engineering series. McGraw-Hill, 1969.
32. R. J. Diperna and P. L. Lions. Global weak solutions of vlasov-maxwell systems. *Communications on Pure and Applied Mathematics*, 42(6):729–757, 1989.
33. P. A. M. Dirac. Quantised singularities in the electromagnetic field,. *Proceedings of the Royal Society of London A: Mathematical, Physical and Engineering Sciences*, 133(821):60–72, 1931.
34. P. A. M. Dirac. The theory of magnetic poles. *Phys. Rev.*, 74:817–830, Oct 1948.
35. B. Eisenberg, Y. Hyon, and C. Liu. Energy variational analysis of ions in water and channels: Field theory for primitive models of complex ionic fluids. *The Journal of Chemical Physics*, 133(10):104104, 2010.
36. S. I. Ellenbroek and J. Van Rheenen. Imaging hallmarks of cancer in living mice. *Nature Reviews Cancer*, 14(6):406–418, 2014.
37. A. C. Eringen. Mechanics of continua. *Huntington, NY, Robert E. Krieger Publishing Co.*, 1980. 606 p., 1, 1980.
38. G. B. Ermentrout and D. H. Terman. *Mathematical Foundations of Neuroscience*. Springer, 1st edition. edition, 2010.
39. E. Fermi and A. Scotti. *Termodinamica*. Programma di mat. fisica elettronica. Bollati Boringhieri, 1972.
40. F. Fiorani. Leonardo da vinci: Experience, experiment and design. *Renaissance Quarterly*, 61(3):921–923, 2008.
41. L. Formaggia, A. Quarteroni, and A. Veneziani, editors. *Cardiovascular Mathematics: Modeling and Simulation of the Circulatory System*. Springer-Verlag, Italy, 2009.
42. A. B. Frakt, , and S. D. Pizer. The promise and perils of big data in health care. *Am J Manag Care*, 22(2):98–99, 2016.
43. P. Fromherz. Neuroelectronics interfacing: Semiconductor chips with ion channels, nerve cells and brain. In R. Weise, editor, *Nanoelectronics and Information Technology*, pages 781–810. Wiley-VCH, Berlin, 2003.
44. V. Girault and P. Raviart. *Finite element methods for Navier-Stokes equations: theory and algorithms*. Springer series in computational mathematics. Springer-Verlag, 1986.
45. I. Gladwell. Numerical solution of ordinary differential equations (I. f. shampine). *SIAM Review*, 37(1):122–123, 1995.
46. A. E. Green and W. Zerna. *Theoretical elasticity*. Courier Corporation, 1992.
47. J. B. Grotberg and O. E. Jensen. Biofluid mechanics in flexible tubes. *Annual Review of Fluid Mechanics*, 36(1):121, 2004.
48. C. N.-T. G. S. Group et al. Comparison of glaucomatous progression between untreated patients with normal-tension glaucoma and patients with therapeutically reduced intraocular pressures. *American journal of ophthalmology*, 126(4):487–497, 1998.
49. G. Guidoboni, A. Harris, S. Cassani, J. Arciero, B. Siesky, A. Amireskandari, L. Tobe, P. Egan,

- I. Januleviciene, and J. Park. Intraocular pressure, blood pressure, and retinal blood flow autoregulation: a mathematical model to clarify their relationship and clinical relevance. *Investigative ophthalmology & visual science*, 55(7):4105–4118, 2014.
50. R. Haase. Reaction rate, activities, and affinities. *Z. Phys. Chem. Neue Folge*, 128:225–228, 1981.
  51. J. Hadfield, M. J. Plank, and T. David. Modeling secondary messenger pathways in neurovascular coupling. *Bull Math Biol.* 2013 Mar;75(3):428–43. doi: 10.1007/s11538-013-9813-x., 2013.
  52. A. Heijl, M. C. Leske, B. Bengtsson, L. Hyman, B. Bengtsson, and M. Hussein. Reduction of intraocular pressure and glaucoma progression: results from the early manifest glaucoma trial. *Archives of ophthalmology*, 120(10):1268–1279, 2002.
  53. N. Higham. *Accuracy and Stability of Numerical Algorithms*. Society for Industrial and Applied Mathematics, second edition, 2002.
  54. B. Hille. *Ionic Channels of Excitable Membranes*. Sinauer Associates, Inc., Sunderland, MA, 2001.
  55. A. Hodgkin and A. Huxley. Currents carried by sodium and potassium ions through the membrane of the giant axon of *loligo*. *Journal of Physiology*, 116:449–472, 1952.
  56. A. Hodgkin and A. Huxley. A quantitative description of membrane current and its application to conduction and excitation in nerve. *Journal of Physiology*, 117:500–544, 1952.
  57. S. A. Hughes. *Physical models and laboratory techniques in coastal engineering*, volume 7. World Scientific, 1993.
  58. G. W. Imbens and D. B. Rubin. *Causal inference in statistics, social, and biomedical sciences*. Cambridge University Press, 2015.
  59. M. Indirli, M. Forni, A. Martelli, B. Spadoni, A. Dusi, C. Alessandri, A. Bertocchi, R. Cami, A. Baratta, A. Procaccio, B. Carpani, P. Clemente, and M. Mucciarella. Development and application of innovative anti-seismic systems for the protection of cultural heritage: New achievements of ENEA. In *Conference Proceedings of the 2002 ASME-Pressure Vessel and Piping Conference, 14th International Symposium on Seismic, Shock and Vibration Isolation*, volume 2, 08 2002. Vancouver, BC, Canada, August 5–9, 2002.
  60. J. Jackson. *Classical Electrodynamics*. Wiley, 23 edition, 1998.
  61. J. W. Jerome. *Analysis of charge transport: a mathematical study of semiconductor devices*. Springer-Verlag, 1996.
  62. J. W. Jerome. Analytical approaches to charge transport in a moving medium. *Transport Theory and Statistical Physics*, 31:333–366, 2002.
  63. J. W. Jerome, B. Chini, M. Longaretti, and R. Sacco. Computational modeling and simulation of complex systems in bio-electronics. *Journal of Computational Electronics*, 7(1):10–13, 2008.
  64. J. W. Jerome and R. Sacco. Global weak solutions for an incompressible charged fluid with multi-scale couplings: Initial-boundary value problem. *Nonlinear Analysis*, 71:e2487–e2497, 2009.
  65. A. Jüngel. *Transport Equations for Semiconductors*. Springer Berlin Heidelberg, Berlin, Heidelberg, 2009.
  66. J. Keener and J. Sneyd. *Mathematical Physiology I: Cellular Physiology*. Springer, 2009.
  67. J. P. Keener and J. Sneyd. *Mathematical Physiology*. Springer, New York, 1998.
  68. J. W. Kiel, M. Hollingsworth, R. Rao, M. Chen, and H. A. Reitsamer. Ciliary blood flow and aqueous humor production. *Progress in Retinal and Eye Research*, 30(1):1 – 17, 2011.
  69. N. A. Kudryashov and I. L. Chernyavskii. Numerical simulation of the process of autoregulation of the arterial blood flow. *Izvestiya Rossiiskoi Akademii Nauk, Mekhanika Zhidkosti i Gaza*, Vol. 43, No. 1, pp. 3856., 2008.
  70. L. Landau and E. Lifshitz. *Statistical Physics*. Number v. 5 in Course of Theoretical Physics. Elsevier Science, 2013.
  71. P. D. Lax and R. D. Richtmyer. Survey of the stability of linear finite difference equations. *Comm. Pure Appl. Math.*, 9:267–293, 1956.
  72. M. C. Leske. Open-angle glaucomaan epidemiologic overview. *Ophthalmic epidemiology*, 14(4):166–172, 2007.
  73. M. C. Leske, A. Heijl, L. Hyman, B. Bengtsson, L. Dong, Z. Yang, E. Group, et al. Predictors of long-term progression in the early manifest glaucoma trial. *Ophthalmology*, 114(11):1965–1972, 2007.

74. Y.-X. Li and J. Rinzel. Equations for InsP<sub>3</sub> receptor-mediated [Ca<sup>2+</sup>]i oscillations derived from a detailed kinetic model: A Hodgkin-Huxley like formalism. *Journal of Theoretical Biology*, 166(4):461 – 473, 1994.
75. M. Longaretti, B. Chini, J. W. Jerome, and R. Sacco. Electrochemical modeling and characterization of voltage operated channels in nano-bio-electronics. *Sensor Letters*, 6(1):49–56, 2008.
76. M. Longaretti, G. Marino, B. Chini, J. W. Jerome, and R. Sacco. Computational models in nano-bioelectronics: Simulation of ionic transport in voltage operated channels. *Journal of Nanoscience and Nanotechnology*, 8(7):3686–3694, 2008.
77. M. Lundstrom. *Fundamentals of Carrier Transport, Edition 2*. University Press, Cambridge, 2009.
78. G. Magonette. Development and application of large-scale continuous pseudo-dynamic testing techniques. *Philosophical Transactions of the Royal Society of London A: Mathematical, Physical and Engineering Sciences*, 359(1786):1771–1799, 2001.
79. P. Markowich. *The Stationary Semiconductor Device Equations*. Springer-Verlag, Wien-New York, 1986.
80. P. Markowich, C. Ringhofer, and C. Schmeiser. *Semiconductor Equations*. Springer-Verlag, 1990.
81. A. G. Mauri, L. Sala, P. Airoldi, G. Novielli, R. Sacco, S. Cassani, G. Guidoboni, B. A. Siesky, and A. Harris. Electro-fluid dynamics of aqueous humor production: simulations and new directions. *Journal for Modeling in Ophthalmology*, 2:48–58, 2016.
82. J. C. Maxwell. *A Treatise on Electricity and Magnetism*:, volume 1. Cambridge University Press, Cambridge, 001 1873.
83. J. C. Maxwell. *A Treatise on Electricity and Magnetism*:, volume 2. Cambridge University Press, Cambridge, 001 1873.
84. R. A. Millikan. On the elementary electrical charge and the avogadro constant. *Phys. Rev.*, 2:109–143, Aug 1913.
85. C. B. Mills. *Designing with Models: A Studio Guide to Architectural Process Models*. John Wiley & Sons, 2011.
86. K. A. Milton. Theoretical and experimental status of magnetic monopoles. *Rept. Prog. Phys.*, 69:1637–1712, 2006.
87. G. E. Moore. Cramming more components onto integrated circuits. *Electronics*, 38(8), 1965. 4pp.
88. Y. Mori. *A Three-Dimensional Model of Cellular Electrical Activity*. PhD thesis, New York University, 2006.
89. R. Muller and T. Kamins. *Device Electronics for Integrated Circuits*. Wiley, 2002. 3rd Ed.
90. D. C. Musch, B. W. Gillespie, P. R. Lichter, L. M. Niziol, N. K. Janz, and C. S. Investigators. Visual field progression in the collaborative initial glaucoma treatment study: the impact of treatment and other baseline factors. *Ophthalmology*, 116(2):200–207, 2009.
91. not available. Ieee standard for binary floating-point arithmetic. *ANSI/IEEE Std 754-1985*, pages 0\_1–, 1985.
92. J. T. Oden, I. Babuska, F. Nobile, Y. Feng, and R. Tempone. Theory and methodology for estimation and control of errors due to modeling, approximation, and uncertainty. *Computer Methods in Applied Mechanics and Engineering*, 194(2):195 – 204, 2005.
93. J. T. Oden and S. Proudhomme. Control of modeling error in calibration and validation processes for predictive stochastic models. *International Journal for Numerical Methods in Engineering*, 87(1-5):262–272, 2011.
94. J. H. Park and J. W. Jerome. Qualitative properties of steady-state Poisson-Nernst-Planck systems: mathematical study. *SIAM J. Appl. Math.*, 57(3):609–630, 1997.
95. T. J. Pedley, B. S. Brook, and R. S. Seymour. Blood pressure and flow rate in the giraffe jugular vein. *Philosophical Transactions of the Royal Society of London B: Biological Sciences*, 351(1342):855–866, 1996.
96. M. L. Petersen and M. J. van der Laan. Causal models and learning from data: integrating causal modeling and statistical estimation. *Epidemiology (Cambridge, Mass.)*, 25(3):418, 2014.
97. R. F. Pierret and G. W. Neudeck. *Advanced Semiconductor Fundamentals*, volume 6. Prentice Hall.
98. A. Quarteroni, R. Sacco, and F. Saleri. *Numerical Mathematics*, volume 37 of *Texts in Applied Mathematics*. Springer, 2007.

99. W. V. Roosbroeck. Theory of the flow of electrons and holes in germanium and other semiconductors. *The Bell System Technical Journal*, 29:560 – 607, 1950.
100. W. V. Roosbroeck. Theory of the flow of electrons and holes in germanium and other semiconductors. *The Bell System Technical Journal*, 29(4):560–607, Oct 1950.
101. Y. Rosenfeld. Free-energy model for the inhomogeneous hard-sphere fluid mixture and density-functional theory of freezing. *Phys. Rev. Lett.*, 63:980–983, Aug 1989.
102. Y. Rosenfeld, M. Schmidt, H. Lowen, and P. Tarazona. Fundamental-measure free energy density functional theory for hard spheres: Dimensional crossover and freezing. *Phys. Rev. E*, 55:4245–4263, 1997.
103. R. Roth. Introduction to density functional theory of classical systems: Theory and applications. Lecture Notes, November 2006. ITAP, Universitaet Stuttgart and Max-Planck-Institut fur Metallforschung, Stuttgart Germany.
104. R. Roth, R. Evans, A. Lang, and G. Kahl. Fundamental measure theory for hard-sphere mixtures revisited: the white bear version. *Journal of Physics: Condensed Matter*, 14(46):12063, 2002.
105. I. Rubinstein. *Electrodiffusion of Ions*. SIAM, Philadelphia, PA, 1990.
106. I. Rubinstein. *Electrodiffusion of Ions*. SIAM, 1990.
107. M. Ruiz Estrada, S. Lai, and M. Umemoto. A simulation of a mega-earthquake in Malaysia: Kuala Lumpur and Penang area. 05 2018.
108. R. Sacco, P. Airoldi, A. G. Mauri, and J. W. Jerome. Three-dimensional simulation of biological ion channels under mechanical, thermal and fluid forces. *Applied Mathematical Modelling*, 43:221 – 251, 2017.
109. R. Sacco, F. Mangani, and J. W. Jerome. Modeling and simulation of thermo-fluid-electrochemical ion flow in biological channels. *Mol. Based Math. Biol.*, 3:78–111, 2015.
110. L. Sala, F. Salerni, and M. Szopos. Mathematical modeling of the cerebrospinal fluid flow and its interactions. In G. Guidoboni, A. Harris, and R. Sacco, editors, *Mathematical Modeling of Ocular Fluid Dynamics: From Theory to Clinical Applications*, Modeling and Simulation in Science, Engineering, and Technology. Springer-Birkhauser (New York), 2018.
111. M. Schmuck. Analysis of the Navier-Stokes-Nernst-Planck-Poisson system. *Mathematical Models and Methods in Applied Sciences*, 19(6):993–1015, 2009.
112. G. Scovazzi and T. J. R. Hughes. Lecture notes on continuum mechanics on arbitrary moving domains. Technical report, Sandia National Laboratories, 2007. Report 2007-6312P.
113. S. Selberherr. *Analysis and Simulation of Semiconductor Devices*. Springer-Verlag, 1984.
114. A. H. Shapiro. Steady flow in collapsible tubes. *Journal of Biomechanical Engineering*, 99(3):126–147, 1977.
115. B. Siesky, A. Harris, N. Kheradiya, C. Rospigliosi, L. McCranor, and R. Ehrich. The clinical significance of vascular factors in glaucoma. *Journal of Current Glaucoma Practice*, 2:12–17, 2007.
116. R. D. Simoni, R. L. Hill, and M. Vaughan. The discovery of insulin: the work of frederick banting and charles best. *Journal of Biological Chemistry*, 277(26):e15–e15, 2002.
117. Y.-C. Tham, S.-H. Lim, P. Gupta, T. Aung, T. Y. Wong, and C.-Y. Cheng. Inter-relationship between ocular perfusion pressure, blood pressure, intraocular pressure profiles and primary open-angle glaucoma: the singapore epidemiology of eye diseases study. *British Journal of Ophthalmology*, pages bjophthalmol–2017, 2018.
118. C. Truesdell. A first course in rational continuum mechanics. *Pure and applied mathematics*, 71:3–375, 1991.
119. G. Ullah, P. Jung, and A. H. Cornell-Bell. Anti-phase calcium oscillations in astrocytes via inositol (1, 4, 5)-trisphosphate regeneration. *Cell Calcium*. 2006 Mar;39(3):197-208., 2005.
120. Z. Wang, M. Tymianski, O. T. Jones, and M. Nedergaard. Impact of cytoplasmic calcium buffering on the spatial and temporal characteristics of intercellular calcium signals in astrocytes. *J. Neurosci.*, 17(19):7359–7351, 1997.
121. J. Wilkinson. *Rounding Errors in Algebraic Processes*. Prentice-Hall, Englewood Cliffs, New York, 1963.
122. S. Wollman. Local existence and uniqueness theory of the vlasov-maxwell system. *Journal of*

- Mathematical Analysis and Applications*, 127(1):103 – 121, 1987.
123. M. W. Zemansky and R. H. Dittman. *Heat and Thermodynamics*. McGraw-Hill Science/Engineering/Math, 1996.
  124. C. Lombardi. A physically based mobility model for numerical simulation of nonplanar devices. *IEEE Transactions on Computer-Aided Design*, 7:1164–1171, 1988.
  125. G. Masetti and M. Severi. Modeling of carrier mobility against carrier concentration in arsenic-, phosphorus-, and boron-doped silicon. *IEEE Transactions on Electron Devices*, 7:764–769, 1983.
  126. C. Canali. Electron and hole drift velocity measurements in silicon and their empirical relation to electric field and temperature. *IEEE Transactions on Electron Devices*, 22:1045–1047, 1975.
  127. A. Schenk. Rigorous theory and simplified model of the band-to-band tunneling in silicon. *Solid-State Electronics*, 36(1):19–34, 1993.
  128. A. G. Chynoweth. Ionization rates for electrons and holes in silicon. *Physical Review*, 109:1537–1540, 1958.
  129. R. van Overstraeten and H. de Man. Measurement of the ionization rates in diffused silicon p-n junctions. *Solid-State Electronics*, 13:583–608, 1970.
  130. Y. P. Varshni. Temperature dependence of the energy gap in semiconductors. *Physica*, 34(1):149–154, 1967.
  131. H. K. Gummel. A self-consistent iterative scheme for one-dimensional steady state transistor calculations. *Electron Devices*, pages 455–465, 1964.
  132. J. W. Jerome. *Analysis of Charge Transport*. Springer, 1996.
  133. R. Bez, E. Camerlenghi, A. Modelli, and A. Visconti *Introduction to flash memory* Proceedings of the IEEE, vol. 91, no. 4, pp. 489–502, 2003.
  134. P. Pavan, R. Bez, P. Olivo, and E. Zanoni, Flash memory cells-an overview Proceedings of the IEEE, vol. 85, no. 8, pp. 1248–1271, 1997.
  135. Y. Taur and T. H. Ning, *Fundamentals of modern VLSI devices* Cambridge university press, 2013.
  136. [http://www.itrs2.net/itrs\\_reports.html](http://www.itrs2.net/itrs_reports.html).
  137. I. Baek, M. Lee, S. Seo, M. Lee, D. Seo, D.-S. Suh, J. Park, S. Park, H. Kim, I. Yoo, et al., *Highly scalable nonvolatile resistive memory using simple binary oxide driven by asymmetric unipolar voltage pulses* Electron Devices Meeting, 2004. IEDM Technical Digest. IEEE International, pp. 587–590, IEEE, 2004.
  138. I. Baek, D. Kim, M. Lee, H.-J. Kim, E. Yim, M. Lee, J. Lee, S. Ahn, S. Seo, J. Lee, *Multi-layer cross-point binary oxide resistive memory (oxram) for post-nand storage application* IEEE International Electron Devices Meeting, 2005. IEDM Technical Digest, pp. 750–753, IEEE, 2005.
  139. S. Lai, *Current status of the phase change memory and its future* Electron Devices Meeting, 2003. IEDM’03 Technical Digest. IEEE International, pp. 10–1, IEEE, 2003.
  140. K. Wang, J. Alzate, and P. K. Amiri, *Low-power non-volatile spintronic memory: Stt-ram and beyond* Journal of Physics D: Applied Physics, vol. 46, no. 7, p. 074003, 2013.
  141. W. Koelmans, T. Bachmann, F. Zipoli, A. Ott, C. Dou, A. Ferrari, O. Cojocaru-Miredin, S. Zhang, C. Scheu, M. Wuttig, et al., *Carbon-based resistive memories* Memory Workshop (IMW), 2016 IEEE 8th International, pp. 1–4, IEEE, 2016.
  142. J. Frenkel, *On pre-breakdown phenomena in insulators and electronic semi-conductors* Physical Review 54 (8) (1938) 647.
  143. S. Manzini, *Electronic processes in silicon nitride*, Journal of Applied Physics 62 (8) (1987) 3278–3284.
  144. S. Makram-Ebeid, M. Lannoo, *Quantum model for phonon-assisted tunnel ionization of deep levels in a semiconductor* Phys. Rev. B 25 (1982) 6406–6424.
  145. P. C. Arnett, *Transient conduction in insulators at high fields* Journal of Applied Physics 46 (12) (1975) 5236–5243.
  146. A.G.Mauri et al. *Comprehensive numerical simulation of threshold-voltage transients in nitride memories* Solid-State Electronics 56 (1) (2011) 23 – 30.
  147. S. R. Ovshinsky. *Reversible electrical switching phenomena in disordered structures*. Phis. Rev. Lett. 21, 1450 (1968).
  148. H. S. P. Wong, S. Raoux, S. Kim, J. Liang, J. P. Reifenberg, B. Rajendran, M. Asheghi, K. E.

- Goodson. *Phase change memory*. Proceedings of the IEEE, 98(12), 2201-2227 (2010).
149. A. E. Owen, J. M. Robertson *Electronic conduction and switching in chalcogenide glasses*. IEEE Trans. Electron Devices, 20, 105 (1973).
  150. D. Adler, M. S. Shur, M. Silver, S. R. Ovshinsky. *Threshold switching in chalcogenide-glass thin films*. J. Appl. Phys. 51, 3289 (1980).
  151. M. Wuttig, N. Yamada. *Phase change materials for rewritable data storage*. Nature Materials, 6, 824-832 (2007).
  152. Tang, T.-Y., Cho, J.-Y., Park, Y.-J. and Joo, Y.-C. *Driving forces for elemental demixing of GeSbTe in phase-change memory: Computational study to design a durable device*. Current Applied Physics; 2013
  153. Novielli, G. *Development of physical and numerical models for mass transport in phase change materials*. Master Degree Thesis; 2013
  154. A.Pirovano, A.L. Lacaita, A. Benvenuti, F. Pellizzer, R. Bez. *Electronic switching in phase-change memories*. IEEE Transaction on Electron Devices, 51, 452-459 (2004).
  155. S. Lai, T. Lowrey. *OUM - A 180 nm nonvolatile memory cell element technology for stand alone and embedded applications*. IEEE International Electron Devices Meeting 2001.
  156. Janek, J., Korte, C. and Lidiard, A. B. *Thermodiffusion in ionic solids - model experiments and theory in book Thermal nonequilibrium phenomena in fluid mixtures*; . Springer, 2002.
  157. Novielli, G. and Ghetti, A. and Varesi, E. and Mauri, A. G. and Sacco, R. *Atomic migration in phase change materials*. Electron Devices Meeting (IEDM), 2013 IEEE International, pp 22.3.1-22.3.4
  158. D. Ielmini. *Threshold switching mechanism by high-field energy gain in the hopping transport of chalcogenide glasses*. Physical Review B, 78, 035308 (2008).
  159. I. Valov, R. Waser, J.R. Jamenson, M.N. Kozicki *Electrochemical metalization memories - fundamentals application, prospects*. nanotechnology, 22 2011.
  160. Ielmini, D. *Filamentary switching model in RRAM for time, energy and scaling projections*. IEEE IEDM Tech. Dig. 409-412, 2011.
  161. Kozicki, M. N., Gopalan, C., Balakrishnan M., Park, M., Mitkova, M. *Non-volatile memory based on solid electrolytes NVMTS*. Proc. Non-Volatile Memory Technology Symp., 10, 2004.
  162. Schindler, C., Thermadam, S. C. P., Waser, R., Kozicki, M. N. *Bipolar and unipolar resistive switching in Cu-doped SiO<sub>2</sub>*. IEEE Trans. Electron Devices, 54, 2007.
  163. Kund, M., Beitel, G., Pinnow, C. U., Rohr, T., Schumann, J., Symanczyk, R., Ufert, K. D., Muller, G. *Conductive bridging RAM (CBRAM): An emerging non-volatile memory technology scalable to sub 20nm*. IEDM Techn. Dig., 754-757, 2005.
  164. R.Waser,R. Dittman, G. Staikov, K. Szot *Redox-Based Resistive Switching Memories -Nanoionic Mechanism, Prospects and Challenges*. Adv.Material, 21, 2632-2663, 2009.
  165. A.Klein SanDisk - Flash Memory Summit. 2015.
  166. K.Parat and K.Dennison IEEE IEDM, 2015.
  167. S. M. Amoroso, C. M. Compagnoni, A. Mauri, A. Maconi, A. S. Spinelli, and A. L.Lacaita, *Semi-analytical model for the transient operation of gate-all-around charge-trap memories*. IEEE Transactions on Electron Devices, vol. 58, no. 9, pp. 3116–3123, 2011.
  168. A. Mauri, S. Amoroso, C. M. Compagnoni, A. Maconi, and A. S. Spinelli, *Comprehensive numerical simulation of threshold-voltage transients in nitride memories*. Solid-State Electronics, vol. 56, no. 1, pp. 23–30, 2011.